

Dissertation zur Erlangung des Doktorgrades
der Fakultät für Chemie und Pharmazie
der Ludwig-Maximilians-Universität München

SnTiO_3 – a lone pair model system for studying
structure-property relationships in photocatalysis,
ferroelectricity and beyond

Leo Peter Otto Diehl

aus

Zweibrücken, Deutschland

2020

Erklärung

Diese Dissertation wurde im Sinne von § 7 der Promotionsordnung vom 28. November 2011 von Frau Prof. Dr. Bettina Lotsch betreut.

Eidesstattliche Versicherung

Diese Dissertation wurde eigenständig und ohne unerlaubte Hilfe erarbeitet.

München, 27.07.2020

Leo Diehl

Dissertation eingereicht am 18.02.2020

1. Gutachterin: Prof. Dr. Bettina Lotsch
2. Gutachter: Prof. Dr. Wolfgang Schnick

Mündliche Prüfung am 08.06.2020

Für Aaron

Acknowledgments

Mein besonderer Dank geht an Frau Prof. Dr. Bettina Lotsch. Die Möglichkeit ein Thema in dieser Vollständigkeit und wissenschaftlichen Tiefe zu bearbeiten, geleitet vom Wunsch nach echter Grundlagenforschung, war nur durch die Geduld, den Rat und die gegebenen Freiräume möglich. Ich habe dadurch viele interessante Aspekte der chemischen Forschung kennenlernen dürfen.

Ich danke ebenso Herrn Prof. Dr. Wolfgang Schnick für die Übernahme des Zweitgutachtens und die immer unkomplizierten Möglichkeiten im Arbeitskreis nach Hilfe zu fragen.

Herrn Prof. Dr. Geoffrey Ozin möchte ich besonders danken für den hohen Motivationsansubch zu Beginn der Doktorarbeit, die Inspiration und das Angebot des „Flexi-PhD“. Leider waren zum Ende die Überschneidungen thematisch nicht mehr so fruchtbar. Trotzdem habe ich jedoch viel von seiner Erfahrung profitiert.

Mein Dank gilt auch Herrn Prof. Dr. Jürgen Köhler für die Sympathie und das frühe Interesse an SnTiO_3 , das mir zusätzliche Motivation für mein Promotionsthema gegeben hat, sowie den weiteren Beisitzern Prof. Dr. Joost Wintterlin, Prof. Dr. Hans-Christian Böttcher und PD Dr. Constantin Hoch, meines Prüfungskomitees.

Ich möchte mich insbesondere auch bei Viola Duppel und Claudia Kamella bedanken. Ihr seid wirklich die guten Seelen dieses Arbeitskreises. Wie Ihr, waren auch alle anderen CTAs und Techniker in Stuttgart stets hilfreich und konnten mir mit beeindruckendem Fachwissen weiterhelfen.

Spezieller Dank gilt auch allen meinen Koautoren, deren Expertisen unerlässlich für meine Projekte waren. Insbesondere möchte ich hier auch Dr. Alberto von Mankowski und Dr. Luzia Germann für das sehr hilfreiche Korrekturlesen danken.

Ich möchte meinen Kollegen in München, Stuttgart und Toronto danken. Die Arbeitsatmosphäre war ausnahmslos gut und ich war immer gerne im Labor mit Euch. Besonders hervorheben möchte ich Hendrik Schlomberg und Sascha Harm, ich bin beeindruckt von Eurem Fachwissen und Eurer Gelassenheit. Auch Dr. Florian Pielnhöfer gilt mein besonderer Dank, da er mir in Zeiten der wissenschaftlichen Zweifel thematisch und begeisterungsmäßig neuen Schub gab.

Ich möchte meinen Kooperationspartnern Dr. Siyuan Zhang, Prof. Dr. Christina Scheu und Dr. Lkhamsuren Bayarjargal, sowie Theresa Bock und Prof. Dr. Rainer Pöttgen besonders danken. Es war stets angenehm mit ihnen zusammenzuarbeiten.

Ich danke insbesondere auch den netten Kollegen der Arbeitskreise Schnick und Johrendt und meinen zahlreichen Hiwis und Praktikanten für ihre wissenschaftlichen Ideen und die persönliche Weiterentwicklung meinerseits.

Liebe Vera, Peter und Nora, ich danke Euch zutiefst für Wärme, nie endendes Interesse und uneingeschränkte Unterstützung nicht nur in den letzten fünf Jahren, sondern schon immer.

Carina, Dir danke ich unendlich für Deine Liebe und das größte Geschenk, das Du mir machen konntest. Ich hoffe unser Glück endet nie.

Our knowledge can only be finite, while our ignorance must necessarily be infinite.

Karl Popper

Summary

Lone pair materials have proven to be of high relevance in many technologically relevant fields. In this work we established SnTiO_3 as a new platform, allowing for an in-depth investigation of lone pairs and their impact on electronic and crystallographic structure. This work focuses on the synthesis of SnTiO_3 , its photocatalytic application and potential ferroelectricity.

The use of a soft chemistry approach enabled the synthesis of the long-sought after SnTiO_3 , circumventing problems of disproportionation and oxidation. We show that SnTiO_3 adopts a crystal structure corresponding to an expanded version of the ilmenite structure-archetype. The heavily stacking faulted nature of bulk SnTiO_3 could be rationalized by the extremely low energetic differences between the polytypes as obtained by DFT calculations. By application of EELS and NMR analysis methods it was possible to show the impact of lone pairs on both the local octahedral and the long-range stacking regime. The ilmenite-type SnTiO_3 itself is, however, unsuitable for ferroelectric applications due to the fact that the dipole moments of neighboring TiO_6 octahedra cancel each other.

Perovskite-type SnTiO_3 , in contrast, has been predicted theoretically to be a potential ferroelectric, offering the advantage of reduced toxicity compared to commercial $\text{Pb}(\text{Ti,Zr})\text{O}_3$. By scanning of the phase space using a data mining and a global search algorithm around the ilmenite-type derived SnTiO_3 several experimentally accessible structure candidates were identified, including two different perovskite-type compounds. A tetragonally distorted SnTiO_3 is predicted to be stable at pressures between 11-15 GPa and an orthorhombic SnTiO_3 at pressures above 15 GPa. However, both do not show freezing of the corresponding soft modes and thereby have no switchable dipole moments and thus no ferroelectric behavior.

In-situ observation of high pressures on SnTiO_3 using diamond anvil cells up to 45 GPa in both Raman spectroscopy and powder diffraction, identified three phase transitions at 1 GPa, 5 GPa and about 20 GPa. They are tentatively assigned to a change in stacking order, an isostructural 2nd order phase transition and a potentially incomplete transition to perovskite-type SnTiO_3 , respectively. Furthermore, the extremely soft nature of SnTiO_3 (bulk modulus = 23 GPa) was in accordance with anisotropic compressibility caused by the van der Waals gap.

The initially expected advantages of SnTiO_3 in photocatalysis regarding light absorption, charge transport and separation are outweighed by the disadvantages of defect formation and surface instability. SnTiO_3 indeed has extremely low hole effective masses at $< 0.2 m_e$ and nearly ideal band gap of about 1.8 eV. However, the intrinsic instability of Sn^{2+} lone pairs suggests that internal heterojunctions remain feasible in principle, but only by using more stable lone pair compounds. The intrinsic presence of surface Sn^{4+} is explained by the extremely low ionization

potential of SnTiO₃. Furthermore the anti-bonding character below the Fermi level makes partial oxidation/hole doping of SnTiO₃ favorable.

Direct interlayer Sn-Sn interactions as identified by DFT and NMR underline the 3D-character of seemingly 2D SnTiO₃, and thus make exfoliation challenging and potentially hamper proper separation over an internal heterojunction. The identification of these strong direct interlayer Sn-Sn interactions allows for rationalizing the found stacking polytypes in SnTiO₃ and potentially opens an approach to even understand the polytypes' range.

The results of this thesis underline the importance of lone pair materials as model systems to study structure-property-relationships. The challenges and opportunities posed by lone pairs, such as stacking faults, rendering single-crystal growth challenging and the convolution of bulk and surface effects (such as presence of Sn⁴⁺) necessitate a kaleidoscope of different specialized analysis techniques while revealing an extremely rich structural, electronic and catalytic chemistry. The position of SnTiO₃ as a link between the 2D transition metal chalcogenides and the 3D perovskite solid state chemistry is unique and therefore promises further revelation of structure-property-relationships and interesting applications of SnTiO₃ beyond photocatalysis and ferroelectricity.

Table of Contents

1. Introduction.....	1
1.1. Structure-property relationships in materials chemistry	1
1.2. The stereochemically active lone pair.....	2
1.3. Photocatalytic water splitting	3
1.3.1. Photocatalytic water splitting in semiconducting metal oxides	6
1.3.2. Band structure engineering	7
1.3.3. Lone pairs in photocatalysts.....	8
1.3.4. Charge carriers in lone pair materials.....	10
1.4. Topotactic “soft” chemistry	11
1.5. Structural disorder induced by lone pairs.....	12
1.5.1. Stacking faults.....	12
1.5.2. Bonding situation in layered lone pair materials.....	13
1.5.3. Octahedral distortions.....	14
1.5.4. Lone pairs under pressure	17
1.6. Objectives.....	19
1.7. References	20
2. Structure-Directing Lone Pairs: Synthesis and Structural Characterization of SnTiO ₃	30
Abstract.....	30
2.1. Introduction	30
2.2. Experimental Procedure.....	31
2.3. Structural Characterization	32
2.4. Summary	38
2.5. Associated Content.....	39
2.6. Author Information.....	39
2.6.1. Corresponding Author	39
2.6.2. Funding Sources.....	39
2.6.3. Notes.....	39
2.7. Acknowledgment	39
2.8. References	40
3. Examining experimentally accessible structural candidates of SnTiO ₃ : The search for novel ferroelectric materials.....	44
Abstract.....	44
3.1. Introduction	44
3.2. Methodology	46
3.3. Results and Discussion	47

3.3.1. Structure Models	47
3.3.2. Energy Landscape	48
3.3.3. Electronic band structures and bulk modulus	51
3.3.4. Possible Ferroelectricity	52
3.4. Conclusions	54
3.5. References	55
4. High-pressure phase transitions of ilmenite-type derived SnTiO ₃	57
Abstract.....	57
4.1. Introduction.....	57
4.2. Crystal Structure at ambient pressure.....	58
4.3. Raman spectroscopy at ambient pressure	59
4.4. Raman spectroscopy at high-pressure.....	62
4.5. Crystal structure (powder diffraction) at high-pressure	65
4.6. Optical absorption spectroscopy at high-pressure.....	69
4.7. Conclusions	70
4.8. Experimental Procedures.....	70
4.8.1. Synthesis	70
4.8.2. High-pressure experiments	70
4.8.3. Raman spectroscopy	70
4.8.4. Second harmonic generation (SHG)	71
4.8.5. Optical absorption spectroscopy	71
4.9. Acknowledgements.....	71
4.10. References.....	72
5. Competing factors in the directed design of photocatalysts: The case of SnTiO ₃	75
Abstract.....	75
5.1. Introduction.....	75
5.2. Results and Discussion	76
5.2.1. Crystal structure and electronic structure of SnTiO ₃ (space group $R\bar{3}$).....	76
5.2.2. Photocatalytic activity	78
5.2.3. Band alignment	80
5.2.4. XPS and TEM and XRD.....	83
5.2.5. ¹¹⁹ Sn-NMR.....	87
5.2.6. ¹¹⁹ Sn Mössbauer spectroscopy.....	89
5.2.7. Excitation probabilities and photoluminescence.....	92
5.3. Conclusions	95
5.4. Methods	96

5.4.1. Synthesis	96
5.4.2. H ₂ evolution (HER)	96
5.4.3. O ₂ evolution reaction (OER).....	96
5.4.4. Photoelectrochemical Characterization (PEC).....	97
5.4.5. UV-Vis spectroscopy and photoluminescence	97
5.4.6. X-ray photoelectron spectroscopy XPS	97
5.4.7. X-ray powder diffraction (XRPD)	97
5.4.8. Nuclear Magnetic Resonance spectroscopy (NMR)	97
5.4.9. ¹¹⁹ Sn Mössbauer spectroscopy	97
5.4.10. Density Functional Theory (DFT)	98
5.5. Acknowledgments	99
5.6. References	100
6.0 Conclusions and Outlook.....	106
A: Supporting Information for	
Structure-Directing Lone Pairs: Synthesis and Structural Characterization of SnTiO ₃	110
A.1 Synthesis	110
A.2 ICP-AES	111
A.3 TGA	111
A.4 TEM	111
A.5 XRPD	112
A.6 Crystal structure details	112
A.7 Structural derivation of possible stacking faults.....	113
A.8 <i>DIFFaX</i> -Simulations (Experimental)	114
A.9 <i>DIFFaX</i> -Simulations (Results)	115
A.10 Microstructure Description by a Multiphase Approach	117
A.11 EELS.....	119
Ti-L _{2,3} edge.....	119
O-K edge	119
A.12 Solid-State NMR Spectroscopy	120
Spectral simulations.....	120
Quantum Chemical Calculations - NMR.....	121
A.13 Quantum Chemical Calculations – Modelling of the polytypes.....	123
A.14 References	124
B: Supporting Information for	
High-pressure phase transitions of ilmenite-type derived SnTiO ₃	126
B.1 SHG of SnTiO ₃ and three reference materials.....	126

B.2 Representation of selected vibrational modes of ABC-type SnTiO ₃ ($R\bar{3}$).....	126
B.3 Analysis of peak maxima and FWHM.....	127
B.4 Computational pressure dependence of Raman modes.....	128
B.5 Grüneisen-Parameters	128
B.6 Temperature dependence.....	129
B.7 Possible high-pressure perovskite-like SnTiO ₃	129
B.8 References	130
C: Supporting Information for	
Competing factors in the directed design of photocatalysts: The case of SnTiO ₃	131
C.1 Electronic and Optical properties.....	131
C.2 Thermogravimetric Analysis (TGA).....	133
C.3 ¹ H ss-NMR.....	133
C.4 X-ray photoelectron spectroscopy (XPS).....	134
C.5 Exfoliation Energy	135
C.6 Composition.....	135
C.7 Photocurrent switching.....	136
C.8 Wavelength dependent H ₂ evolution.....	137
C.9 Dielectric constants for SnTiO ₃ , directional dependence.....	138
C.10 References.....	139
D. List of Publications and Contributions.....	140

1. Introduction

1.1. Structure-property relationships in materials chemistry

Ever since the beginning of humankind, it has been the essence of humanity to use materials or tools to create something new. The use of a sharp edge of a stone to cut a piece of meat may seem intuitive, but it is less straight forward to use a combination of KNO_3 , charcoal and sulfur as gunpowder¹ or an early galvanic cell as local analgesia², and completely unintuitive to use PbTiO_3 as a little motor to move a stage by only a few nanometers³. However, it is also the essence of humanity to explore the potential for further applications of a material or tool. This exploration can take months, years, or even millennia. It is humanities' dream to fully understand each and every (natural) parameter and ultimately be able to predict, if not design from scratch, new applications and properties.

In the field of solid-state and materials chemistry both syntheses and applications remain mostly explorative. This is not surprising keeping in mind the myriad of combinatorial possibilities in the periodic table of elements, let alone the addition of parameters such as particle size, defect chemistry, and many more. To the day, new and unexpected chemical bonds are being identified in solids⁴ and the more recent identification of new physical states of matter, such as topological insulators,⁵ adds more variables to the playground. Yet, science has made huge steps towards the detailed understanding of the correlation between structure, property, and eventually, applications. Especially the systematic synthesis of new compounds, i.e. the "chemist's core business", to study hypotheses around certain structure-property relationships, remains of tremendous interest.

Compounds with lone pair cations are good examples where introduction of a certain structural element has allowed for deeper understanding of correlating properties. Since the 1950s lone pairs have been identified as major reason for piezoelectric distortions in lead titanates³ and more recently received attention due to the discovery of hybrid perovskites as efficient solar absorbers⁶. In both cases lone pairs have allowed to extract structure-property relationships. Despite decades of research lone pair materials therefore still allow for a deep understanding of the correlation between electronic and crystallographic structure, with many applications.

1.2. The stereochemically active lone pair

In the following paragraphs, we want to first define the class of lone pair materials, then introduce photocatalysis as a general concept and eventually elaborate on the use of lone pair cations in photocatalysts as an alternative for valence band tuning, highlighting possible advantages.

According to IUPAC a lone pair is defined as “two paired electrons localized in the valence shell on a single atom.”⁷. Classically, these occur on anions and define molecular structures. Their stereochemical activity is explained by hybridization of *s*- and *p*-orbitals. In the most simple case of H₂O, the O *s*- and O *p*-orbitals are combined to give four *sp*³-orbitals of which two form bonds to the hydrogen atoms and the other two form lone pairs occupying the space through maximum repulsion forming a tetrahedron.

Likewise, lone pairs also appear on post-transition metal cations and their stereochemical activity was described historically by a hybridization of *s*- and *p*-orbitals on the cation resembling the observations made for anions⁸. In 2011 Walsh *et al.*⁹ revised this classical model for lone pairs emphasizing the role of the anion, which had first been proposed by Watson and Parker in 1999¹⁰ for α -PbO and has since been further discussed¹¹⁻¹⁴. The revised model allows, for example, the accurate prediction of the structural symmetries found in the series from SnO, SnS to SnSe, and SnTe. SnO crystallizes in the tetragonal litharge structure, while SnS and SnSe are cubic and SnTe possesses the rocksalt structure without any distortions.

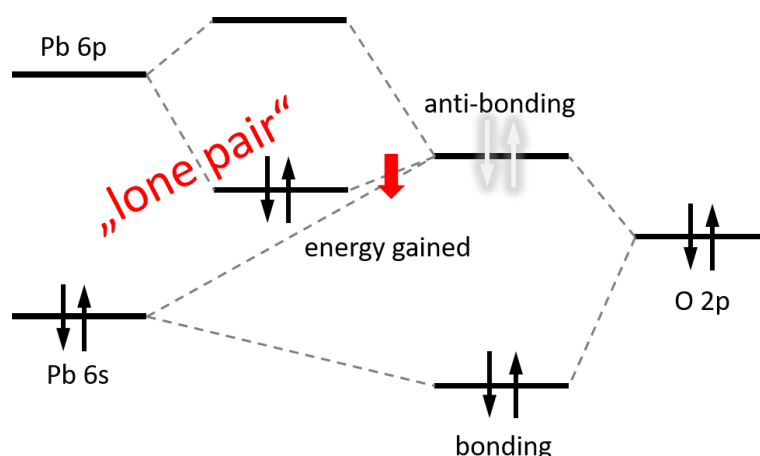


Figure 1.1. Scheme showing the revised lone pair model according to Walsh *et al.*⁹. The hybridization between the anti-bonding orbital of Pb 6s and O 2p with the Pb 6p states leads to the formation of the stereochemically active lone pair. The energy gained by occupation of the new hybrid orbital drives the formation of lone pairs.

Walsh *et al.* show that only if the anion’s *p*-orbital and the post-transition metal’s *s*-orbital are energetically aligned, hybridization is possible and, consequently lead to stereochemically active lone pairs. More specifically, it is the anti-bonding hybrid orbital formed between the cation

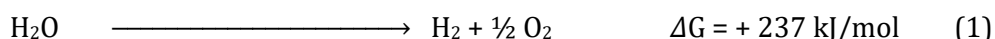
s-orbital and the anion *p*-orbital, interacting with the *p*-orbital of the cation that eventually induces the stereochemical activity (Figure 1.1). If the energy gained through anti-bonding orbital stabilization is higher than the energy lost through smaller coordination number, (stereochemically active) lone pairs form. Materials fulfilling the condition of stereochemically active and as such structure-directing lone pairs are thus termed “lone pair materials”, according to the nomenclature of Walsh.

The influence of lone pairs may be differentiated by the impact on electronic structure by hybridization and involved absolute electronic energies on the one hand, and by the impact on spatial arrangement of atoms by their stereochemical activity on the other hand. Both of these structure-property relationships are studied in this work, by correlating the electronic structure with the photocatalytic properties and by correlation of the crystallographic structure with distortions and faults, potentially inducing ferroelectric properties. It is obvious that both are intertwined at all times and may only be considered separate on a conceptual level.

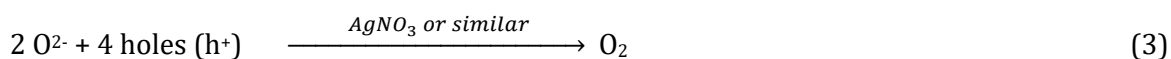
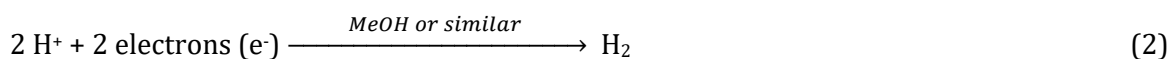
1.3. Photocatalytic water splitting

The EU population’s energy demand is mainly nourished by coal and natural gas¹⁵. These fossil fuels form CO₂ upon combustion, a greenhouse gas identified as major contributor to climate change. One alternative approach to avoid the formation of CO₂ could be switching to an H₂-based energy economy¹⁶. In comparison to carbon combustion only H₂O will form, which is easier to reintegrate into a sustainable cycle. To date, however, the large scale production of H₂ is either based on the steam reformation of fossil fuels or the electrolysis of water, an energy intensive process, both hampering the use of H₂ as a sustainable and clean fuel¹⁷⁻¹⁹.

Photocatalytic water splitting offers a solution to the energetic problem, as directly exploiting abundant sun light as the energy source for H₂ is a sustainable alternative. While plants perform photosynthesis, and thereby produce products of higher energetic value, photocatalysis in the narrow sense only enables thermodynamically favored reactions.^{20, 21} The complete water splitting reaction²² (1) is indeed endergonic and can thus not be performed by a simple photocatalytic process:



only the two half-reactions, H₂-evolution (2) and O₂-evolution (3) may be exergonic²⁰, when using additional sacrificial donors:



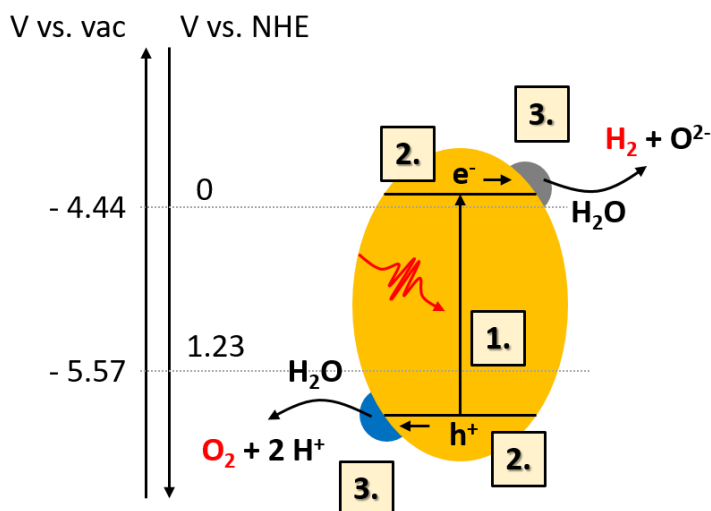


Figure 1.2. Scheme of photocatalytic water splitting on a semiconductor particle with the respective energy ranges of band positions both against vacuum and Normal Hydrogen Electrode (NHE) at pH 0. 1. Absorption of a photon and excitation process, 2. charge separation process, and 3. surface catalytic reaction to form both H_2 and O_2 from H_2O .

In the photocatalytic reaction, at least three main processes can be distinguished. Firstly, the provision of the respective electrons and holes²³ by absorption of a photon in a semiconductor (Figure 1.2). Secondly, the charge carriers will need to separate spatially and migrate to the surface, more precisely the co-catalyst. At the surface, in a third step, the charge carriers either recombine at defects or, ideally, are transferred to the electrolyte. Only the last step is classically described by heterogeneous catalysis, which is the interaction of the reactants with a surface such that the thermodynamic equilibrium is reached faster²⁴. Yet, photon absorption and charge carrier separation are an integral part^{25, 26} of the reaction and are mostly determined by the electronic structure of the semiconductor. Thus, lone pairs can strongly influence these processes. This introduction will therefore focus on internal or intrinsic properties of semiconductors and less on the charge transfer and thus surface related problems such as the choice of co-catalysts or similar. To have the full picture in mind a short overview of all required steps is given in the following paragraphs including a short history of photocatalytic water splitting.

Fundamental for photon interaction with the semiconductor is the appropriate energy of the photon required to overcome the band gap. At the same time, a minimum energy, 1.23 eV per electron for water splitting, is required to drive the desired photocatalytic reaction. Shockley and Queisser have shown this for photovoltaic materials, which have an efficiency optimum depending on the quantity of available photons with suitable energy, the so-called Shockley-Queisser limit²⁷.

1. Introduction

In addition to the appropriate energies required, also the electronic density of states will limit the amount of potentially excitable electrons. Furthermore, depending on the symmetry of the involved orbitals, additional selection rules may limit the efficiency of light absorption.

After absorption of a photon, an exciton is generated. Excitons are characterized mainly by the electrostatic binding energy (the exciton binding energy) between the electron and its mirror charge: the “hole”. Generation of separated charges will need to overcome this energy. For effective migration of the charge carriers, the crystal has to be of high quality (defect-free) and the migration pathway to the surface should ideally be short, as for example in nanostructures²⁸. Strong interaction of the excited charge with the materials’ lattice (electron-phonon-coupling) may trap charge carriers locally²⁹ and hence hinder efficient charge carrier migration.

In general one distinguishes between systems with full water splitting capability, catalyzing both half-reactions, and systems that only catalyze one half-reaction, in which the opposite charge carrier can either be quenched by a so-called “sacrificial agent” or transported to another electrode, often aided by an additional voltage in photoelectrochemical cells³⁰. For all setups, the essential requirement is the minimum required energy for the water splitting reaction provided by the absorbed photon. 1.23 V (118 kJ/mol (normalized to one electron)) on the electrochemical scale is the minimum energy required to enable the full reaction. In real systems, overpotentials will add to the 1.23 V. It has to be emphasized that the role of the co-catalysts³¹ and as such the classical heterogeneous catalysis is the reduction of these overpotentials. Band bending and therefore surface overpotentials do not only depend on the type, size and distribution of the applied cocatalyst³², but also intrinsically on the provided amount of separated charge carriers²⁵.

The H₂-evolution half-reaction is generally considered to be less complex. The less intricate use of only two electrons per evolved H₂ and the well-established co-catalysts such as Pt nanoparticles and also Ni nanoparticles³³ have made H₂-evolution rates possible in the range of mmols·g⁻¹·h⁻¹³⁴. These catalysts still rely on either additionally applied voltages or the use of the previously mentioned sacrificial donors, which quench the holes due to their more negative oxidation potential compared to H₂O. The most commonly used donors, such as methanol and amines (triethanolamine or triethylamine), are consumed³⁵ during the reaction. Evidently, for large-scale use a sustainable and continuous supply of electrons is necessary. Therefore, it is of great importance to also find good catalysts for the O₂-evolution half-reaction³⁶, which would provide these electrons. This reaction, in contrast to H₂-evolution, is intrinsically more intricate, due to four holes/electrons involved per stoichiometrically evolved O₂. The higher amount of electrons transferred require higher retention times of the intermediates on the catalysts’ surface, concurrently increasing the probability of the back reaction. It has been shown that certain core shell structures^{37, 38} may hamper the reverse reactions.

Nonetheless, for scientific purposes it has proven to be practical to observe only one half-reaction at a time. Ideally, the use of the “sacrificial agent”^{35, 39} shifts the rate-limiting step towards the half-reaction to be observed. Change of parameters and potential improvement of photocatalytic rates will thus be correlated to the half-reaction that one intends to optimize. Of course, appropriate dark and blank runs are indispensable to exclude current doubling⁴⁰, catalyst self-oxidation,²⁵ or other factors reducing the evolution of the desired H₂ or O₂ products.

1.3.1. Photocatalytic water splitting in semiconducting metal oxides

In 1972 Honda and Fujishima⁴¹ first showed successful water splitting on TiO₂. Since then, metal oxides are an extremely promising class of materials for water splitting applications as well as detailed structure-property relationship studies. The ease of nanostructuring, compositional variety as well as the stability under photocatalytic conditions are fundamental requirements for water splitting, which are relatively simple to fulfill with metal oxides.

The enormous literature with thousands of publications every week dealing with smaller and bigger problems of photocatalysis is out of scope for this introduction. We will therefore focus on structure-property relationships of ternary titanates and compounds with lone pair electrons.

The following paragraph is closely inspired by a review article sketching the history of photocatalysis by Maeda⁴². After the discovery of photocatalytic water splitting activity for TiO₂ it was an intuitive step to try this reaction on titanates as well. Shortly afterwards, successful water splitting on SrTiO₃ was reported⁴³. Still inspired by classical heterogeneous catalysis the reactions were carried out using water vapor. Inoue *et al.* reported BaTi₄O₉⁴⁴ and Na₂Ti₆O₁₃⁴⁵ to have photocatalytic water splitting activity in the early 1990s, thereby broadening the family of catalysts beyond perovskite-type structures. With the discovery of K₄Nb₆O₁₇⁴⁶ the first example of non-titanate-like photocatalyst was found. Niobates and also tantalates⁴⁷ have the benefit of conduction band minima (CBM)⁴⁸ with more negative energies on the electrochemical energy scale, therefore facilitating the charge transfer from the semiconductor to the electrolyte.

Titanates are very well suited for a huge variety of compositions due to their ability to condensate the TiO₆-octahedra into extended sheet-like structural motifs⁴⁹. Especially the exfoliation^{50, 51} into 2D materials by first ion-exchange and then applying shearing forces, through shaking or sonication, led to materials of very high surface area and therefore increased activity^{52, 53}. On the search for catalysts with high surface areas, layered Ruddlesden-Popper and Dion-Jacobson phases were studied by Domen *et al.*⁵⁴ and are still actively discussed today by Osterloh^{28, 55-58} and others⁵⁹.

The full exfoliation into monolayers of many structures, however, has not led to the expected multiplication of catalytic rates. As potential reasons bad charge separation, high surface

recombination and small quantum yield due to the reduced interaction possibilities for the photons with the semiconductor are discussed by Osterloh²⁸.

1.3.2. Band structure engineering

All photocatalysts with d^0 electron configuration (Ti^{4+} , Nb^{5+} , Ta^{5+}) mentioned until now share the disadvantage of being only UV-light active. Due to the small amount of photons (6% on the earth's surface⁶⁰) with energies of 3 eV or more in the solar spectrum the overall water splitting activity for these catalysts is limited. To broaden the energy spectrum useful for water splitting, band structure engineering has been applied successfully. One strategy for band structure engineering is cation substitution, often referred to as "doping"⁶¹⁻⁶³, a terminology that will be used throughout this thesis. The dopant introduces additional electronic states within the large band gap of the semiconductor thus allowing excitation into the conduction band with lower energy photons⁶⁴. For obvious reasons, substitution of CBM-forming d^0 transition metals will affect the CBM (Figure 1.3). However, upon reaching the (stability) limit of substitution the photocatalytic activity might quench completely due to inadequate band alignment with the electrolyte or formation of undesired side phases (Figure 1.3), if an unsuitable dopant is chosen.

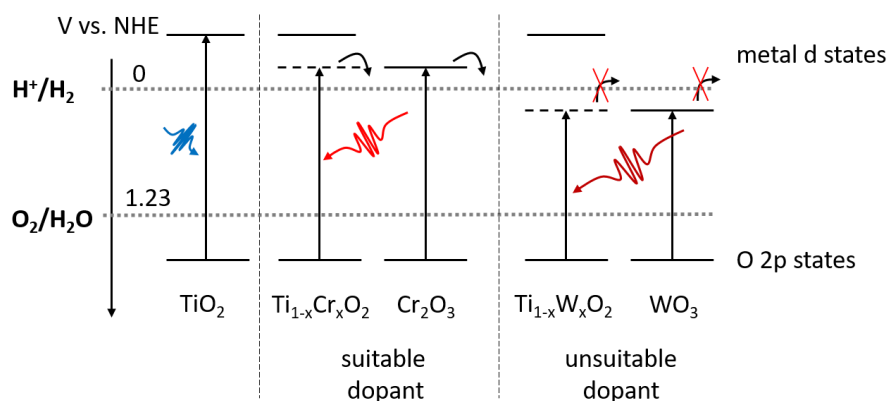


Figure 1.3. Scheme showing band positions of TiO_2 semiconductor upon (hypothetical) introduction of Cr^{3+} dopant with suitable absolute band positions and or W^{6+} dopant with unsuitable impact on the CBM. While the Cr^{3+} introduction in TiO_2 induces visible-light absorption, still allowing for charge transfer to H^+ , W^{6+} pushes the CBM towards too positive potentials.

Furthermore, doping has the disadvantage of introducing potential recombination pathways for the excited and separated charge carriers, due to singular electronic states instead of delocalized bands throughout the crystal⁶². The role of lone pairs in this context is discussed in Chapter 1.3.4. Charge carriers in lone pair materials.

Another strategy to broaden the energy spectrum useful for water splitting is the addition of photosensitizers such as pigments, which will transfer the charge carriers onto the actual catalyst and is discussed in detail in the dye-sensitized solar cell literature⁶⁵⁻⁶⁷. This strategy is closely

interconnected with the design of so-called *p-n*-heterojunctions, which will be discussed in the context “internal heterojunctions” in Chapter 1.3.3 .

The directed tuning of the valence band for visible-light activity has been established by Asahi *et al.* in 2001 with the successful doping of nitrogen into TiO₂⁶⁸. Based on this work many other nitrogen doped or substituted catalysts have been demonstrated to yield efficient visible-light active photocatalysts, such as BaTaO₂N⁶⁹, LaTiO₂N⁷⁰, Ta₃N₅⁷¹, and many more. The possibilities for valence band tuning⁷² in oxides by introduction of or even full substitution with other anions is limited due to the small variety of suitable anions (S²⁻, Se²⁻, Cl⁻, Br⁻, N³⁻, P³⁻). Moreover, decreasing stability of non-oxidic substances under water splitting conditions is observed, e.g. in sulfur doped BiVO₄⁷³, BiOCl^{74, 75}, or CdS⁷⁶⁻⁷⁸, making this approach challenging for use under real conditions.

1.3.3. Lone pairs in photocatalysts

As early as 1998 Kudo *et al.*^{79, 80} reported the use of lone pair containing BiVO₄ as a visible-light active photo(electro)catalyst for oxygen evolution. Soon after, they identified Bi³⁺ as a promising design principle for overall water splitting catalysts⁸¹. As of today BiVO₄^{73, 82, 83} is a well-studied example for a lone pair containing photocatalyst. The disadvantage, however, is the absolute position of the conduction band, which is beneath the water reduction potential⁸⁴. Inspired by the discovery of the highly efficient photovoltaic material methylammonium leadiodide (MAPI) in the year 2009 by Kojima *et al.*⁸⁵, main group elements forming lone pairs have become an even more intriguing design parameter⁸⁶ for synthetic variety in photocatalytic oxides and have been actively investigated in recent years, for example in PbWO₄⁸⁷, SnWO₄^{88, 89}, or PbSb₂O₆⁹⁰. With the emergence of better density functional theory (DFT) calculation methods, Walsh *et al.*¹³ were able to calculate the band structure for BiVO₄, showing that the hybridization of Bi *s*-orbitals and O *p*-orbitals is constituting the valence band maximum (VBM) as speculated by Kudo *et al.*⁷⁹ and later described in the revised lone pair model. Inoue points out that a large dispersion of the band gap forming states may facilitate charge transport and hence catalytic activity⁹¹ and indeed lone pair materials often have steep dispersion at the valence band maximum⁹². A closer look at the charge transport properties in lone pair materials will be given further down in Chapter 1.3.4 Charge carriers in lone pair materials.

It has long been established that charge separation can be aided by either adding an electron or hole sink in the form of a co-catalyst or by designing a *p-n*-heterojunction⁹³. In Figure 1.4, a *p*-doped semiconductor and an *n*-doped semiconductor are shown in contact to aid the spatial charge separation⁹⁴. In the context of polymer solar cells a more intimate mixture of the two conduction pathways^{95, 96} was realized such that a charge separation on nearly molecular level (down to few nm) is achieved in so-called bulk heterojunctions.

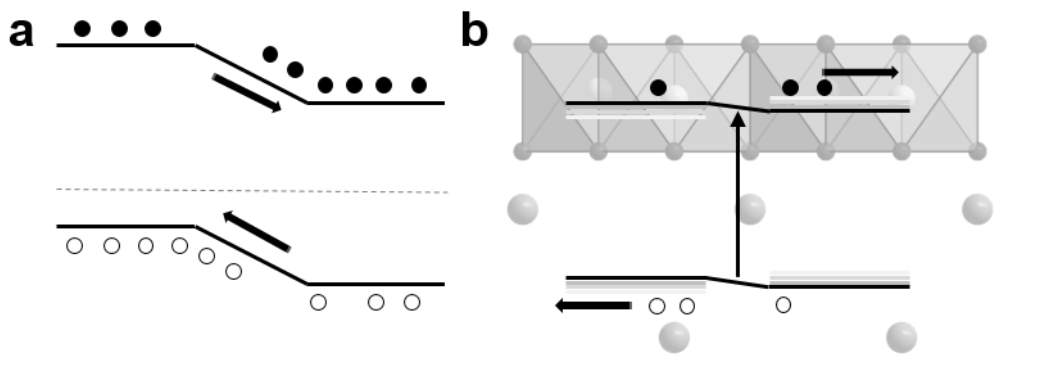


Figure 1.4. a) Scheme of a “classical” p-n-heterojunction, formed due to a suitable band alignment of two semiconductors. Excited charges (filled circles = electrons, empty circles = holes) are energetically favored to accumulate in spatially separated sides of the electrodes. b) “Internal heterojunction” as proposed for Bi₂WO₆, in which the transition metal oxide dominated CBM allows for electron transport and the VBM mainly constituted by the post-transition metal lone pair induces hole transport. The driving factor for charge transport are the band dispersion and small structural deviations.

Upon use of quantum dots of FeS₂ and CdS₂ a similar concept has been realized as “all-inorganic bulk heterojunctions”⁹⁷. During the excitation process, an electron may also move into spatially different orbitals⁹⁴, as known for charge-transfer excitons⁹⁸. If both valence band maximum and conduction band minimum consist of relatively well dispersed bands and allow quick and easy charge dissipation, one can imagine that across band gap excitation will also separate the electron-hole pair. This idea of sub-nanometer charge separation has successfully been established more recently in the 2D material of exfoliated Bi₂WO₆^{81, 99}. The Bi-O-layer forms the VBM, while the spatially separated W-O layer constitutes the CBM, introduced as an “internal heterojunction” (Figure 1.4).

The combination of continuous 2D layers which at the same time constitute CBM and VBM only makes few materials eligible. Fortunately, lone pairs tend to cluster,^{100, 101} thus often forming 2D-like structures dominated by van der Waals-like gaps (as discussed in the context of stacking faults the true nature of bonding across these gaps is more complicated). As mentioned above, these lone pairs often form the VBM, which is highly anisotropic and typically expands perpendicular to the stacking direction. Examples for this type of sheet-like architecture are the mentioned Bi₂WO₆⁹⁹, as well as SnNb₂O₆¹⁰², Sn₂Nb₂O₇¹⁰³ PbSb₂O₆⁹⁰, Bi₂MoO₆¹⁰⁴, Bi₂W₂O₇⁸¹ among others.

Moreover, other examples than 2D-materials are known for lone pair containing photocatalysts, such as Sn₂TiO₄, with a more complicated tetragonal crystal system composed of isolated TiO₆-octahedra bridged through Sn²⁺ ions. Also SnWO₄¹⁴, the above mentioned BiVO₄⁷⁹ and Sr₂Bi₂O₅¹⁰⁵, have isolated lone pairs in common.

1.3.4. Charge carriers in lone pair materials

Lone pairs can help tackling two fundamental issues regarding efficient charge carrier transport. One is the introduction of bands with steep dispersion. The concept of effective masses has been applied successfully to rationalize the easier movement of charge carriers in an electric field. Hautier *et al.*^{92, 106, 107} have identified a number of promising candidates, such as the lone pair materials $K_2Sn_2O_3$ and even tetragonal $PbTiO_3$. Not surprisingly, lower masses indicate less inertia and thus better transport properties. Walsh *et al.*¹⁰¹ were able to show that certain conduction pathways may also benefit from the fact that lone pairs tend to cluster (similar to the van der Waals gaps in 2D materials) in which holes may travel macroscopic distances.

The other fundamental issue is the quantity of charge carriers. Effective doping has been mostly applied for *n*-type (electron conducting) materials; for example in F-doped SnO_2 or Sn-doped In_2O_3 . With regards to intrinsic conductivity oxygen vacancies tend to induce *n*-type defects¹⁰⁸. In contrast, in the lone pair containing SnO ¹⁰⁹ and $Sn_2Nb_{2-x}Ta_xO_7$ ¹¹⁰ *p*-type conduction has been realized. Hosono *et al.* have predicted *p*-type conduction even for mixed valence Sn(II)/Sn(IV) oxides¹¹¹ making them candidates for *p*-type transparent conducting oxides (TCOs)¹¹².

However, while lone pairs offer low effective masses and intrinsic *p*-type conduction, many of these materials have very low density of states¹¹³ at the valence band maximum, which is intrinsic to the steep dispersion. In addition, these bands at higher potentials are often prone to oxidation¹¹⁴.

Charge carrier transport under light may impose additional problems. On the one hand, lone pairs have been discussed to be the reason for relatively high defect tolerance by pushing defects out of the band gap^{115, 116}. More precisely, it is the anti-bonding hybrid orbital which is always higher in energy compared to the individual constituting *s*- or *p*-orbitals hence causing any dangling bonds (individual *s*- or *p*-orbitals) created by cation vacancies to remain within the valence band (Figure 1.5).

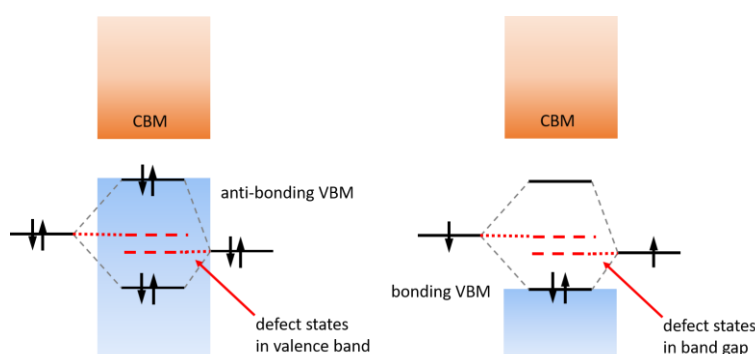


Figure 1.5. Lone pairs leading to defect tolerance by occupation of anti-bonding hybridized states, thus pushing the Fermi level up above the individual atomic defect states.

On the other hand, lone pairs may also be the reason for charge self-trapping¹¹⁷, as described in the form of Pb^{3+} species in hybrid perovskites^{118, 119} and lead halides¹²⁰, which are however also discussed to be centered on the anion^{121, 122}. The self-trapped charges are stable forming mixed-valence states¹²³. Charge self-trapping is a major reason for non-radiative recombination (Figure 1.6), and thus has to be considered when discussing photon-to-hydrogen conversion efficiencies in photocatalysis¹¹⁷.

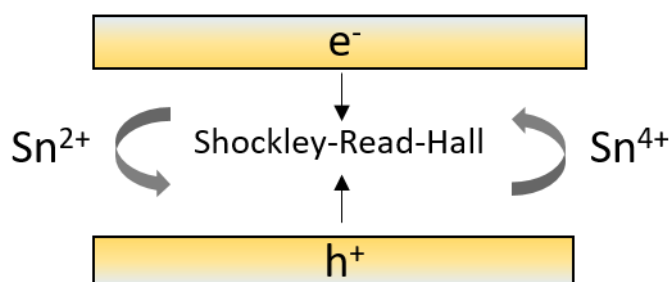


Figure 1.6. Mechanism of non-radiative charge recombination (Shockley-Read-Hall) for a semiconductor with the ability to switch between Sn^{2+} - and Sn^{4+} -defect states within the band gap.

2D structures are known to form quantum wells¹²⁴⁻¹²⁶, due to the very different dielectric constants in the metal dominated layer vs. the organic layer in 2D hybrid perovskites, or the van der Waals layer in lone pair materials. This may further increase exciton binding energies, sometimes above energies that can thermally be achieved at room temperature and, consequently, reduce the photon efficiency drastically.

1.4. Topotactic “soft” chemistry

Topotactic or topochemical reactions have been shown to be a conducive method for the synthesis of layered compounds¹²⁷. In this reaction type, it is possible to take advantage of preformed structural motifs. The motifs kept are, for example, more strongly bound octahedra within a layer compared to the weaker ionic or even van der Waals bound between two layers, which are more prone to react. The target materials are then often accessible by “soft” synthesis routes¹²⁸, such as ion exchange and ion intercalation¹²⁹. The use of soft synthetic routes is of special importance in materials in which multivalent ions, e.g. lone pair cations, are targeted in a specific oxidation state to avoid disproportionation or formation of thermodynamically favored fully oxidized phases. This is exemplified in Figure 1.7 for the reaction of Na_2IrO_3 to delafossite $\text{Cu}(\text{I})_3(\text{NaIr}_2)\text{O}_6$ ¹³⁰ at relatively low temperatures of 400 °C. Although soft chemistry routes for layered compounds mostly focus on solution-based approaches, such as hydrothermal or ionothermal conditions (salt melts)¹³¹, direct reactions via metathesis¹³² may be considered as relatively soft approaches as well. For example, the formation of alkali halides (NaCl, KCl) can drive solid-state reactions to

completion due to their large formation enthalpies and can thus give access to a new “thermodynamic niche”.

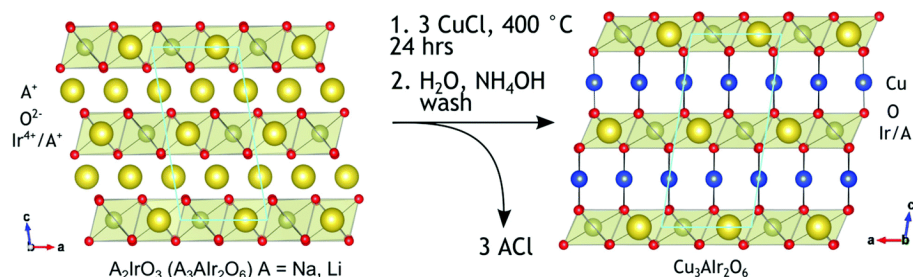


Figure 1.7. Example of a topotactic ion exchange reaction to form a Cu(I) delafossite from a layered precursor at low temperatures by formation of alkali chlorides (ACl) with high lattice energy. (Copyright © The Royal Society of Chemistry 2016).

1.5. Structural disorder induced by lone pairs

Disorder is a common phenomenon present in real structures and may influence (drastically) the physical properties of materials. Even at 0 K, crystals show non-perfect ordering due to presence of dynamic disorder and the resulting configurational entropy gain (zero-point energy). In contrast, static disorder is not derivable from a specific molecular vibration, and includes impurities (intentionally or unintentionally), distortions or stacking faults. If lone pairs with stereochemical activity are introduced in materials, they may influence the crystal both globally, inducing stacking faults, and locally inducing octahedral distortions. For a complete crystallographic treatment the reader is referred to the Crystallographic Tables B¹³³.

1.5.1. Stacking faults

Stacking faults have been studied in detail in close-packed systems such as metals in which *hcp*-type stacking may easily switch to *fcc*-type stacking. The more or less random switching between stacking types leads to polytypism¹³⁴ found not only in metals but also SiC or diamond and are commonly denoted¹³⁵ by the Ramsdell notation (e.g. 9R), Jagodzinski-Wyckoff (e.g. hc) or the ABC notation. In the case of the switching from *fcc* to *hcp* the stacking can be described by only two characteristic stacking vectors (Figure 1.8). Basically, the constraints given by the close packing only allow two energetic minima of the next layer. Stacking vectors leading to AA-type stacking therefore are thermodynamically unfavored (Figure 1.8).

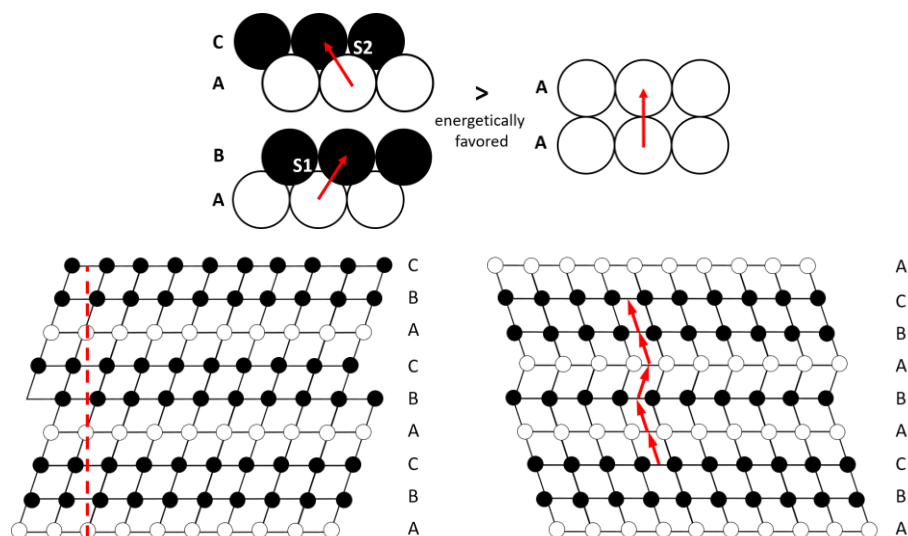


Figure 1.8. a) Close-packing of *fcc*-type stacking (ABC), with the A-layer highlighted in white. b) close-packed system of *fcc*-type stacking with *hcp*-type stacking fault (ABA). The red arrows show the two different stacking vector directions.

1.5.2. Bonding situation in layered lone pair materials

Layered materials in general are prone to stacking faults, especially undergoing exfoliation and restacking. The restacked material shows turbostratic (random) disorder with more than few stacking vectors and with the characteristic reflection broadening in certain crystallographic directions¹³⁶. As-synthesized powders, however, may also show stacking faults, and must hence be characterized by local stacking polytypes^{137, 138}. For simulation and refinement of such faults Dinnebier and Bette describe the principles of stacking faults very well in the recent book *Rietveld Refinement*¹³⁹. The authors point out the possibility of stacking faults to have a certain range. Consequently, after the occurrence of a change in stacking sequence, indicated by the change of a stacking vector, a certain amount of layers may be required for the system to allow for another fault, leading to a microstructure dominated by local twinning. Very recently, Mio *et al.* have come up with a potential explanation for the occurrence of ranges in layered phase-change materials¹⁴⁰. They argue that stacking faults have to be differentiated according to the bonding type between the individual layers. Turbostratic or random faults can only occur, if the layers interact very weakly and locally, as for example found in true van der Waals materials such as graphene. If a “stacking range” and therefore twinning-like behavior is identified, it must be the consequence of long-range next nearest neighbor interactions¹⁴⁰. Taking into account that in the revised lone pair model, lone pairs are strongly dependent on both cation and anion contributions, it is intuitive to understand that through the anionic contribution long-range interactions are possible. In the context of phase-change materials Wuttig *et al.* are even proposing a new bonding type; so-called metavalent bonding¹⁴¹, which is however under debate¹⁴². The presence of direct interactions between the lone pair ions are the consequence of the anti-bonding nature at the VBMs¹⁴³. Hence,

in the real structures electrons will “reshuffle” from anti-bonding lone pairs into bonding cation-cation interactions⁴. This type of bonding is similar to Peierls distortions found for group 15 elements, which are a consequence of an electron deficit. Only by assumption of resonance or delocalization, these types of interactions can be explained properly and thus are intrinsically of a long-range character¹⁴⁴. The van der Waals bonding is in contrast described by local dipole interactions. True van der Waals materials are hence only present if no such range is observed and the two layers are dielectrically and structurally screened from each other. The exact nature of stacking faults may therefore reveal information about the type of interlayer bonding present in layered materials and have shown to be highly important for technologically important applications, such as phase-change materials¹⁴⁰.

1.5.3. Octahedral distortions

In the following paragraphs, ferroelectricity in ATiO_3 titanates will be illuminated as a consequence of local distortions. Here, similar to stacking faults, lone pairs and their respective bonding nature are of decisive influence for the observed phenomena.

As early as 1935 ferroelectric behavior had been observed in the low temperature phase of KH_2PO_4 (KDP)¹⁴⁵. Only after the discovery of ferroelectricity in the perovskite-type titanate BaTiO_3 ¹⁴⁶ the development of macroscopic dipole moments was accepted as a more common phenomenon. Öpik and Pryce¹⁴⁷ first described dipole moments as a consequence of (pseudo-) Jahn-Teller distortion of octahedra. Bersuker then applied this explanation to ferroelectric distortions in titanates^{148, 149}. Ever since chemists and physicists have tried to understand the physics behind this curious and rather unlikely¹⁵⁰ manifestation of structural instability.

Titanates have been synthesized in a plethora of stoichiometries, e.g. the layered compounds BaTi_4O_9 ⁴⁴ and $\text{Na}_2\text{Ti}_6\text{O}_{13}$ ⁴⁵ (see discussion about 2D structures). The technologically most relevant titanates are, however, of ATiO_3 or related composition (Figure 1.9). In 1926 Goldschmidt¹⁵¹ determined a tolerance factor (t) for materials of stoichiometry ABX_3 to estimate which structure-type they would obtain, see formula (4):

$$\frac{R_A + R_X}{\sqrt{2}(R_B + R_X)} = t \quad (4)$$

with R being the radius of the cations A and B, and the anion X, respectively.

For t ranging between 0.8 and 1.0 the structure crystallizes in the perovskite-type structure, below 0.8 it will crystallize in the ilmenite-type and above 1.0 in the calcite-type structure. Hence, relatively big A-site cations will likely result in the (distorted) perovskite-type (e.g. BaTiO_3 , PbTiO_3), while smaller A-site cations will crystallize in the ilmenite-type (e.g. FeTiO_3 , CoTiO_3).

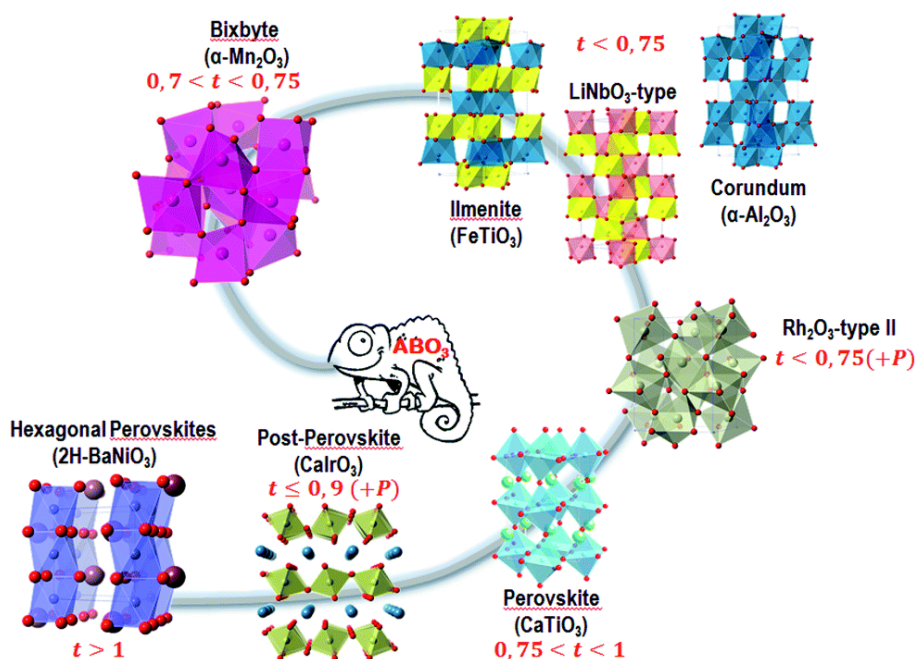


Figure 1.9. Structural family of compounds with ABO_3 stoichiometry, with different Goldschmidt tolerance factors, ranging from Bixbyte ($0.7 < t < 0.75$) to perovskite-type structures ($0.75 < t < 1$). (Copyright © The Royal Society of Chemistry 2015).

An overview of the relationship between the two major structure types for titanates has been given by Navrotsky¹⁵², highlighting that ilmenite-type and perovskite-type structures are interlinked through a $LiNbO_3$ -type structure (as shown in Figure 1.10) and can be interpreted as ordered variants of corundum ($\alpha-Al_2O_3$). The individual layers of edge-sharing AO_6 - and BO_6 -octahedra transform into intermixed layers of $(A,B)O_6$ -octahedra upon transition from ilmenite-type to $LiNbO_3$ -type.

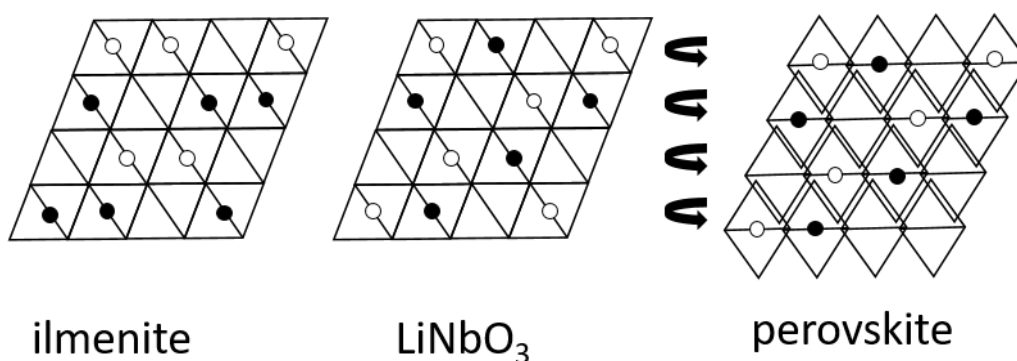


Figure 1.10. Occupation of close packed oxygen octahedra occupied by either A-site cation (white), B-site cation (black) or no cation (empty) in ilmenite-, $LiNbO_3$ - and perovskite-type structures. Arrows indicate the rearrangement required for the transition of edge-sharing BO_6 octahedra in $LiNbO_3$ to corner-sharing in perovskite-type structures by octahedral rotations.

One implication of this phase transition is the change from a centrosymmetric ($R\bar{3}$) to one of the non-centrosymmetric ($R3c$) space groups without inversion symmetry. These space groups “allow” for the manifestation of a dipole moment within a unit cell. If this dipole moment changes in an external electric field, ferroelectric behavior is observed.

It remains out of scope of this introduction to give a complete overview of the current state of discussion about the origins of ferroelectricity. Here, we will therefore stick to the two major lone-pair related mechanisms¹⁵³ and explain them for titanates in perovskite-type structures.

The first mechanism (Figure 1.11) is of displacive type: the Ti-atom moves to an off-center position in all unit cells simultaneously upon reaching the phase transition. The displacement direction from the off-center position will define whether the distortion is tetragonal, orthorhombic or rhombohedral. The sudden change in the atomic position is accompanied by the development of soft phonons in (many) perovskite-type titanates. These phonons (their point groups) foreshadow the symmetry of the distortion and freeze at the point of the phase transition.

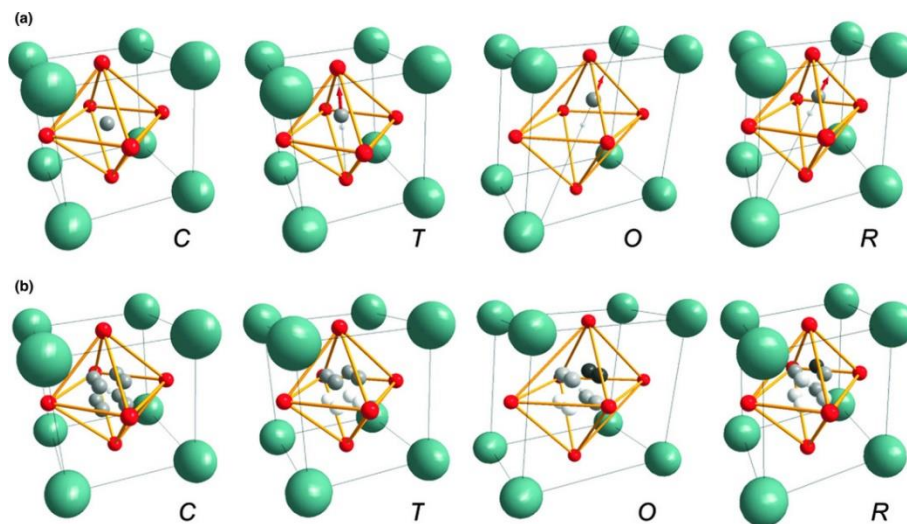


Figure 1.11. Comparison of the two major mechanisms used for explanation of ferroelectricity in perovskite-type structures. a) Displacive picture, with central atom moving into certain crystallographic directions inducing either tetragonal, orthorhombic or rhombohedral distortions. b) Order-disorder type picture showing eight sites occupied with different probabilities as indicated by shades of grey, distortions are induced if certain positions are occupied with higher (black) probability than others (white). (Copyright © Journal of the American Ceramic Society 2011).

The “competing” mechanism (Figure 1.11) is of order-disorder type: the Ti-atom follows a statistical distribution on eight different positions within the octahedron such that each unit cell is distorted individually. If the point of phase transition is reached certain positions are occupied predominantly inducing a macroscopic dipole moment. Both mechanisms can be considered as extrema never really occurring exclusively in reality.

With the discovery of PbTiO_3 and the advancement to $\text{Pb}(\text{Ti,Zr})\text{O}_3^3$ (PZT) lone pairs were discovered as a potent design parameter^{154, 155} for inducing non-centrosymmetric distortions. Especially the higher transition temperature as well as the bigger dipole moment were desired properties correlating with the introduction of the lone pair cation. The intuitive advantage of lone pairs is the inherently non-centrosymmetric environment around the respective cation¹⁵⁶. Only few examples were reported in which lone pair cations do not induce the desired distortion^{157, 158}.

The exact role of lone pairs is still a matter of discussion. Following the chemical intuition, B-site driven non-centrosymmetry is said to be the reason for ferroelectricity. However, the actual reason for the structural instability is still under debate. Schütz *et al.*¹⁵⁹ have shown that covalency and thus directional bonding of the lone pair cation may induce instabilities and also Benedek and Fennie¹⁵⁰ argue that the A-site bonding situation heavily influences the phonon modes enabling ferroelectricity.

One major goal of current research is the establishment of lead-free alternatives¹⁶⁰⁻¹⁶⁴ to PZT. LiNbO_3 -type structures are one way of realizing lead-free ferroelectrics. With the perspective of thin film applications also 2D materials such as NbOCl_2 ¹⁶⁵ or Dion-Jacobson phases have been shown to be potentially viable¹⁶⁶. Other suitable approaches include the use of the less toxic Sn^{2+} ^{167, 168} and Bi^{3+} lone pair cations. Bi^{3+} is often combined with a monovalent alkali metal to make perovskite-type structures like $(\text{Bi,Na})\text{TiO}_3$ ¹⁵⁹ or $(\text{Bi,K})\text{TiO}_3$ accessible. Through introduction of magnetically active B-site cations (BiFeO_3 ¹⁶⁹ or BiMnO_3 ¹⁷⁰), additional coupling of electric and magnetic phenomena (multiferroicity¹⁷¹) could be realized. Regardless the efforts, none of the developed structures reach the high dipole moment of PZT, or combines promising lone pair induced non-centrosymmetry and processability of 2D materials.

1.5.4. Lone pairs under pressure

Ferroelectric phase transitions are usually discussed in the context of temperature. Another parameter, which may strongly influence the bonding and symmetry behavior in solids, is pressure. High pressure can be applied through diamond anvil cells (DACs)¹⁷² amongst others. In DACs, two diamonds sandwich the single or polycrystalline sample (Figure 1.12), which is held in place by a metal gasket (W, Re), filled with pressure-medium (Ne, Ar, liquids or salts). In general, the pressure is checked via the red shift of luminescence of a ruby crystal¹⁷³, placed into the cavity beside the sample.

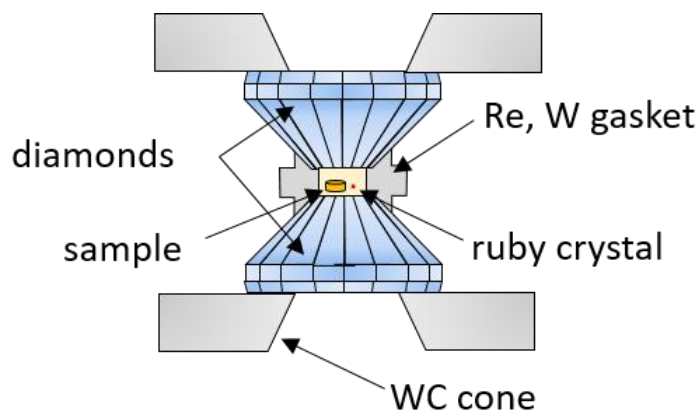


Figure 1.12. Scheme of a diamond anvil cell of the Boehler-Almax type. WC cones for pressure transduction, diamonds sandwiching a sample chamber filled with pressure medium and ruby crystal for pressure determination, held in place by a metal gasket.

At least three basic principles of high-pressure chemistry have been established over the past decades¹⁷⁴: the pressure-distance paradox, describing the unintuitive fact of increasing atom distances under pressure; the pressure-homologue rule, stating that the high-pressure structures from elements of low atomic number obtain the same structures as ambient pressure structures from elements of higher atomic number from the same group; and the pressure-coordination rule. The transition from ilmenite- to perovskite-type structures under pressure is an illustrative example for the latter pressure-coordination rule, as the A-site cation will change from 6-fold coordination in ilmenite-type to 12-fold coordination in ideal perovskite-type structures upon the phase transition. However, this coordination is usually lower due to octahedral distortions, rendering it a 10+2- or 8+4-fold coordination. Perovskite-type structures obtained by high-pressure approaches may not be stable at ambient conditions. ZnTiO_3 ¹⁷⁵⁻¹⁷⁷ and others^{178, 179} are quenched to a LiNbO_3 -type (also non-centrosymmetric) crystal structure. However, in cases of tolerance factors higher than approximately 0.8 either amorphization or stabilization of the perovskite has been observed¹⁸⁰.

In case of lone pairs additional difficulties in high-pressure experiments are reported. For example perovskite-type compounds with lone pairs have shown smaller enthalpies of formation¹⁸¹, compared to the expected enthalpies at this tolerance factor. This means that the lone pair containing perovskite is less stable than a perovskite with the same tolerance factor, but without lone pair cation. Most probably, the additional pressure (energy) required to suppress the steric effect is leading to this deviation. Lone pair compounds often are extremely soft and show bulk moduli as low as 23 GPa (litharge-type PbO). As we have seen before, lone pair materials commonly form (pseudo-)2D crystal structures. Upon application of pressure these tend to compress anisotropically, often concurrent with second-order isostructural phase transitions. Change of hybridizations and also stereochemical activity of the lone pair can then induce

semiconductor-to-(semi)metal transitions^{182, 183}, called Lifshitz transitions¹⁸⁴ or electronic topological phase transitions (ETT)¹⁸⁵. Stereochemical activity, however, does not always change upon application of pressure¹⁸⁶ and ferroelectricity might even re-appear at extreme pressures¹⁸⁷ making the outcome of an experiment highly unpredictable.

1.6. Objectives

Bearing in mind the energy sector as well as the IT industry, two of the futures most relevant fields are heavily depending on the deep and detailed understanding of semiconductors. The aim of this work is the establishment of a new platform, allowing for an in-depth investigation of the role of lone pairs regarding the electronic and crystallographic structure. Especially, lone pair induced structure-property relationships relevant for the above-mentioned applications are elucidated.

Many lead and bismuth-based lone pair compounds have been synthesized, but the comparably low stability of Sn(II) with regard to its oxidized counterpart Sn(IV) make Sn related semiconductors relatively scarce. Hence in Chapter 2, first the synthesis of a new Sn(II) titanate is presented. Herein, special focus is given on the impact of structural disorder induced by the anisotropic lone pair cations, comprising both the local octahedral and the long-range stacking regime.

Pressure is a parameter allowing for specific alteration of chemically relevant aspects such as atomic distances. By correlation of this parameter with changes in both electronic and crystallographic structure, pressure offers the chance to extract true structure-property-relationships. In Chapter 3 the phase space is scanned by DFT calculations around the ilmenite-type derived SnTiO₃ and analyzed on a theoretical basis with regards to potential ferroelectricity. Chapter 4 shows the results for high-pressure experiments in diamond anvil cells; adding to the understanding of lone pairs in the high-pressure regime, including identification of second-order, electronic phase transitions and a short discussion of the potential high pressure phase transition to perovskite-like structures.

Chapter 5 of this work targets the complicated process of photocatalytic water splitting with its requirements regarding electron excitation, charge diffusion and charge transfer and the role of lone pairs therewith. While the lone pair brings about many advantages, such as very low hole effective masses, it also induces very low ionization potentials, leading to surface oxidation and the anti-bonding VBM favors bulk oxidation, both hampering catalytic activity.

1.7. References

1. Andrade, T., *The gunpowder age: China, military innovation, and the rise of the West in world history*. Princeton University Press: 2017.
2. Keyser, P. T., The purpose of the Parthian galvanic cells: a first-century AD electric battery used for analgesia. *Journal of Near Eastern Studies* **1993**, 52, (2), 81-98.
3. Berlincourt, D.; Cmolik, C.; Jaffe, H., Piezoelectric properties of polycrystalline lead titanate zirconate compositions. *Proceedings of the IRE* **1960**, 48, (2), 220-229.
4. Küpers, M.; Konze, P. M.; Maintz, S.; Steinberg, S.; Mio, A. M.; Cojocar-Mirédin, O.; Zhu, M.; Müller, M.; Luysberg, M.; Mayer, J.; Wuttig, M.; Dronskowski, R., Unexpected Ge-Ge Contacts in the Two-Dimensional Ge₄Se₃Te Phase and Analysis of Their Chemical Cause with the Density of Energy (DOE) Function. *Angewandte Chemie International Edition* **2017**, 56, (34), 10204-10208.
5. Hasan, M. Z.; Kane, C. L., Colloquium: Topological insulators. *Reviews of Modern Physics* **2010**, 82, (4), 3045-3067.
6. Lotsch, B. V., Ein Klassiker im neuen Gewand: Perowskit-Solarzellen. *Angewandte Chemie* **2014**, 126, (3), 647-649.
7. lone (electron) pair. In *IUPAC. Compendium of Chemical Terminology*, 2 ed.; McNaught, A. D.; Wilkinson, A., Eds. Blackwell Scientific Publications: Oxford, 1997.
8. Orgel, L. E., 769. The stereochemistry of B subgroup metals. Part II. The inert pair. *Journal of the Chemical Society (Resumed)* **1959**, (0), 3815-3819.
9. Walsh, A.; Payne, D. J.; Egdell, R. G.; Watson, G. W., Stereochemistry of post-transition metal oxides: revision of the classical lone pair model. *Chemical Society Reviews* **2011**, 40, (9), 4455-4463.
10. Watson, G. W.; Parker, S. C., Origin of the Lone Pair of α -PbO from Density Functional Theory Calculations. *The Journal of Physical Chemistry B* **1999**, 103, (8), 1258-1262.
11. Payne, D. J.; Egdell, R. G.; Walsh, A.; Watson, G. W.; Guo, J.; Glans, P. A.; Learmonth, T.; Smith, K. E., Electronic Origins of Structural Distortions in Post-Transition Metal Oxides: Experimental and Theoretical Evidence for a Revision of the Lone Pair Model. *Physical Review Letters* **2006**, 96, (15), 157403.
12. Payne, D. J.; Robinson, M. D. M.; Egdell, R. G.; Walsh, A.; McNulty, J.; Smith, K. E.; Piper, L. F. J., The nature of electron lone pairs in BiVO₄. *Applied Physics Letters* **2011**, 98, (21), 212110.
13. Walsh, A.; Yan, Y.; Huda, M. N.; Al-Jassim, M. M.; Wei, S.-H., Band Edge Electronic Structure of BiVO₄: Elucidating the Role of the Bi s and V d Orbitals. *Chemistry of Materials* **2009**, 21, (3), 547-551.
14. Stoltzfus, M. W.; Woodward, P. M.; Seshadri, R.; Klepeis, J.-H.; Bursten, B., Structure and Bonding in SnWO₄, PbWO₄, and BiVO₄: Lone Pairs vs Inert Pairs. *Inorganic Chemistry* **2007**, 46, (10), 3839-3850.
15. Primary energy consumption by fuel in EU-28. In Statistical Office of the European Union (Eurostat): 2018.
16. Armaroli, N.; Balzani, V., The Future of Energy Supply: Challenges and Opportunities. *Angewandte Chemie International Edition* **2007**, 46, (1-2), 52-66.
17. Ogden, J. M., PROSPECTS FOR BUILDING A HYDROGEN ENERGY INFRASTRUCTURE. *Annual Review of Energy and the Environment* **1999**, 24, (1), 227-279.
18. Turner, J. A., Sustainable Hydrogen Production. *Science* **2004**, 305, (5686), 972.
19. Staffell, I.; Scamman, D.; Velazquez Abad, A.; Balcombe, P.; Dodds, P. E.; Ekins, P.; Shah, N.; Ward, K. R., The role of hydrogen and fuel cells in the global energy system. *Energy & Environmental Science* **2019**, 12, (2), 463-491.
20. Osterloh, F. E., Photocatalysis versus Photosynthesis: A Sensitivity Analysis of Devices for Solar Energy Conversion and Chemical Transformations. *ACS Energy Letters* **2017**, 2, (2), 445-453.
21. Takanabe, K., Photocatalytic Water Splitting: Quantitative Approaches toward Photocatalyst by Design. *ACS Catalysis* **2017**, 7, (11), 8006-8022.
22. Wang, Z.; Li, C.; Domen, K., Recent developments in heterogeneous photocatalysts for solar-driven overall water splitting. *Chemical Society Reviews* **2019**, 48, (7), 2109-2125.

23. Chen, S.; Takata, T.; Domen, K., Particulate photocatalysts for overall water splitting. *Nature Reviews Materials* **2017**, *2*, 17050.
24. Catalyst (heterogeneous). In *IUPAC. Compendium of Chemical Terminology*, 2 ed.; McNaught, A. D.; Wilkinson, A., Eds. Blackwell Scientific Publications: Oxford, 1997.
25. Qureshi, M.; Takanabe, K., Insights on Measuring and Reporting Heterogeneous Photocatalysis: Efficiency Definitions and Setup Examples. *Chem. Mater.* **2017**, *29*, (1), 158-167.
26. Hisatomi, T.; Takanabe, K.; Domen, K., Photocatalytic Water-Splitting Reaction from Catalytic and Kinetic Perspectives. *Catal Lett* **2015**, *145*, (1), 95-108.
27. Shockley, W.; Queisser, H. J., Detailed Balance Limit of Efficiency of p-n Junction Solar Cells. *Journal of Applied Physics* **1961**, *32*, (3), 510-519.
28. Osterloh, F. E., Nanoscale Effects in Water Splitting Photocatalysis. In *Solar Energy for Fuels*, Tüysüz, H.; Chan, C. K., Eds. Springer International Publishing: 2016; Vol. 371, pp 105-142.
29. Williams, R. T.; Song, K. S., The self-trapped exciton. *Journal of Physics and Chemistry of Solids* **1990**, *51*, (7), 679-716.
30. Sivula, K.; van de Krol, R., Semiconducting materials for photoelectrochemical energy conversion. *Nature Reviews Materials* **2016**, *1*, 15010.
31. Yang, J.; Wang, D.; Han, H.; Li, C., Roles of Cocatalysts in Photocatalysis and Photoelectrocatalysis. *Acc. Chem. Res.* **2013**, *46*, (8), 1900-1909.
32. Nakibli, Y.; Kalisman, P.; Amirav, L., Less Is More: The Case of Metal Cocatalysts. *The Journal of Physical Chemistry Letters* **2015**, *6*, (12), 2265-2268.
33. Xu, Y.; Xu, R., Nickel-based cocatalysts for photocatalytic hydrogen production. *Applied Surface Science* **2015**, *351*, 779-793.
34. Li, J.; Wu, N., Semiconductor-based photocatalysts and photoelectrochemical cells for solar fuel generation: a review. *Catalysis Science & Technology* **2015**, *5*, (3), 1360-1384.
35. Pellegrin, Y.; Odobel, F., Sacrificial electron donor reagents for solar fuel production. *Comptes Rendus Chimie* **2017**, *20*, (3), 283-295.
36. Fabbri, E.; Haberer, A.; Waltar, K.; Kotz, R.; Schmidt, T. J., Developments and perspectives of oxide-based catalysts for the oxygen evolution reaction. *Catalysis Science & Technology* **2014**, *4*, (11), 3800-3821.
37. Maeda, K.; Teramura, K.; Lu, D.; Saito, N.; Inoue, Y.; Domen, K., Noble-Metal/Cr2O3 Core/Shell Nanoparticles as a Cocatalyst for Photocatalytic Overall Water Splitting. *Angewandte Chemie International Edition* **2006**, *45*, (46), 7806-7809.
38. Liu, Q.; Zhang, L.; Crozier, P. A., Structure–reactivity relationships of Ni–NiO core–shell cocatalysts on Ta2O5 for solar hydrogen production. *Applied Catalysis B: Environmental* **2015**, *172-173*, 58-64.
39. Hainer, A. S.; Hodgins, J. S.; Sandre, V.; Vallieres, M.; Lanterna, A. E.; Scaiano, J. C., Photocatalytic Hydrogen Generation Using Metal-Decorated TiO2: Sacrificial Donors vs True Water Splitting. *ACS Energy Letters* **2018**, *3*, (3), 542-545.
40. Schneider, J.; Bahnemann, D. W., Undesired Role of Sacrificial Reagents in Photocatalysis. *The Journal of Physical Chemistry Letters* **2013**, *4*, (20), 3479-3483.
41. Fujishima, A.; Honda, K., Electrochemical Photolysis of Water at a Semiconductor Electrode. *Nature* **1972**, *238*, (5358), 37-38.
42. Maeda, K., Photocatalytic water splitting using semiconductor particles: History and recent developments. *Journal of Photochemistry and Photobiology C: Photochemistry Reviews* **2011**, *12*, (4), 237-268.
43. Domen, K.; Naito, S.; Soma, M.; Onishi, T.; Tamaru, K., Photocatalytic decomposition of water vapour on an NiO–SrTiO3 catalyst. *Journal of the Chemical Society, Chemical Communications* **1980**, (12), 543-544.
44. Inoue, Y.; Niiyama, T.; Asai, Y.; Sato, K., Stable photocatalytic activity of BaTi4O9 combined with ruthenium oxide for decomposition of water. *Journal of the Chemical Society, Chemical Communications* **1992**, (7), 579-580.
45. Inoue, Y.; Kubokawa, T.; Sato, K., Photocatalytic activity of sodium hexatitanate, Na2Ti6O13, with a tunnel structure for decomposition of water. *Journal of the Chemical Society, Chemical Communications* **1990**, (19), 1298-1299.

46. Domen, K.; Kudo, A.; Shinozaki, A.; Tanaka, A.; Maruya, K.-i.; Onishi, T., Photodecomposition of water and hydrogen evolution from aqueous methanol solution over novel niobate photocatalysts. *Journal of the Chemical Society, Chemical Communications* **1986**, (4), 356-357.
47. Meng, X. Y.; Liu, D. Y.; Qin, G. W., Band engineering of multicomponent semiconductors: a general theoretical model on the anion group. *Energy & Environmental Science* **2018**, 11, (3), 692-701.
48. Zhang, P.; Zhang, J.; Gong, J., Tantalum-based semiconductors for solar water splitting. *Chemical Society Reviews* **2014**, 43, (13), 4395-4422.
49. Zhang, Y.; Jiang, Z.; Huang, J.; Lim, L. Y.; Li, W.; Deng, J.; Gong, D.; Tang, Y.; Lai, Y.; Chen, Z., Titanate and titania nanostructured materials for environmental and energy applications: a review. *RSC Advances* **2015**, 5, (97), 79479-79510.
50. Nicolosi, V.; Chhowalla, M.; Kanatzidis, M. G.; Strano, M. S.; Coleman, J. N., Liquid Exfoliation of Layered Materials. *Science* **2013**, 340, (6139), 1226419.
51. Sasaki, T.; Watanabe, M., Osmotic Swelling to Exfoliation. Exceptionally High Degrees of Hydration of a Layered Titanate. *Journal of the American Chemical Society* **1998**, 120, (19), 4682-4689.
52. Ebina, Y.; Sasaki, T.; Harada, M.; Watanabe, M., Restacked Perovskite Nanosheets and Their Pt-Loaded Materials as Photocatalysts. *Chemistry of Materials* **2002**, 14, (10), 4390-4395.
53. Ida, S.; Kim, N.; Ertekin, E.; Takenaka, S.; Ishihara, T., Photocatalytic Reaction Centers in Two-Dimensional Titanium Oxide Crystals. *Journal of the American Chemical Society* **2015**, 137, (1), 239-244.
54. Takata, T.; Furumi, Y.; Shinohara, K.; Tanaka, A.; Hara, M.; Kondo, J. N.; Domen, K., Photocatalytic Decomposition of Water on Spontaneously Hydrated Layered Perovskites. *Chemistry of Materials* **1997**, 9, (5), 1063-1064.
55. Chamousis, R. L.; Osterloh, F. E., Use of potential determining ions to control energetics and photochemical charge transfer of a nanoscale water splitting photocatalyst. *Energy & Environmental Science* **2014**, 7, (2), 736-743.
56. Compton, O. C.; Osterloh, F. E., Niobate Nanosheets as Catalysts for Photochemical Water Splitting into Hydrogen and Hydrogen Peroxide. *The Journal of Physical Chemistry C* **2009**, 113, (1), 479-485.
57. Sabio, E. M.; Chamousis, R. L.; Browning, N. D.; Osterloh, F. E., Photocatalytic Water Splitting with Suspended Calcium Niobium Oxides: Why Nanoscale is Better than Bulk – A Kinetic Analysis. *The Journal of Physical Chemistry C* **2012**, 116, (4), 3161-3170.
58. Sabio, E. M.; Chi, M.; Browning, N. D.; Osterloh, F. E., Charge Separation in a Niobate Nanosheet Photocatalyst Studied with Photochemical Labeling. *Langmuir* **2010**, 26, (10), 7254-7261.
59. Maeda, K.; Mallouk, T. E., Comparison of two- and three-layer restacked Dion–Jacobson phase niobate nanosheets as catalysts for photochemical hydrogen evolution. *Journal of Materials Chemistry* **2009**, 19, (27), 4813-4818.
60. Moan, J., *7 Visible Light and UV Radiation*. 2001.
61. Bloh, J. Z.; Dillert, R.; Bahnemann, D. W., Designing Optimal Metal-Doped Photocatalysts: Correlation between Photocatalytic Activity, Doping Ratio, and Particle Size. *The Journal of Physical Chemistry C* **2012**, 116, (48), 25558-25562.
62. Herrmann, J.-M.; Disdier, J.; Pichat, P., Effect of chromium doping on the electrical and catalytic properties of powder titania under UV and visible illumination. *Chem. Phys. Lett.* **1984**, 108, (6), 618-622.
63. Choi, W.; Termin, A.; Hoffmann, M. R., The role of metal ion dopants in quantum-sized TiO₂: correlation between photoreactivity and charge carrier recombination dynamics. *The Journal of Physical Chemistry* **1994**, 98, (51), 13669-13679.
64. Martha, S.; Chandra Sahoo, P.; Parida, K. M., An overview on visible light responsive metal oxide based photocatalysts for hydrogen energy production. *RSC Advances* **2015**, 5, (76), 61535-61553.
65. Hagfeldt, A.; Boschloo, G.; Sun, L.; Kloo, L.; Pettersson, H., Dye-Sensitized Solar Cells. *Chemical Reviews* **2010**, 110, (11), 6595-6663.

66. Nazeeruddin, M. K.; Baranoff, E.; Grätzel, M., Dye-sensitized solar cells: A brief overview. *Solar Energy* **2011**, 85, (6), 1172-1178.
67. Hardin, B. E.; Snaith, H. J.; McGehee, M. D., The renaissance of dye-sensitized solar cells. *Nature Photonics* **2012**, 6, 162.
68. Asahi, R.; Morikawa, T.; Ohwaki, T.; Aoki, K.; Taga, Y., Visible-Light Photocatalysis in Nitrogen-Doped Titanium Oxides. *Science* **2001**, 293, (5528), 269.
69. Higashi, M.; Abe, R.; Teramura, K.; Takata, T.; Ohtani, B.; Domen, K., Two step water splitting into H₂ and O₂ under visible light by ATaO₂N (A=Ca, Sr, Ba) and WO₃ with IO₃⁻/I⁻ shuttle redox mediator. *Chemical Physics Letters* **2008**, 452, (1), 120-123.
70. Aguiar, R.; Kalytta, A.; Reller, A.; Weidenkaff, A.; Ebbinghaus, S. G., Photocatalytic decomposition of acetone using LaTi(O,N)₃ nanoparticles under visible light irradiation. *Journal of Materials Chemistry* **2008**, 18, (36), 4260-4265.
71. Go, H.; Akio, I.; Tsuyoshi, T.; N., K. J.; Michikazu, H.; Kazunari, D., Ta₃N₅ as a Novel Visible Light-Driven Photocatalyst ($\lambda < 600$ nm). *Chemistry Letters* **2002**, 31, (7), 736-737.
72. Kato, D.; Hongo, K.; Maezono, R.; Higashi, M.; Kunioku, H.; Yabuuchi, M.; Suzuki, H.; Okajima, H.; Zhong, C.; Nakano, K.; Abe, R.; Kageyama, H., Valence Band Engineering of Layered Bismuth Oxyhalides toward Stable Visible-Light Water Splitting: Madelung Site Potential Analysis. *J. Am. Chem. Soc.* **2017**, 139, (51), 18725-18731.
73. Lamers, M.; Li, W.; Favaro, M.; Starr, D. E.; Friedrich, D.; Lardhi, S.; Cavallo, L.; Harb, M.; van de Krol, R.; Wong, L. H., Enhanced carrier transport and bandgap reduction in sulfur-modified BiVO₄ photoanodes. *Chemistry of Materials* **2018**, 30, (23), 8630-8638.
74. Haider, Z.; Zheng, J. Y.; Kang, Y. S., Surfactant free fabrication and improved charge carrier separation induced enhanced photocatalytic activity of {001} facet exposed unique octagonal BiOCl nanosheets. *Physical Chemistry Chemical Physics* **2016**, 18, (29), 19595-19604.
75. Stephenson, J.; Celorrio, V.; Tiwari, D.; Hall, S. R.; Green, D. C.; Fermín, D. J., Photoelectrochemical properties of BiOCl microplatelets. *Journal of Electroanalytical Chemistry* **2018**, 819, 171-177.
76. Lian, Z.; Sakamoto, M.; Matsunaga, H.; Vequizo, J. J. M.; Yamakata, A.; Haruta, M.; Kurata, H.; Ota, W.; Sato, T.; Teranishi, T., Near infrared light induced plasmonic hot hole transfer at a nano-heterointerface. *Nature Communications* **2018**, 9, (1), 2314.
77. Simon, T.; Bouchonville, N.; Berr, M. J.; Vaneski, A.; Adrović, A.; Volbers, D.; Wyrwich, R.; Döblinger, M.; Susha, A. S.; Rogach, A. L.; Jäckel, F.; Stolarczyk, J. K.; Feldmann, J., Redox shuttle mechanism enhances photocatalytic H₂ generation on Ni-decorated CdS nanorods. *Nature Materials* **2014**, 13, 1013.
78. Choi, J.; Ryu, S. Y.; Balcerski, W.; Lee, T. K.; Hoffmann, M. R., Photocatalytic production of hydrogen on Ni/NiO/KNbO₃/CdS nanocomposites using visible light. *Journal of Materials Chemistry* **2008**, 18, (20), 2371-2378.
79. Kudo, A.; Omori, K.; Kato, H., A Novel Aqueous Process for Preparation of Crystal Form-Controlled and Highly Crystalline BiVO₄ Powder from Layered Vanadates at Room Temperature and Its Photocatalytic and Photophysical Properties. *J. Am. Chem. Soc.* **1999**, 121, (49), 11459-11467.
80. Kudo, A.; Ueda, K.; Kato, H.; Mikami, I., Photocatalytic O₂ evolution under visible light irradiation on BiVO₄ in aqueous AgNO₃ solution. *Catal Lett* **1998**, 53, (3-4), 229-230.
81. Akihiko, K.; Satoshi, H., H₂ or O₂ Evolution from Aqueous Solutions on Layered Oxide Photocatalysts Consisting of Bi³⁺ with 6s² Configuration and d⁰ Transition Metal Ions. *Chemistry Letters* **1999**, 28, (10), 1103-1104.
82. Zachäus, C.; Abdi, F. F.; Peter, L. M.; van de Krol, R., Photocurrent of BiVO₄ is limited by surface recombination, not surface catalysis. *Chemical Science* **2017**, 8, (5), 3712-3719.
83. Ziwrtsch, M.; Müller, S.; Hempel, H.; Unold, T.; Abdi, F. F.; van de Krol, R.; Friedrich, D.; Eichberger, R., Direct Time-Resolved Observation of Carrier Trapping and Polaron Conductivity in BiVO₄. *ACS Energy Letters* **2016**, 1, (5), 888-894.
84. McCrory, C. C. L.; Jung, S.; Peters, J. C.; Jaramillo, T. F., Benchmarking Heterogeneous Electrocatalysts for the Oxygen Evolution Reaction. *Journal of the American Chemical Society* **2013**, 135, (45), 16977-16987.

85. Kojima, A.; Teshima, K.; Shirai, Y.; Miyasaka, T., Organometal Halide Perovskites as Visible-Light Sensitizers for Photovoltaic Cells. *Journal of the American Chemical Society* **2009**, 131, (17), 6050-6051.
86. Ganose, A. M.; Savory, C. N.; Scanlon, D. O., Beyond methylammonium lead iodide: prospects for the emergent field of ns² containing solar absorbers. *Chem. Commun.* **2017**, 53, (1), 20-44.
87. Kadowaki, H.; Saito, N.; Nishiyama, H.; Kobayashi, H.; Shimodaira, Y.; Inoue, Y., Overall Splitting of Water by RuO₂-Loaded PbWO₄ Photocatalyst with d¹⁰s²-d⁰ Configuration. *The Journal of Physical Chemistry C* **2007**, 111, (1), 439-444.
88. Cho, I.-S.; Kwak, C. H.; Kim, D. W.; Lee, S.; Hong, K. S., Photophysical, Photoelectrochemical, and Photocatalytic Properties of Novel SnWO₄ Oxide Semiconductors with Narrow Band Gaps. *The Journal of Physical Chemistry C* **2009**, 113, (24), 10647-10653.
89. Kölbach, M.; Pereira, I. J.; Harbauer, K.; Plate, P.; Höflich, K.; Berglund, S. P.; Friedrich, D.; van de Krol, R.; Abdi, F. F., Revealing the Performance-Limiting Factors in α -SnWO₄ Photoanodes for Solar Water Splitting. *Chemistry of Materials* **2018**, 30, (22), 8322-8331.
90. Zhang, K.-L.; Lin, X.-P.; Huang, F.-Q.; Wang, W.-D., A novel photocatalyst PbSb₂O₆ for degradation of methylene blue. *Journal of Molecular Catalysis A: Chemical* **2006**, 258, (1), 185-190.
91. Inoue, Y., Photocatalytic water splitting by RuO₂-loaded metal oxides and nitrides with d⁰- and d¹⁰ -related electronic configurations. *Energy & Environmental Science* **2009**, 2, (4), 364-386.
92. Ha, V.-A.; Ricci, F.; Rignanese, G.-M.; Hautier, G., Structural design principles for low hole effective mass s-orbital-based p-type oxides. *Journal of Materials Chemistry C* **2017**, 5, (23), 5772-5779.
93. Marschall, R., Heterojunctions in Composite Photocatalysts. In *Solar Energy for Fuels*, Tüysüz, H.; Chan, C. K., Eds. Springer International Publishing: 2016; Vol. 371, pp 143-172.
94. Li, J.; Zhan, G.; Yu, Y.; Zhang, L., Superior visible light hydrogen evolution of Janus bilayer junctions via atomic-level charge flow steering. *Nat Commun* **2016**, 7.
95. Sariciftci, N. S.; Smilowitz, L.; Heeger, A. J.; Wudl, F., Photoinduced Electron Transfer from a Conducting Polymer to Buckminsterfullerene. *Science* **1992**, 258, (5087), 1474-1476.
96. Kim, J. Y.; Lee, K.; Coates, N. E.; Moses, D.; Nguyen, T.-Q.; Dante, M.; Heeger, A. J., Efficient Tandem Polymer Solar Cells Fabricated by All-Solution Processing. *Science* **2007**, 317, (5835), 222-225.
97. Kirkeminde, A.; Scott, R.; Ren, S., All inorganic iron pyrite nano-heterojunction solar cells. *Nanoscale* **2012**, 4, (24), 7649-7654.
98. Zhu, X.; Monahan, N. R.; Gong, Z.; Zhu, H.; Williams, K. W.; Nelson, C. A., Charge Transfer Excitons at van der Waals Interfaces. *Journal of the American Chemical Society* **2015**, 137, (26), 8313-8320.
99. Zhou, Y.; Zhang, Y.; Lin, M.; Long, J.; Zhang, Z.; Lin, H.; Wu, J. C. S.; Wang, X., Monolayered Bi₂WO₆ nanosheets mimicking heterojunction interface with open surfaces for photocatalysis. *Nat Commun* **2015**, 6.
100. Kumada, N.; Yonesaki, Y.; Takei, T.; Kinomura, N.; Wada, S., Preparation and crystal structure of a new tin titanate containing Sn²⁺; Sn₂TiO₄. *Materials Research Bulletin* **2009**, 44, (6), 1298-1300.
101. Wahila, M. J.; Butler, K. T.; Lebens-Higgins, Z. W.; Hendon, C. H.; Nandur, A. S.; Treharne, R. E.; Quackenbush, N. F.; Sallis, S.; Mason, K.; Paik, H.; Schlom, D. G.; Woicik, J. C.; Guo, J.; Arena, D. A.; White, B. E.; Watson, G. W.; Walsh, A.; Piper, L. F. J., Lone-Pair Stabilization in Transparent Amorphous Tin Oxides: A Potential Route to p-Type Conduction Pathways. *Chem. Mater.* **2016**, 28, (13), 4706-4713.
102. Noureldine, D.; Anjum, D. H.; Takanabe, K., Flux-assisted synthesis of SnNb₂O₆ for tuning photocatalytic properties. *Physical Chemistry Chemical Physics* **2014**, 16, (22), 10762-10769.
103. Noureldine, D.; Takanabe, K., State-of-the-art Sn²⁺-based ternary oxides as photocatalysts for water splitting: electronic structures and optoelectronic properties. *Catalysis Science & Technology* **2016**, 6, (21), 7656-7670.

104. Wu, X.; Hart, J. N.; Wen, X.; Wang, L.; Du, Y.; Dou, S. X.; Ng, Y. H.; Amal, R.; Scott, J., Improving the Photo-Oxidative Performance of Bi₂MoO₆ by Harnessing the Synergy between Spatial Charge Separation and Rational Co-Catalyst Deposition. *ACS Applied Materials & Interfaces* **2018**, 10, (11), 9342-9352.
105. Shan, Z.; Xia, Y.; Yang, Y.; Ding, H.; Huang, F., Preparation and photocatalytic activity of novel efficient photocatalyst Sr₂Bi₂O₅. *Mater. Lett.* **2009**, 63, (1), 75-77.
106. Hautier, G.; Miglio, A.; Ceder, G.; Rignanese, G.-M.; Gonze, X., Identification and design principles of low hole effective mass p-type transparent conducting oxides. *Nature Communications* **2013**, 4, 2292.
107. Hautier, G.; Miglio, A.; Waroquiers, D.; Rignanese, G.-M.; Gonze, X., How Does Chemistry Influence Electron Effective Mass in Oxides? A High-Throughput Computational Analysis. *Chemistry of Materials* **2014**, 26, (19), 5447-5458.
108. Ganduglia-Pirovano, M. V.; Hofmann, A.; Sauer, J., Oxygen vacancies in transition metal and rare earth oxides: Current state of understanding and remaining challenges. *Surface Science Reports* **2007**, 62, (6), 219-270.
109. Ogo, Y.; Hiramatsu, H.; Nomura, K.; Yanagi, H.; Kamiya, T.; Hirano, M.; Hosono, H., p-channel thin-film transistor using p-type oxide semiconductor, SnO. *Applied Physics Letters* **2008**, 93, (3), 032113.
110. Kikuchi, N.; Samizo, A.; Ikeda, S.; Aiura, Y.; Mibu, K.; Nishio, K., Carrier generation in a p-type oxide semiconductor: Sn₂Nb_{2-x}TaxO₇. *Physical Review Materials* **2017**, 1, (2), 021601.
111. Wang, J.; Umezawa, N.; Hosono, H., Mixed Valence Tin Oxides as Novel van der Waals Materials: Theoretical Predictions and Potential Applications. *Advanced Energy Materials* **2016**, 6, (1), 1501190.
112. Zhang, K. H. L.; Xi, K.; Blamire, M. G.; Egdell, R. G., P-type transparent conducting oxides. *Journal of Physics: Condensed Matter* **2016**, 28, (38), 383002.
113. Endres, J.; Egger, D. A.; Kulbak, M.; Kerner, R. A.; Zhao, L.; Silver, S. H.; Hodes, G.; Rand, B. P.; Cahen, D.; Kronik, L.; Kahn, A., Valence and Conduction Band Densities of States of Metal Halide Perovskites: A Combined Experimental-Theoretical Study. *The Journal of Physical Chemistry Letters* **2016**, 7, (14), 2722-2729.
114. de Kergommeaux, A.; Faure-Vincent, J.; Pron, A.; de Bettignies, R.; Malaman, B.; Reiss, P., Surface Oxidation of Tin Chalcogenide Nanocrystals Revealed by ¹¹⁹Sn-Mössbauer Spectroscopy. *Journal of the American Chemical Society* **2012**, 134, (28), 11659-11666.
115. Brandt, R. E.; Stevanović, V.; Ginley, D. S.; Buonassisi, T., Identifying defect-tolerant semiconductors with high minority-carrier lifetimes: beyond hybrid lead halide perovskites. *MRS Communications* **2015**, 5, (2), 265-275.
116. Walsh, A.; Zunger, A., Instilling defect tolerance in new compounds. *Nature Materials* **2017**, 16, 964.
117. Kim, S.; Park, J.-S.; Hood, Samantha N.; Walsh, A., Lone-pair effect on carrier capture in Cu₂ZnSnS₄ solar cells. *Journal of Materials Chemistry A* **2019**, 7, (6), 2686-2693.
118. Cortecchia, D.; Yin, J.; Bruno, A.; Lo, S.-Z. A.; Gurzadyan, G. G.; Mhaisalkar, S.; Brédas, J.-L.; Soci, C., Polaron self-localization in white-light emitting hybrid perovskites. *Journal of Materials Chemistry C* **2017**, 5, (11), 2771-2780.
119. Colella, S.; Todaro, M.; Masi, S.; Listorti, A.; Altamura, D.; Caliandro, R.; Giannini, C.; Carignani, E.; Geppi, M.; Meggiolaro, D.; Buscarino, G.; De Angelis, F.; Rizzo, A., Light-Induced Formation of Pb³⁺ Paramagnetic Species in Lead Halide Perovskites. *ACS Energy Letters* **2018**, 3, (8), 1840-1847.
120. Iwanaga, M.; Shirai, M.; Tanaka, K.; Hayashi, T., Self-trapped states and related luminescence in $\{\text{PbCl}\}_2$ crystals. *Physical Review B* **2002**, 66, (6), 064304.
121. Kim, G. Y.; Senocrate, A.; Yang, T.-Y.; Gregori, G.; Grätzel, M.; Maier, J., Large tunable photoeffect on ion conduction in halide perovskites and implications for photodecomposition. *Nature Materials* **2018**, 17, (5), 445-449.
122. Senocrate, A.; Moudrakovski, I.; Kim, G. Y.; Yang, T.-Y.; Gregori, G.; Grätzel, M.; Maier, J., The Nature of Ion Conduction in Methylammonium Lead Iodide: A Multimethod Approach. *Angewandte Chemie International Edition* **2017**, 56, (27), 7755-7759.

123. Biswas, K.; Lany, S.; Zunger, A., The electronic consequences of multivalent elements in inorganic solar absorbers: Multivalency of Sn in Cu₂ZnSnS₄. *Appl. Phys. Lett.* **2010**, 96, (20), 201902.
124. Hanamura, E.; Nagaosa, N.; Kumagai, M.; Takagahara, T., Quantum wells with enhanced exciton effects and optical non-linearity. *Materials Science and Engineering B: Solid-State Materials for Advanced Technology* **1988**, 1, (3-4), 255-258.
125. Ueda, K.; Hiramatsu, H.; Hirano, M.; Kamiya, T.; Hosono, H., Wide-gap layered oxychalcogenide semiconductors: Materials, electronic structures and optoelectronic properties. *Thin Solid Films* **2006**, 496, (1), 8-15.
126. Shinada, M.; Sugano, S., Interband Optical Transitions in Extremely Anisotropic Semiconductors. I. Bound and Unbound Exciton Absorption. *Journal of the Physical Society of Japan* **1966**, 21, (10), 1936-1946.
127. Uppuluri, R.; Sen Gupta, A.; Rosas, A. S.; Mallouk, T. E., Soft chemistry of ion-exchangeable layered metal oxides. *Chemical Society Reviews* **2018**, 47, (7), 2401-2430.
128. Gopalakrishnan, J., Chimie Douce Approaches to the Synthesis of Metastable Oxide Materials. *Chemistry of Materials* **1995**, 7, (7), 1265-1275.
129. Jacobson, A. J.; Nazar, L. F., Intercalation Chemistry. *Encyclopedia of Inorganic and Bioinorganic Chemistry* **2011**.
130. Roudebush, J. H.; Ross, K. A.; Cava, R. J., Iridium containing honeycomb Delafossites by topotactic cation exchange. *Dalton Transactions* **2016**, 45, (21), 8783-8789.
131. Liu, X.; Fechler, N.; Antonietti, M., Salt melt synthesis of ceramics, semiconductors and carbon nanostructures. *Chemical Society Reviews* **2013**, 42, (21), 8237-8265.
132. Fenton, J. L.; Schaak, R. E., Structure-Selective Cation Exchange in the Synthesis of Zincblende MnS and CoS Nanocrystals. *Angewandte Chemie International Edition* **2017**, 56, (23), 6464-6467.
133. Frey, F.; Boysen, H.; Jagodzinski, H., Disorder diffuse scattering of X-rays and neutrons. In *International Tables for Crystallography*, 2010; Vol. B, pp 492-539.
134. Pártay, L. B.; Ortner, C.; Bartók, A. P.; Pickard, C. J.; Csányi, G., Polyttypism in the ground state structure of the Lennard-Jonesium. *Physical Chemistry Chemical Physics* **2017**, 19, (29), 19369-19376.
135. Parthe, E.; Yvon, K., On the crystal chemistry of the close packed transition metal carbides. II. A proposal for the notation of the different crystal structures. *Acta Crystallographica Section B* **1970**, 26, (2), 153-163.
136. Warren, B. E., X-Ray Diffraction in Random Layer Lattices. *Physical Review* **1941**, 59, (9), 693-698.
137. Bette, S.; Dinnebier, R. E.; Freyer, D., Structure solution and refinement of stacking-faulted NiCl(OH). *J. Appl. Crystallogr.* **2015**, 48, (6), 1706-1718.
138. Bette, S.; Takayama, T.; Kitagawa, K.; Takano, R.; Takagi, H.; Dinnebier, R. E., Solution of the heavily stacking faulted crystal structure of the honeycomb iridate H₃LiIr₂O₆. *Dalton Transactions* **2017**, 46, (44), 15216-15227.
139. Dinnebier Robert, E.; Leineweber, A.; Evans John, S. O., *Rietveld Refinement, Practical Powder Diffraction Pattern Analysis using TOPAS*. 2018.
140. Mio, A. M.; Konze, P. M.; Meledin, A.; Küpers, M.; Pohlmann, M.; Kaminski, M.; Dronskowski, R.; Mayer, J.; Wuttig, M., Impact of Bonding on the Stacking Defects in Layered Chalcogenides. *Advanced Functional Materials* **2019**, 29, (37), 1902332.
141. Wuttig, M.; Deringer, V. L.; Gonze, X.; Bichara, C.; Raty, J.-Y., Incipient Metals: Functional Materials with a Unique Bonding Mechanism. *Advanced Materials* **2018**, 30, (51), 1803777.
142. Jones, R. O., Bonding in phase change materials: concepts and misconceptions. *Journal of Physics: Condensed Matter* **2018**, 30, (15), 153001.
143. Konze, P. M.; Dronskowski, R.; Deringer, V. L., Exploring Chemical Bonding in Phase-Change Materials with Orbital-Based Indicators. *physica status solidi (RRL) – Rapid Research Letters* **2019**, 13, (4), 1800579.
144. Deringer, V. L.; Dronskowski, R.; Wuttig, M., Microscopic Complexity in Phase-Change Materials and its Role for Applications. *Advanced Functional Materials* **2015**, 25, (40), 6343-6359.

145. Busch, G.; Scherrer, P., Eine neue seignette-elektrische Substanz. *Naturwissenschaften* **1935**, 23, (43), 737-737.
146. Hulm, J. K., Dielectric Properties of Single Crystals of Barium Titanate. *Nature* **1947**, 160, (4056), 127-128.
147. Öpik, U.; Pryce, M. H. L., Studies of the Jahn-Teller effect. I. A survey of the static problem. *Proceedings of the Royal Society of London. Series A. Mathematical and Physical Sciences* **1957**, 238, (1215), 425-447.
148. Bersuker, I. B., On the origin of ferroelectricity in perovskite-type crystals. *Physics Letters* **1966**, 20, (6), 589-590.
149. Bersuker, I. B., Pseudo-Jahn-Teller effect • A two-state paradigm in formation, deformation, and transformation of molecular systems and solids. *Chemical Reviews* **2013**, 113, (3), 1351-1390.
150. Benedek, N. A.; Fennie, C. J., Why Are There So Few Perovskite Ferroelectrics? *The Journal of Physical Chemistry C* **2013**, 117, (26), 13339-13349.
151. Goldschmidt, V. M., Die Gesetze der Krystallochemie. *Naturwissenschaften* **1926**, 14, (21), 477-485.
152. Navrotsky, A., Energetics and Crystal Chemical Systematics among Ilmenite, Lithium Niobate, and Perovskite Structures. *Chemistry of Materials* **1998**, 10, (10), 2787-2793.
153. Bussmann-Holder, A.; Dalal, N., Order/Disorder Versus or with Displacive Dynamics in Ferroelectric Systems. In *Ferro- and Antiferroelectricity: Order/Disorder versus Displacive*, Dalal, N. S.; Bussmann-Holder, A., Eds. Springer Berlin Heidelberg: Berlin, Heidelberg, 2007; pp 1-21.
154. Baettig, P.; Schelle, C. F.; LeSar, R.; Waghmare, U. V.; Spaldin, N. A., Theoretical Prediction of New High-Performance Lead-Free Piezoelectrics. *Chemistry of Materials* **2005**, 17, (6), 1376-1380.
155. Shen, Y.; Cai, J.; Ding, H.-C.; Shen, X.-W.; Fang, Y.-W.; Tong, W.-Y.; Wan, X.-G.; Zhao, Q.; Duan, C.-G., Role of Lone-Pairs in Driving Ferroelectricity of Perovskite Oxides: An Orbital Selective External Potential Study. *Advanced Theory and Simulations* **2019**, 2, (6), 1900029.
156. Cohen, R. E., Origin of ferroelectricity in perovskite oxides. *Nature* **1992**, 358, 136-138.
157. Belik, A. A.; Iikubo, S.; Kodama, K.; Igawa, N.; Shamoto, S.-i.; Maie, M.; Nagai, T.; Matsui, Y.; Stefanovich, S. Y.; Lazoryak, B. I.; Takayama-Muromachi, E., BiScO₃: Centrosymmetric BiMnO₃-type Oxide. *Journal of the American Chemical Society* **2006**, 128, (3), 706-707.
158. Seshadri, R., Lone pairs in insulating pyrochlores: Ice rules and high-k behavior. *Solid State Sciences* **2006**, 8, (3), 259-266.
159. Schütz, D.; Deluca, M.; Krauss, W.; Feteira, A.; Jackson, T.; Reichmann, K., Lone-Pair-Induced Covalency as the Cause of Temperature- and Field-Induced Instabilities in Bismuth Sodium Titanate. *Advanced Functional Materials* **2012**, 22, (11), 2285-2294.
160. Lee, M. H.; Kim, D. J.; Park, J. S.; Kim, S. W.; Song, T. K.; Kim, M.-H.; Kim, W.-J.; Do, D.; Jeong, I.-K., High-Performance Lead-Free Piezoceramics with High Curie Temperatures. *Advanced Materials* **2015**, 27, (43), 6976-6982.
161. Saito, Y.; Takao, H.; Tani, T.; Nonoyama, T.; Takatori, K.; Homma, T.; Nagaya, T.; Nakamura, M., Lead-free piezoceramics. *Nature* **2004**, 432, 84-87.
162. Shrout, T. R.; Zhang, S. J., Lead-free piezoelectric ceramics: Alternatives for PZT? *Journal of Electroceramics* **2007**, 19, (1), 113-126.
163. Wang, X.; Wu, J.; Xiao, D.; Zhu, J.; Cheng, X.; Zheng, T.; Zhang, B.; Lou, X.; Wang, X., Giant Piezoelectricity in Potassium-Sodium Niobate Lead-Free Ceramics. *Journal of the American Chemical Society* **2014**, 136, (7), 2905-2910.
164. Rödel, J.; Jo, W.; Seifert, K. T. P.; Anton, E.-M.; Granzow, T.; Damjanovic, D., Perspective on the Development of Lead-free Piezoceramics. *Journal of the American Ceramic Society* **2009**, 92, (6), 1153-1177.
165. Jia, Y.; Zhao, M.; Gou, G.; Zeng, X. C.; Li, J., Niobium oxide dihalides NbOX₂: a new family of two-dimensional van der Waals layered materials with intrinsic ferroelectricity and antiferroelectricity. *Nanoscale Horizons* **2019**.

166. Strayer, M. E.; Gupta, A. S.; Akamatsu, H.; Lei, S.; Benedek, N. A.; Gopalan, V.; Mallouk, T. E., Emergent Noncentrosymmetry and Piezoelectricity Driven by Oxygen Octahedral Rotations in $n = 2$ Dion–Jacobson Phase Layer Perovskites. *Advanced Functional Materials* **2016**, *26*, (12), 1930-1937.
167. Schöneegger, S.; Jantz, S. G.; Saxer, A.; Bayarjargal, L.; Winkler, B.; Pielhofer, F.; Höpfe, H. A.; Huppertz, H., Synthesis and Characterization of the First Tin Fluoride Borate $\text{Sn}_3[\text{B}_3\text{O}_7]\text{F}$ with Second Harmonic Generation Response. *Chemistry–A European Journal* **2018**, *24*, (60), 16036-16043.
168. Carpentier, C.; Nitsche, R., Ferroelectricity in $\text{Sn}_2\text{P}_2\text{S}_6$. *Materials Research Bulletin* **1974**, *9*, (8), 1097-1100.
169. Sosnowska, I.; Neumaier, T. P.; Steichele, E., Spiral magnetic ordering in bismuth ferrite. *Journal of Physics C: Solid State Physics* **1982**, *15*, (23), 4835-4846.
170. Seshadri, R.; Hill, N. A., Visualizing the Role of Bi 6s “Lone Pairs” in the Off-Center Distortion in Ferromagnetic BiMnO_3 . *Chemistry of Materials* **2001**, *13*, (9), 2892-2899.
171. Hill, N. A., Why Are There so Few Magnetic Ferroelectrics? *The Journal of Physical Chemistry B* **2000**, *104*, (29), 6694-6709.
172. Boehler, R., New diamond cell for single-crystal x-ray diffraction. *Review of Scientific Instruments* **2006**, *77*, (11), 115103.
173. Mao, H. K.; Xu, J.; Bell, P. M., Calibration of the ruby pressure gauge to 800 kbar under quasi-hydrostatic conditions. *Journal of Geophysical Research: Solid Earth* **1986**, *91*, (B5), 4673-4676.
174. Kleber, W.; Wilke, K.-T., Synthese und Kristallchemie anorganischer Stoffe bei hohen Drücken und Temperaturen. *Kristall und Technik* **1969**, *4*, (2), 165-199.
175. Akaogi, M.; Abe, K.; Yusa, H.; Kojitani, H.; Mori, D.; Inaguma, Y., High-pressure phase behaviors of ZnTiO_3 : ilmenite–perovskite transition, decomposition of perovskite into constituent oxides, and perovskite–lithium niobate transition. *Physics and Chemistry of Minerals* **2015**, *42*, (6), 421-429.
176. Inaguma, Y.; Aimi, A.; Shirako, Y.; Sakurai, D.; Mori, D.; Kojitani, H.; Akaogi, M.; Nakayama, M., High-Pressure Synthesis, Crystal Structure, and Phase Stability Relations of a LiNbO_3 -Type Polar Titanate ZnTiO_3 and Its Reinforced Polarity by the Second-Order Jahn–Teller Effect. *Journal of the American Chemical Society* **2014**, *136*, (7), 2748-2756.
177. Bernert, T.; Ruiz-Fuertes, J.; Bayarjargal, L.; Winkler, B., Synthesis and high (pressure, temperature) stability of ZnTiO_3 polymorphs studied by Raman spectroscopy. *Solid State Sciences* **2015**, *43*, 53-58.
178. Leinenweber, K.; Utsumi, W.; Tsuchida, Y.; Yagi, T.; Kurita, K., Unquenchable high-pressure perovskite polymorphs of MnSnO_3 and FeTiO_3 . *Physics and Chemistry of Minerals* **1991**, *18*, (4), 244-250.
179. Wu, X.; Qin, S.; Dubrovinsky, L., Investigation into high-pressure behavior of MnTiO_3 : X-ray diffraction and Raman spectroscopy with diamond anvil cells. *Geoscience Frontiers* **2011**, *2*, (1), 107-114.
180. Yusa, H., Structural Relaxation of Oxide Compounds from the High-Pressure Phase. In *Nanoinformatics*, Tanaka, I., Ed. Springer Singapore: Singapore, 2018; pp 259-277.
181. Inaguma, Y., High-Pressure Perovskite: Synthesis, Structure, and Phase Relation. In *Handbook of Solid State Chemistry*, 2017.
182. Gavriluk, A. G.; Struzhkin, V. V.; Lyubutin, I. S.; Ovchinnikov, S. G.; Hu, M. Y.; Chow, P., Another mechanism for the insulator-metal transition observed in Mott insulators. *Physical Review B* **2008**, *77*, (15), 155112.
183. Pereira, A. L. J.; Sans, J. A.; Vilaplana, R.; Gomis, O.; Manjón, F. J.; Rodríguez-Hernández, P.; Muñoz, A.; Popescu, C.; Beltrán, A., Isostructural Second-Order Phase Transition of $\beta\text{-Bi}_2\text{O}_3$ at High Pressures: An Experimental and Theoretical Study. *The Journal of Physical Chemistry C* **2014**, *118*, (40), 23189-23201.
184. Lifshitz, I., Anomalies of electron characteristics of a metal in the high pressure region. *Sov. Phys. JETP* **1960**, *11*, (5), 1130-1135.
185. Devidas, T. R.; Chandra Shekar, N. V.; Sundar, C. S.; Chithaiah, P.; Sorb, Y. A.; Bhadrani, V. S.; Chandrabhas, N.; Pal, K.; Waghmare, U. V.; Rao, C. N. R., Pressure-induced structural changes

- and insulator-metal transition in layered bismuth triiodide, BiI₃: a combined experimental and theoretical study. *Journal of Physics: Condensed Matter* **2014**, 26, (27), 275502.
186. Friedrich, A.; Juarez-Arellano, E. A.; Haussuhl, E.; Boehler, R.; Winkler, B.; Wiehl, L.; Morgenroth, W.; Burianek, M.; Muhlberg, M., Persistence of the stereochemical activity of the Bi³⁺ lone electron pair in Bi₂Ga₄O₉ up to 50 GPa and crystal structure of the high-pressure phase. *Acta Crystallographica Section B* **2010**, 66, (3), 323-337.
187. Janolin, P. E.; Bouvier, P.; Kreisel, J.; Thomas, P. A.; Kornev, I. A.; Bellaiche, L.; Crichton, W.; Hanfland, M.; Dkhil, B., High-Pressure Effect on PbTiO₃: An Investigation by Raman and X-Ray Scattering up to 63 GPa. *Physical Review Letters* **2008**, 101, (23), 237601.

2. Structure-Directing Lone Pairs: Synthesis and Structural Characterization of SnTiO₃

Leo Diehl, Sebastian Bette, Florian Pielnhöfer, Sophia Betzler, Igor Moudrakovski, Geoffrey A. Ozin, Robert Dinnebier and Bettina V. Lotsch.

Published in: *Chem. Mater.* **2018**, *30* (24), 8932-8938.

DOI: 10.1021/acs.chemmater.8b04261

Formatting and number of figures were changed.

Adapted with permission from The American Chemical Society.

Abstract

SnTiO₃ was successfully synthesized for the first time in bulk form by soft chemistry. STEM and Rietveld refinement show that SnTiO₃ adopts a structure similar to the archetypal ilmenite-type structure, forming a honeycomb lattice of edge-sharing TiO₆-octahedra, which are decorated with Sn²⁺. Given the formation of a van der Waals gap between the individual layers and hence close energetic minima of different stacking types, SnTiO₃ forms multiple stacking orders and twinning domains that we describe by systematic DIFFaX-simulations. The structure is governed by the tin lone pairs, which influence the stacking of the layers as well as local distortions observed by EELS and NMR potentially leading to a wide range of applications.

2.1. Introduction

Titanates have proven to be one of the most diverse classes of materials, with applications ranging from ferroelectrics and photocatalysis¹ to thermoelectrics²⁻³ and batteries⁴. Oxidic titanates with ABX₃ stoichiometry, where B is Ti⁴⁺ (d⁰) and A is a metal of +II oxidation state, can further be classified according to the Goldschmidt tolerance factor into either hexagonal ilmenite-type or cubic perovskite-type structures⁵. If A is a post-transition metal with ns² electron configuration, the effect of lone pairs may have interesting implications for their structure and properties⁶⁻⁷. In recent years, such lone pair materials have received increased attention, especially since hybrid perovskites⁸ and related structures⁹ have proven to be potent photovoltaic materials and show promising optoelectronic properties.

One famous example is Pb(Zr,Ti)O₃ (PZT)¹⁰, the technologically most relevant piezoelectric. The 6s²-orbital induces a tetragonal distortion¹¹ between 230 and 500 °C depending on the Zr content. This principle has been successfully applied to other ferroelectric materials, such as the multiferroic BiFeO₃⁷, but the exact role of the lone pairs remains a matter of scientific debate¹².

Lead-based compounds have negative consequences for both environment and health¹³. Therefore, the scientific community has actively been searching for suitable nontoxic alternatives.

The most promising candidates have been BaTiO₃, (Na,Bi)TiO₃ and (Na,K)NbO₃, neither of which has come close to the piezoelectric coefficient d_{33} of PZT¹⁴⁻¹⁶. SnTiO₃, however, has been predicted to have a polarization of up to 1.1 C m⁻² in the tetragonal perovskite modification¹⁷⁻¹⁸. Sparked by this forecast, a plethora of theoretical papers has discussed the physical properties of the hypothetical SnTiO₃ perovskite¹⁹⁻²⁴. Despite all such efforts, the synthesis of this "simple" bulk SnTiO₃ has remained unsuccessful until today. Notably, while Taib *et al.* predicted the perovskite²² to be the most stable modification, Hautier *et al.* predicted the ilmenite-type SnTiO₃ to be more stable²⁵.

Sn₂TiO₄ is the only known tin titanate²⁶⁻²⁸, which has recently been proposed as a photocatalytic material for hydrogen evolution, while other titanates containing Sn²⁺ were either doped TiO₂²⁹, doped layered potassium titanates³⁰ or doped SrTiO₃^{31,32}. SnTiO₃ has been realized as an epitaxial thin film on SrTiO₃ and the structure was proposed to be of ilmenite-type (FeTiO₃, $R\bar{3}$), yet this proposition was based on hexagonal SAED patterns only³³. Following up very recently, Chang *et al.* reported a ferroelectrically responsive thin film with SnTiO_x stoichiometry³⁴⁻³⁵. Generally, oxides featuring Sn²⁺ are barely amenable to solid-state synthesis due to their low disproportionation temperature of about 350 °C. Besides the binary oxides – red SnO³⁶, black SnO, as well as some mixed-valence oxides such as Sn₂O₃, Sn₃O₄ etc³⁷ – only few nondoped ternary Sn²⁺ oxides are known, including SnNb₂O₆, Sn₂Nb₂O₇³⁸, SnWO₆³⁹, SnTa₂O₆ and Sn₂Ta₂O₆⁴⁰⁻⁴¹.

2.2. Experimental Procedure

As pointed out above, it is experimentally challenging to avoid the disproportionation of Sn²⁺ into Sn⁰ and Sn⁴⁺. In order to bypass this scenario, a layered potassium titanate precursor was synthesized to enable a low-temperature ion exchange reaction of potassium by tin²⁸. First, a mixture of K₂CO₃ and TiO₂-nanoparticles (P25) was heated up to 600 °C in air for 12 h.

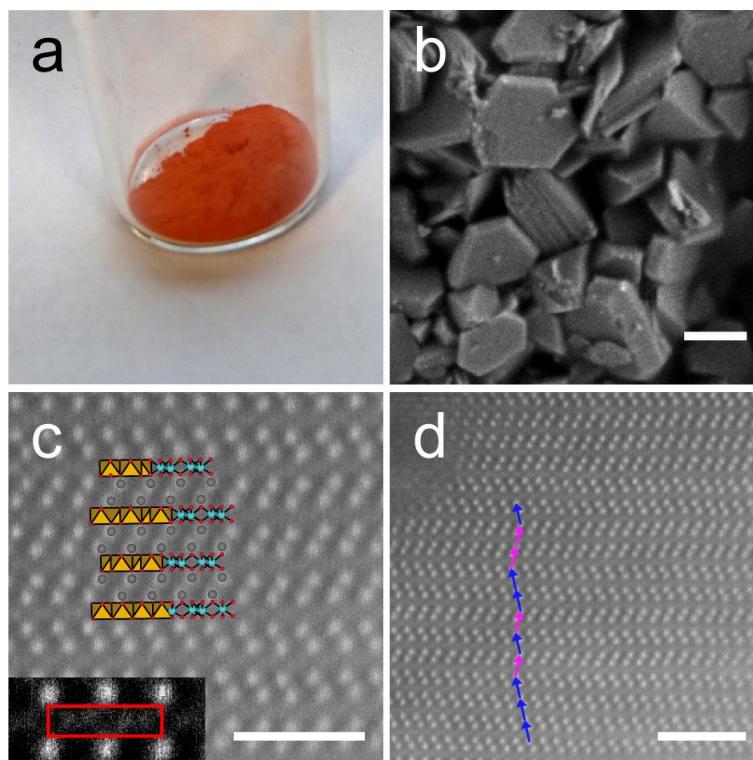


Figure 2.1. a) Photograph of red SnTiO₃ powder, b) Scanning electron micrograph of the material, showing its hexagonal, layered morphology (scale bar 200 nm). c) Dark field STEM with crystal structure as inset (scale bar 2 nm). Note the atomic columns of smaller intensity indicating the presence of differing Ti-positions (inset with enhanced contrast). d) Stacking faults with respective stacking vectors (scale bar 3 nm).

Then, the formed layered potassium titanate precursor K₂Ti₂O₅ was ground together with SnCl₂ · 2 H₂O until a lemon yellow powder formed, similar to observations made by Kudo *et al.*³⁰ This powder was transferred into an ampule and dehydrated in two steps: 2.5 h at 130 °C and then another 2.5 h at 200 °C under dynamic vacuum. Eventually the powder was annealed at 300 °C for 24 hours under static vacuum until SnTiO₃ formed. For removal of KCl the obtained SnTiO₃ powder was washed twice with H₂O and once with ethanol; a homogeneous powder of red color was obtained (Figure 2.1a). SEM images show that the powder consists of small platelets of several hundreds of nanometers in lateral and few tens of nanometers in axial direction (Figure 2.1b).

STEM revealed a layer-type structure, confirming the macroscopic platelet morphology (Figure 2.1d). It is apparent that the structure is heavily stacking faulted (as indicated by the two stacking vectors **S1** (blue) and **S2** (pink)) and shows no type of regular superstructure ordering.

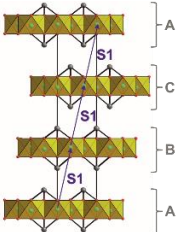
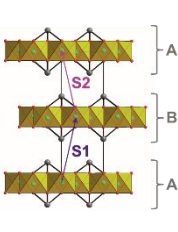
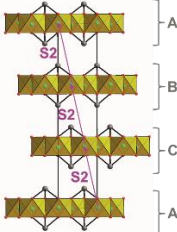
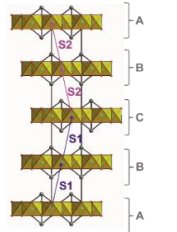
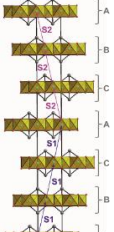
2.3. Structural Characterization

An initial structural model of SnTiO₃ was derived from the observations made by Fix *et al.*³³ According to this model, SnTiO₃ is expected to crystallize in an ilmenite-type structure that exhibit Ti₆O₁₂O_{12/2}¹²⁻ honeycombs. Because of the heavily stacking faulted nature (STEM in

2. Structure-Directing Lone Pairs: Synthesis and Structural Characterization of SnTiO₃

Figure 2.1 a and b), indexing attempts using ilmenite derived symmetry and also an iterative use of singular value decomposition for indexing (LSI-indexing) the XRPD pattern⁴² was not possible. Other stacking faulted diffraction patterns had successfully been modeled by the superposition of differently stacked hypothetical polytypes⁴³⁻⁴⁵; thus, analogous structural considerations were carried out for SnTiO₃. In total, five distinct polytypes, representing five different stacking orders, were considered (Table 2.1).

Table 2.1. Refined lattice parameters of all five polytypes of SnTiO₃, representing distinct stacking orders at ambient conditions. The layer position is indicated by a capital Latin letter.

Polytype	ABC-type	AB-type	ACB-type	ABCB-type	ABCACB-type
Space Group	$R\bar{3}$	$P\bar{3}$	$R\bar{3}$	$P\bar{3}$	$P\bar{3}$
$a/\text{\AA}$	5.0750(2)	5.0750(2)	5.0750(2)	5.0750(2)	5.0750(2)
$b/\text{\AA}$	5.0750(2)	5.0750(2)	5.0750(2)	5.0750(2)	5.0750(2)
$c/\text{\AA}$	$3 \cdot 6.8961(3)$	$2 \cdot 6.8961(3)$	$3 \cdot 6.8961(3)$	$4 \cdot 6.8961(3)$	$6 \cdot 6.8961(3)$
$\alpha/^\circ$	90	90	90	90	90
$\beta/^\circ$	90	90	90	90	90
$\gamma/^\circ$	120	120	120	120	120
$V/\text{\AA}^3$	$3 \cdot 153.82(2)$	$2 \cdot 153.82(2)$	$3 \cdot 153.82(2)$	$4 \cdot 153.82(2)$	$6 \cdot 153.82(2)$
R-F ² / % ^a	4.00	3.30	4.39	4.36	4.22
Graphical representation of polytypes					
R-wp/ % ^a	10.54				

^aR-F² and R-wp given as defined in TOPAS⁴⁶

It was assumed that a change in the stacking order of the SnTiO₃-layers causes neither a variation of the layer constitution nor a deviation from the basic trigonal layer symmetry, as further supported by EELS and DFT (Figure 2.4). Rietveld refinement of SnTiO₃ was carried out with the program TOPAS 6.0⁴⁶. SnO₂ and K₂Ti₈O₁₇ occur as minor impurity phases and were included in the refinement (Figure 2.3, orange and blue reflection positions). Accordingly, the five hypothetical polytypes were created in a pseudotrigoonal cell in space group $P1$ and with constrained lattice parameters, which were determined by a LeBail-Fit⁴⁷ with peak profiles being modeled by the fundamental parameter approach⁴⁸. The refined atomic coordinates of one individual layer are

presented in Table 2.2, and the result of the final associated Rietveld refinement⁴⁹ is shown in Figure 2.3.

Table 2.2. Refined atomic coordinates of a layer in the crystal structure of SnTiO₃ at ambient conditions.

site	x ^a	y ^a	z ^{a,b}	site	x ^a	y ^a	z ^{a,b}
Ti(1)	0	0	0.0014(26)	Ti(2)	$\frac{2}{3}$	$\frac{1}{3}$	-0.010(28)
Sn(1)	$\frac{1}{3}$	$\frac{2}{3}$	-0.320(2)	Sn(2)	$\frac{1}{3}$	$\frac{2}{3}$	0.322(2)
O(1a)	$\frac{1}{3}$	0	0.160(12)	O(2a)	$\frac{1}{3}$	$\frac{1}{3}$	-0.140(10)
O(1b)	0	$\frac{1}{3}$	0.160(12)	O(2b)	$\frac{2}{3}$	0	-0.140(10)
O(1c)	$\frac{2}{3}$	$\frac{2}{3}$	0.160(12)	O(2c)	0	$\frac{2}{3}$	-0.140(10)

^a For creation of stacking types, the layers have to be added by using the stacking vectors given in eq. 2 (SI).

^b The *z*-coordinates are given for a unit cell containing one layer, i.e. $c = 6.8961(3)$ Å, for the creation of different stacking patterns, they must be divided by the total number of layers in the cell.

The crystal structure of SnTiO₃ consists of layers of edge-sharing TiO₆-octahedra perpendicular to the *c*-axis. Within the layers $\frac{1}{3}$ of the Ti-sites are vacant, which results in a honeycomb like lattice (Figure 2.2a) and is consistent with other ilmenite-type oxides⁵⁰⁻⁵¹. In contrast to “3D ilmenites”, however, Sn²⁺ ions are positioned directly above and below a Ti-vacancy, forming two layers⁵² that are separated by a van der Waals gap (Figure 2.2a).

In addition, in the crystal structure of SnTiO₃, the Sn²⁺ ions exhibit a tetrahedral coordination sphere with the electron lone pair situated at an apical position, which contrasts with the octahedral coordination of the A-site cations in ordinary ilmenite-type structures. The subsequent layer is positioned such that the distance between the lone pair of Sn²⁺ and the O²⁻-sites at the bottom of the subsequent layer is maximized, as depicted by plots of the electron localization function (ELF). The induced van der Waals gap is also manifesting in an elongated *c*-axis compared to ilmenite-type structures (i.e., $c = 14.0855$ Å in FeTiO₃⁵¹, compared to $c = 3 \cdot 6.8961$ Å in SnTiO₃).

The Ti⁴⁺ ions exhibit an octahedral coordination sphere and the atomic distances indicate a trigonal distortion (Table S A.3). We note that although the refined Ti-O distances are equal within the estimated standard deviations (ESDs), they still indicate a slight tendency for acentric symmetry. When taking a closer look at the HR-STEM image from the inset in Figure 2.1c, the titanium positions vary indeed, also explaining the relatively high ESD from Rietveld refinement. The nature of the TiO₆-octahedra will be further discussed below.

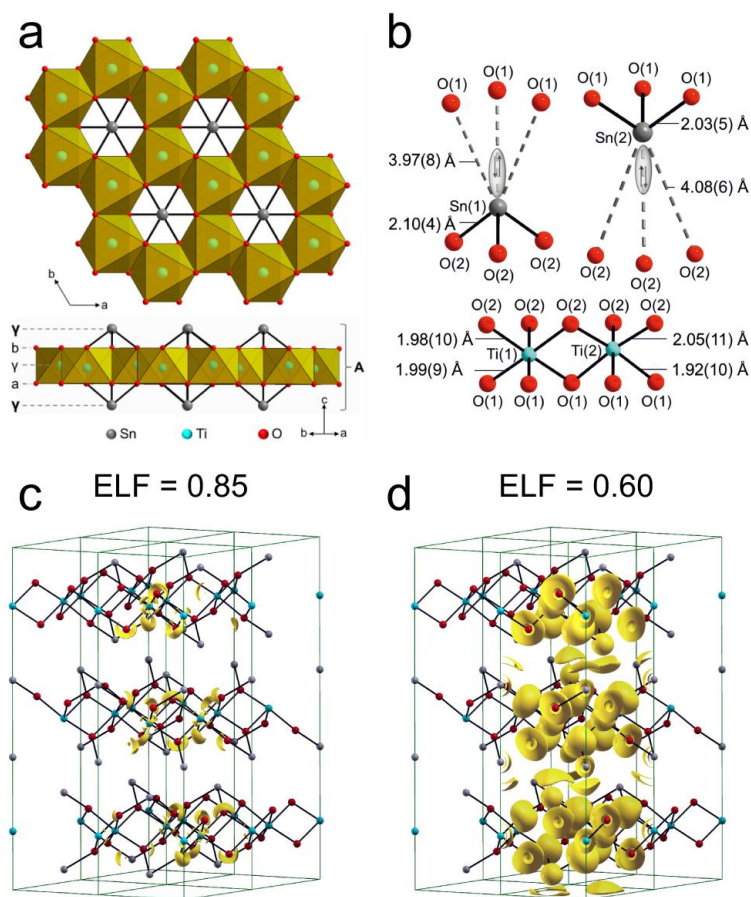


Figure 2.2. a) Crystal structure and packing diagrams of the layers in the crystal structure of SnTiO₃. The positions of Ti⁴⁺ are indicated by small Greek letters, the positions of Sn²⁺ by bold small Greek letters, and the positions of O²⁻ by small Latin letters. The position of a whole layer is indicated by capital Latin letters. b) Coordination spheres of Ti⁴⁺ and Sn²⁺ in the crystal structure of SnTiO₃. c) ELF (isosurface at 0.85) showing the attractors of the Ti-O bonds and O lone pairs, and d) ELF (isosurface at 0.6) showing the structure directing lone pair of Sn²⁺ between the layers.

As mentioned above, the stacking order of the layers in SnTiO₃ is determined by the positions of the Sn²⁺ ions, in particular by their electron lone pairs, such that one of the Ti⁴⁺-ions of layer *i*+1 must be situated exactly above the Sn²⁺-site of the preceding layer *i*. According to the honeycomb structural motif six stacking vectors are theoretically possible; however, because of the trigonal symmetry of the honeycomb, only two of them are nonsymmetry-equivalent: stacking in $\frac{2}{3}x$ - and $\frac{1}{3}y$ -direction, **S1**, and stacking in reverse direction: $\frac{1}{3}x$ and $\frac{2}{3}y$, **S2**. In an ilmenite-type structure, only stacking vectors in one direction (either **S1** or **S2**) are present. Therefore, the overall stacking order reduces to ABC (or ACB). As seen above, this is not true for SnTiO₃. Here only a multiphase approach using both stacking vectors describes the diffraction pattern satisfactorily. Because of the derivation from the ideal ilmenite-type structure, a transition from stacking vector **S1** to **S2** can be considered as stacking fault.

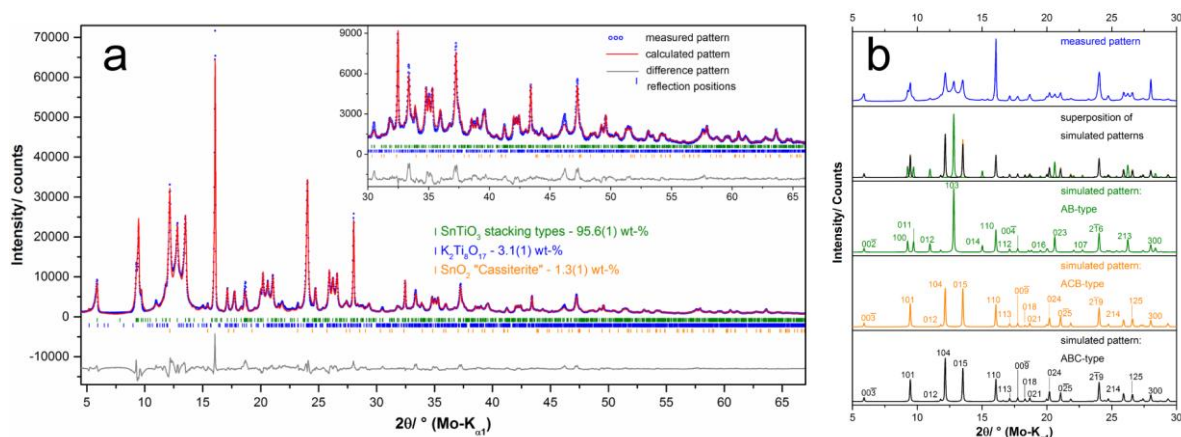


Figure 2.3. a) Final Rietveld refinement of the crystal structure of SnTiO₃ employing different polytypes in order to represent coherently scattering domains that exhibit different stacking orders. The region above 30° 2 θ is enlarged for clarity (insert). b) Comparison of simulated XRPD patterns with different stacking orders of SnTiO₃ with the measured XRPD pattern.

To better understand the nature of the stacking faults, systematic studies using the *DIFFaX*-program⁵³ were carried out. The XRPD patterns of the basic stacking types ABC- (Figure 2.3b, black pattern), ACB- (orange pattern), and AB-type (green pattern) were simulated and compared to the measured XRPD pattern (blue line) of SnTiO₃. Apparently, the measured pattern exhibits more reflections than each individual basic stacking type. A superposition of the three basic stacking types, however, exhibits close similarity to the measured pattern and especially to the characteristic “triplets” around 12.5°, 21° and 26° 2 θ . The “outer” two reflections (104) and (015) correlate with ABC/ACB-type stacking (**S1 or S2** only) while the “central” reflection (103) correlates with AB-type stacking (**S1 and S2**), respectively. It should be noted that differentiation between ABC- and ACB-type stacking from the XRPD-pattern is very difficult as the simulated XRPD-patterns (Figure 2.3b black and orange pattern) exhibit the same number of reflections at identical positions and only differing in certain reflection intensities. We conclude that in the microstructure of SnTiO₃ coherently scattering domains of each of these stacking types are present.

With further *DIFFaX*-simulations it becomes apparent that occasional AB-type stacking defects do not completely describe faulting (Figure S A.5). Given the very small coherently scattering domain, the central reflection would have a rather broad profile, which is not observed in the powder pattern. Only by additional consideration of twinning ranges larger than zero and the respective stacking types (ABCB and ABCACB) the sharp reflection profile is reproduced. The measured XRPD pattern of SnTiO₃ is satisfactorily described ($R_w = 10.54\%$) by the multiphase approach. The largest difference between calculated and measured pattern is observed for the 110 reflection ($\approx 16^\circ$ 2 θ), which indicates that modeling of the twinning domain size by separate phases is not

completely sufficient. An extension of the approach towards even more phases, however, would lead to an overparametrization of the refinement.

To further elucidate the stacking fault nature of the structure, DFT calculations on the relative stabilities of the different stacking polytypes were performed: (1) ABC/ACB-type, (2) AB-type, (3) ABCB-type and (4) ABCACB-type. Irrespective of the applied exchange correlation functional (LDA, GGA, HSE06), all applied structural models differ by less than 0.14 kJ mol⁻¹ (LDA; PBE: 0.06 kJ mol⁻¹; HSE06: 0.01 kJ mol⁻¹). These strikingly close energetic minima corroborate that at finite temperatures all stacking motifs will be present. The obtained volume per formula unit with the HSE06 hybrid functional (V_{FU}) of $\sim 77.5 \text{ \AA}^3$ is in very good agreement with 76.9 \AA^3 from the Rietveld refinement. The increase of V_{FU} from $\sim 53 \text{ \AA}^3$ in ordinary ilmenite-type structures (e.g., FeTiO₃) to the lone pair containing SnTiO₃ is reminiscent of the increase observed from $\sim 57 \text{ \AA}^3$ in SrTiO₃ to 63 \AA^3 in PbTiO₃. However, the significantly smaller increase in the latter testifies to the fact that the lone pair in perovskite-type PbTiO₃ is confined in the cuboctahedral voids, while the lone pairs in SnTiO₃ form van der Waals gaps⁵⁴ and hence can occupy more space (see also ELF in Figure 2.2).

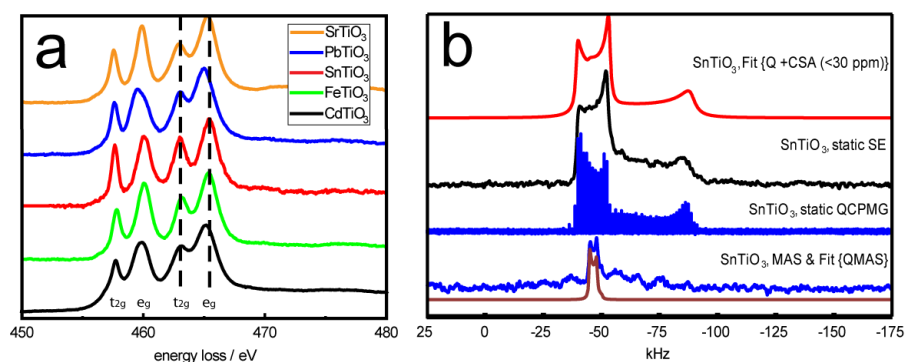


Figure 2.4. a) EELS spectra of the Ti L_{2,3} edge for different titanates, b) 21.1 T high field ss-NMR of ^{47,49}Ti under static solid-echo (black) and QCPMG (blue) conditions with corresponding fit (red), assuming two central transitions with 2nd order quadrupolar interactions.

The local symmetry of the TiO₆ octahedra was further analyzed by means of EELS and solid-state NMR. The white lines of the Ti-L_{2,3} edge are split to form two doublets, which is caused by energetic splitting of t_{2g}- and e_g-orbitals. This splitting is characteristic for octahedral crystal fields,⁵⁵ thus confirming TiO₆-octahedra as the major structural motif. Specifically, the e_g-level in EELS (at $\sim 460 \text{ eV}$) is known to be sensitive towards tetragonal distortions in PbTiO₃⁵⁶ (Figure 2.4). In contrast, trigonal distortions as in corundum-type Ti₂O₃⁵⁷ and other ilmenite-type materials⁵⁸ do not have an effect on the e_g-level. As there is no peak splitting observable for SnTiO₃, it can be concluded that potential distortions of the TiO₆-octahedra are constrained to D_{3d} symmetry.

Consequently, it is reasonable to only refine the z-coordinates of the atomic sites, as done in the Rietveld refinement.

Detailed analysis of the Ti-L_{2,3} edge of different titanates yields varying crystal field splittings (CFS) between 1.9 and 2.5 eV (Table S A.6). The CFS was measured at the $P_{3/2}$ level due to the reduced e_g-splitting. Interestingly, the presence of a lone pair in the structures causes a drastically reduced CFS in perovskite-type structures from 2.36 eV in SrTiO₃ to 1.91 eV in PbTiO₃, while it increases in ilmenite-type structures from about 2.06 eV in FeTiO₃ to 2.27 eV in SnTiO₃. At the same time the e_g-peak intensity decreases and the e_g-peak fwhm increases similarly for both structure type due to the presence of a lone pair in the structure⁵⁹. The peak broadening has been explained by differing hybridizations of the involved orbitals and consequently differing transition probabilities⁶⁰. High-field solid state-NMR spectroscopy confirms the distortion of the TiO₆-octahedra (Figure 2.4 and Table S A.8). The obtained quadrupole constant C_Q of SnTiO₃ is 7.29 MHz, which suggests that a local distortion at the Ti site is at play. In contrast, other compounds with the ideal ilmenite-type structure such as CdTiO₃ or ZnTiO₃ (Figure S A.8 and Table S A.8) show even larger C_Qs with some exceeding 15 MHz. It is thus surprising that in contrast to the strong increase observed from undistorted perovskite-type SrTiO₃ to distorted perovskite-type PbTiO₃⁶¹⁻⁶² the effect of the lone pair is reversed in SnTiO₃, as has also been seen in CFS from EELS. Since the Electric Field Gradient (EFG) is indirectly a function of the cell volume, a strong increase of the V_{FU} from FeTiO₃ to SnTiO₃ could potentially level the effect of the lone pair.

A still relatively high value of the experimental C_Q together with the η_Q = 0.0 suggest an axially symmetric distortion along the rotational axis higher than C₂. Periodic structure DFT calculations, based on the undistorted structure model presented above, suggest values of about 6.04 MHz for C_Q. While the calculated value is smaller than the experimental one by about 20%, the agreement here is much better than for other models, such as the unexpanded ilmenite-type structure. The discrepancy should be connected to effects induced by the stacking faults as well as the large variation in the Ti-position within its octahedron, see Fig. 2.1c. Note, however, that even at the very high field of 21.1 T, it was not possible to discriminate between different Ti sites.

2.4. Summary

Bulk SnTiO₃ was synthesized for the first time by a metathesis reaction between the layered K₂Ti₂O₅ and hydrated SnCl₂ using a soft chemistry protocol at < 350 °C. The bulk structure of SnTiO₃ was determined by a combination of XRPD, STEM/EELS, and solid-state NMR. Layers of honeycombs consisting of edge-sharing TiO₆-octahedra that are decorated with Sn²⁺ ions are the main structural motif in SnTiO₃. This arrangement gives rise to an “expanded” ilmenite-derived structure featuring van der Waals gaps due to the stereochemically active lone pairs of Sn²⁺, which likewise directs the stacking order of the layers. Stacking faults in the form of coherently

scattering domains with different stacking orders are apparent in the crystal structure and were confirmed by STEM imaging. The microstructure of SnTiO₃ was successfully modelled by a multiphase approach using different phases for each basic stacking order and twinning domains that were derived from structural considerations. Systematic *DIFFaX*-simulations confirm the result of the multiphase approach. DFT and ELF calculations support the lone pairs as structure-directing motif as well as the stacking fault nature of the material. EELS spectra of the Ti-L_{2,3} edge confirm the octahedral environment and restrict potential distortions to trigonal symmetry. Solid-state NMR confirms the trigonal distortion. In perspective, SnTiO₃ presents an interesting test-bed to study lone pair induced structural distortions, which may be relevant in such diverse applications as ferroelectrics, photocatalysis, and beyond.

2.5. Associated Content

Supporting Information. The Supporting Information is available free of charge on the ACS Publications website at DOI: 10.1021/acs.chemmater.8b04261. Details as well as additional information about the applied methods and experimental conditions (PDF)

2.6. Author Information

2.6.1. Corresponding Author

*E-Mail: b.lotsch@fkf.mpg.de

ORCID.

Sebastian Bette: 0000-0003-3575-0517

Geoffrey A. Ozin: 0000-0002-6315-0925

Bettina V. Lotsch: 0000-0002-3094-303X

2.6.2. Funding Sources

Max-Planck-Society and Nanosystems Initiative Munich

2.6.3. Notes

The authors declare no competing financial interest.

2.7. Acknowledgment

The authors thank Viola Duppel for SEM imaging, Prof. Jürgen Köhler and Prof. Annette Bussmann-Holder for fruitful discussions and V. Tersikh for help with the UHF NMR experiments. Access to the 900 MHz NMR spectrometer was provided by the National Ultrahigh Field NMR Facility for 826 Solids managed by University of Ottawa, Ottawa, Canada (<http://www.nmr900.ca>).

2.8. References

1. Zhang, P.; Ochi, T.; Fujitsuka, M.; Kobori, Y.; Majima, T.; Tachikawa, T., Topotactic Epitaxy of SrTiO₃ Mesocrystal Superstructures with Anisotropic Construction for Efficient Overall Water Splitting. *Angew. Chem. Int. Ed.* **2017**, *56* (19), 5299-5303.
2. Dynys, F. W.; Berger, M.-H.; Sehirlioglu, A., Thermoelectric Properties of Undoped and Doped (Ti_{0.75}Sn_{0.25})O₂. *J. Am. Ceram. Soc.* **2012**, *95* (2), 619-626.
3. Moore, L. A.; Smith, C. M., Reduced Strontium Titanate Thermoelectric Materials. In *Ceramics for Environmental and Energy Applications II*, John Wiley & Sons, Inc.: 2014; pp 43-55.
4. Xie, F.; Zhang, L.; Su, D.; Jaroniec, M.; Qiao, S.-Z., Na₂Ti₃O₇@N-Doped Carbon Hollow Spheres for Sodium-Ion Batteries with Excellent Rate Performance. *Adv. Mater.* **2017**, *29* (24), 1700989.
5. Dos santos-Garcia, A. J.; Solana-Madruga, E.; Ritter, C.; Avila-Brandé, D.; Fabelo, O.; Saez-Puche, R., Synthesis, structures and magnetic properties of the dimorphic Mn₂CrSbO₆ oxide. *Dalton Transactions* **2015**, *44* (23), 10665-10672.
6. Wahila, M. J.; Butler, K. T.; Lebens-Higgins, Z. W.; Hendon, C. H.; Nandur, A. S.; Treharne, R. E.; Quackenbush, N. F.; Sallis, S.; Mason, K.; Paik, H.; Schlom, D. G.; Woicik, J. C.; Guo, J.; Arena, D. A.; White, B. E.; Watson, G. W.; Walsh, A.; Piper, L. F. J., Lone-Pair Stabilization in Transparent Amorphous Tin Oxides: A Potential Route to p-Type Conduction Pathways. *Chem. Mater.* **2016**, *28* (13), 4706-4713.
7. Walsh, A.; Payne, D. J.; Egdell, R. G.; Watson, G. W., Stereochemistry of post-transition metal oxides: revision of the classical lone pair model. *Chem. Soc. Rev.* **2011**, *40* (9), 4455-4463.
8. Lotsch, B. V., Ein Klassiker im neuen Gewand: Perowskit-Solarzellen. *Angew. Chem.* **2014**, *126* (3), 647-649.
9. Lerner, C.; Birkhold, S. T.; Moudrakovski, I. L.; Mayer, P.; Schoop, L. M.; Schmidt-Mende, L.; Lotsch, B. V., Toward Fluorinated Spacers for MAPI-Derived Hybrid Perovskites: Synthesis, Characterization, and Phase Transitions of (FC₂H₄NH₃)₂PbCl₄. *Chem. Mater.* **2016**, *28* (18), 6560-6566.
10. Jaffe, B.; Jr., W. R. C.; Jaffe, H., *Piezoelectric Ceramics*. Academic Press: London and New York, 1971.
11. Cohen, R. E., Origin of ferroelectricity in perovskite oxides. *Nature* **1992**, *358*, 136-138.
12. Stoltzfus, M. W.; Woodward, P. M.; Seshadri, R.; Klepeis, J.-H.; Bursten, B., Structure and Bonding in SnWO₄, PbWO₄, and BiVO₄: Lone Pairs vs Inert Pairs. *Inorg. Chem.* **2007**, *46* (10), 3839-3850.
13. Restriction of the use of certain hazardous substances (RoHS). In *Directive 2011/65/EU*, Union, E., Ed. 2011.
14. Shrout, T. R.; Zhang, S. J., Lead-free piezoelectric ceramics: Alternatives for PZT? *J. Electroceram.* **2007**, *19* (1), 113-126.
15. Rödel, J.; Jo, W.; Seifert, K. T. P.; Anton, E.-M.; Granzow, T.; Damjanovic, D., Perspective on the Development of Lead-free Piezoceramics. *J. Am. Ceram. Soc.* **2009**, *92* (6), 1153-1177.
16. Saito, Y.; Takao, H.; Tani, T.; Nonoyama, T.; Takatori, K.; Homma, T.; Nagaya, T.; Nakamura, M., Lead-free piezoceramics. *Nature* **2004**, *432*, 84-87.
17. Parker, W. D.; Rondinelli, J. M.; Nakhmanson, S. M., First-principles study of misfit strain-stabilized ferroelectric SnTiO₃. *Physical Review B* **2011**, *84* (24), 245126.
18. Matar, S. F.; Baraille, I.; Subramanian, M. A., First principles studies of SnTiO₃ perovskite as potential environmentally benign ferroelectric material. *Chem. Phys.* **2009**, *355* (1), 43-49.
19. Pitike, K. C.; Parker, W. D.; Louis, L.; Nakhmanson, S. M., First-principles studies of lone-pair-induced distortions in epitaxial phases of perovskite SnTiO₃ and PbTiO₃. *Physical Review B* **2015**, *91* (3), 035112.
20. Ribeiro, R. A. P.; de Lazaro, S. R., DFT/PBE0 study on structural, electronic and dielectric properties of SnZr_{0.50}Ti_{0.50}O₃ lead-free ferroelectric material. *J. Alloys Compd.* **2017**, *714* (Supplement C), 553-559.
21. Ye, H.; Zhang, R.; Wang, D.; Cui, Y.; Wei, J.; Wang, C.; Xu, Z.; Qu, S.; Wei, X., First-principles Calculation of Lead-Free Perovskite SnTiO₃. *Int. J. Mod Phys B* **2013**, *27* (24), 1350144.

22. Taib, M. F. M.; Yaakob, M. K.; Badrudin, F. W.; Kudin, T. I. T.; Hassan, O. H.; Yahya, M. Z. A., First Principles Calculation of Tetragonal (P4 mm) Pb-free Ferroelectric Oxide of SnTiO₃. *Ferroelectrics* **2014**, *459* (1), 134-142.
23. Taib, M. F. M.; Yaakob, M. K.; Badrudin, F. W.; Rasiman, M. S. A.; Kudin, T. I. T.; Hassan, O. H.; Yahya, M. Z. A., First-Principles Comparative Study of the Electronic and Optical Properties of Tetragonal (P4mm) ATiO₃ (A = Pb,Sn,Ge). *Integrated Ferroelectrics* **2014**, *155* (1), 23-32.
24. Taib, M. F. M.; Yaakob, M. K.; Hassan, O. H.; Yahya, M. Z. A., Structural, Electronic, and Lattice Dynamics of PbTiO₃, SnTiO₃, and SnZrO₃: A Comparative First-Principles Study. *Integrated Ferroelectrics* **2013**, *142* (1), 119-127.
25. Hautier, G.; Jain, A.; Ong, S. P., From the computer to the laboratory: materials discovery and design using first-principles calculations. *Journal of Materials Science* **2012**, *47* (21), 7317-7340.
26. Boltersdorf, J.; Sullivan, I.; Shelton, T. L.; Wu, Z.; Gray, M.; Zoellner, B.; Osterloh, F. E.; Maggard, P. A., Flux Synthesis, Optical and Photocatalytic Properties of n-type Sn₂TiO₄: Hydrogen and Oxygen Evolution under Visible Light. *Chem. Mater.* **2016**, *28* (24), 8876-8889.
27. Burton, L. A.; Walsh, A., A photoactive titanate with a stereochemically active Sn lone pair: Electronic and crystal structure of Sn₂TiO₄ from computational chemistry. *J. Solid State Chem.* **2012**, *196*, 157-160.
28. Kumada, N.; Yonesaki, Y.; Takei, T.; Kinomura, N.; Wada, S., Preparation and crystal structure of a new tin titanate containing Sn²⁺; Sn₂TiO₄. *Mater. Res. Bull.* **2009**, *44* (6), 1298-1300.
29. Boppana, V. B. R.; Jiao, F.; Newby, D.; Laverock, J.; Smith, K. E.; Jumas, J. C.; Hutchings, G.; Lobo, R. F., Analysis of visible-light-active Sn(ii)-TiO₂ photocatalysts. *PCCP* **2013**, *15* (17), 6185-6189.
30. Hosogi, Y.; Kato, H.; Kudo, A., Photocatalytic Activities of Layered Titanates and Niobates Ion-Exchanged with Sn²⁺ under Visible Light Irradiation. *The Journal of Physical Chemistry C* **2008**, *112* (45), 17678-17682.
31. Wang, T.; Pitike, K. C.; Yuan, Y.; Nakhmanson, S. M.; Gopalan, V.; Jalan, B., Chemistry, growth kinetics, and epitaxial stabilization of Sn²⁺ in Sn-doped SrTiO₃ using (CH₃)₆Sn₂ tin precursor. *APL Materials* **2016**, *4* (12), 126111.
32. Suzuki, S.; Honda, A.; Iwaji, N.; Higai, S. i.; Ando, A.; Takagi, H.; Kasatani, H.; Deguchi, K., Ferroelectricity of Sn-doped SrTiO₃ perovskites with tin at both A and B sites. *Physical Review B* **2012**, *86* (6), 060102.
33. Fix, T.; Sahonta, S. L.; Garcia, V.; MacManus-Driscoll, J. L.; Blamire, M. G., Structural and Dielectric Properties of SnTiO₃, a Putative Ferroelectric. *Crystal Growth & Design* **2011**, *11* (5), 1422-1426.
34. Chang, S.; Selvaraj, S. K.; Choi, Y.-Y.; Hong, S.; Nakhmanson, S. M.; Takoudis, C. G., Atomic layer deposition of environmentally benign SnTiO_x as a potential ferroelectric material. *Journal of Vacuum Science & Technology A: Vacuum, Surfaces, and Films* **2016**, *34* (1), 01A119.
35. Agarwal, R.; Sharma, Y.; Chang, S.; Pitike, K. C.; Sohn, C.; Nakhmanson, S. M.; Takoudis, C. G.; Lee, H. N.; Tonelli, R.; Gardner, J.; Scott, J. F.; Katiyar, R. S.; Hong, S., Room-temperature relaxor ferroelectricity and photovoltaic effects in tin titanate directly deposited on a silicon substrate. *Physical Review B* **2018**, *97* (5), 054109.
36. Köhler, J.; Tong, J.; Dinnebier, R.; Simon, A., Crystal Structure and Electronic Structure of Red SnO. *Z. Anorg. Allg. Chem.* **2012**, *638* (12-13), 1970-1975.
37. Wang, J.; Umezawa, N.; Hosono, H., Mixed Valence Tin Oxides as Novel van der Waals Materials: Theoretical Predictions and Potential Applications. *Advanced Energy Materials* **2016**, *6* (1), 1501190.
38. Hosogi, Y.; Shimodaira, Y.; Kato, H.; Kobayashi, H.; Kudo, A., Role of Sn²⁺ in the Band Structure of SnM₂O₆ and Sn₂M₂O₇ (M = Nb and Ta) and Their Photocatalytic Properties. *Chem. Mater.* **2008**, *20* (4), 1299-1307.
39. Jeitschko, W.; Sleight, A. W., Stannous tungstate: properties, crystal structure and relationship to ferroelectric SbTaO₄ type compounds. *Acta Crystallographica Section B* **1974**, *30* (9), 2088-2094.

40. Mizoguchi, H.; Sleight, A. W.; Subramanian, M. A., Low temperature synthesis and characterization of SnTa₂O₆. *Mater. Res. Bull.* **2009**, *44* (5), 1022-1024.
41. Mizoguchi, H.; Wattiaux, A.; Kykyneshi, R.; Tate, J.; Sleight, A. W.; Subramanian, M. A., Synthesis and characterization of Sn²⁺ oxides with the pyrochlore structure. *Mater. Res. Bull.* **2008**, *43* (8), 1943-1948.
42. Bette, S.; Dinnebier, R. E.; Freyer, D., Structure solution and refinement of stacking-faulted NiCl(OH). *J. Appl. Crystallogr.* **2015**, *48* (6), 1706-1718.
43. Wallace, D. C.; Brown, C. M.; McQueen, T. M., Evolution of magnetism in the Na_{3-δ}(Na_{1-x}Mg_x)Ir₂O₆ series of honeycomb iridates. *J. Solid State Chem* **2015**, *224*, 28-35.
44. Wallace, D. C.; McQueen, T. M., New honeycomb iridium(v) oxides: NaIrO₃ and Sr₃CaIr₂O₉. *Dalton Trans.* **2015**, *44* (47), 20344-20351.
45. Bette, S.; Takayama, T.; Kitagawa, K.; Takano, R.; Takagi, H.; Dinnebier, R. E., Solution of the heavily stacking faulted crystal structure of the honeycomb iridate H₃LiIr₂O₆. *Dalton Trans.* **2017**.
46. *TOPAS 6.0*, Bruker AXS: 2017.
47. Le Bail, A.; Duroy, H.; Fourquet, J. L., Ab-initio structure determination of LiSbWO₆ by X-ray powder diffraction. *Mater. Res. Bull.* **1988**, *23* (3), 447-452.
48. Cheary, R. W.; Coelho, A., A fundamental parameters approach to X-ray line-profile fitting. *J. Appl. Crystallogr.* **1992**, *25* (2), 109-121.
49. Rietveld, H. M., A profile refinement method for nuclear and magnetic structures. *J. Appl. Crystallogr.* **1969**, *2* (2), 65-71.
50. Newnham, R. E.; Fang, J. H.; Santoro, R. P., Crystal structure and magnetic properties of CoTiO₃. *Acta Crystallographica* **1964**, *17* (3), 240-242.
51. Wechsler, B. A.; Prewitt, C. T., Crystal structure of ilmenite (Fe Ti O₃) at high temperature and high pressure. *Am. Mineral.* **1984**, *69*, 176-185.
52. Prasad, B. E.; Kanungo, S.; Jansen, M.; Komarek, A. C.; Yan, B.; Manuel, P.; Felser, C., AgRuO₃, a Strongly Exchange-Coupled Honeycomb Compound Lacking Long-Range Magnetic Order. *Chemistry – A European Journal* **2017**, *23* (19), 4680-4686.
53. M. M. J. Treacy, J. M. N., M. W. Deem, A general recursion method for calculating diffracted intensities from crystals containing planar faults. *Proceedings of the Royal Society of London. Series A: Mathematical and Physical Sciences* **1991**, *433* (1889), 499-520.
54. Winterton, R. H. S., Van der Waals forces. *Contemporary Physics* **1970**, *11* (6), 559-574.
55. Brydson, R.; Sauer, H.; Engel, W.; Thomass, J. M.; Zeitler, E.; Kosugi, N.; Kuroda, H., Electron energy loss and X-ray absorption spectroscopy of rutile and anatase: a test of structural sensitivity. *J. Phys.: Condens. Matter* **1989**, *1* (4), 797-812.
56. Eberg, E.; Helvoort, A. T. J. v.; Takahashi, R.; Gass, M.; Mendis, B.; Bleloch, A.; Holmestad, R.; Tybell, T., Electron energy loss spectroscopy investigation of Pb and Ti hybridization with O at the PbTiO₃/SrTiO₃ interface. *J. Appl. Phys.* **2011**, *109* (3), 034104.
57. Stoyanov, E.; Langenhorst, F.; Steinle-Neumann, G., The effect of valence state and site geometry on Ti L_{3,2} and O K electron energy-loss spectra of Ti_xO_y phases. *Am. Mineral.* **2007**, *92* (4), 577-586.
58. Radtke, G.; Lazar, S.; Botton, G. A., High-resolution EELS investigation of the electronic structure of ilmenites. *Physical Review B* **2006**, *74* (15), 155117.
59. Sefat, A. S.; Amow, G.; Wu, M.-Y.; Botton, G. A.; Greedan, J. E., High-resolution EELS study of the vacancy-doped metal/insulator system, Nd_{1-x}TiO₃, x=0 to 0.33. *J. Solid State Chem.* **2005**, *178* (4), 1008-1016.
60. de Groot, F. M. F.; Fuggle, J. C.; Thole, B. T.; Sawatzky, G. A., L_{2,3} x-ray-absorption edges of d₀ compounds: K⁺, Ca²⁺, Sc³⁺, and Ti⁴⁺ in Oh (octahedral) symmetry. *Physical Review B* **1990**, *41* (2), 928-937.
61. Padro, D.; Jennings, V.; Smith, M. E.; Hoppe, R.; Thomas, P. A.; Dupree, R., Variations of Titanium Interactions in Solid State NMR Correlations to Local Structure. *The Journal of Physical Chemistry B* **2002**, *106* (51), 13176-13185.

62. Lucier, B. E. G.; Huang, Y., Chapter One - Reviewing 47/49Ti Solid-State NMR Spectroscopy: From Alloys and Simple Compounds to Catalysts and Porous Materials. In *Annual Reports on NMR Spectroscopy*, Webb, G. A., Ed. Academic Press: 2016; Vol. 88, pp 1-78.

3. Examining experimentally accessible structural candidates of SnTiO₃: The search for novel ferroelectric materials

Florian Pielnhöfer, [Leo Diehl](#), Alberto Jiménez-Solano, Annette Bußmann-Holder, J. Christian Schön, Bettina V. Lotsch*

To be submitted.

Abstract

Driven by the recent successful synthesis and characterization of bulk SnTiO₃, its energy landscape was studied by means of density functional theory, applying different exchange-correlation and hybrid functionals. Both a data mining and global exploration approach identified experimentally accessible structure candidates with composition ABO₃. Besides the common octahedral coordination of Ti, interestingly, 4- and 5-fold coordination spheres emerged to be reasonable structural motifs. Among the predicted high-pressure modifications, the tetragonal perovskite structure turned out to be stable at pressures between 8 and 12 GPa. The paraelectric-to-ferroelectric phase transition of the tetragonal perovskite structure was investigated by modelling the phonon spectra and soft mode behavior. In spite of substantially long wavelength transverse optical mode softening, the predicted high *c/a*-ratio in tetragonal perovskite SnTiO₃ inhibits the formation of a spontaneous reversible polarization.

3.1. Introduction

Recently, we reported about the first successful synthesis and structural characterization of bulk SnTiO₃¹. The structure can be understood as a heavily stacking faulted variant of an expanded ilmenite-type structure, which was proven by high resolution transmission electron microscopy (TEM) and X-ray powder diffraction (XRPD) investigations. The α -TlSbO₃-type accounts for this expansion, yet also does not fully describe the crystal structure of SnTiO₃. Common to both structure types is the main structural motif of honeycomb layers of edge-sharing TiO₆ octahedra that are decorated with Sn²⁺ cations. In order to understand the similarity between α -TlSbO₃ (space group $P\bar{3}1c$) and SnTiO₃ (space group $R\bar{3}$) it is helpful to observe the hexagonal definition of the latter space group (SG). Both structures are of (pseudo-)layered character, $P\bar{3}1c$ being a double and $R\bar{3}$ being a triple layer cell. The lone pair of both Tl and Sn in α -TlSbO₃ and SnTiO₃ leads to an expansion into the stacking direction, which can be rationalized by the stereochemical activity of the lone pair electrons and differentiates them from the actual ilmenite structure-type. To stay in accordance with the nomenclature of the introduced perovskite-type derived structures, we also use the [FeTiO₃] notation were applicable, but add an “e” to explicitly emphasize were we mean the expanded ilmenite structure-type in this text.

3. Examining experimentally accessible structural candidates of SnTiO₃: The search for novel ferroelectric materials

The weak out-of-plane interaction in SnTiO₃ induces stacking faults. To account for these faults, SnTiO₃ was described using five different polytype models that also are energetically quasi-identical¹ as obtained by density functional theory (DFT).

Whether the ilmenite-type derived modification is metastable or thermodynamically favored had been discussed controversially by Nakhmanson *et al.* and Hautier *et al.* According to Nakhmanson², the tetragonal perovskite structure with SG $P4mm$ is the ground state for SnTiO₃, whereas Hautier³ predicted the ilmenite-type to be the thermodynamically stable form. It is however the perovskite-type structure of SnTiO₃ that is intensively discussed as a promising lead-free ferroelectric material among the solid state and materials science community, whereas centrosymmetric SnTiO₃ is not expected to show polar distortions⁴⁻¹³.

Experimental work by Fix *et al.*¹⁴ has shown that also thin films of SnTiO₃ show a characteristic hexagonal diffraction pattern of the ilmenite-type structure. The lattice parameters of the thin film material show a distortion ($a \neq b$) due to substrate induced strain. The c -axis was determined to be 14.56 Å, which is 2/3 of our findings¹. Despite the structural distortion, no ferroelectricity was observed. Based on weak reflections in XRPD reciprocal space maps they further speculated about minor amounts of tetragonal perovskite SnTiO₃ present in the films.

Scott *et al.*¹⁵ even reported relaxor ferroelectricity in SnTiO₃ films grown on Si substrates by atomic layer deposition. They claimed several crystallite orientations of perovskite-like structures with different c/a - and a/b -ratios. The provided structural XRPD characterization is, however, rudimentary. The quality of the presented powder pattern does not allow for any conclusions concerning the crystal structure. Indeed, Scott *et al.* revised their claim to have prepared perovskite-like SnTiO₃ in a recent report¹⁶. They disclose to have drawn erroneous conclusions from both XRPD and ferroelectric measurements.

The most prominent ferroelectrics¹⁷ are Pb(Ti,Zr)O₃, and variants of BaTiO₃ among the large family of perovskite materials¹⁸. Besides perovskites, also the LiNbO₃-type structures exhibit high piezoelectric coefficients. Due to the center of inversion, compounds that crystallize in an ilmenite-type structure have to be excluded as candidate ferroelectrics. However, ABX_3 ilmenite-type titanates can be transformed into perovskite-type structures by applying high pressure, as has been demonstrated for (Mg,Fe)TiO₃¹⁹, ZnTiO₃²⁰⁻²¹, and for CdTiO₃, the latter showing a ferroelectric phase transition at only around 2 GPa and 600 °C²². The phase transition to perovskite-type structures was observed in germanates, stannates (CdSnO₃), silicates and even vanadates (MnVO₃)²³⁻²⁶. In many cases, these phase transitions cannot be stabilized at room temperature, where then the LiNbO₃-type phase is obtained instead²⁷. To rationalize the observed effects under pressure the Goldschmidt tolerance factor has been frequently used. This

3. Examining experimentally accessible structural candidates of SnTiO₃: The search for novel ferroelectric materials

method is, however, inconclusive since it requires the knowledge of exact ionic radii, which in the case of Sn²⁺ are unreliable.

Lone pairs may induce, besides ferroelectricity, novel electronic properties under high pressure. For example, disproportionation in PbCrO₃ leads to an insulator-to-metal transition²⁸. Generally, lone pair containing materials have been shown to have interesting anisotropic phase transitions²⁹⁻³⁰.

In this work SnTiO₃ was modeled in more than 40 ABX₃ structure types at the *ab initio* level to explore its energy landscape in order to identify experimentally accessible ferroelectric modifications. Suitable structure candidates were chosen by data mining and a global search algorithm. We predict two high-pressure modifications by equation of state calculations. Phonon spectra for the predicted structures are calculated in order to check for their dynamical stability. Electronic and mechanical properties as well as viable paraelectric-to-ferroelectric phase transitions of the most promising candidates were further investigated.

3.2. Methodology

Structure optimization and total energy comparison for five different polytypes derived from the ilmenite-type structure have already been performed in our previous work¹. The different stacking variants as used for the structure determination from powder diffraction all exhibit very similar volumes per formula unit and differ in energy by max. 0.14 kJ mol⁻¹ depending on the functional used for the modeling. These results are also employed in this work.

By data mining of (all) ABX₃ structures from the inorganic crystal structure database (ICSD) much of the energy landscape can be covered. To go beyond these known structure types, a global search routine based on empirical potentials for all sorts of atoms was applied. In order to obtain reliable results for Sn(II) it was required to use a dumbbell-like or puckered potential, which had already been successfully employed in the prediction of Sn(II) compounds³¹. The results from the data mining and the global exploration approach were further optimized locally at an *ab initio* level. While the symmetry was restricted to the SG for the database structures, the models from the empirical potential landscape search were first optimized in *P1* and the real SG was determined afterwards for the fully relaxed models with the *KPLOT* software as embedded in Endeavour³². In total, 44 structure types were modeled at DFT and hybrid level for SnTiO₃. A full list of the applied structure models is given in Table 3.1.

3. Examining experimentally accessible structural candidates of SnTiO₃:
The search for novel ferroelectric materials

Table 3.1. Calculated cell volumes per formula unit and energy difference to the most stable structure types (ΔE (HSE) \leq 115 kJ/mol) as obtained with the LDA, GGA and HSE06 functionals, ordered according to HSE energies differences.

Structure type	Space group	LDA		GGA		HSE06	
		$V / \text{\AA}^3$	$\Delta E / \text{kJ mol}^{-1}$	$V / \text{\AA}^3$	$\Delta E / \text{kJ mol}^{-1}$	$V / \text{\AA}^3$	$\Delta E / \text{kJ mol}^{-1}$
e-[FeTiO₃]	$R\bar{3}$	70.96	0.1	78.88	0.0	77.45	0.0
[\alpha-TlSbO₃]	$P\bar{3}1c$	70.87	0.0	79.08	0.1	77.68	0.0
[PX-PbTiO₃]	$I4/m$	67.46	8.6	73.70	13.9	71.77	24.1
[MgVO₃]	$Cmc2_1$	82.25	55.3	87.16	32.2	84.66	30.1
SnTiO₃-mP10	$P2_1/m$	64.20	17.9	71.97	19.8	69.67	33.6
[MgSiO₃]	$P2_1/c$	75.14	54.2	83.55	26.7	80.54	41.3
[BaTiO₃]	$P4mm$	61.62	21.0	68.68	30.4	66.60	49.0
optimized-[HgVO₃]	$P2_1/m$	62.83	33.0	70.36	38.2	67.61	54.5
[CaTaO₂N]	$Pmc2_1$	60.91	22.8	67.34	37.0	65.47	54.5
[LiNbO₃]	$R3c$	60.28	25.5	64.95	45.0	63.06	63.7
[SrTiO₃-oI20]	$Ima2$	60.27	25.5	65.53	43.9	63.47	63.8
[NaNbO₃-oP40]	$Pbcm$	60.09	38.1	68.75	50.2	66.92	69.6
[ScUS₃]	$Cmcm$	60.85	41.4	67.28	59.6	67.23	73.3
SnTiO₃-mP10-II	Pm	65.83	78.2	86.58	66.2	84.46	77.6
[BiMnO₃]	$C2/c$	59.03	39.8	64.22	62.9	62.65	84.5
[GdFeO₃]	$Pnma$	58.69	46.4	62.53	72.2	61.23	97.0
[CaIrO₃]	$Cmcm$	58.49	46.5	62.20	73.3	60.68	100.2
[BaPbO₃]	$Imma$	58.31	46.7	62.02	74.1	60.70	102.2
[CaSiO₃-tP40]	$P4_2/nmcz$	58.39	47.6	61.96	74.3	60.42	103.0
[BaFeO_{2+x}]	$P6_3/mmc$	60.52	57.5	64.40	77.5	62.53	103.2
[Sr₃CoSb₂O₉]	$Immm$	58.89	52.2	62.52	78.2	60.94	104.0
[NdAlO₃]	$R\bar{3}c$	58.25	48.4	61.83	76.2	60.12	105.0
[KCuF₃-tI20]	$I4/mcm$	58.21	48.6	61.73	75.5	60.10	105.1
[CaSiO₃-cI40]	$Im\bar{3}$	58.33	49.0	61.86	76.5	60.17	105.6
SnTiO₃-mP10-III	Pm	65.83	78.2	72.60	79.8	70.01	106.1
[CaTiO₃]	$Pm\bar{3}m$	58.57	53.5	62.14	81.0	60.28	107.0
[AgSbO₃]	$Fd\bar{3}mz$	61.81	63.9	65.72	84.8	63.61	107.6
[KSbO₃]	$Pn\bar{3}$	60.51	65.6	64.97	87.3	63.16	112.7
[\beta-TlSbO₃]	$P6_322$	-	-	86.16	105.1	85.12	114.0

3. Examining experimentally accessible structural candidates of SnTiO₃:
The search for novel ferroelectric materials

Energy versus volume optimization was carried out for all models and the obtained points were fitted to various (Birch, Birch-Murnaghan, Vinet and Poirier-Tarantola) equations of state (EoS). The local optimizations on an *ab initio* level were performed within the local density approximation (LDA), the generalized gradient approximation (GGA) and the hybrid functional HSE06 with 25 % of the exact Fock exchange, as it is reasonable to compare different functionals to gain better insight in the quantitative validity of the results.

3.3. Results and Discussion

3.3.1. Structure Models

As stated above, the experimentally obtained structure of SnTiO₃ can be represented by five different stacking variants as determined from Rietveld refinement of powder diffraction data. The polytypes (denoted with AB, ABC, ACB, ABCB and ABCACB) contain both the prominent e-[FeTiO₃]-type structure (ABC) and the [α-TiSbO₃]-type structure (AB). Since the energy minima and volume per formula unit of the relaxed structures are almost identical (+/-0.1 kJ mol⁻¹; ΔV: +/-0.3 %) and all stacking variants can be derived from AB and ABC, the present study focuses on the e-[FeTiO₃] and [α-TiSbO₃] polytypes, when comparing the experimental structure.

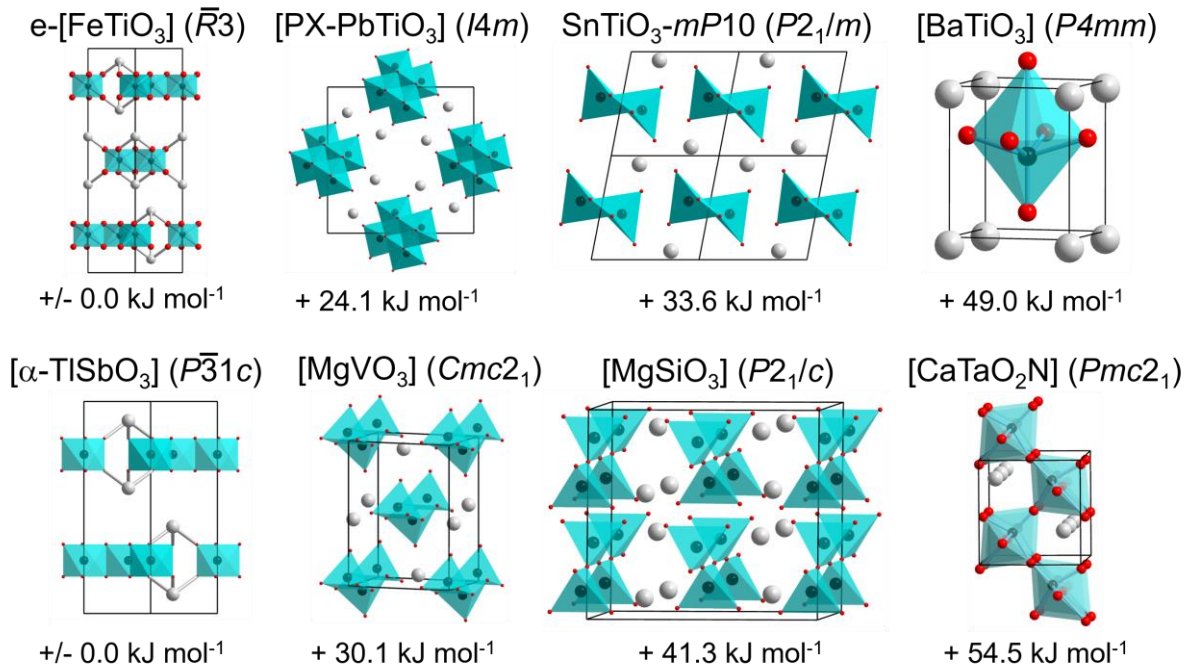


Figure 3.1. Most stable predicted structure types and respective total electronic energies from HSE06 calculations.

Among the (theoretical) structures investigated, the major differences can be found in the coordination spheres of Ti, which includes the perovskite-derivatives with (tilted/distorted) BX_6 -octahedra and the silicate analogous structures with tetrahedral B-site environment. To

3. Examining experimentally accessible structural candidates of SnTiO_3 : The search for novel ferroelectric materials

fully cover all possible B-site coordination environments even an exotic five-fold coordination of B is modeled within the $[\text{HgVO}_3]$ -type. A further differentiation can be made by comparing the different linkages of the polyhedra, which is corner-sharing in the perovskite-derivatives, while it is edge-sharing in $e\text{-}[\text{FeTiO}_3]$ and $[\alpha\text{-TlSbO}_3]$ and face sharing in $[\text{BaNiO}_3]$ -type, for example. While the data mining approach remains primarily controlled by chemical intuition, the predictive power of a global structure search was proven to be very successful in the recent past. Although no *ab initio* DFT potential input during the global search could be used due to convergence problems and had to be replaced by an empirical potential, indeed one of the identified structure models exhibits chains of edge-sharing BX_5 square pyramids as found in HgVO_3 , thus proving the method to be chemically viable.

3.3.2. Energy Landscape

Comparable to the study by Hautier *et al.*, we find that the experimentally determined structure, which is in fact more complex than just ordinary $e\text{-}[\text{FeTiO}_3]$ and $[\alpha\text{-TlSbO}_3]$ is lowest in energy and therefore identified as the most stable configuration independent of the applied functionals (Fig. 3.2). Here, PBE and HSE06 reveal qualitatively the same trends and LDA significantly differs in the magnitude of total energies. Results obtained by HSE06 perfectly reproduced the experimental lattice parameters a and c^* . Therefore, we stick to the HSE06-based results in this work, and only note the difference to LDA where required.

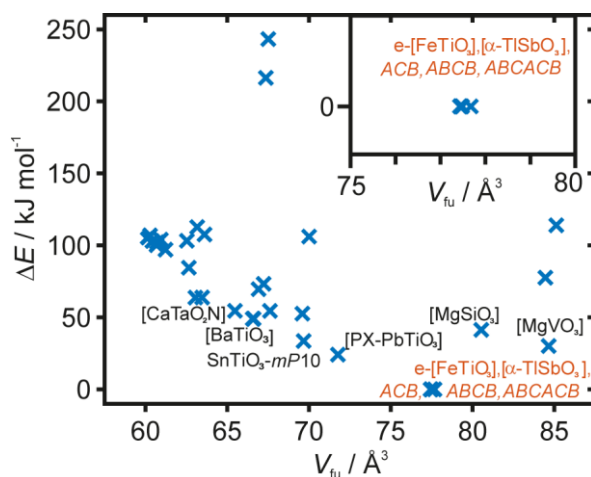


Figure 3.2. Minima of energy versus volume plots of all modeled structure types for SnTiO_3 (HSE06 calculations). Inset showing close up of polytype region.

Among the found structure models, the $[\text{PX-PbTiO}_3]$ ³³ structure type is within energetic proximity to $e\text{-}[\text{FeTiO}_3]$ - and $[\alpha\text{-TlSbO}_3]$ -type SnTiO_3 . This structure consists of edge-sharing one dimensional octahedral TiO_6 chains and has been realized for PbTiO_3 by hydrothermally treating slurries of soluble lead and titanium precursors³⁴. This polymorph is predicted to be less stable

3. Examining experimentally accessible structural candidates of SnTiO₃: The search for novel ferroelectric materials

by only +24 kJ mol⁻¹ and exhibits lower cell volume (67.46 Å³) than the experimental model. The [PX-PbTiO₃]-type is thus the model energetically closest to experimental SnTiO₃.

Moreover, a structure with 5-fold coordination of Ti as present for example in the [MgVO₃]-type structure is only +30 kJ mol⁻¹ higher in energy and exhibits the largest cell volume within the probed structure types. The [MgVO₃]-type structure is built up from one-dimensional zigzag chains of edge-sharing TiO₅ quadratic pyramids.

A model with the same Ti coordination as e-[FeTiO₃]-type SnTiO₃ but another TiO₆ sublattice is found (SnTiO₃-*mP10*) at +33.6 kJ mol⁻¹ and 69.67 Å³. This model with space group *P2₁/m* was predicted by the global search algorithm and features similar anionic double pyramidal chains as present in the [HgVO₃]-type, differing only in the stacking of the chains. This quadratic pyramidal coordination of Ti is present also in the layered K₂Ti₂O₅, which served as a starting material when synthesizing SnTiO₃. The actual [HgVO₃]-type is less favored for SnTiO₃ by another +20 kJ mol⁻¹. A tetrahedral coordination of Ti such as found in the [MgSiO₃]-type model leads to a large cell volume of 80.53 Å³ and is energetically shifted by already +41 kJ mol⁻¹ above the e-[FeTiO₃]- and [α-TlSbO₃]-type.

The desired candidate ferroelectric tetragonal perovskite-type structure ([BaTiO₃] SG *P4mm*) is only the 6th most stable configuration for SnTiO₃, with an energy difference of +49 kJ mol⁻¹. It features, however, a lower cell volume (66.6 Å³), suggesting a potential high-pressure transformation. Also the orthorhombic (*Pna2₁*), monoclinic (*Cm*, *Cc*) and triclinic versions of the perovskite-type structures converged into the same minimum of the energy hypersurface with exactly the same structure and symmetry (*P4mm*) within the error margin, indicating a large but not very deep basin in the energy landscape. The [CaTaO₂N]-type (SG *Pmc2₁*) structure, which is also found at a lower cell volume (63.06 Å³) is another representative of the large family among *ABX₃* perovskites with corner-sharing octahedra only, being energetically destabilized by +54.5 kJ mol⁻¹.

The fact that many of the modeled hypothetical structures indeed exhibit lower cell volumes than the ground state SnTiO₃ suggests the possibility for pressure-induced phase transitions. Therefore, all the *E-V* curves were fitted to equations of state (EoS) and translated to ΔH vs. *p* diagrams. Fig. 3.3 shows the full range of stable high-pressure configurations up to 20 GPa. Indeed, the e-[FeTiO₃]- and [α-TlSbO₃]-type SnTiO₃ show a phase transition to the tetragonal [BaTiO₃]-perovskite type at 11 GPa and a further transition from this tetragonal perovskite to the [CaTaO₂N]-type is predicted at 15 GPa. Both pressures can routinely be realized in diamond anvil cells and even multianvil setups, thus making the experimental realization of these structures a realistic scenario. Note that no further high-pressure phases are predicted when increasing the pressure up to an extreme of 200 GPa (data not shown).

3. Examining experimentally accessible structural candidates of SnTiO₃: The search for novel ferroelectric materials

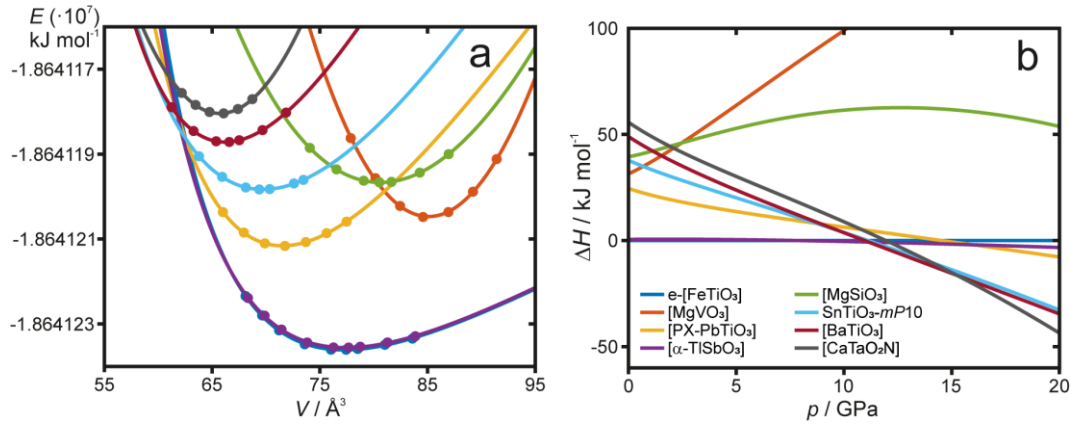


Figure 3.3 a) Energy vs volume curves as calculated by DFT-HSE06, fitted with Birch-Murnaghan (3rd order) equations of state and b) ΔH vs. p plots referenced to the e-[FeTiO₃]- and [α-TlSbO₃]-type SnTiO₃ (color code in both Figures corresponds to the color assigned in b).

In the following paragraph we discuss the results of our proposed high-pressure phase transitions in the context of previous theoretical work. Matar *et al.* predict an a lattice parameter of 3.80 Å for the [BaTiO₃] phase and a c/a ratio of 1.09 based on LDA calculations. Parker *et al.* propose a slightly larger c/a ratio of 1.13 (LDA) and 1.15 (GGA). However, the results and the quality of the calculations have to be taken with care in view of the prediction of the tetragonal perovskite structure as most stable polymorph. Furthermore, our experimental and theoretical work as well as calculations by Hautier *et al.* have disproven this result. With LDA, PBE and HSE06, we indeed arrive at a lattice parameter a that is comparable to the previous theoretical studies, however the c parameter and therefore the c/a ratio significantly differ by more than 5% for GGA ($c/a = 1.22$) and HSE06 ($c/a = 1.21$). The shortest Ti-O distance in the tetragonally distorted TiO₆ octahedra is 1.71 Å and the longest is 2.90 Å, thus corresponding to an extreme distortion. PbTiO₃ (SG $P4mm$) in contrast has for example Ti-O distances of 1.79 Å and 2.36 Å. The relaxed structure of the second predicted high-pressure phase [CaTaO₂N] (SG $Pmc2_1$) exhibits slightly smaller Ti-O distances at 1.77 Å and 2.82 Å, but still remains more strongly distorted than tetragonal PbTiO₃.

To check if these strong distortions remain within the dynamic stability limits, both high-pressure phases were probed by calculating the phonon frequencies. Due to the very high computational costs with the HSE06 functional the phonon spectra shown here (Fig. 3.4) were calculated at the GGA level. Only minor imaginary frequencies at the Γ -point of $i1.5$ cm⁻¹ and $i6.2$ cm⁻¹ were obtained for the [BaTiO₃] and [CaTaO₂N]-type structure, respectively. Note that even the experimentally realized e-[FeTiO₃] and [α-TlSbO₃]-type structures gave imaginary frequencies of $i3.1$ cm⁻¹ (data not shown). Thus, realization of both phases by application of high hydrostatic pressure indeed seems feasible.

3. Examining experimentally accessible structural candidates of SnTiO₃: The search for novel ferroelectric materials

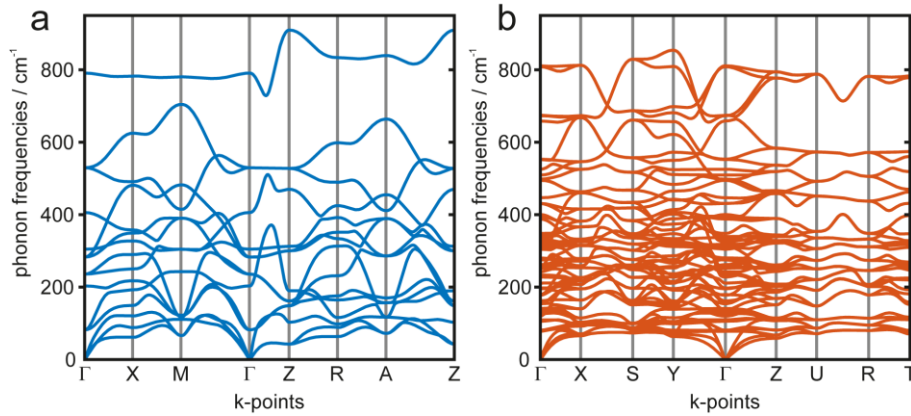


Figure 3.4. Phonon dispersion of the a) $P4mm$ and b) $Pmc2_1$ high-pressure polymorphs of SnTiO₃ as calculated by DFT-GGA.

3.3.3. Electronic band structures and bulk modulus

Band structure calculations with the hybrid functional HSE06 (Fig. 3.5) characterize both predicted high-pressure polymorphs as indirect gap semiconductors with slightly smaller band gaps compared to tetragonal PbTiO₃ (PBE: 2.08 eV, exp. \sim 3 eV taken from citation)³⁵⁻³⁶. The calculated values for both theoretically predicted polymorphs of SnTiO₃ at 1.87 eV for [BaTiO₃]-type and 1.95 eV for [CaTaO₂N]-type are very similar as expected due to a comparable bonding situation. Furthermore, the fitted EoS allow for the determination of the bulk moduli B_0 . The e-[FeTiO₃]-type structure has a very small B_0 of 24 GPa, which is in accordance with the later determined experimental value of 23 GPa (see Chapter 4 of this thesis). In contrast the bulk modulus of the first predicted HP-phase ([BaTiO₃]-type) is 59.4 GPa and the second HP-phase ([CaTaO₂N]-type) has a B_0 of 82.9 GPa. This is reasonable since HP-polymorphs are generally less compressible than the standard modifications.

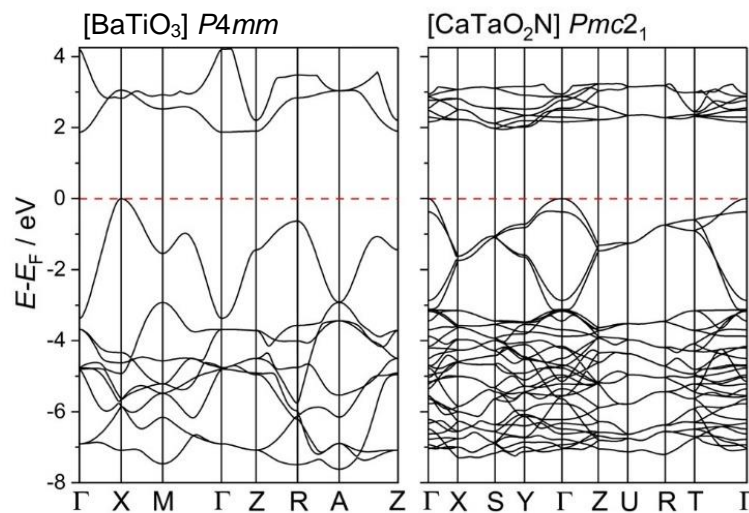


Figure 3.5. Electronic band structures of predicted high-pressure polymorphs of SnTiO₃: the [BaTiO₃]-type and [CaTaO₂N]-type (HSE06 calculations).

3.3.4. Possible Ferroelectricity

Within the family of perovskite titanates $ATiO_3$ various members are indeed ferroelectric (BaTiO₃, PbTiO₃) or close to a ferroelectric instability (SrTiO₃, CaTiO₃). A characteristic signature of a ferroelectric phase transition is the observation of the softening of a long wavelength transverse optical (TO) mode, which freezes at the transition and determines the low temperature structural transformation. This is realized in both BaTiO₃ and PbTiO₃, but incomplete in SrTiO₃ and CaTiO₃ due to quantum fluctuations in the former and negative transition temperatures in the latter. The modelling of mode softening in all compounds has been performed within the polarizability model¹⁸, which is based on a self-consistently derived double-well potential in the electron-ion interaction. In order to explore possible ferroelectricity in SnTiO₃ we use this exact model, however, due to the lack of experimental data the potential is taken to be the same as in SrTiO₃. This choice is rather ambiguous, but justifiable by the a -axis lattice parameter of SnTiO₃ which is closest to SrTiO₃. The A -ion sublattice mass is replaced by Sn, whereas all other parameters are taken to be identical. It is important to note that as a number of strong assumptions have been made in the modelling the results presented here have to be taken with care.

Upon consideration of the hypothetical cubic structure type, mode softening takes place in SnTiO₃, which closely resembles the findings for SrTiO₃ with an extrapolated T_c of 15 K (Fig. 3.6). Quantum fluctuations set in around 35 K as seen from the positive value for ω^2_{TO} at 0 K thus hindering a phase transition. Since however, the cubic structure can definitely not be realized for SnTiO₃, we included the theoretically predicted tetragonal distortions. For this, the c/a ratio is artificially enlarged while keeping the cell volume constant. All other parameters remain identical to the undistorted compound. With increasing c/a ratio the soft mode increasingly hardens (as seen from the steeper slopes in Fig. 3.6) and the transition temperatures shift into the negative regime, thus strongly disfavoring any polar instability.

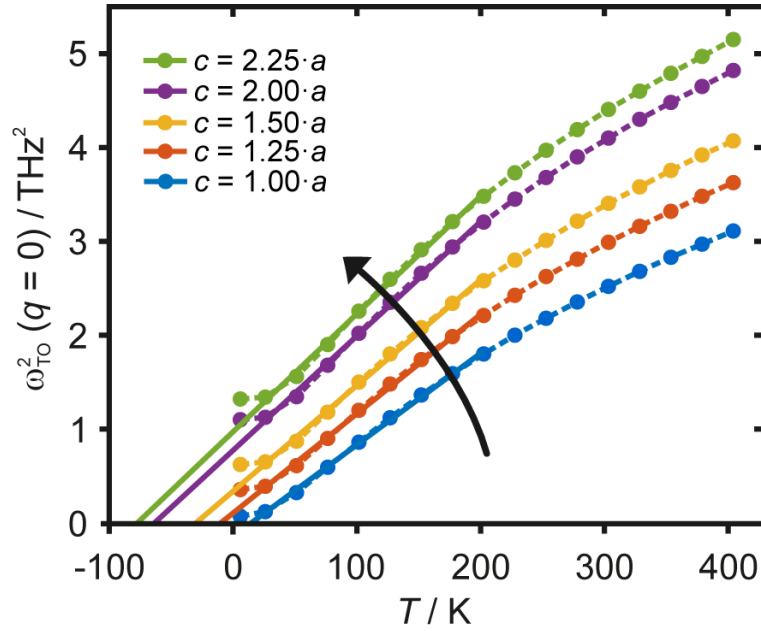


Figure 3.6. The squared soft mode frequency $\omega_{T_0}^2$ (wavevector $q = 0$) as a function of temperature for various c/a ratios as indicated in the figure. The heavy lines are extrapolations of the linear temperature regions indicating possible transition temperatures.

It must thus be concluded that in spite of the possibility for strong optical mode softening in SnTiO₃, tetragonal distortions rapidly suppress the appearance of a finite transition temperature. This is also true for the hypothetical cubic phase where an instability is suppressed by quantum fluctuations (nonzero $\omega_{T_0}^2$ at 0 K). Possible applications of the high-pressure phases of SnTiO₃ are nevertheless feasible, since a large dielectric constant in the cryogenic temperature region is expected, if the tetragonal perovskite phase can be quenched to ambient conditions.

3.4. Conclusions

We have explored the energy landscape of the compound SnTiO₃. The previous prediction³ of the expanded ilmenite-type structure to be the most stable phase can be confirmed. We further predict two metastable high-pressure polymorphs: The [BaTiO₃]-type SG $P4mm$ at pressures between 11 GPa and 15 GPa and the [CaTaO₂N]-type SG $Pmc2_1$ above $p = 15$ GPa. The existence of the [BaTiO₃]-type and its potential as a possible ferroelectric material has been intensively studied in the literature. We predict a much stronger tetragonal distortion of the tetragonal perovskite structure with $c/a = 1.21$ than previous studies suggested. This immense distortion prevents a hypothetical tetragonal perovskite SnTiO₃ from undergoing a paraelectric-to-ferroelectric phase transition. Hence, the phonon mode that describes the displacement of the Ti atom from the center of its octahedral environment cannot freeze and thus excludes a ferroelectric instability.

3.5. References

1. Diehl, L.; Bette, S.; Pielhofer, F.; Betzler, S.; Moudrakovski, I.; Ozin, G. A.; Dinnebier, R.; Lotsch, B. V., Structure-Directing Lone Pairs: Synthesis and Structural Characterization of SnTiO₃. *Chem. Mater.* **2018**, *30* (24), 8932-8938.
2. Parker, W. D.; Rondinelli, J. M.; Nakhmanson, S. M., First-principles study of misfit strain-stabilized ferroelectric SnTiO₃. *Physical Review B* **2011**, *84* (24), 245126.
3. Hautier, G.; Jain, A.; Ong, S. P., From the computer to the laboratory: materials discovery and design using first-principles calculations. *Journal of Materials Science* **2012**, *47* (21), 7317-7340.
4. Agarwal, R.; Sharma, Y.; Chang, S.; Pitike, K. C.; Sohn, C.; Nakhmanson, S. M.; Takoudis, C. G.; Lee, H. N.; Tonelli, R.; Gardner, J.; Scott, J. F.; Katiyar, R. S.; Hong, S., Room-temperature relaxor ferroelectricity and photovoltaic effects in tin titanate directly deposited on a silicon substrate. *Physical Review B* **2018**, *97* (5), 054109.
5. Pitike, K. C.; Parker, W. D.; Louis, L.; Nakhmanson, S. M., First-principles studies of lone-pair-induced distortions in epitaxial phases of perovskite SnTiO₃ and PbTiO₃. *Physical Review B* **2015**, *91* (3), 035112.
6. Wang, T.; Pitike, K. C.; Yuan, Y.; Nakhmanson, S. M.; Gopalan, V.; Jalan, B., Chemistry, growth kinetics, and epitaxial stabilization of Sn²⁺ in Sn-doped SrTiO₃ using (CH₃)₆Sn₂ tin precursor. *APL Materials* **2016**, *4* (12), 126111.
7. Ribeiro, R. A. P.; de Lazaro, S. R., Structural, electronic and elastic properties of FeBO₃ (B = Ti, Sn, Si, Zr) ilmenite: a density functional theory study. *RSC Advances* **2014**, *4* (104), 59839-59846.
8. Ribeiro, R. A. P.; de Lazaro, S. R., DFT/PBE0 study on structural, electronic and dielectric properties of SnZr_{0.50} Ti_{0.50} O₃ lead-free ferroelectric material. *J. Alloys Compd.* **2017**, *714* (Supplement C), 553-559.
9. Taib, M. F. M.; Yaakob, M. K.; Badrudin, F. W.; Kudin, T. I. T.; Hassan, O. H.; Yahya, M. Z. A., First Principles Calculation of Tetragonal (P4 mm) Pb-free Ferroelectric Oxide of SnTiO₃. *Ferroelectrics* **2014**, *459* (1), 134-142.
10. Taib, M. F. M.; Yaakob, M. K.; Badrudin, F. W.; Rasiman, M. S. A.; Kudin, T. I. T.; Hassan, O. H.; Yahya, M. Z. A., First-Principles Comparative Study of the Electronic and Optical Properties of Tetragonal (P4mm) ATiO₃ (A = Pb,Sn,Ge). *Integrated Ferroelectrics* **2014**, *155* (1), 23-32.
11. Taib, M. F. M.; Yaakob, M. K.; Hassan, O. H.; Yahya, M. Z. A., Structural, Electronic, and Lattice Dynamics of PbTiO₃, SnTiO₃, and SnZrO₃: A Comparative First-Principles Study. *Integrated Ferroelectrics* **2013**, *142* (1), 119-127.
12. Ye, H.; Zhang, R.; Wang, D.; Cui, Y.; Wei, J.; Wang, C.; Xu, Z.; Qu, S.; Wei, X., First-principles Calculation of Lead-Free Perovskite SnTiO₃. *Int. J. Mod Phys B* **2013**, *27* (24), 1350144.
13. Matar, S. F.; Baraille, I.; Subramanian, M. A., First principles studies of SnTiO₃ perovskite as potential environmentally benign ferroelectric material. *Chem. Phys.* **2009**, *355* (1), 43-49.
14. Fix, T.; Sahonta, S. L.; Garcia, V.; MacManus-Driscoll, J. L.; Blamire, M. G., Structural and Dielectric Properties of SnTiO₃, a Putative Ferroelectric. *Crystal Growth & Design* **2011**, *11* (5), 1422-1426.
15. Chang, S.; Selvaraj, S. K.; Choi, Y.-Y.; Hong, S.; Nakhmanson, S. M.; Takoudis, C. G., Atomic layer deposition of environmentally benign SnTiO_x as a potential ferroelectric material. *Journal of Vacuum Science & Technology A: Vacuum, Surfaces, and Films* **2016**, *34* (1), 01A119.
16. Gardner, J.; Thakre, A.; Kumar, A.; Scott, J. F., Tin titanate—the hunt for a new ferroelectric perovskite. *Rep. Prog. Phys.* **2019**, *82* (9), 092501.
17. Cohen, R. E., Origin of ferroelectricity in perovskite oxides. *Nature* **1992**, *358*, 136-138.
18. Bussmann-Holder, A., The polarizability model for ferroelectricity in perovskite oxides. *J. Phys.: Condens. Matter* **2012**, *24* (27), 273202.
19. Linton Jennifer, A.; Fei, Y.; Navrotsky, A., The MgTiO₃-FeTiO₃ join at high pressure and temperature. In *American Mineralogist*, 1999; Vol. 84, p 1595.

3. Examining experimentally accessible structural candidates of SnTiO₃:
The search for novel ferroelectric materials

20. Akaogi, M.; Abe, K.; Yusa, H.; Kojitani, H.; Mori, D.; Inaguma, Y., High-pressure phase behaviors of ZnTiO₃: ilmenite–perovskite transition, decomposition of perovskite into constituent oxides, and perovskite–lithium niobate transition. *Phys. Chem. Miner.* **2015**, *42* (6), 421-429.
21. Inaguma, Y.; Aimi, A.; Shirako, Y.; Sakurai, D.; Mori, D.; Kojitani, H.; Akaogi, M.; Nakayama, M., High-Pressure Synthesis, Crystal Structure, and Phase Stability Relations of a LiNbO₃-Type Polar Titanate ZnTiO₃ and Its Reinforced Polarity by the Second-Order Jahn–Teller Effect. *J. Am. Chem. Soc.* **2014**, *136* (7), 2748-2756.
22. Liebertz, J.; Rooymans, C. J. M., Die Ilmenit/Perowskit-Phasenumwandlung von CdTiO₃ unter hohem Druck. In *Zeitschrift für Physikalische Chemie*, 1965; Vol. 44, p 242.
23. Liu, L.-G., Post-ilmenite phases of silicates and germanates. *Earth. Planet. Sci. Lett.* **1977**, *35* (1), 161-168.
24. Yusa, H.; Akaogi, M.; Sata, N.; Kojitani, H.; Yamamoto, R.; Ohishi, Y., High-pressure transformations of ilmenite to perovskite, and lithium niobate to perovskite in zinc germanate. *Phys. Chem. Miner.* **2006**, *33* (3), 217-226.
25. Yusa, H., Structural Relaxation of Oxide Compounds from the High-Pressure Phase. In *Nanoinformatics*, Tanaka, I., Ed. Springer Singapore: Singapore, 2018; pp 259-277.
26. Leinenweber, K.; Utsumi, W.; Tsuchida, Y.; Yagi, T.; Kurita, K., Unquenchable high-pressure perovskite polymorphs of MnSnO₃ and FeTiO₃. *Phys. Chem. Miner.* **1991**, *18* (4), 244-250.
27. Navrotsky, A., Energetics and Crystal Chemical Systematics among Ilmenite, Lithium Niobate, and Perovskite Structures. *Chem. Mater.* **1998**, *10* (10), 2787-2793.
28. Cheng, J.; Kweon, K. E.; Larregola, S. A.; Ding, Y.; Shirako, Y.; Marshall, L. G.; Li, Z. Y.; Li, X.; dos Santos, A. M.; Suchomel, M. R.; Matsubayashi, K.; Uwatoko, Y.; Hwang, G. S.; Goodenough, J. B.; Zhou, J. S., Charge disproportionation and the pressure-induced insulator–metal transition in cubic perovskite PbCrO₃. *Proceedings of the National Academy of Sciences of the United States of America* **2015**, *112* (6), 1670-1674.
29. Zhang, J.; Han, Y.; Liu, C.; Ren, W.; Li, Y.; Wang, Q.; Su, N.; Li, Y.; Ma, B.; Ma, Y.; Gao, C., Electrical Transport Properties of SnO under High Pressure. *The Journal of Physical Chemistry C* **2011**, *115* (42), 20710-20715.
30. Olsen, L. A.; Balić-Žunić, T.; Makovicky, E., High-Pressure Anisotropic Distortion of Pb₃Bi₂S₆: a Pressure-Induced, Reversible Phase Transition with Migration of Chemical Bonds. *Inorg. Chem.* **2008**, *47* (15), 6756-6762.
31. Zagorac, D.; Schön, J. C.; Jansen, M., Identification of promising chemical systems for the synthesis of new materials structure types: An ab initio minimization data mining approach.
32. Putz, H.; Schön, J. C.; Jansen, M., Combined method for ab initio structure solution from powder diffraction data. *J. Appl. Crystallogr.* **1999**, *32* (5), 864-870.
33. Wang, J.; Wylie-van Eerd, B.; Sluka, T.; Sandu, C.; Cantoni, M.; Wei, X.-K.; Kvasov, A.; McGilly, L. J.; Gemeiner, P.; Dkhil, B.; Tagantsev, A.; Trodahl, J.; Setter, N., Negative-pressure-induced enhancement in a freestanding ferroelectric. *Nature Materials* **2015**, *14* (10), 985-990.
34. Cheng, H.; Ma, J.; Zhao, Z.; Qiang, D.; Li, Y.; Yao, X., Hydrothermal Synthesis of Acicular Lead Titanate Fine Powders. *J. Am. Ceram. Soc.* **1992**, *75* (5), 1123-1128.
35. Stashans, A.; Zambrano, C.; Sanchez, A.; Procel, L. M., Structural properties of PbTiO₃ and PbZr_xTi_{1-x}O₃: A quantum-chemical study. *Int. J. Quantum Chem* **2002**, *87* (3), 145-151.
36. Wang, L.; Yuan, P.; Wang, F.; Liang, E.; Sun, Q.; Guo, Z.; Jia, Y., First-principles study of tetragonal PbTiO₃: Phonon and thermal expansion. *Mater. Res. Bull.* **2014**, *49*, 509-513.

4. High-pressure phase transitions of ilmenite-type derived SnTiO₃

Leo Diehl, Lkhamsuren Bayarjargal, Florian Pielhofer, Victor Milman, Keith Refson, Björn Winkler and Bettina V. Lotsch

To be submitted.

Abstract

SnTiO₃ in the perovskite modification is predicted to have a very high dipole moment, but has not been realized synthetically. Here, we show high-pressure experiments with diamond anvil cells (DACs) up to 45 GPa on ilmenite-type derived SnTiO₃. Raman spectroscopy, in-situ powder diffraction on a synchrotron source and UV-Vis spectroscopy allow the assignment of three new phase transitions under pressure. At below 1 GPa the stacking order changes, at about 5 GPa an isostructural, electronic phase transition occurs and above 20 GPa a further phase transition is observed, potentially consistent with the phase transition to the perovskite-like SnTiO₃, as recently predicted theoretically. The observed phase transitions add to the understanding of lone pair induced electronic and crystallographic structures and their behavior under extreme pressures.

4.1. Introduction

Lone pair containing titanates have proven to be technologically relevant in many applications, of which ferroelectrics are the most prominent. Pb(Zr,Ti)O₃ (PZT)¹ is the textbook example for ferroelectric (pseudo) Jahn-Teller distortions in low temperature modifications. In a simplistic picture, the stereochemically active lone pair induces a non-centrosymmetric distortion² of the TiO₆-octahedra leading to the ferroelectric moment. The exact role of the lone pair remains under debate³, especially, when keeping in mind that also titanates without lone pairs show ferroelectric behavior⁴ and vice versa⁵.

Computationally, SnTiO₃ is theoretically predicted to be a suitable non-toxic alternative to PZT⁴ with a benchmark dipole moment of 1.1 C·m⁻²⁶⁻⁷. This dipole moment, however, is only computed for a (tetragonally) distorted perovskite modification⁸⁻¹², which has not been realized synthetically¹³. In Chapter 2 of this thesis we have shown that dipole switching might not be possible also for perovskite-type SnTiO₃, still leaving perovskite-type SnTiO₃ as a potential piezoelectric.

We have recently been able to synthesize an ilmenite-type derived layered modification of SnTiO₃¹⁴, making it the first example for an ilmenite-type derived titanate with lone pairs. Realization of this long-sought after material may shed new light on the complicated set of parameters determining the degree of distortion as well as influence on important ferroelectric

phase transitions, both temperature- and pressure-dependent. Indeed, SnTiO_3 shows Jahn-Teller distorted TiO_6 -octahedra as evidenced by solid-state NMR and STEM.

$(\text{Mg,Fe})\text{TiO}_3$ ¹⁵, MgSiO_3 and MgGeO_3 ¹⁶ with ilmenite-type derived structures have a phase transition to perovskite-like structures at high pressures, which often can be quenched to ambient conditions in the (non-centrosymmetric) LiNbO_3 structure-type with space group $R3c$ ¹⁷⁻¹⁹. A. Navrotsky has given a comprehensive description of the relationship between ilmenite-type, LiNbO_3 -type and perovskite-type structures²⁰. As shown in ZnTiO_3 ¹⁹, another example for an ilmenite-type titanate at ambient conditions, high-pressure experiments did allow the synthesis of a non-centrosymmetric polymorph: LiNbO_3 -type ZnTiO_3 with corner-sharing TiO_6 -octahedra. For SnTiO_3 we had calculated (Chapter 2 of this thesis) the $P4mm$ and $Pmc2_1$ perovskite-like structures to be the most stable modifications at pressures above 8 and 12 GPa, respectively.

High pressure, in general, is a synthesis parameter leading to interesting semiconductor-to-metal transitions in 2D van der Waals materials, for example in MoS_2 ²¹, MoSe_2 ²² and also WSe_2 ²³. In these cases, the electronic phase transitions were only accompanied by very small structural changes or even of isostructural nature. Most interestingly the lone pair dominated litharge-type SnO shows this type of phase transition at pressures $p > 5$ GPa²⁴.

Here, we present results of the search for perovskite-type SnTiO_3 by a high-pressure approach. We identify three phase transitions using Raman spectroscopy, optical absorption spectroscopy and X-ray powder diffraction (XRPD) and discuss the nature of these phase transitions.

4.2. Crystal Structure at ambient pressure

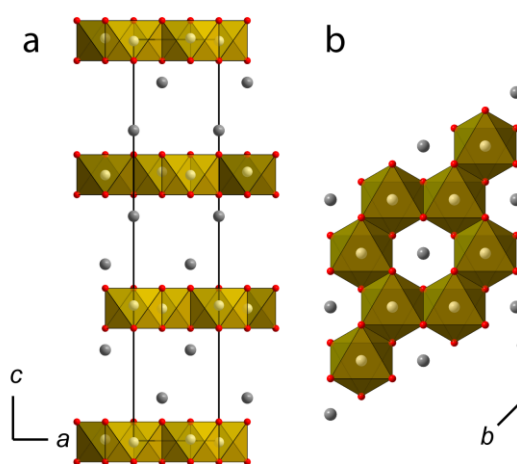


Figure 4.1. Crystal structure of ilmenite-type derived SnTiO_3 ($R\bar{3}$), grey representing Sn^{2+} , white Ti^{4+} and red representing O^{2-} ions. The $[010]$ -direction emphasizes the rhombohedral ABC-type stacking pattern (a) and the typical honeycomb structure can be seen from $[001]$ -direction (b).

Despite the elaborate description of the crystal structure in *Chemistry of Materials*¹⁴, we would like to take the reader through the character of the SnTiO₃ crystal structure once more. As mentioned in the introduction, SnTiO₃ crystallizes in an ilmenite-type derived structure, characterized by TiO₃-honeycombs with Sn²⁺ above and below the voids (Fig. 4.1). Due to the structure-directing lone pairs, the individual layers are separated through a van der Waals-like gap as also found in the only other ilmenite-type lone pair material α -TlSbO₃²⁵. As another consequence of this van der Waals gap, the individual layers do not strictly obey the rhombohedral ABC-type stacking pattern of ilmenite-type structures, but are heavily stacking faulted. Full description of the crystal structure only was possible with several polytypes of which AB-type stacking can be considered as manifestation of the stacking faults. The structure had been refined without restrictions regarding centrosymmetry in order to allow for the broad distribution of Ti-O distances found especially in STEM images¹⁴. DFT calculations in this work are based on a structural model in $P3$ or $R3$, although relaxation optimizes the structure into a centrosymmetric $R\bar{3}$ space group. We have further confirmed the centrosymmetric nature of the structure by SHG measurements (Fig. S B.1).

4.3. Raman spectroscopy at ambient pressure

Raman spectroscopy is a very sensitive tool to observe structural changes in solids, including micron-sized samples. Therefore, we first used Raman spectroscopy to identify possible phase transitions.

The ambient pressure spectrum (Fig. 4.2) shows (at least) ten different modes as summarized in Tab. 4.1. Ten is the expected amount of Raman active vibrations from group theory for the space group $R\bar{3}$ (no.148)²⁶. The spectra are in reasonable agreement regarding both peak positions and relative intensities. The calculated peak maxima are shifted by a factor of 6% towards lower energies due the fact that DFT calculations are carried out for 0 K, while measurements were taken at room temperature (~300 K). Upon calculation of the Raman spectra without centrosymmetric restrictions each individual layer shows very similar vibrations. The small structural deviations (varying Ti positions within their octahedra) in each layer cause a distribution of exact excitation energies, which in turn broaden the peaks significantly.

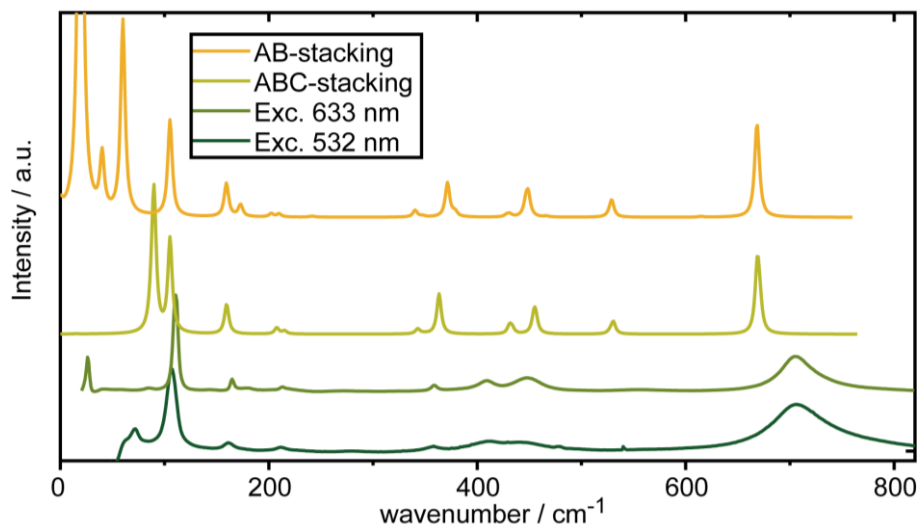


Figure 4.2. Raman spectra of polycrystalline SnTiO_3 at ambient conditions, using two different excitation wavelengths, as well as the calculated spectra for ABC-, ACB-, and AB-type stacking and 532 nm excitation, all normalized to the peak at around 105 cm^{-1} .

The mode around 700 cm^{-1} can be assigned to TiO_6 -octahedral breathing vibrations (Fig. 4.2) as also seen in other titanates, such as MgTiO_3 ¹⁵ or $(\text{Bi,Na})\text{TiO}_3$ ²⁷. Relatively strong broadening further supports the fact that strongly distorted TiO_6 -octahedra and a rather broad distribution of Ti-O bond lengths are present. The mode at around 110 cm^{-1} fits very well to the E_g mode found in pure layered SnO ²⁸. We therefore assume a similar energy for Sn-O-vibrations in SnTiO_3 . This is further supported by DFT-calculations (Fig. S B.2) clearly showing in-plane movement of Sn. Interestingly, also the A_g mode in SnO at 210 cm^{-1} shows that potentially the 217 cm^{-1} mode involves Sn-O-vibrations, however the graphical representation (Fig. S B.2) emphasizes that mostly O ions are moving against the more static Sn ions. We will discuss the role of Sn-O-vibrations in the context of soft modes further down.

4. High-pressure phase transitions of ilmenite-type derived SnTiO₃

Table 4.1. Raman modes of SnTiO₃ at ambient pressure and temperature with corresponding modes from DFT calculations and ilmenite-type CdTiO₃.

# of mode	532 nm	633 nm	DFT (ABC-type)		Int.	DFT (AB-type)		Int.	CdTiO ₃ ²⁹
		60				A _g	60	224	
1	72	84	A _g	90	521				118
2	107	110	E _g	105	251	E _g	105	156	146
		143							
3	162	165	A _g	159	330	A _g	159	220	223
			E _{ug}	171	35	E _g	173	44	
		179	A _{ug}	183	14				
4	212	212	E _g	208	32	E _g	210	17	249
5		272	A _g	363	133	A _g	371	135	343
6	357	359	E _g	342	806	E _g	340	370	332
						E _{ug}	379	47 (IR?)	
7	410	411	A _g	431	234	E _g	449	340	474
8	442	449	E _g	456	333	E _g	466	16	466
9		555	E _g	530	404	E _g	529	440	602
						A _g	614	37	
10	706	707	A _g	668	4885	A _g	668	3905	699

Rationalizing the additional modes is more ambiguous, especially due to the presence of many stacking faults. When assuming ABC-type (ilmenite-type) stacking as the non-faulted archetype, AB-type stacking can be considered as the “fault”. By calculating Raman modes for both stacking types, we therefore identified a mode that might only correspond to occurrence of stacking faults, such as the very low energy mode at 60 cm⁻¹. Potentially, explaining why these can not be observed in other (non-faulted) substances with ilmenite-type structure. DFT calculations for the ABC-type stacking revealed that the lowest energy mode at 89 cm⁻¹ shows the vibration of Ti atoms exactly perpendicular to the layers. Hence changing the stacking sequence from ABA to ABC changes the next neighbor environment for those atoms. The strong dependence of the intensity on the exact excitation energy, stacking type and extension of the respective polytype has been studied in detail for other 2D materials, including for example the layered lone pair material Bi₂Se₃³⁰⁻³¹. Additionally, the strong deviation of the measured mode at 410 cm⁻¹ by 21 cm⁻¹ to the calculated ABC-type and by even 39 cm⁻¹ to the calculated AB-type stacking can be rationalized by a strong

stacking dependency and may thus be unique to ilmenite-type derived heavily stacking faulted structures such as SnTiO₃.

The additional modes with small intensity are observed for the spectra excited with a 633 nm laser. Observation of side phases with small volume fractions and small particle sizes in Raman spectra are unlikely and the modes at 143 cm⁻¹ and 179 cm⁻¹ are neither explained by the ABC- nor the AB-type stacking. One possible explanation of the mode at 143 cm⁻¹ could be presence of TiO₂ nanoparticles, as rutile TiO₂ has its most intense Raman mode at this position. Other known impurities, such as SnO₂, remain invisible in the obtained Raman spectra. Regarding the mode at 179 cm⁻¹, DFT predicted IR-active modes at 171 cm⁻¹ and 183 cm⁻¹ in the ABC-type. The simultaneous occurrence of IR- and Raman-active modes is a sign for non-centrosymmetry at least in local domains. Also in CdTiO₃²⁹ small additional modes appeared upon the phase transition to the ferroelectric modification with off-centered TiO₆-octahedra. The broad distribution of Ti-O bond lengths in SnTiO₃ thus might induce local domains of non-centrosymmetry. The broad distribution of Ti positions is known from other ferroelectric titanates and is usually occurring in order-disorder (eight-site model) dominated ferroelectric phase transitions.

4.4. Raman spectroscopy at high pressure

With increasing pressure the lowest energy mode #1 at 84 cm⁻¹, which is assigned to movement of Ti along the *c*-axis in ABC-type stacking disappears irreversibly (Fig. 4.4a), thus marking the first phase transition at about 0.8 GPa (PT-I). Upon changing the stacking order from ABC-type to AB-type the out-of-plane vibration of Ti will heavily depend on the previous and next layer position of countermoving Ti. Therefore, the A_g out-of-plane Ti vibration in AB-type stacking is predicted from DFT at even lower energies as discussed in the paragraph above. Another phase transition (PT-II) of reversible nature at around 5 GPa is observable with occurrence of an additional Raman mode at around 110 cm⁻¹ with small intensity (Fig. 4.4a). Due to overlap with the high intensity mode #2 at 110 cm⁻¹, it is difficult to define the exact onset. We therefore analyzed the full width at half maxima (FWHM) (Fig. S B.3) of modes clearly only representing one vibration and deduced a phase transition point at between 4 and 5 GPa. Fitting of Grüneisen parameters for each Raman mode further supports the transition point. The Grüneisen parameter reduces for some Raman modes by more than 50% before and after PT-II (Tab. S B.1). The magnitude of the determined Grüneisen parameters for SnTiO₃ is relatively low ($\gamma_{\text{average}} = 0.15$) compared to other ilmenite-type structures, which indicates that most energy is initially consumed for anisotropic compression of the Sn lone pair. This behavior has been observed in layered BiI₃ upon an insulator-to-metal transition³², but in this publication no Grüneisen parameters were determined unfortunately. The interesting implications of PT-II will further be discussed below in the sections about XRPD and visible-light optical absorption spectroscopy.

The third phase transition PT-III is identified at pressures around 19 GPa (Fig. 4.4d). Here most Raman modes show loss of intensity and broadening. As we will discuss further in the section about high-pressure XRPD, PT-III may indicate ordering into corner-shared TiO_6 -octahedra, but clear assignment of Raman modes or a crystal structure remains speculative.

The two modes at 217 cm^{-1} and 351 cm^{-1} observed in Raman spectroscopy (Fig. 4.4 a and b) are softening over a range of at least 5 GPa to 20 GPa (Grüneisen parameters $\gamma_{217} = -0.06$ and $\gamma_{363} = -0.06$ after PT-II respectively). The very small negative Grüneisen parameters of $\gamma_{217} = -0.05$ and $\gamma_{363} = -0.03$ below PT-II indicate also soft mode behavior before the phase transition. Both modes have strong contributions from oxygen movement, while Sn is relatively static (Fig. 4.3a).

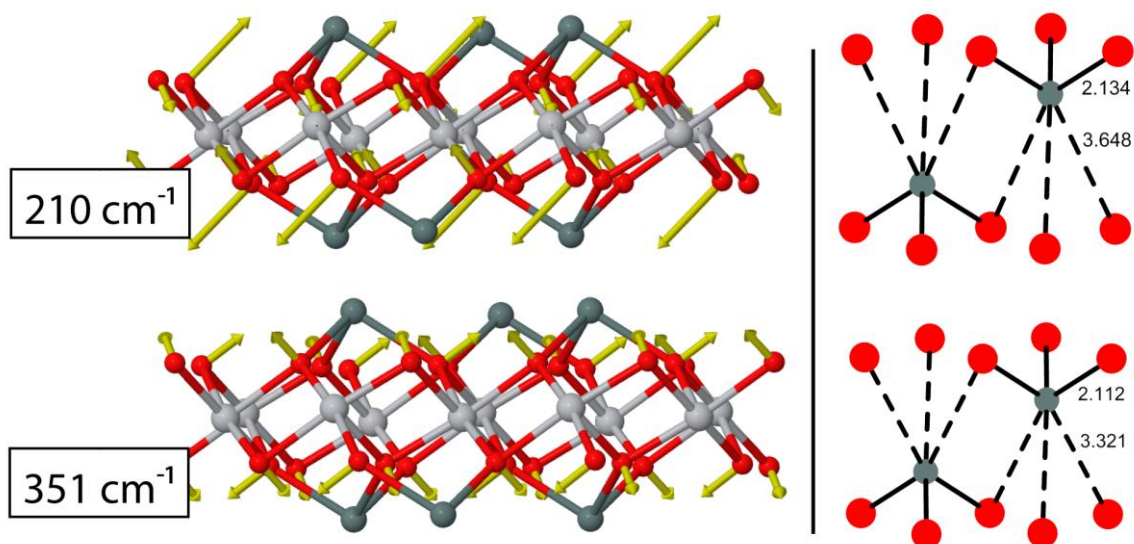


Figure 4.3. a) Two graphical representations (yellow vectors) of the pressure dependent soft modes at the calculated wavenumbers 210 cm^{-1} and 351 cm^{-1} . b) Scheme of Sn-O bond lengths between two layers with increasing pressure calculated by DFT. Light grey represents Ti, dark grey Sn and red O.

With increasing pressures, interactions such as the interlayer Sn-Sn bonds³³ as well as the overlap with next layer O p-orbitals³⁴ are enhanced. As a consequence, the initial bond strength in the three short Sn-O bonds from the same layer will lower and mode softening for both modes is observed. This has also been observed for the ferroelectric phase transition in $(\text{Bi,Na})\text{TiO}_3$ ²⁷ and is further supported by DFT calculations (Fig. 4.3 b), which show a nearly constant Sn-O-distance (2.13 \AA to 2.11 \AA) in the high-pressure structure at $\sim 7 \text{ GPa}$, while the long Sn-O distances drastically reduce from around 3.65 \AA to 3.32 \AA . At the same time the Sn-Sn distance reduces to 3.35 \AA , which has been reported to be below the distance required for a semimetallic behavior in SnO. The comparably high Grüneisen parameter ($\gamma_{110} = 0.6$, $\gamma_{\text{average}} = 0.15$) for the mode at 110 cm^{-1} also indicates a strong pressure dependence for vibrations of the Sn-atoms.

In fact, off-center displacement of the A-site cation (in an ABO_3 -type oxide) has been calculated to be the major reason for ferroelectric phase transitions in contrast to the text book assumption of B-site driven octahedral distortions³⁵. We may therefore speculate that the observed soft modes can be connected to a phase transition into a theoretically predicted non-centrosymmetric PbTiO_3 -type ($P4mm$) space group or more likely into the CaTaO_2N -type ($Pmc2_1$) at 19 GPa (PT-III).

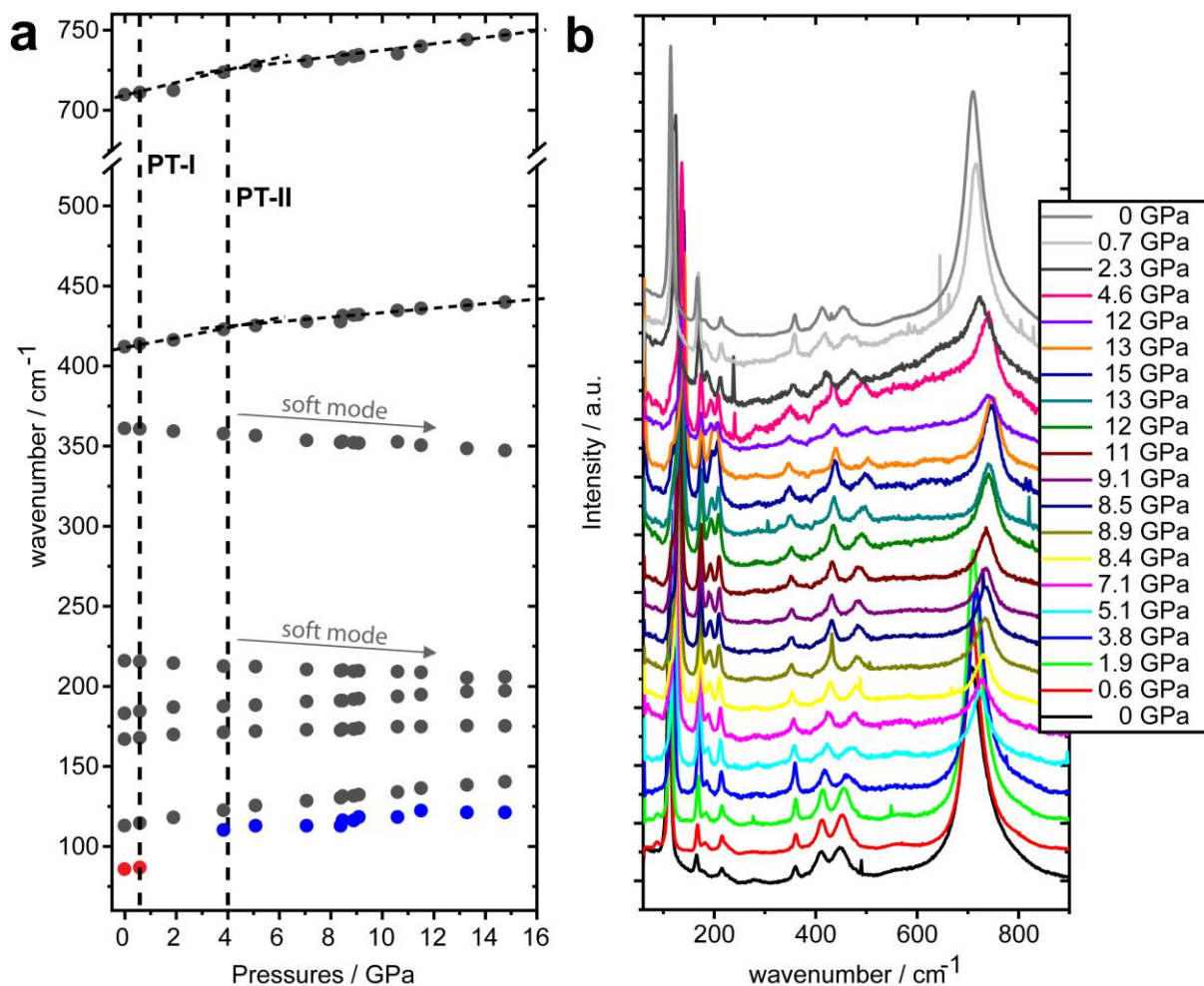


Figure 4.4. a) Raman modes showing the loss of the “stacking mode” at $\sim 80 \text{ cm}^{-1}$ (marked in red) at pressures below 1 GPa (PT-I) and the appearance of an additional mode at around 4-5 GPa (PT-II, marked in blue). Soft mode behavior of the modes at 212 cm^{-1} and at 359 cm^{-1} is seen and two different pressure dependencies above and below 4 GPa are marked by trendlines for the modes at around 400 cm^{-1} and 700 cm^{-1} . b) Corresponding raman spectra from 0 GPa to 15 GPa, including depressurization.

4.5. Crystal structure (powder diffraction) at high pressure

To gain further insight into the high-pressure behavior of SnTiO_3 , in-situ synchrotron XRPD ($\lambda = 0.289880 \text{ \AA}$) was carried out. Several diamond anvil cells (DACs) were loaded with polycrystalline powder and the pressure was slowly increased up to 20 GPa and in one case up to

45 GPa. Fig. 4.5a shows the obtained diffractograms as received. The characteristic triplets of the SnTiO_3 crystal structure are present at ambient conditions. From pressures around 5 GPa, additional reflections of Neon appear due to solidification of the pressure medium. Two apparent changes are marked by boxes in Fig. 4.5a.

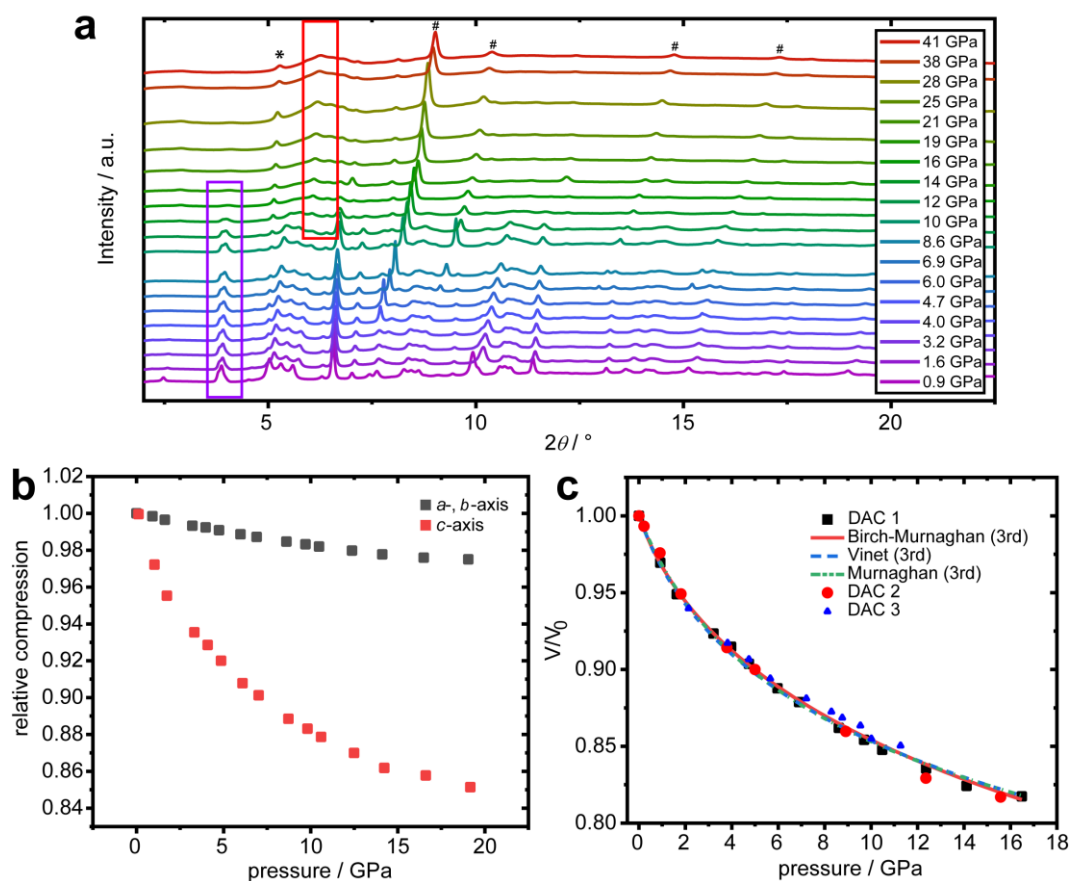


Figure 4.5. a) The in-situ high-pressure synchrotron XRPD patterns with boxes indicating two representative changes with pressure. Purple box indicating the loss of intensity for any reflection correlating with the ilmenite-type derived structure and the red box indicating the intensity increase of the reflection at $6.1^\circ 2\theta$. The SnO_2 side phase is marked with an asterisk *, and the pressure medium Neon with #. The powder could not be measured at ambient pressure, due to the loading procedure in DACs. b) Normalized lattice parameters from Rietveld refinement with increasing pressures up to 20 GPa. c) Volume-Pressure curves with three different datasets and different fits of equations of states (fitted with EoS Fit⁷³⁶⁻³⁷). The fit with Birch Murnaghan (3rd order) obtaining $B_0 = 23$ GPa and $B' = 16$ GPa, fitting with the Vinet (3rd order) model gives $B_0 = 23$ GPa and $B' = 13$ GPa and fitting the Murnaghan (3rd order) model $B_0 = 25$ GPa and $B' = 10$ GPa.

Rietveld fitting of the diffractograms with structural model of SnTiO_3 from Diehl *et al.*¹⁴ allowed extraction of lattice parameters up to pressures of 19 GPa. As expected from the 2D character of SnTiO_3 , the powder is compressed anisotropically. While the a - and b -parameters are lowering by only 2% over a pressure range of 20 GPa, the c -direction with the van der Waals gap compresses by 15% (Fig. 4.5b). This leads to a volume reduction of almost 20%. The Equation of State (EoS)

using the Birch-Murnaghan 3rd order model gives $B_0 = 23$ GPa and $B' = 16$ GPa (Fig. 4.5c), which is an extremely soft bulk modulus for titanates and also compared to SnO with 38 GPa²⁴ and other 2D materials with van der Waals gaps such as 48 GPa for BiOCl³⁸ or 56 GPa in WTe₂³⁹. The theoretically obtained values by DFT calculations of $B_0 = 23$ GPa and $B' = 12$ GPa are in very good agreement with the experimental data.

PT-I is difficult to identify, however the powder shows small intensity differences within the triplets (Fig. 4.6a). As we had discussed in *Chemistry of Materials*¹⁴, the ratio between the outer two reflections and the inner central reflection of a triplet corresponds roughly to the ratio of AB-type stacking and ABC-type stacking. As can be seen from Fig. 4.6a indeed the intensity of the inner reflection is higher relative to the right reflection, which is not overlapped by SnO₂ after application of pressure. Hence, an increasing loss of order with regards to the ilmenite-type derived structure occurs at the first phase transition, either due to amorphization or randomization of stacking. The required pressures of less than 1 GPa can also easily be obtained during grinding of the powder and PT-I therefore heavily depends on sample history.

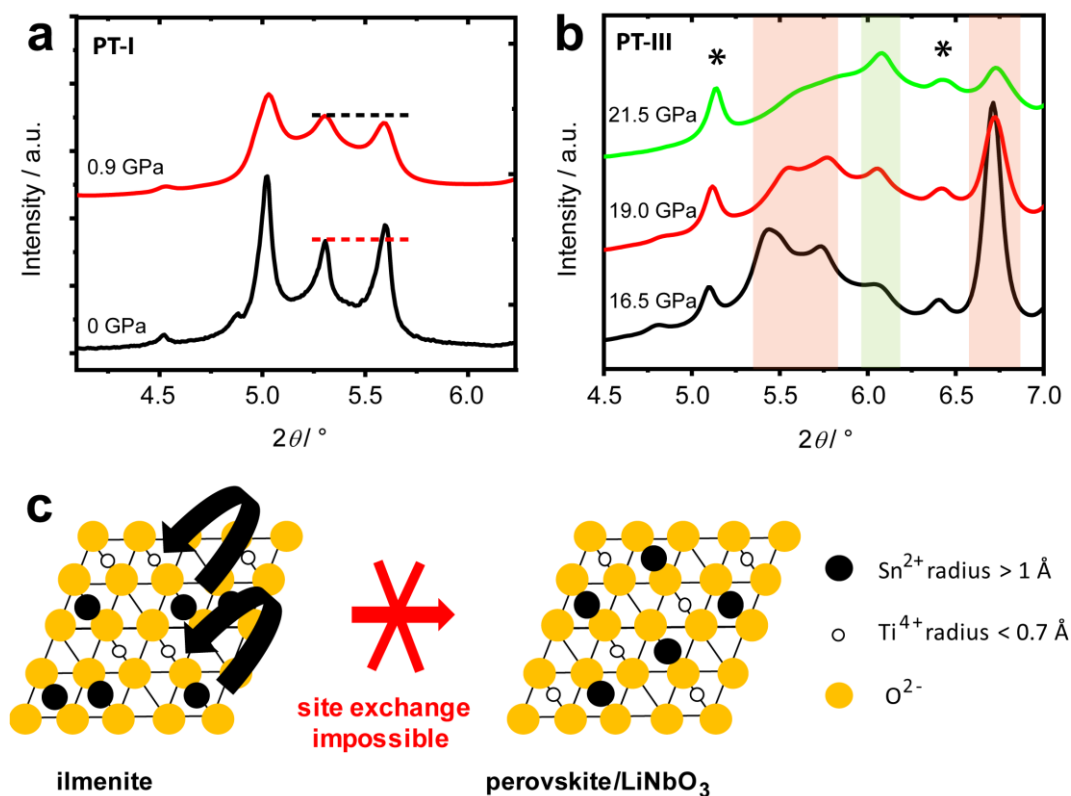


Figure 4.6. a) PT-I: change in intensity between the “outer” reflections and the “inner” reflection of the characteristic triplet of the ilmenite-type derived SnTiO_3 structure at pressures below 1 GPa. b) PT-III: loss of intensity and broadening of reflections at the triplet marked with red box, while the reflection at $6.1^\circ 2\theta$ gains intensity through the phase transition pressure of about 19 GPa marked with green box. The side phase SnO_2 is marked by an asterisk. c) Scheme to show that large A-site cations such as Sn^{2+} cannot easily allow for the phase transition to perovskite- or LiNbO_3 -type structures, due to difficult diffusion.

PT-III is also observable in the powder diffractograms (Fig. 4.5a). At pressures around 18.5 to 19 GPa the characteristic triplet and also the prominent reflections at $4^\circ 2\theta$ (marked in purple box in Fig. 4.5a) and $6.7^\circ 2\theta$ disappear, while a reflection around $6.1^\circ 2\theta$ gains intensity. Most other reflections are either broadened or lose intensity, usually explained by a transition to lower crystalline order, if not amorphization. The sharper reflections especially at $5.1^\circ 2\theta$ and $6.4^\circ 2\theta$ correspond to a small amount of SnO_2 side phase, which is present from the beginning.

The broad “reflection” with increasing intensity at $6.1^\circ 2\theta$ (Fig. 4.6b) indicates lattice planes more or less characteristic of the perovskite-like structures (both $P4mm$ and $Pmc2_1$ have their strongest reflection at this position) as we show by simple comparison to the theoretical powder pattern (Fig. S B.6). However, also the binary SnO is predicted to have the strongest reflection at this position, making an accurate assignment impossible. The formation of SnO should be accompanied with formation of another Ti-containing phase, which we have no indication of. Therefore, we cannot conclude undoubtedly that the predicted high-pressure perovskite-like phases have emerged, but also cannot exclude their formation fully.

Further application of pressure (without heating) never fully crystallized the powder. If a phase transition is kinetically hindered, usually laser heating allows a full conversion into the thermodynamically stable phases. Sn(II)O compounds are known to be prone to disproportionation or decomposition at temperatures above 350 °C. In our laser heating experiments the Raman modes of the decomposition products fit to TiO₂ and SnO₂ (Fig. S B.6). Therefore, conventional high temperature laser heating sources are unsuitable. Upon application of a more gentle laser heating source by using the ruby laser with a wavelength of 457 nm and a power of about 5 min at 1 W, the powder again decomposes into mostly the binary compounds SnO₂ and TiO₂ in their high-pressure modifications (Fig. S B.5). As ZnTiO₃ had shown the phase transition into the perovskite at pressures around 16 GPa, we can thus speculate that Sn²⁺ might simply be “too big” for switching sites with Ti⁴⁺ (Fig. 4.6c) The delicate dependence on pressure and temperature for the formation of either ilmenite-type or perovskite-type CdTiO₃⁴⁰⁻⁴² indicate that large A-site cations with radii of around 1 Å make it difficult to control the structure-type upon formation, although Cd²⁺ might in fact even behave as a smaller cation due to the closed-shell configuration. Unfortunately, the ionic radius of Sn²⁺ with the lone pair is extremely versatile and may lie between 1.03 Å (Cd²⁺) and 1.19 Å (Pb²⁺) in the six-fold coordination⁴³ and thus application of the Goldschmidt tolerance factor is not feasible.

Interestingly, PT-II cannot be identified in the diffractograms. Neither a change in compression behavior nor a symmetry change is observed. Although small changes might be difficult to detect due to the heavily stacking faulted character of SnTiO₃ an isostructural 2nd order phase transition is likely. As mentioned in the section about high-pressure Raman spectroscopy, the reversibility of the phase transition further supports the fact of very subtle changes in the crystal structure, if any at all. Isostructural phase transitions have been observed in other lone pair containing substances and especially materials with strong 2D character (WSe₂, WTe₂)²³. Zhao *et al.*³⁸ discuss isostructural phase transitions in BiOCl, a material similar to SnTiO₃ in that it also contains lone pairs and a prominent van der Waals gap. Taking together the reversibility of the phase transition and the examples known for similar structures, SnTiO₃ would – to our knowledge – be the first example for a ternary tin oxide compound with an isostructural, maybe electronic only, phase transition.

Why an additional hybridization or increased orbital overlap similar to SnO₃³³ across two layers does not change the bulk modulus significantly in SnTiO₃ as for example observed in β -Bi₂O₃⁴⁴ remains an open question. Possibly, the very gradual change is not observable easily in the low quality data sets at hand. Hybridization or bond formation/covalency has been discussed as important factor for induction of ferroelectricity, for example in the more covalent, perovskite-type CdTiO₃ versus its ionic counterpart CaTiO₃⁴⁵. Lone pair activity and hybridization has also been discussed as the reason for second-order phase transitions, for example in Bi₂O₃⁴⁴ and

Sb_2O_3 ⁴⁶ and also titanates such as $(\text{Bi,Na})\text{TiO}_3$ ²⁷, but also binary compounds such as SnO and PbO ⁴⁷. Strain has been calculated theoretically as reason for a semiconductor-to-metal transition in SnO ³³. *Zhou* and *Umezawa* conclude that mostly increased direct lone pair interactions cause the observed change in electric conductivity.

4.6. Optical absorption spectroscopy at high pressure

To better understand the isostructural phase transition PT-II at 5 GPa additional absorption data were obtained. Fitting absorption onset with increasing pressure shows the typical red shift in energy (Fig. 4.7a), changing the color from dark red just below 5 GPa to black above 5 GPa (Fig. 4.7b). When migrating over the point of the phase transition the pressure-dependent shift of the absorption onset reduces from about 25 nm GPa^{-1} to 10 nm GPa^{-1} (Fig. 4.7c).

The band gap is heavily influenced by the electronic structure³³. It is known from other lone pair materials that hybrid anti-bonding orbitals of lone pairs and O p-orbitals dominate the valence band maximum³⁴ and thus it is not surprising that at the point of the presumed second-order transition PT-II a change of absorption behavior is observed. The band gap of 1.4 eV remains too big for a metallic state as observed in SnO or a semimetallic state, as seen in SnSe ⁴⁸ at pressures around 12.6 GPa. Following the argument of increasing lone pair interaction with pressure, we thus assign the additional Raman mode appearing at 5 GPa to an interlayer interaction.

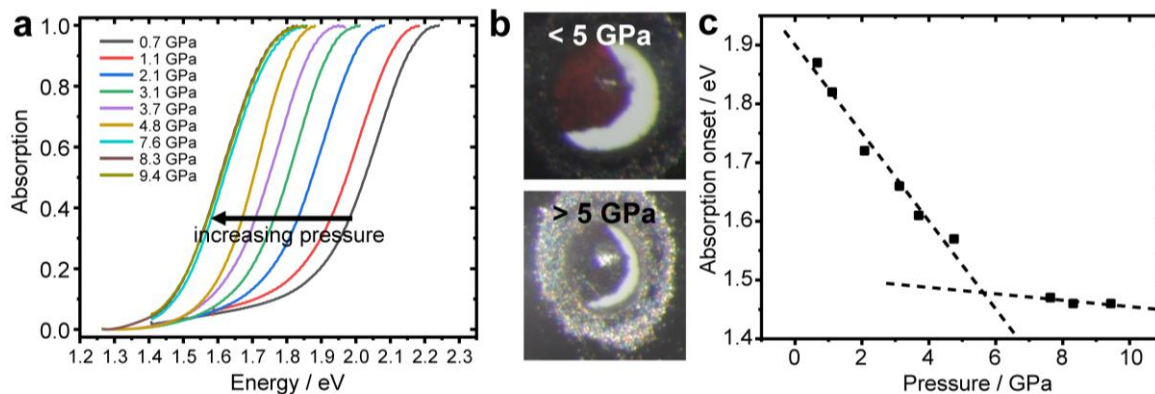


Figure 4.7. a) Absorption spectra with increasing pressure, b) pictures of the powder in the DACs below and above the phase transition. c) Change of absorption onset with increasing pressure and linear fits of regions above and below phase transition pressure PT-II, showing the change of absorption behavior and thus an electronic phase transition.

4.7. Conclusions

Taken the above presented evidence together, we tentatively conclude that SnTiO₃ under high pressure shows three phase transitions up to 45 GPa, which are however difficult to discern and hence, assign. At PT-I the stacking order likely changes from ilmenite-type ABC stacking to a higher degree of random stacking faults or AB-type. At PT-III SnTiO₃ undergoes an irreversible phase transition to low crystalline order, maybe kinetically (and sterically) hindered to fully convert into a perovskite-like structure type. If this hypothesis was valid, very gentle heating above pressures at 20 GPa, might allow the realization of either *P4mm* or *Pmc2₁* perovskite-like SnTiO₃, however the pronounced thermal instability has so far hampered progress in this direction. Finally, PT-II does not entail a structure change and is hence to be second-order, as observed in several other 2D van der Waals type materials. Evaluation of the soft modes and correlation with DFT calculations points to an increased interlayer interaction. Low Grüneisen parameters indicate comparably high tolerance towards pressure due to the very low bulk modulus of 23 GPa, mostly caused by the Sn lone pair “absorbing” the pressure.

4.8. Experimental Procedures

4.8.1. Synthesis

SnTiO₃ was synthesized as reported elsewhere¹⁴ using K₂CO₃ (BerndKraft GmbH > 98%), SnCl₂ · 2 H₂O (Grüssing GmbH 99.5 %) and P25 (TiO₂) (Aldrich ≥ 99.5 %).

4.8.2. High-pressure experiments

High-pressure experiments were performed in Böhler-Almax type diamond anvil cells. The loose or compacted powder samples were loaded into holes with a diameter of 90-130 μm in a tungsten or a rhenium gasket preindented to thicknesses of 35-45 μm. Ne was used as a pressure transmitting medium. Small pieces of ruby were loaded for pressure determination. We used the reference scale by Mao et al.⁴⁹ for the determination of pressures. The synchrotron source provided $\lambda = 0.289880 \text{ \AA}$ and the powder diffractograms were generated by integrating the 2D diffractograms with the software Dioptas_Win64_0.5.0⁵⁰.

4.8.3. Raman spectroscopy

All optical data (Raman, VIS-optical absorption spectroscopy and SHG) were measured with a grating spectrometer (Acton, SP-2356) equipped with a CCD detector (Pixis 256E) and an microscope objective (Mitutoyo). The spectral resolution of our spectrometer is around 3 cm⁻¹. The experimental set-up has been described in detail elsewhere. [Bayaragal *et al.*⁵¹] Raman spectra were collected in backscattering geometry by using the 532.14 nm line of an frequency-doubled Nd:YAG laser with the laser power of between 1-100 mW. The exposure time for Raman

spectra was between 1-200 s. The measured spectra were corrected by subtracting a background spectrum and the Raman peaks were fitted with Lorentzian functions.

4.8.4. Second harmonic generation (SHG)

The powder SHG method developed by Kurtz and Perry⁵² is commonly used to estimate the absence of an inversion center in crystalline structures. Here, powder SHG measurements were performed at ambient conditions in transmission geometry. An Optical Parametric Oscillator (OPO) pumped with a Q-switched Nd:YAG laser system (Continuum, Surelite), operating with a repetition rate of 10 Hz and a pulse width of 6 ns was used for the generation of the fundamental pump wave at 1460 nm light. The generated SHG signal at 730 nm was collected with the spectrometer which is described above. As reference materials Al₂O₃, Quartz, KDP and (KH₂PO₄) were used.

4.8.5. Optical absorption spectroscopy

The visible-light absorption data were collected using the same spectrometer and white light excitation source (Leica, KL1500) with an exposure time of 1 s. Each spectrum was corrected by first dividing the sample spectrum and the background. The curves were smoothed by averaging through 100 datapoints in order to better fit the absorption onset.

4.9. Acknowledgements

We acknowledge DESY (Hamburg, Germany), a member of the Helmholtz Association HGF, for the provision of experimental facilities. Parts of this research were carried out at PETRA III, extreme conditions beamline P02.2 and we thank Wolfgang Morgenroth for his helpful advice at the beamline. We also want to thank Jannes Binck and Dominik Spahr for assisting during the beamtime. Additionally, LD wants to thank Sebastian Wendl, Dr. Sebastian Vogel and Dr. Simon Kloß for experimental advice during the conceptual phase of this project. For assistance and experimental skills in providing the high-temperature Raman spectra we would like to especially acknowledge Armin Schulz, MPI-FKF. The authors (LB, BW) thank the Deutsche Forschungsgemeinschaft – Germany (FOR 2125, BA4020) for financial support.

4.10. References

1. Jaffe, B.; Jr., W. R. C.; Jaffe, H., *Piezoelectric Ceramics*. Academic Press: London and New York, 1971.
2. Cohen, R. E., Origin of ferroelectricity in perovskite oxides. *Nature* **1992**, *358*, 136-138.
3. Bussmann-Holder, A.; Dalal, N., Order/Disorder Versus or with Displacive Dynamics in Ferroelectric Systems. In *Ferro- and Antiferroelectricity: Order/Disorder versus Displacive*, Dalal, N. S.; Bussmann-Holder, A., Eds. Springer Berlin Heidelberg: Berlin, Heidelberg, 2007; pp 1-21.
4. Shrout, T. R.; Zhang, S. J., Lead-free piezoelectric ceramics: Alternatives for PZT? *J. Electroceram.* **2007**, *19* (1), 113-126.
5. Belik, A. A.; Iikubo, S.; Kodama, K.; Igawa, N.; Shamoto, S.-i.; Maie, M.; Nagai, T.; Matsui, Y.; Stefanovich, S. Y.; Lazoryak, B. I.; Takayama-Muromachi, E., BiScO₃: Centrosymmetric BiMnO₃-type Oxide. *J. Am. Chem. Soc.* **2006**, *128* (3), 706-707.
6. Parker, W. D.; Rondinelli, J. M.; Nakhmanson, S. M., First-principles study of misfit strain-stabilized ferroelectric SnTiO₃. *Physical Review B* **2011**, *84* (24), 245126.
7. Matar, S. F.; Baraille, I.; Subramanian, M. A., First principles studies of SnTiO₃ perovskite as potential environmentally benign ferroelectric material. *Chem. Phys.* **2009**, *355* (1), 43-49.
8. Agarwal, R.; Sharma, Y.; Chang, S.; Pitike, K. C.; Sohn, C.; Nakhmanson, S. M.; Takoudis, C. G.; Lee, H. N.; Tonelli, R.; Gardner, J.; Scott, J. F.; Katiyar, R. S.; Hong, S., Room-temperature relaxor ferroelectricity and photovoltaic effects in tin titanate directly deposited on a silicon substrate. *Physical Review B* **2018**, *97* (5), 054109.
9. Pitike, K. C.; Parker, W. D.; Louis, L.; Nakhmanson, S. M., First-principles studies of lone-pair-induced distortions in epitaxial phases of perovskite SnTiO₃ and PbTiO₃. *Physical Review B* **2015**, *91* (3), 035112.
10. Taib, M. F. M.; Yaakob, M. K.; Badrudin, F. W.; Kudin, T. I. T.; Hassan, O. H.; Yahya, M. Z. A., First Principles Calculation of Tetragonal (P4 mm) Pb-free Ferroelectric Oxide of SnTiO₃. *Ferroelectrics* **2014**, *459* (1), 134-142.
11. Taib, M. F. M.; Yaakob, M. K.; Badrudin, F. W.; Rasiman, M. S. A.; Kudin, T. I. T.; Hassan, O. H.; Yahya, M. Z. A., First-Principles Comparative Study of the Electronic and Optical Properties of Tetragonal (P4mm) ATiO₃ (A = Pb,Sn,Ge). *Integrated Ferroelectrics* **2014**, *155* (1), 23-32.
12. Taib, M. F. M.; Yaakob, M. K.; Hassan, O. H.; Yahya, M. Z. A., Structural, Electronic, and Lattice Dynamics of PbTiO₃, SnTiO₃, and SnZrO₃: A Comparative First-Principles Study. *Integrated Ferroelectrics* **2013**, *142* (1), 119-127.
13. Gardner, J.; Thakre, A.; Kumar, A.; Scott, J., Tin Titanate: the hunt for a new ferroelectric perovskite. *arXiv preprint arXiv:1906.03229* **2019**.
14. Diehl, L.; Bette, S.; Pielnhofer, F.; Betzler, S.; Moudrakovski, I.; Ozin, G. A.; Dinnebier, R.; Lotsch, B. V., Structure-Directing Lone Pairs: Synthesis and Structural Characterization of SnTiO₃. *Chem. Mater.* **2018**, *30* (24), 8932-8938.
15. Linton Jennifer, A.; Fei, Y.; Navrotsky, A., The MgTiO₃-FeTiO₃ join at high pressure and temperature. In *American Mineralogist*, 1999; Vol. 84, p 1595.
16. Liu, L.-G., Post-ilmenite phases of silicates and germanates. *Earth. Planet. Sci. Lett.* **1977**, *35* (1), 161-168.
17. Bernert, T.; Ruiz-Fuertes, J.; Bayarjargal, L.; Winkler, B., Synthesis and high (pressure, temperature) stability of ZnTiO₃ polymorphs studied by Raman spectroscopy. *Solid State Sciences* **2015**, *43*, 53-58.
18. Ruiz-Fuertes, J.; Winkler, B.; Bernert, T.; Bayarjargal, L.; Morgenroth, W.; Koch-Müller, M.; Refson, K.; Milman, V.; Tamura, N., Ferroelectric soft mode of polar ZnTiO₃ investigated by Raman spectroscopy at high pressure. *Physical Review B* **2015**, *91* (21), 214110.
19. Inaguma, Y.; Aimi, A.; Shirako, Y.; Sakurai, D.; Mori, D.; Kojitani, H.; Akaogi, M.; Nakayama, M., High-Pressure Synthesis, Crystal Structure, and Phase Stability Relations of a LiNbO₃-Type Polar Titanate ZnTiO₃ and Its Reinforced Polarity by the Second-Order Jahn-Teller Effect. *J. Am. Chem. Soc.* **2014**, *136* (7), 2748-2756.
20. Navrotsky, A., Energetics and Crystal Chemical Systematics among Ilmenite, Lithium Niobate, and Perovskite Structures. *Chem. Mater.* **1998**, *10* (10), 2787-2793.

21. Nayak, A. P.; Bhattacharyya, S.; Zhu, J.; Liu, J.; Wu, X.; Pandey, T.; Jin, C.; Singh, A. K.; Akinwande, D.; Lin, J.-F., Pressure-induced semiconducting to metallic transition in multilayered molybdenum disulphide. *Nature Communications* **2014**, *5*, 3731.
22. Zhao, Z.; Zhang, H.; Yuan, H.; Wang, S.; Lin, Y.; Zeng, Q.; Xu, G.; Liu, Z.; Solanki, G. K.; Patel, K. D.; Cui, Y.; Hwang, H. Y.; Mao, W. L., Pressure induced metallization with absence of structural transition in layered molybdenum diselenide. *Nature Communications* **2015**, *6*, 7312.
23. Wang, X.; Chen, X.; Zhou, Y.; Park, C.; An, C.; Zhou, Y.; Zhang, R.; Gu, C.; Yang, W.; Yang, Z., Pressure-induced iso-structural phase transition and metallization in WSe₂. *Scientific Reports* **2017**, *7*, 46694.
24. Wang, X.; Zhang, F. X.; Loa, I.; Syassen, K.; Hanfland, M.; Mathis, Y.-L., Structural properties, infrared reflectivity, and Raman modes of SnO at high pressure. *physica status solidi (b)* **2004**, *241* (14), 3168-3178.
25. Nalbandyan, V. B.; Avdeev, M.; Pospelov, A. A., Ion exchange reactions of NaSbO₃ and morphotropic series MSbO₃. *Solid State Sciences* **2006**, *8* (12), 1430-1437.
26. Rousseau, D. L.; Bauman, R. P.; Porto, S., Normal mode determination in crystals. *Journal of Raman Spectroscopy* **1981**, *10* (1), 253-290.
27. Schütz, D.; Deluca, M.; Krauss, W.; Feteira, A.; Jackson, T.; Reichmann, K., Lone-Pair-Induced Covalency as the Cause of Temperature- and Field-Induced Instabilities in Bismuth Sodium Titanate. *Adv. Funct. Mater.* **2012**, *22* (11), 2285-2294.
28. Saji, K. J.; Tian, K.; Snure, M.; Tiwari, A., 2D Tin Monoxide—An Unexplored p-Type van der Waals Semiconductor: Material Characteristics and Field Effect Transistors. *Advanced Electronic Materials* **2016**, *2* (4), 1500453.
29. Rodrigues, J. E.; Ferrer, M. M.; Cunha, T. R.; Costa, R. C.; Sambrano, J. R.; Rodrigues, A. D.; Pizani, P. S., First-principles calculations and Raman scattering evidence for local symmetry lowering in rhombohedral ilmenite: temperature- and pressure-dependent studies. *J. Phys.: Condens. Matter* **2018**, *30* (48), 485401.
30. Liang, L.; Puzdov, A. A.; Sumpter, B. G.; Meunier, V., Interlayer bond polarizability model for stacking-dependent low-frequency Raman scattering in layered materials. *Nanoscale* **2017**, *9* (40), 15340-15355.
31. Luo, X.; Lu, X.; Cong, C.; Yu, T.; Xiong, Q.; Ying Quek, S., Stacking sequence determines Raman intensities of observed interlayer shear modes in 2D layered materials – A general bond polarizability model. *Scientific Reports* **2015**, *5*, 14565.
32. Devidas, T. R.; Chandra Shekar, N. V.; Sundar, C. S.; Chithaiah, P.; Sorb, Y. A.; Bhadram, V. S.; Chandrabhas, N.; Pal, K.; Waghmare, U. V.; Rao, C. N. R., Pressure-induced structural changes and insulator-metal transition in layered bismuth triiodide, BiI₃: a combined experimental and theoretical study. *J. Phys.: Condens. Matter* **2014**, *26* (27), 275502.
33. Zhou, W.; Umezawa, N., Band gap engineering of bulk and nanosheet SnO: an insight into the interlayer Sn-Sn lone pair interactions. *PCCP* **2015**, *17* (27), 17816-17820.
34. Walsh, A.; Payne, D. J.; Egdell, R. G.; Watson, G. W., Stereochemistry of post-transition metal oxides: revision of the classical lone pair model. *Chem. Soc. Rev.* **2011**, *40* (9), 4455-4463.
35. Benedek, N. A.; Fennie, C. J., Why Are There So Few Perovskite Ferroelectrics? *The Journal of Physical Chemistry C* **2013**, *117* (26), 13339-13349.
36. Angel Ross, J.; Alvaro, M.; Gonzalez-Platas, J., EosFit7c and a Fortran module (library) for equation of state calculations. In *Zeitschrift für Kristallographie - Crystalline Materials*, 2014; Vol. 229, p 405.
37. Gonzalez-Platas, J.; Alvaro, M.; Nestola, F.; Angel, R., EosFit7-GUI: a new graphical user interface for equation of state calculations, analyses and teaching. *J. Appl. Crystallogr.* **2016**, *49* (4), 1377-1382.
38. Zhao, J.; Xu, L.; Liu, Y.; Yu, Z.; Li, C.; Wang, Y.; Liu, Z., Isostructural Phase Transition in Bismuth Oxide Chloride Induced by Redistribution of Charge under High Pressure. *The Journal of Physical Chemistry C* **2015**, *119* (49), 27657-27665.
39. Zhou, Y.; Chen, X.; Li, N.; Zhang, R.; Wang, X.; An, C.; Zhou, Y.; Pan, X.; Song, F.; Wang, B.; Yang, W.; Yang, Z.; Zhang, Y., Pressure-induced Td to 1T' structural phase transition in WTe₂. *AIP Advances* **2016**, *6* (7), 075008.

40. Liebertz, J.; Rooymans, C. J. M., Die Ilmenit/Perowskit-Phasenumwandlung von CdTiO₃ unter hohem Druck. In *Zeitschrift für Physikalische Chemie*, 1965; Vol. 44, p 242.
41. Neil, J.; Navrotsky, A.; Kleppa, O., Enthalpy of ilmenite-perovskite transformation in cadmium titanate. *Inorg. Chem.* **1971**, *10* (9), 2076-2077.
42. Liebermann, R. C., Elasticity of the ilmenite - perovskite phase transformation in CdTiO₃. *Earth. Planet. Sci. Lett.* **1976**, *29* (2), 326-332.
43. Shannon, R., Revised effective ionic radii and systematic studies of interatomic distances in halides and chalcogenides. *Acta Crystallographica Section A* **1976**, *32* (5), 751-767.
44. Pereira, A. L. J.; Sans, J. A.; Vilaplana, R.; Gomis, O.; Manjón, F. J.; Rodríguez-Hernández, P.; Muñoz, A.; Popescu, C.; Beltrán, A., Isostructural Second-Order Phase Transition of β-Bi₂O₃ at High Pressures: An Experimental and Theoretical Study. *The Journal of Physical Chemistry C* **2014**, *118* (40), 23189-23201.
45. Hiroki, T.; Hiroki, M.; Toshirou, Y.; Mitsuru, I., Raman Scattering Study on the Phase Transition Dynamics of Ferroelectric Oxides. **2012**.
46. Pereira, A. L. J.; Gracia, L.; Santamaría-Pérez, D.; Vilaplana, R.; Manjón, F. J.; Errandonea, D.; Nalin, M.; Beltrán, A., Structural and vibrational study of cubic Sb₂O₃ under high pressure. *Physical Review B* **2012**, *85* (17), 174108.
47. Giefers, H.; Porsch, F., Shear induced phase transition in PbO under high pressure. *Physica B: Condensed Matter* **2007**, *400* (1), 53-58.
48. Yan, J.; Ke, F.; Liu, C.; Wang, L.; Wang, Q.; Zhang, J.; Li, G.; Han, Y.; Ma, Y.; Gao, C., Pressure-driven semiconducting-semimetallic transition in SnSe. *PCCP* **2016**, *18* (6), 5012-5018.
49. Mao, H. K.; Xu, J.; Bell, P. M., Calibration of the ruby pressure gauge to 800 kbar under quasi-hydrostatic conditions. *Journal of Geophysical Research: Solid Earth* **1986**, *91* (B5), 4673-4676.
50. Prescher, C.; Prakapenka, V. B., DIOPTAS: a program for reduction of two-dimensional X-ray diffraction data and data exploration. *High Pressure Research* **2015**, *35* (3), 223-230.
51. Bayarjargal, L.; Fruhner, C. J.; Schrodtr, N.; Winkler, B., CaCO₃ phase diagram studied with Raman spectroscopy at pressures up to 50 GPa and high temperatures and DFT modeling. *Physics of the Earth and Planetary Interiors* **2018**, *281*, 31-45.
52. Kurtz, S. K.; Perry, T. T., A Powder Technique for the Evaluation of Nonlinear Optical Materials. *J. Appl. Phys.* **1968**, *39* (8), 3798-3813.

5. Competing factors in the directed design of photocatalysts: The case of SnTiO₃

Leo Diehl, Douglas Fabini, Theresa Block, Nella Vargas-Barbosa, Alberto Jiménez-Solano,
Florian Pielnhofer, Tanmay Banerjee, Viola Duppel, Kathrin Küster, Rainer Pöttgen
and Bettina V. Lotsch

To be submitted.

Abstract

Directed design of new photocatalysts remains a challenging task in materials chemistry. Here, we present a new photocatalyst with H₂ evolution activity, in which the lone pair induces low hole effective masses and visible-light activity. Yet, the presence of surface Sn⁴⁺ species, as found by multiple experimental methods, explain the comparatively low catalytic performance. We explain the intrinsic presence of surface Sn⁴⁺ by the extremely low ionization potential of SnTiO₃. The anti-bonding character below the Fermi level make partial oxidation/hole doping of SnTiO₃ favorable. Furthermore, direct interlayer Sn-Sn interactions as identified by DFT and NMR underline the 3D character of seemingly 2D SnTiO₃. We show that for the design of new photocatalysts, the competition between favorable properties, such as low effective masses, and unfavorable properties, such as instability towards oxidation, have to be balanced.

5.1. Introduction

The directed design of photocatalytically active semiconductors remains a desirable but challenging goal in materials chemistry¹. Many different tuning parameters have been explored, upon which nanostructuring, co-catalyst and crystal facet engineering are only few examples, well summarized in the comprehensive review by Li *et al.*². Band structure tuning is one of the most intuitive and widespread approaches toward improved photocatalytic water splitting and very well suited for a detailed understanding of structure-property-relationships. Especially doping on cationic positions has been applied successfully and is generally referred to as “conduction band tuning”, valence band tuning on the other hand has been used in significantly fewer cases^{3, 4}, especially due to the small variety of potential anions³ and also often due to the relative instability against their respective oxides.

One alternative approach for valence band tuning is the use of so-called “lone pair” cations⁵, which are characterized by an occupied *s*-orbital on the outer shell⁶. Examples with main group elements are the well-studied BiVO₄⁷, many tungstates, niobates and tantalates such as Bi₂WO₆⁸, PbWO₄⁹, SnNb₂O₆¹⁰, SnTa₂O₆¹¹ and titanates Sn₂TiO₄¹². Most of these materials have visible-light band gaps for water splitting, therefore using sun light efficiently. This can be rationalized by an elevation of the valence band maximum (VBM) due to the lone pairs^{5, 6, 13}. Next to the

advantageous influence on the band gap, many lone pair materials form (pseudo-)2D crystal structures. Here, charge carriers may separate more easily due to charge separation over an “internal heterojunction”^{8, 14}, if the dissimilar regions are large enough to avoid any significant spatial overlap of hole and electron localization. Wahila *et al.*¹⁵ have shown that the lone pairs can also aid minority carrier transport of holes through the semiconductors. Hole transport limits in many cases the oxidation half-reaction. Hautier *et al.*^{16, 17} showed that Sn²⁺ lone pair materials can have extremely low hole effective masses. Yet, even the fully exfoliated Bi₂WO₆⁸ with high surface area evolved H₂ with rates as low as 1.6 μmolg⁻¹h⁻¹. The intrinsic reason for this surprisingly bad performance of many lone pair based photocatalysts has been elusive.

Here, we present SnTiO₃¹⁸ as a nanostructured, visible-light active photocatalyst with close-to-ideal band gap and very low hole effective mass, which is able to evolve hydrogen under visible-light excitation. We first show that SnTiO₃ intrinsically oxidizes due to an extremely small ionization potential, forming Sn⁴⁺ species on the surface. These hinder efficient charge transfer to the electrolyte due to non-ideal band alignment. We can correlate the low ionization potential with the small electrostatic stabilization by direct comparison with other Sn (II and IV) oxides. We identify direct Sn-Sn interactions by both theory and experiment making the seemingly 2D SnTiO₃ a lone pair material with 3D character. Furthermore, we computationally find anti-bonding states below the Fermi level, making partial bulk oxidation energetically favorable as seen by Mössbauer spectroscopy, possibly enabling radiation-less recombination pathways. Therefore, advantageous properties have to be balanced with the respective disadvantages for every lone pair photocatalyst.

5.2. Results and Discussion

5.2.1. Crystal structure and electronic structure of SnTiO₃ (space group $R\bar{3}$)

The crystal structure of SnTiO₃ was described elsewhere in detail¹⁸. Similar to the ilmenite-archetype, honeycombs of TiO₆-octahedra decorated with Sn²⁺ ions form layers that are stacked with different stacking orders. In contrast to actual ilmenite-type structures, the *c*-axis is strongly elongated due to the stereochemical activity of the lone pairs. The pseudo-2D character of the crystal structure is reflected in the morphology of the crystallites (hexagonal plates).

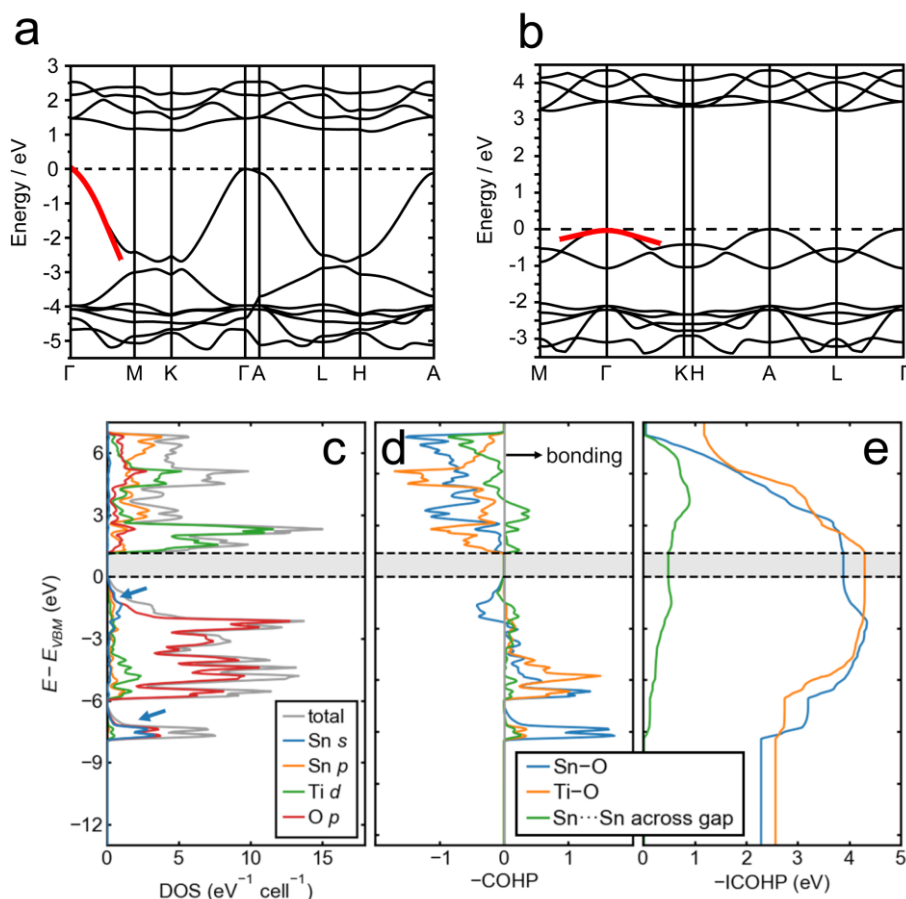


Figure 5.1. a) DFT band structure of bulk SnTiO₃ with $m_h = 0.12 m_e$ as determined by fitting a parabola to the VBM at Γ and b) single layer slab SnTiO₃, indicating significantly increased hole effective masses $m_h = 0.63 m_e$ and, hence, dependence of hole conduction pathways on Sn-Sn interactions. c) Density of states (DOS) for the relevant region around E_F including the individual elemental contributions in partial DOS. d) COHP and e) iCOHP of SnTiO₃ indicating the anti-bonding character of Sn-O interactions at the VBM as well as significant bonding interactions of Sn-Sn.

Polycrystalline powders of SnTiO₃ are of bright orange to red color (Fig. S C.1 b). Kubelka-Munk analysis gives a band gap of 1.82 eV, when assuming an indirect band gap as calculated by DFT. This is considered to be close-to-ideal for very high quantum efficiency water splitting devices²; at the same time, it is slightly too small for potential applications as a *p*-type transparent conducting oxide. The band gaps determined by DFT calculations (HSE-D3) are 1.1 eV for an indirect transition and 1.47 eV for direct transitions, see Figure 5.1 a. The conduction band is mainly comprised by Ti 3*d*-orbitals, while the valence band is of strong Sn 5*s*-character, which has been observed in multiple other lone pair materials. More precisely, it is the anti-bonding Sn 5*s*-O 2*p*-Sn 5*p* orbitals dominating the VBM (Fig. 5.1c), fitting well to the revised lone pair model as proposed by Walsh *et al*¹⁹. The implications of this anti-bonding character are discussed further down in the sections about Mössbauer spectroscopy and photoluminescence.

The band structure of SnTiO₃ shows very high dispersion at the VBM in the Γ -M, Γ -K and A-L, A-H directions (Fig. 5.1a). Hence, SnTiO₃ has comparatively light hole effective masses into the in-plane crystallographic direction (compare visualization of Brillouin zone in Fig. S C.3). Estimation via fitting with a parabola at the Γ -point gives values as low as 0.12 m_e for bulk SnTiO₃, which is in the range of electron masses for traditional *n*-type transparent conducting oxides (TCOs)²⁰ and much lower than 1.5 m_e generally considered to be the higher limit for *p*-type TCOs. To our knowledge, this is among the lowest hole effective masses predicted for Sn(II) oxides^{16, 17}. Calculating the band structures of slabs reduced in thickness along the *c*-direction can give valuable insights into how electronically separated the individual layers are. The three- and two-layer slabs closely resemble the bulk band structure of SnTiO₃ with slightly increased band gaps and an almost identical hole effective mass of about 0.16 m_e . Only for the single layer slab the band structure changes drastically, giving an almost quadrupled hole effective mass of 0.63 m_e . It can hence be concluded that two adjacent layers are required to provide a hole conduction pathway. As already discussed by Zhou and Umezawa for *p*-type SnO²¹, direct Sn-Sn interactions are needed for (in-plane) hole conduction. While Zhou and Umezawa find dominating anti-bonding interactions when calculating the overlap of atomic orbitals, not including the hybridizations that form the lone pair, we can indeed confirm lone pair bonding interactions in SnO (Fig. S C.4). Direct Sn-Sn interlayer interactions can also be observed in SnTiO₃ when having a look at the integrated COHP (iCOHP) (Fig. 5.1e, green line). The energies are significant at the Fermi level and in a comparable range to SnO interlayer interactions.

Taking together the ideally suited band gap and the very low hole effective masses, SnTiO₃ seems to have potential for high photocatalytic activity.

5.2.2. Photocatalytic activity

Indeed, the Pt-modified SnTiO₃ shows visible-light activity for H₂ evolution from 10 vol% methanol solution. Hydrogen gas was steadily generated over at least 20 hours ($\sim 4 \mu\text{mol g}^{-1}\text{h}^{-1}$) after a short activation period (max. 3 h) due to the photodeposition of the Pt-cocatalyst^{22, 23} and with repeated exchange of the headspace (Figure 5.2a). As expected from the determined band gap, SnTiO₃ evolves H₂ with photon energies down to ~ 2 eV (see Fig. 5.2b). Yet, the absolute amounts evolved are far from any commercially viable or benchmark material, even when considering visible-light active catalysts only²⁴.

Moreover, O₂ evolution was observable under full spectrum Xenon light, use of Na₂S₂O₈ sacrificial agent and use of an *in-situ* deposited CoO_x co-catalyst. In contrast to H₂ evolution, however, it was not possible to show visible-light activity. It remains to be shown if this O₂ evolves directly through H₂O oxidation, or if the used sacrificial agent Na₂S₂O₈ supports if not induces the observed small amounts of O₂ via a light-induced radical reaction²⁵. The choice of

relatively basic conditions (0.1 M KOH) made the use of the alternative sacrificial agent AgNO₃ impossible, as silver oxide precipitates under these conditions. SnTiO₃ is at least partially involved during the catalytic process, as evolution of O₂ was observed only from samples well dispersed in the reactor and adding the hole quenching methanol did stop the evolution of O₂. Also, it is conceivable that only holes from oxygen states near the (oxidized) surface (e.g. from SnO₂) are suited for an efficient oxidation reaction due to a larger driving force for hole transfer. The role of transition probabilities and charge transfer will be discussed in the context of photoluminescence further down. Final proof for the mechanism involved can only be given by properly labelling the involved precursors with ¹⁸O isotopes.

Characterization before and after catalysis demonstrates that the catalyst remained unchanged regarding crystal structure (XRPD) and surface (XPS) under the chosen photocatalytic conditions (see Fig. S C.7). Further down we will see, however, that the catalyst as used in the reactor cannot be regarded as pure bulk SnTiO₃. Interestingly, a preference for Pt deposition could be assigned to the {001} crystallographic facet from the backscattering electron images in Figure 5.2c and d. This has been observed in other materials with 2D character²⁶ and is typical for the anisotropic charge transport behavior^{27, 28}. The 2D character might also imply the assignment of a heterojunction-like behavior, which corresponds to the observation of the VBM being dominated by Sn-O and the CBM, being mostly of Ti character (Fig. S C.1). Despite this assumption of different localization of photo-excited electrons and holes the description of SnTiO₃ as an “internal heterojunction” is ambiguous. The separation over less than a nanometer is expected to be within the exciton radius.

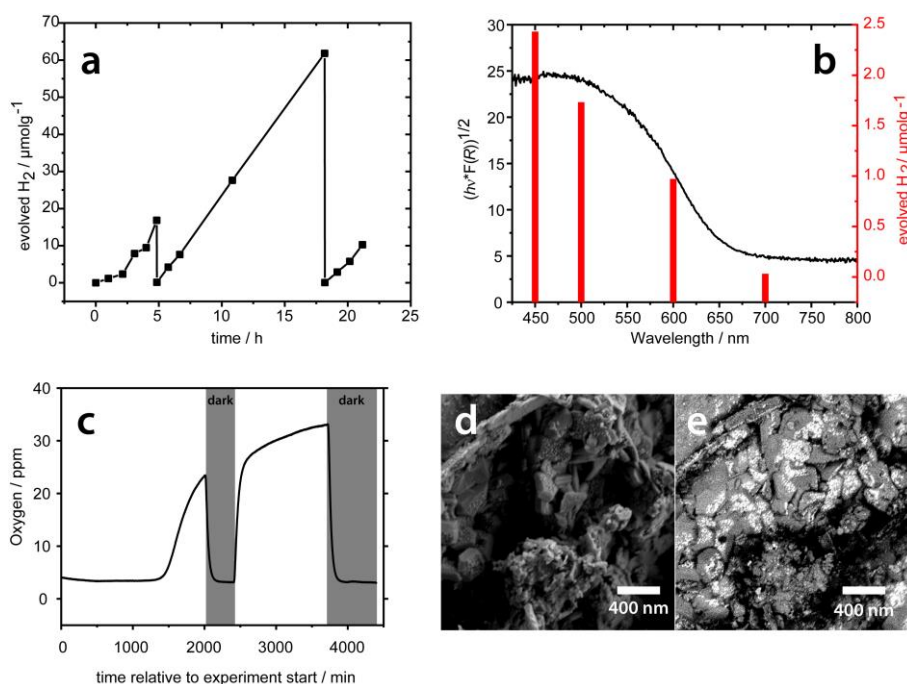


Figure 5.2. a) H₂ evolution from aqueous methanol solution and Pt co-catalyst, b) wavelength dependent H₂ evolution c) O₂ evolution from solution with Na₂S₂O₈ sacrificial agent d) SE-SEM image of catalyst after catalysis, e) BSE-SEM image of catalyst after H₂ evolution showing Pt particles on {001} facets.

In the following paragraphs we present a rationale for the relatively low gas evolution rates compared to other catalysts², and deduce a potential explanation for why lone pair containing photocatalysts have not brought about the breakthrough for water splitting as lone pair compounds (hybrid-perovskites)^{29,30} have for photovoltaic applications.

5.2.3. Band alignment

One potential explanation for relatively low H₂ evolution rates found in SnTiO₃ may be unsuitable band alignment (intrinsically or due to surface oxidation processes). Therefore, we used two methods to determine the actual valence and conduction band positions with respect to the electrochemical potential scale. By analyzing the frequency – and potential – dependent capacitance of the semiconductor-electrolyte junction, it is possible to obtain the flat band potential (E_{fb}) of the conduction band of SnTiO₃ films (Mott-Schottky analysis). It is important to mention that the E_{fb} does not correspond to the surface conduction band minimum potential as it is dependent on the intrinsic Fermi level position of the semiconductor. Matsumoto has shown that depending on the space charge layer thickness, the actual band position may be shifted by up to 400 mV, if the semiconductor shows a resistance of more than $> 10^4 \text{ Ohm}\cdot\text{cm}$ ³¹. The resistance is directly related to the Fermi level position and thus the degree of doping.

For films of SnTiO₃ drop-casted on FTO and sintered at 250 °C, an E_{fb} of + 0.21 V vs. RHE was obtained. This is corresponding to – 4.75 eV vs vacuum and thus lies below (positive of on the electrochemical scale) the required potential for H₂ evolution at – 4.44 eV. The substrate FTO

alone showed a significantly shifted position of + 0.13 V vs. RHE and can thus be easily distinguished from SnTiO₃. Even when assuming an average correction of 200 mV based on the propositions of Matsumoto, the CBM of the film is positioned just below of the thermodynamically required potential for H₂ evolution, such that the driving force for the HER is expected to be very low at best.

This finding is seemingly in contrast to our slab calculations within GGA-DFT. These calculations indicate the VBM of SnTiO₃ is quite shallow with respect to vacuum (ionization potential, IP = 4.44 eV) and hence the corresponding CBM. Ionization potentials were additionally computed for litharge SnO, foolite SnNb₂O₆, and rutile SnO₂, and the resulting band alignments (taking electron affinity, EA = IP - E_g , using the experimental bandgaps) are shown Figure 5.3b, together with previously reported values where available³²⁻³⁴. Consistent with expectation, the ionization potentials of the Sn(II) oxides are substantially less than for Sn(IV)O₂, in the order SnO < SnTiO₃ < SnNb₂O₆ < SnO₂. The large difference between the two layered ternary compounds SnTiO₃ and SnNb₂O₆ can be rationalized by the different electrostatic contributions. When correlating the “energy density” (electrostatic energy per volume) with the average oxidation state in the calculated compounds, a linear relationship is found. SnTiO₃ has an average cation oxidation state of 3+ ((Sn²⁺+Ti⁴⁺)/2), while SnNb₂O₆ is at 4+, causing a higher stabilization of the overall structure.

Hence, the surface measured in Mott-Schottky did not resemble the bulk properties of SnTiO₃ but rather an oxidized surface instead. Surface layers influence the position and conduction type (*n* vs. *p*) of the E_{fb} ³⁵. The same trend can be observed from comparison of rutile TiO₂ with a negative potential of - 0.05 V (and anatase TiO₂ even - 0.28 V) vs NHE at pH = 2³⁶ and rutile-type SnO₂ is positive at + 0.4 V vs NHE at pH = 1³⁷. In case of SnNb₂O₆, Hosogi *et al.*³⁸ postulated that Sn⁴⁺ states are introduced as in-gap states below the CBM. Hence, the observed band positions of SnTiO₃ are only barely suited for H₂ evolution, if at all, and in case there are significant amounts of Sn⁴⁺ species present, for example as a surface-layer of SnO₂, the surface might resemble a core-shell structure, in which electrons cannot effectively be transferred to the electrolyte due to an effective “SnO₂” barrier.³⁹⁻⁴¹

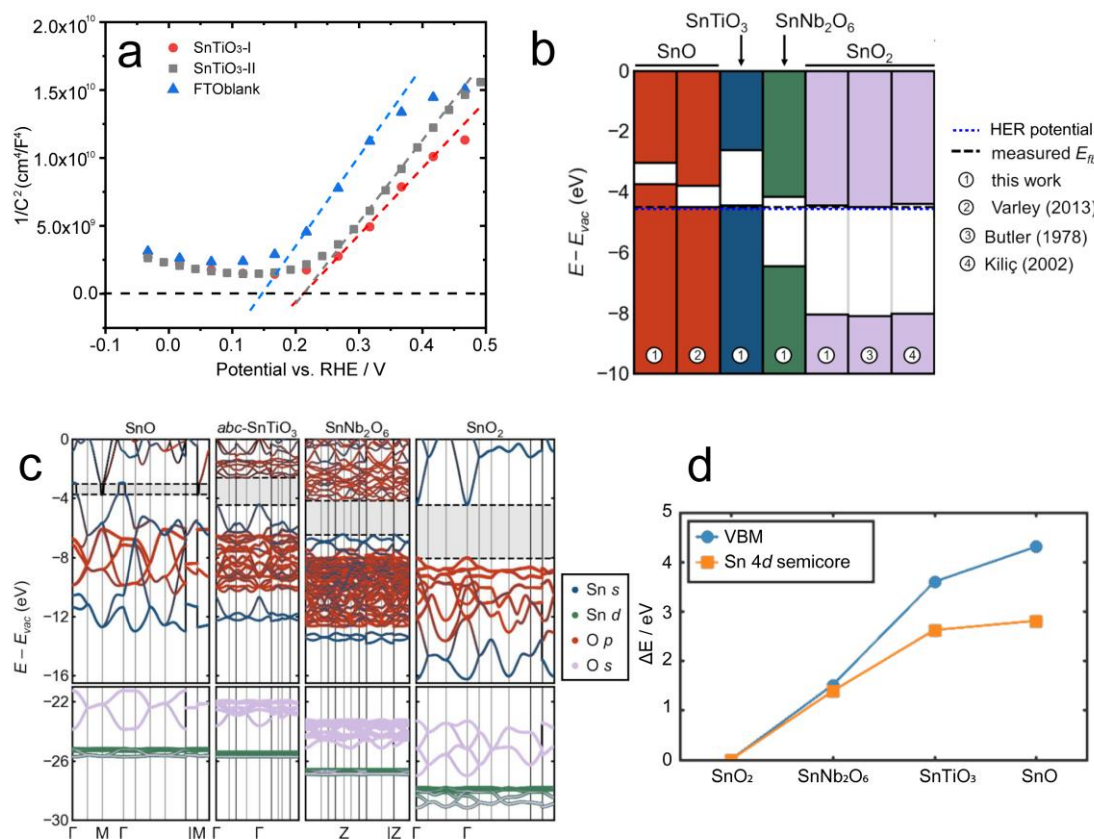


Figure 5.3. a) Mott-Schottky measurement of two different “SnTiO₃” films on FTO sintered at 250 °C under vacuum. b) Calculated band alignments³⁹ for several Sn(II) oxides and Sn(IV)O₂ with previously reported values for comparison (SnO: Varley 2013³² ; SnO₂: Butler 1978³³ and Kiliç 2002³⁴). Where only ionization potentials are reported, the electron affinity is computed from the experimentally reported bandgap, and vice versa. The flat band potential, E_b , measured for “SnTiO₃” from Mott–Schottky analysis is indicated by the black dashed line, and is seen to align well with the CBM of SnO₂. See the main text for a discussion of methodological differences and error analysis. c) Band structures (DFT-PBE) including core level states for SnO, SnTiO₃, SnNb₂O₆ and SnO₂, showing that the trend of ionization energies is routed in a holistic influence (the electrostatic potential) on the electronic structure. d) correlation of the Sn 4*d* semicore level position (indicative of electrostatic contributions) and VBM position. The difference of VBM and semicore level can be read as the valence band width. The band positions are normalized relative to the respective values for SnO₂ (ΔE).

The measured flat band potential of SnTiO₃ samples from Mott–Schottky analysis is seen to be consistent with the CBM of SnO₂, and incompatible with the CBM of SnTiO₃, even allowing for several hundred meV of error. This lends further support to the hypothesis that SnTiO₃ tends to further oxidize to SnO₂ and other phases at the surface. Speaking more generally, the very small ionization potentials of SnO and SnTiO₃ suggest facile oxidation, consistent with the extremely narrow stability window for SnO⁴² and the observed surface degradation of SnTiO₃ reported here (see chapter 5.2.4). Small photocatalytic activity for H₂ evolution can therefore only be

observed if the SnO₂ layer is either thin enough, enables electron tunneling directly to the electrolyte, or does not completely cover the bulk of SnTiO₃. Evidence for the latter case is presented further below in the section about TEM.

Regarding the accuracy of the slab method for absolute band alignments, Moses and coworkers⁴³ found that GGA-PBE underestimates ionization potentials of III-nitrides by 300 to 600 meV (shifting the band positions to more negative values on the electrochemical scale) compared to HSE06. Brgoch and coworkers⁴⁴ found a similar discrepancy of 300 meV for 2H-PbI₂ (500 meV without spin-orbit coupling). Across all the metallic elements, De Waele and coworkers⁴⁵ found an average 300 meV underestimate of the work functions by GGA-PBE with respect to experiment. Though these errors are significant on the scale of achievable experimental error with careful photoemission or electrochemical methods, they are notably small with respect to the differences observed across these materials and the conclusions drawn here.

Furthermore, if taking a look at the photoresponse (see Fig. S C.10 and description SI) the presence of defect states at the surface is confirmed. A photocurrent switching effect from cathodic currents at more negative to anodic currents at more positive potentials was observed at about 0.7 V vs RHE. The observation of a cathodic photoresponse between 0 and 0.7 V vs RHE is not an effect of electrolyte reduction as the thermodynamic potential for H₂ evolution is not reached and hence no electron transfer is possible. It can therefore be assumed that the electrons excited by light are transferred to a surface species instead, and thus trapped. Moreover, the photoresponse was not strongly light intensity-dependent, which means that instead the density of states or more generally the availability of charge carriers are the limiting factors in this case.

5.2.4. XPS and TEM and XRD

In order to confirm surface oxidization of SnTiO₃, we take a closer look at the surface. In Figure 5.4 the XP-spectra of washed SnTiO₃ (and Sn₂TiO₄ in Fig. S C.8) and powders sputtered for 45 min are shown. The energy corrected spectra of Sn 3d show two species: one at around 486.7 eV and another one at 485.3 eV. Species of higher binding energy in XPS are usually of higher oxidation state (more negative absolute band position against vacuum). We thus assign the peak at 486.7 eV to a Sn⁴⁺ and the 485.3 eV to the Sn²⁺ oxidation state. However, Boltersdorf *et al.* have assigned the former peak to the Sn²⁺ species in Sn₂TiO₄ arguing that the shoulder is metallic Sn⁰. Although metallic species have been observed for XP-spectra of other lone pair (Pb²⁺) materials⁴⁶ this observation is rather unlikely in our case. Moreover, SnWO₄⁴⁷ in contrast has been reported to show two peaks at 486.6 eV and 485.5 eV which were assigned to Sn⁴⁺ and Sn²⁺ respectively, fitting well reports for SnO⁴⁸ and SnO₂⁴⁹. As XPS is a surface sensitive method of not more than few nanometers penetration depth, our data are supporting surface oxidation.

Surprisingly, prolonged sputtering with Ar⁺ did not significantly change the ratio between the two peaks. Only the lower amount of O relative to Sn may speak for Sn in lower oxidation states deeper in the sample. Since Ar⁺-sputtering is a rather invasive method the observed trend is possibly a consequence of *in situ* oxidation of exposed areas as well as selective sputtering of the lighter elements due to a higher sputtering cross section with Ar⁺ compared to the heavier Sn^{50, 51}.

Table 5.1. Evaluation of the XP-spectra SnTiO₃ deposited on indium foil after different sputtering times. The atomic ratios are normalized to the Sn signals, respectively.

Time sputtered	Ti* : Sn	Ti* : Sn : O	O : Sn	Sn ⁴⁺ /Sn ²⁺
0 min	0.22	2.2 : 10 : 18.3	1.8	2.97
5 min	0.23	2.3 : 10 : 16.7	1.7	2.94
15 min	0.21	2.1 : 10 : 16.1	1.6	3.02
45 min	0.23	2.3 : 10 : 14.8	1.5	2.62

* Sn₂TiO₄ also showed a similar underestimation of the Ti signal on the order of a factor 4-5 relative to the expected stoichiometry of the ternary phase, supporting a Ti-depleted surface species, such as SnO₂.

XPS also allows for direct probing of the electronic structure of the VBM (Fig. 5.4f). The comparison of the VBM of pure SnO₂ and SnTiO₃ proves partial oxidation at the surface. Yet, the significant electronic contribution at about 2-3 eV⁵²⁻⁵⁴ for SnTiO₃, shows that the surface oxidized species must be relatively thin. This lends further support to the idea of photoexcited electrons being able to reach the electrolyte despite oxidation of the surface.

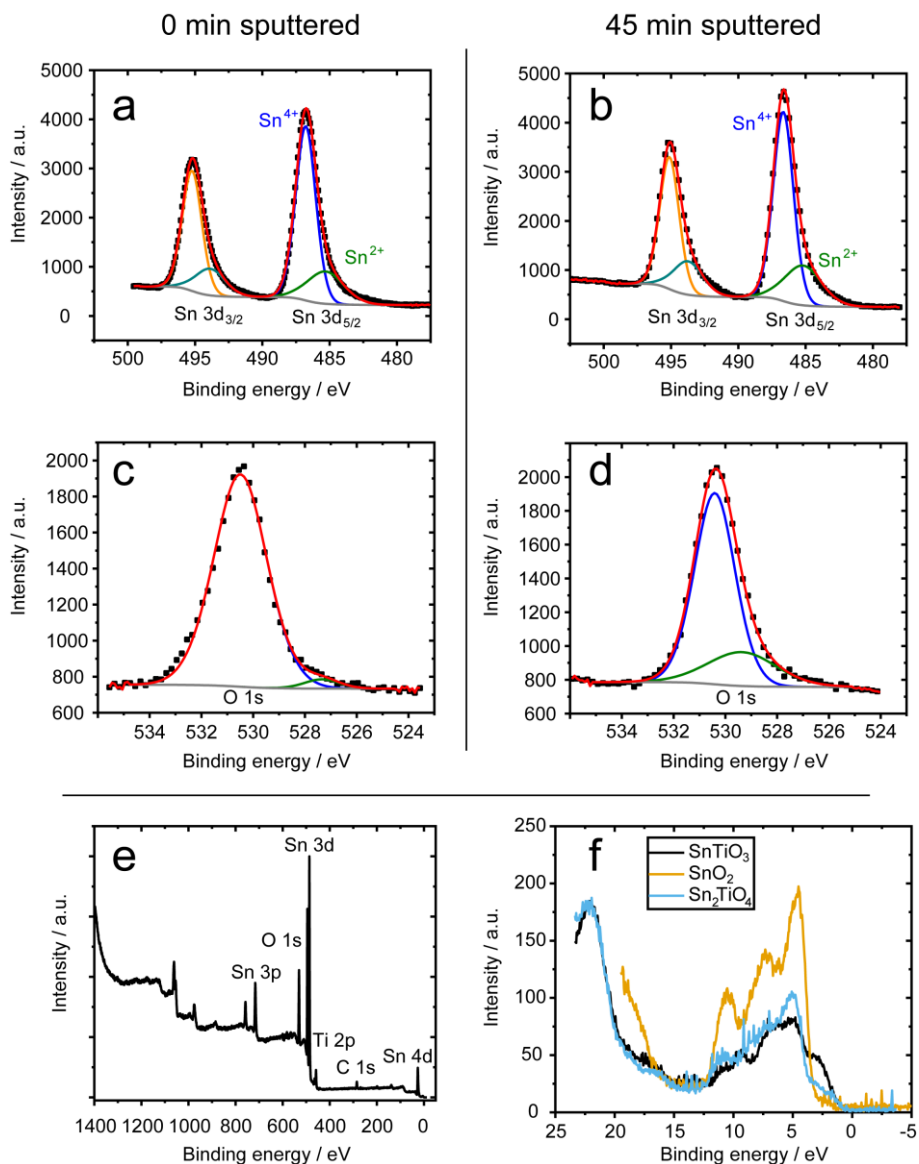


Figure 5.4. a) Detailed XP-spectrum of Sn 3d_{3/2} and Sn 3d_{5/2} of as-synthesized SnTiO₃, showing two Sn species. The blue peak with maximum at 486.6 eV is assigned to Sn⁴⁺ and the green peak at 485.5 eV to Sn²⁺. b) Same sample after 45 min of Ar⁺ sputtering. Signals remain almost identical, only the area of Sn²⁺ is slightly increased. c) Detailed XP-spectrum of O 1s of unspattered SnTiO₃, showing two oxygen species of which one peak (green) corresponds to surface species and d) spectrum after 45 min of sputtering showing a slightly reduced O amount. e) Survey XP-spectrum of SnTiO₃ with relevant peaks labeled, f) VBM of SnTiO₃, SnO₂ and Sn₂TiO₄ in direct comparison. All spectra are aligned by the amorphous carbon peak.

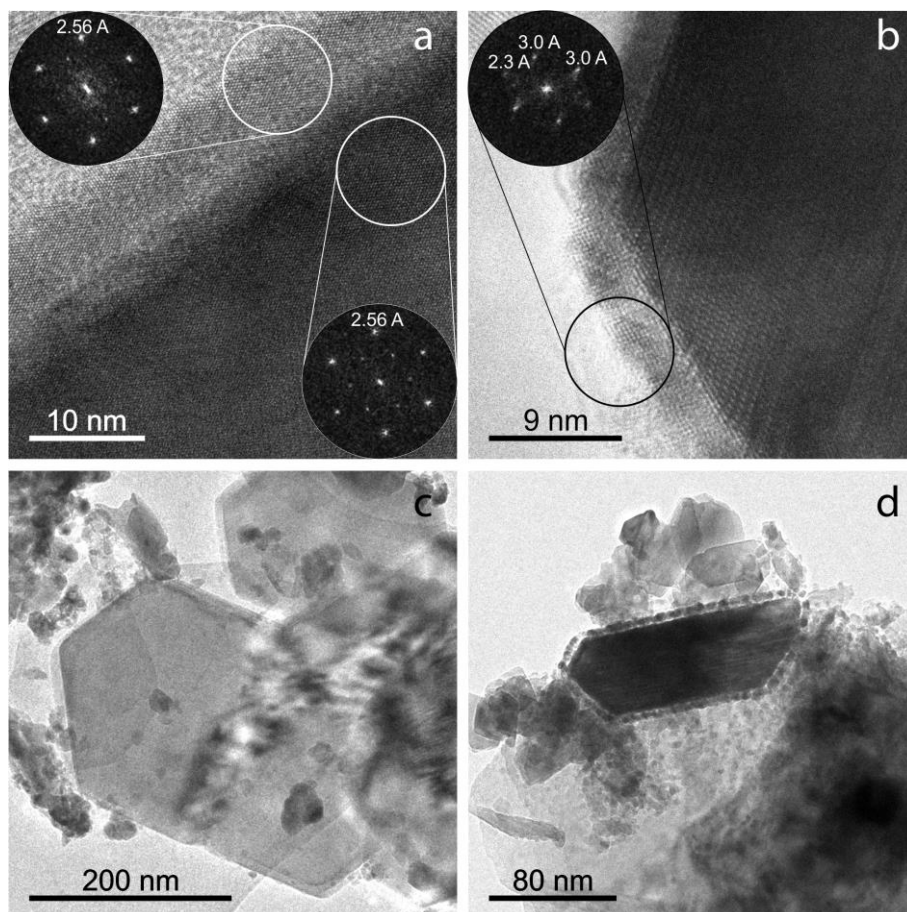


Figure 5.5. a) SnTiO₃ platelet without any SnO₂ surface particles, as seen in bright-field TEM, including FFTs for the surface and the bulk both showing the typical hexagonal diffraction pattern for SnTiO₃. The difference in thickness explain the different intensities, b) surface particles on SnTiO₃ and corresponding FFT, which is different from the lattice parameters shown in a), thus supporting the presence of SnO₂ surface species; c) overview image of corresponding clean particles and d) example of nanoparticles covering a SnTiO₃ particle.

Presence of significant amounts of Sn⁴⁺ is very well known from different other (layered) Sn(II) transition metal oxides. In many cases people have simply adapted the respective stoichiometric formulas. For example SnNb₂O₆ is proposed to actually correspond to Sn_{1.79}(Nb_{1.92}Sn^{IV}_{0.08})O_{6.77}⁵⁵ or Sn_{1.34}(Nb_{1.68}Sn^{IV}_{0.32})O_{6.18}⁵⁶. Others⁵⁷ argue that the presence of Sn⁴⁺ would not lead to compensation by excess presence of O, but rather induce *p*-type doping. Certainly, it is convincing to also assume anti-site defects of Sn⁴⁺ on Ti⁴⁺ (Sn_{Ti}) positions for SnTiO₃, which unlike for Sn_{Nb} do not need charge compensation and are known also from Sn-doped TiO₂⁵⁸ and other titanates⁵⁹. But the chosen synthesis conditions, starting from a layered preformed titanate and reacting the mixture at only 300 °C make significant site exchange relatively unlikely. Moreover, no titanate side phase has been identified, while the excess of Sn determined after washing is at only 3.5 mol%, which is more consistent with the amounts of crystalline side-phase SnO₂ and, hence, the existence of a surface SnO₂ species (Tab. S C.1).

As TEM only gives a local picture, a statistical overview is difficult to obtain. Bulk methods such as XRD and NMR (see next paragraphs) confirmed the presence of small amounts of crystalline SnO₂, which nonetheless did not exceed 2 wt% in either case (Fig. 5.6). Due to the relatively high batch-to-batch variation we paid careful attention to only compare samples directly from the same batches for XRD, NMR and Mössbauer in this work.

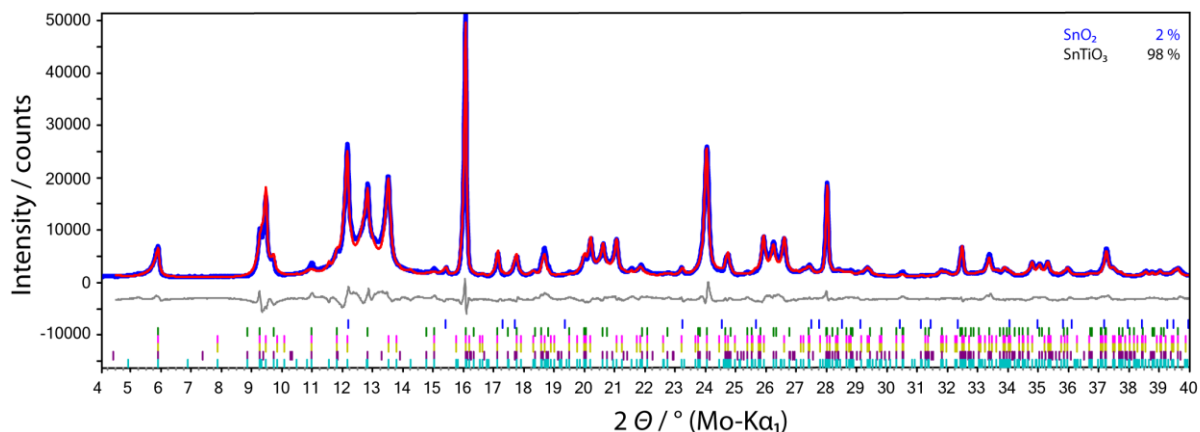


Figure 5.6. Rietveld refined sample of SnTiO₃ showing ~ 2 wt% of crystalline SnO₂ (peak positions indicated by dark blue ticks) and colored ticks indicating the different polytypes of SnTiO₃¹⁸ needed to describe the structure.

5.2.5. ¹¹⁹Sn-NMR

The ¹¹⁹Sn NMR in Figure 5.7a show spectra obtained at two different spinning speeds to identify the isotropic peak positions. The signal at - 459 ppm dominates the spectrum while the very small signal (< 2 %) at - 602 ppm corresponds well to literature values of SnO₂⁶⁰. No other significant contributions of Sn species could be identified. In particular, no tin species of amorphous (invisible to XRD) character were found as confirmed by HETCOR (Fig. 5.7c) experiments, clearly indicating that the ¹H present in the structure is well correlated with the SnO₂ signal at - 602 ppm. The two signals at - 655 ppm and - 552 ppm correspond to hydroxide species known from surfaces of SnO₂ nanosheets⁶¹, which are more pronounced due to polarization transfer from adjacent ¹H, an abundant NMR nucleus. Other layered Sn(II) niobates⁶² show very similar chemical shifts for ¹¹⁹Sn: SnNb₂O₆ at - 387 ppm and Sn₂Nb₂O₇ at - 403 ppm, given that the chemical shift range for Sn(II) compounds is rather larger, with values ranging from - 296 ppm for SnO to SnS at + 297 ppm. Other Sn²⁺ species show chemical shifts of - 387 ppm for SnI₂ and - 529 ppm for SnI₂(dmsO)⁶³. The NMR measurements therefore confirm that the Sn species contained in the sample can largely be assigned to Sn²⁺.

SnTiO₃ shows a triplet-like splitting with a large coupling constant of 1788 Hz. J-coupling is usually explained by indirect interactions through covalent bonds. Thus large coupling constants are usually considered as evidence for covalency of the bonds as shown for Sn-F in α-SnF₂⁶⁴.

Indirect ⁴J-coupling through two Sn-O and two Ti-O bonds is unlikely (see Figure 5.7b⁵) in SnTiO₃. Large coupling constants over four bonds (⁴J) on the order of 1700 Hz have only been observed in organotin compounds in which the (organic) bonds show significant covalent character⁶⁶. In most other cases the coupling is on the order of only 10² Hz⁶⁷ or not resolved⁶⁸. The large coupling constant therefore speaks for appreciable Sn-Sn interaction, similar to what has been observed for litharge-type SnO⁶⁰ (8280 Hz), and consistent with our calculations of COHP (Fig. 5.1d). The calculation of interlayer energies for SnTiO₃ further confirmed an increased interlayer interaction different from pure van der Waals gaps, concluded by the fact that the interaction potential cannot be fit with a normal Morse potential function (Fig. S C.9). Moreover, normal exfoliation energies are on the order of 15 and 17 kJ mol⁻¹ for phosphorene and MoS₂ respectively⁶⁹, while SnTiO₃ has an energy of 25 kJ mol⁻¹ according to calculations on the PBE+D2 level of theory. The large coupling found in NMR therefore further supports the quasi 3D character of SnTiO₃ as identified theoretically.

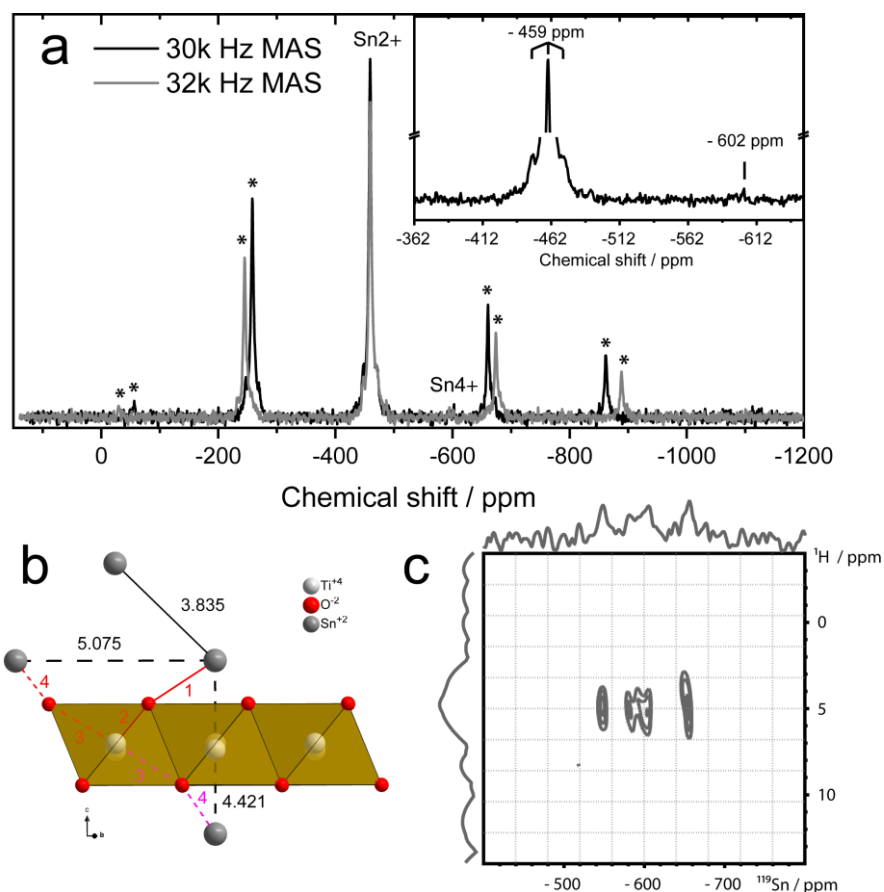


Figure 5.7. a) ¹¹⁹Sn-direct excitation NMR (149.21 MHz) at two different spinning speeds stated in the spectrum, SF=149.21 MHz, showing two different isotropic chemical shifts, with close up in inset of relevant isotropic peaks at - 602 ppm and - 459 ppm. Spinning side bands are marked with an asterisk. b) relevant atomic distances and potential coupling pathways for Sn in part of SnTiO₃ crystal structure. Blue and grey indicating Sn, red is O and white Ti. c) HETCOR ¹H and ¹¹⁹Sn NMR showing the presence of protons only in proximity of SnO₂ species (¹H spectrum in Fig. S C.6).

5.2.6. ¹¹⁹Sn Mössbauer spectroscopy

Figure 5.8a top shows the ¹¹⁹Sn Mössbauer spectrum for as-synthesized SnTiO₃ with a quadrupole split signal of Sn²⁺ at $\delta = 2.9 \text{ mm}\cdot\text{s}^{-1}$ and a signal with small isomer shift corresponding to SnO₂ at $-0.02 \text{ mm}\cdot\text{s}^{-1}$. In stark contrast to NMR and XRD, the amounts of SnO₂ identified are on the order of 15%, although Mössbauer spectroscopy is considered to show similar sensitivity to the bulk of the material, including the surface, as NMR spectroscopy. The discrepancy between the results of the two bulk sensitive methods ¹¹⁹Sn-NMR and Mössbauer spectroscopy from the same sample are surprising and no satisfying explanation for this observation can be offered at this stage. Notably, similar discrepancies have been observed by other groups studying tin(II) niobates before⁵⁶.

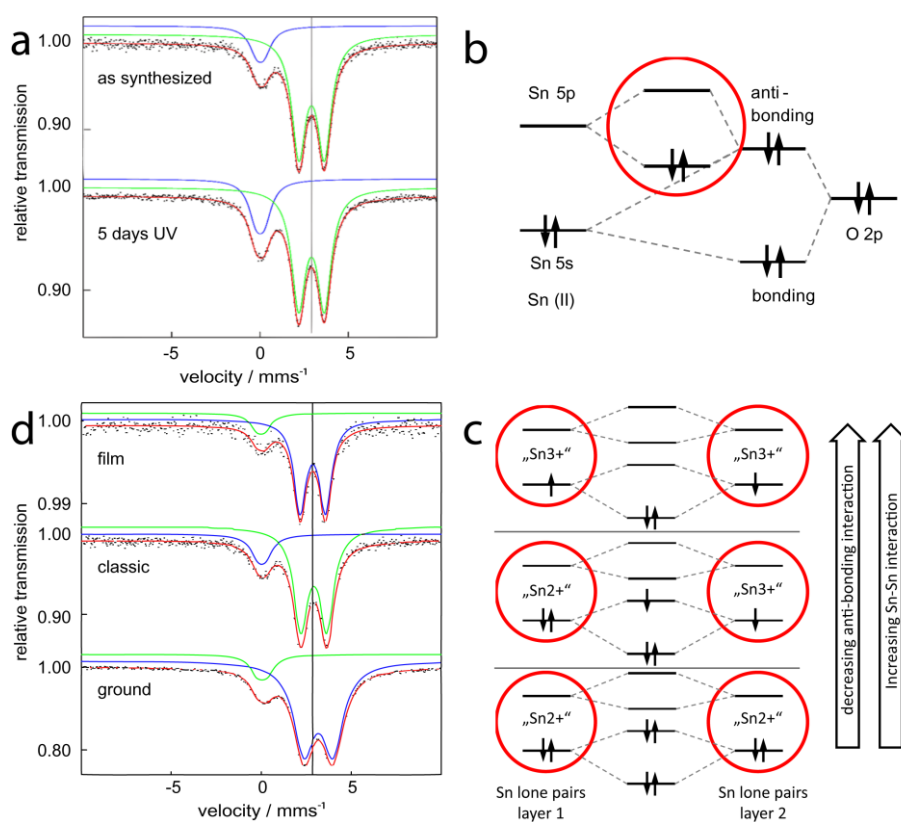


Figure 5.8. a) Experimental (data points) and simulated (colored lines) ¹¹⁹Sn Mössbauer spectra of SnTiO₃ as-synthesized (top) and after 5 days of exposure to 150 W mercury lamp (bottom), showing a Sn⁴⁺ species around 0 mms⁻¹ and a quadrupole split signal of Sn²⁺ at 2.8 mms⁻¹. b) Scheme showing anti-bonding character of the lone pair according to the revised lone pair model by Walsh *et al.* c) MO-scheme showing inter-layer lone pair interactions, in which electron depletion of anti-bonding state leads to increasing Sn-Sn bonding. d) ¹¹⁹Sn Mössbauer spectra (78 K data) of different SnTiO₃ samples: (top) thin film material, (middle) classical bulk material, (bottom) ground powder. The vertical line serves as a guide to the eye for distinguishing the isomer shifts.

Table 5.2. Fitting parameters of ¹¹⁹Sn-Mössbauer spectroscopic measurements at 78 K; δ = isomer shift, ΔE_Q = electric quadrupole splitting, Γ = experimental line width.

Compound	δ (mm·s ⁻¹)	ΔE_Q (mm·s ⁻¹)	Γ (mm·s ⁻¹)	ratio
SnTiO ₃ as-synthesized (top)	2.918(3)	1.449(5)	0.967(8)	84(1)
	- 0.02(1)	0.44(6)	1.02(7)	16(1)
SnTiO ₃ after UV irradiation (bottom)	2.912(2)	1.454(3)	0.961(5)	77(1)
	0.01(1)	0.48(2)	1.00(3)	23(1)
SnTiO ₃ film (top)	2.858(7)	1.41(1)	0.82(2)	86(1)
	- 0.01(4)	0.5(1)	0.9(2)	14(1)
SnTiO ₃ classic (middle)	2.917(3)	1.446(5)	0.958(8)	84(1)
	0.03(1)	0.42(6)	1.01(7)	16(1)
SnTiO ₃ ground (bottom)	3.175(2)	1.614(2)	1.400(4)	88(1)
	0.048(6)	0.52(2)	1.00(3)	12(1)

The amount of Sn⁴⁺ further increases to 23 % by prolonged (5 days) exposure to UV light (Tab. 5.2). The light effect has been used in the past to selectively oxidize surface deposited SnCl₂ “sensitizers” on the micron scale by UV light⁷⁰⁻⁷². It is not trivial to distinguish the effects of photons and local heating. However, as known from TGA experiments (Fig. S[°]C.5), SnTiO₃ is stable to at least 100 °C in air, which is significantly above the temperatures expected by UV (150W mercury vapor lamp) light induced heating (~50 °C, personal communication).

The presence of larger amounts of Sn⁴⁺ was further confirmed by total oxidation of as-synthesized SnTiO₃ powder (Fig. S C.5). When assuming complete coverage of small SnTiO₃ platelets (200 x 200 x 50 nm) by a 3 nm layer of SnO₂, assuming an extreme case of what had been identified in TEM only on few positions, a maximum of 20 mol% Sn⁴⁺ is present in the structure. This fits surprisingly well to the values found for Sn⁴⁺ by Mössbauer spectroscopy. Yet, with Sn⁴⁺ simply present as SnO₂ at the surface, grinding should have further increased the Sn⁴⁺ fraction due to an increase in exposed surface area⁷³. The ratio of Sn⁴⁺ to Sn²⁺, however, was not dependent on grinding of SnTiO₃ (Fig. 5.8d), while the FWHM of the Sn²⁺ signal^{74, 75} did in fact increase.

The evaluation of the Mössbauer signal assigned to SnTiO₃ shows that the isomer shift is very close to values reported for SnO (2.7 mm·s⁻¹)⁶⁰ and is strongly dependent on sample history as we will discuss further down. Other Sn(II) compounds show shifts higher than 3 mm·s⁻¹, such as SnS⁷³ with 3.25 mm·s⁻¹. Taking a look at the SnS crystal structure from the perspective of the revised lone pair concept, it is known that the *p*-orbital anti-bonding character is smaller in SnS

compared to SnO. This results from a higher *s*-orbital character and leads to reduced stereoactivity of the lone pair. The smaller stereoactivity in turn increases the electron density at Sn, mirrored in the strong isomer shift in the Mössbauer spectrum⁷⁶. Following this argument SnTiO₃ has strongly active lone pairs with relatively small electron density at Sn itself. The isomer shifts of other ternary compounds also are distinctly different from SnTiO₃, for example SnNb₂O₆⁵⁷ has a shift of $\sim 3 \text{ mm}\cdot\text{s}^{-1}$ or Sn₂Nb₂O₇⁵⁵ even at $3.2 \text{ mm}\cdot\text{s}^{-1}$, or α - and β -SnWO₄⁷⁷ with over $3.4 \text{ mm}\cdot\text{s}^{-1}$. The only published Sn(II) titanium oxide is the Kegginite-type Pigment Orange 82⁷⁸, which also showed a shift of more than $3 \text{ mm}\cdot\text{s}^{-1}$. SnTiO₃ therefore behaves more similar to SnO than to other ternary Sn(II) oxides (compare also band alignment calculations in Fig. 5.3 b).

In SnO it was calculated that the small isomer shift correlates with direct Sn-Sn interactions, which we have also seen for SnTiO₃ both by DFT and as large coupling constant in ¹¹⁹Sn NMR. Direct Sn-Sn (lone pair) interaction has also been observed as a consequence of vacancies in amorphous Zn-Sn-O⁷⁹ (a-ZTO) or as Ge-Ge bonding for amorphous GeTe or Ge₄Se₃Te⁸⁰⁻⁸². In Fig. 5.8 b we show the simplified molecular orbital scheme of Sn 5*s* and O 2*p* for the oxidation (potentially also light-induced, see Fig. 5.8 a bottom) of Sn²⁺. When taking out electrons from the anti-bonding orbitals at the VBM (COHP analysis Fig. 5.1 c in DFT part), stabilization of the overall structure is achieved. More precisely, the drop in the iCOHP just below the Fermi level for the Sn-O interactions indicates that oxidation can additionally stabilize the structure. The direct Sn-Sn interaction also profits from a slight lowering of the Fermi level. This would correspond to the MO theory picture of lone pairs only interacting stronger than van der Waals bonds in case that not every single electron is paired and thus of non-bonding nature (Fig. 5.8b, c). Single layers of rock-salt BiSe have recently been shown to be stabilized by depopulation of anti-bonding Bi-Se states by introduction of additional electron accepting layers⁸³. Biswas *et al.*⁸⁴ showed the corresponding case for Cu₂ZnSn(IV)S₄ in which the reduction from Sn⁴⁺ to Sn²⁺ and the occupation of lone pair states did increase the Sn-Sn distances due to increasing anti- or non-bonding interactions. One would also expect relaxation of the crystallographic structure upon changes in oxidation state for SnTiO₃, if present in substantial amounts. However, the presence of stacking faults in SnTiO₃ does not allow assessment of detailed structural parameters, i.e. local distortions by Rietveld refinement or similar methods.

The specific observation of a change in isomer shift to higher values after grinding can also be rationalized by the found Sn-Sn bonding. These weak interlayer bonds are affected strongly by grinding. Hence, the introduction of even more stacking faults (compare high-pressure phase transition at below 1 GPa in chapter 4) might in fact lead to redistribution of electrons such that they are of more Sn *s*-orbital (higher isomer shift) and less bonding Sn-Sn character. Küpers *et al.* have suggested this type of “electron reshuffling” from anti-bonding orbitals into direct Ge-Ge bonding as the reason for stabilization of the hexagonal Ge₄Se₃Te⁸¹. Another explanation

involves overlapping of two different Sn species (for example close to the surface and bulk), leading to a seemingly broadened line width and a change of isomer shift due to a change in the respective fraction. Importantly however, the shift to higher isomer shifts corresponds to more reduced “Sn²⁺”, which would mean that grinding counterintuitively induced reduction instead of oxidation. Whether applying a more local picture of two Sn species with slightly different oxidation states or a band-like picture in which some of the Sn²⁺ dominated VBM is partially “oxidized” in SnTiO₃, will depend heavily on the dynamics of the hole transport and detailed spectroscopic analysis is required.

Any redox-chemistry involving reduced Ti³⁺ to explain Sn oxidation is unlikely⁸⁵, and EELS and NMR have shown very clean Ti⁴⁺ environments¹⁸. Moreover, no magnetic moments could be measured for SnTiO₃ (unpublished, private communication). A potential partial oxidation can thus only involve charge transfer (charge self-regulation⁸⁶) between O, Sn and the respective vacancies. For example it has been shown that neutral V₀ are a stable configuration next to Sn²⁺, which means they lose their electron donating ability and do not obtain their typical positively charged state⁸⁷. Moreover, Dalpian *et al.*⁸⁸ have shown how, for perovskite-type CsSnI₃ and closely related double-perovskite Cs₂SnI₆, the induction of Sn vacancies and hence (formal) oxidation state increase to Sn⁴⁺ leads to surprisingly low change in actual charge density around the Sn. They explain this by *s*-orbital electron depletion on Sn while at the same time “backfilling” occurs into Sn *p*-orbitals. Xiao *et al.*⁸⁹ even argued that the oxidation state of Sn in this compound was more closely to Sn²⁺ than the intuitive Sn⁴⁺, due to formation of two ligand holes instead.

Taking into account the formation of direct Sn-Sn interactions in SnTiO₃, we propose that Xiao and Dalpian both describe the depletion of the anti-bonding interaction at the VBM by either taking electrons out of the 5*s* orbital at Sn or the hybridizing O 2*p* orbitals (Fig. 5.8b, d). This picture would be in complete consistency with the revised lone pair model by Walsh, which emphasizes the fact that the lone pair electrons are constituted of both cation and anion contributions.

5.2.7. Excitation probabilities and photoluminescence

Independent of potential surface or bulk oxidation of Sn²⁺, the transition probabilities are highly dependent on local symmetries of the involved orbitals, which in turn can affect the quantum yield for H₂ evolution. It has been shown that by calculation of the dipole transition matrix elements it is theoretically possible to rationalize the different absorption behavior of GaAs or Cu₂O. Experimentally, SnWO₄, which has transition metals dominating the CBM and the Sn lone pairs dominating the VBM, is a good example in which it has been shown that excitations from deeper in the valence band are more efficient⁴⁷.

When looking at the transition probabilities similar to Cu₂O or GaAs⁹⁰, no unusual features can be identified for SnTiO₃ (data not shown). In Figure 5.9b we have calculated the absorption coefficients for VBM to CBM excitations parallel and perpendicular to the layers of SnTiO₃. The absorption coefficients correlate well with the joint density of states (JDOS) for most parts, except for one feature at about 3.2 eV. This transition corresponds to the onset potential of O 2*p* orbitals as seen from the orbital selective DOS (Fig. 5.1d) and can even be found in the absorption spectrum of SnTiO₃, where an additional absorption increase can be found starting at energies around 3.2 eV (< 400 nm) (see Fig. 5.9a and b orange line).

Knowing the high stereochemical activity of SnTiO₃ from Mössbauer spectroscopy, it is possible to rationalize the “observations” made from DFT. While the lone pair of high *s*-character as found in SnWO₄ has to “obey” the selection rules more strictly upon excitation into the W 5*d*-orbital, the lone pair in SnTiO₃ is of stronger *p*-character and thus satisfies the required imparity in quantum numbers (compare to Laporte rule in coordination chemistry). Although the crystal symmetry (influencing direct vs. indirect band gap etc.) is also relevant in this context, we can conclude that charge excitation efficiencies – likely correlating with H₂ evolution rates – in SnTiO₃ are not strongly influenced by transition probabilities in first approximation. Only the transitions from orbitals with even higher *p*-orbital character and thus higher imparity with regards to the Ti 3*d*-orbital in the “pure” O *p*-orbitals induced a slightly increased excitation probability (Fig. 5.9b). As we have observed, indeed the O₂ evolution was dependent on UV-light (Fig. 5.2c). It remains open whether holes generated in O 2*p* dominated bands of SnTiO₃ or holes generated in surface SnO₂ are really favored to reach the catalyst’s surface compared to holes formed in Sn 5*s* dominated bands of SnTiO₃.

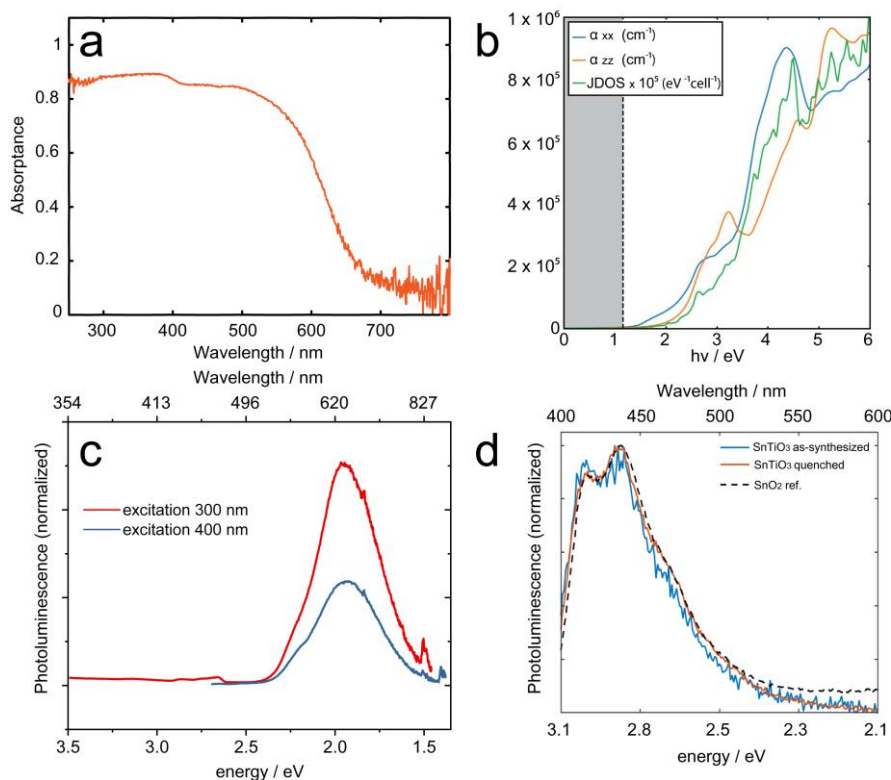


Figure 5.9. a) Absorbance behavior of SnTiO₃. b) Calculated (DFT-GGA) absorption coefficients vs. joint Density of States for SnTiO₃ with increased absorption coefficient at 3.2 eV corresponding to the onset of O 2p orbitals in the partial DOS. c) Photoluminescence spectra of a SnTiO₃ sample at two different excitation wavelengths, d) photoluminescence spectra from powder covered with SnO₂, including the reference measurement of SnO₂ under the same conditions; note that at the same wavelengths in c) we also find small peaks.

The luminescence behavior of SnTiO₃ is complicated to assess due to small emission intensities and their dependency on sample history and preparation conditions. Only in one case it was possible to obtain photoemission spectra at a wavelength correlating to the band gap of SnTiO₃. In most other cases either the luminescence of surface SnO₂ dominated (Fig. 5.9d) or no signal could be obtained at all. In the case when photoluminescence was observed the emission maximum was at 630 nm (Fig. 5.9c), corresponding to an energy of 1.97 eV. Two small additional – potentially defect related – emissions are observed at 674 nm (1.84 eV) and 827 nm (1.5 eV). The sample that showed these emissions was of relatively large particle size. Possibly the relatively small surface area and thus smaller amounts of surface SnO₂ made observation of these features possible.

Another more speculative explanation goes along with Kim *et al.*⁹¹. They showed that the formation of anion vacancies in Cu₂ZnSnS₄ may allow for charge reordering and emerging in-gap states from Sn⁴⁺ 5s-S²⁻ 3p anti-bonding orbitals. The delicate charge balancing between vacancies and a multivalent element such as Sn is very difficult to access and much of the discussion

provided here remains on a qualitative level. As stated above, only the detailed assessment of vacancy formation energies under different synthesis conditions and subsequent relaxation of electronic and crystallographic structures will allow for detailed understanding of the optoelectronic properties. It is indeed known from Cu₂ZnSnS₄ that the presence of in-gap states caused by oxidation of Sn²⁺ to Sn⁴⁺ through light (and also through synthesis) leads to Shockley-Read-Hall recombination⁹², which is non-radiative and could therefore explain why most samples of SnTiO₃ did not show emission. This is further underlined by the fact that prolonged treatment with UV light did in fact increase the amount of SnO₂ present in the sample significantly (Fig. 5.8a bottom). One could speculate that the formation of defect or vacancy states within bulk SnTiO₃ is occurring simultaneously, for example similar to other lone pair materials showing charge trapping phenomena. Cortecchia *et al.*⁹³ discuss the charge trapping of both electrons and holes on Pb²⁺. While electron trapping forms Pb₂³⁺-dimers, holes can be trapped as Pb³⁺. Pb³⁺ as hole traps have been considered as early as 1993 by Robertson *et al.* for PZT⁹⁴ and thus known not only for hybrid perovskite-type materials.

5.3. Conclusions

We conclude that SnTiO₃ is an example for an ideal photocatalyst on paper, but despite the promising prerequisites such as very low hole effective masses and a close-to-ideal band gap, shows low photocatalytic activity. We identify Sn⁴⁺ species – predominantly in the form of SnO₂ - to be present on the surface, which influences the charge transfer efficiency to the electrolyte. We could rationalize the tendency to oxidize by the very low ionization potential of SnTiO₃. Moreover, the anti-bonding nature of Sn-O bonds at the VBM favor partial (bulk) oxidation and direct interlayer Sn-Sn interactions. SnTiO₃ thus has significant 3D character and charge separation similar to other (internal) heterojunction materials will not be efficient. We therefore conclude that it remains challenging to design photocatalysts using lone pairs as their positive properties come along with relatively low stability.

5.4. Methods

5.4.1. Synthesis

Synthesis of the material was carried out as described before¹⁸. First K₂CO₃ and P25 (TiO₂) were thoroughly ground and then reacted at 600 °C for 12 hours to form a potassium titanate precursor. We realized that use of hydrated precursors (K₂CO₃ · 1.5 H₂O) was advantageous for the further reaction. Subsequently the precursor was ground together with SnCl₂ · 2 H₂O until an amorphous lemon yellow powder formed. This powder was transferred into an ampule and dehydrated in two steps: 2.5 hours at 130 °C and then another 2.5 hours at 200 °C under dynamic vacuum respectively. Eventually the powder was heated at 300 °C for 24 hours under static vacuum. For removal of the KCl the obtained SnTiO₃ powder was washed twice with H₂O and once with Ethanol.

5.4.2. H₂ evolution (HER)

For stable H₂ evolution over more than 10 hours it was crucial to stabilize the suspension. Here it proved practical to work in 0.1 M KOH solution as too acidic conditions would dissolve the SnTiO₃ catalyst and the point of zero charge was determined to be around pH = 7. As stable suspensions are usually obtained at zeta potentials of over ±20-30 mV⁹⁵ the choice of relatively basic conditions was reasonable, despite the increasing thermodynamic requirements. 30 mg of lightly ground SnTiO₃ were therefore dispersed in an aqueous solution of 0.1 M KOH and 10 vol% methanol solution. After sonication for 5 min the dispersion was added to the top irradiation photoreactors. Subsequently, H₂PtCl₆ · 8 H₂O was added to obtain the desired Pt amount and finally the whole reactor was degassed. Under constant stirring and held at 25 °C by a Lauda thermostat, each reactor was irradiated at not more than 1 sun (100 mW/cm²) by a 300 W Xe-spectrum filtered through a Thorlabs 420 nm-cut-off visible light filter. The H₂ gas was detected by a gas chromatograph (Thermo Scientific TRACE GC Ultra) with customized on-line sample injection and Ar carrier gas and TCD detector.

5.4.3. O₂ evolution reaction (OER)

For the O₂ evolution reaction 7.5 mg of the Pt-modified SnTiO₃ (used for H₂ evolution experiments before) were suspended in 5 mL of a 0.1 M KOH solution with Na₂S₂O₈ (1 mmol) and 12.5 µL of 2 mM Co(NO₃)₂ · 6 H₂O stock solution. The suspension was then held under constant Ar flow of 20 mL/min until the background O₂ evolution was below 2 ppm. For irradiation we used full spectrum 300 W Xenon lamp at 120 mW/cm². A temperature corrected PreSens Oxygen sensor was used for O₂ evolution from the solution. Additional addition of methanol quenched the O₂ evolution, indirectly proving hole transfer onto the electrolyte (H₂O).

5.4.4. Photoelectrochemical Characterization (PEC)

FTO electrodes (7 Ohm) were contacted with Cu wire and silver paste and epoxide resin covered the contact points. The powder was applied by drop casting thick ethanolic suspensions of SnTiO₃. Subsequently the electrodes were annealed in dynamic vacuum at 250 °C. The electrode was measured in a custom-built electrochemical cell with quartz window. Due to the small amounts of catalyst on the electrodes, high light intensities of up to three suns had to be applied. The electrolyte was 0.1 M KOH.

5.4.5. UV-Vis spectroscopy and photoluminescence

Absorbance and photoluminescence spectra were obtained on a FLS1000 Photoluminescence Spectrometer (Edinburgh Instruments) from powder samples.

5.4.6. X-ray photoelectron spectroscopy XPS

X-ray photoelectron spectra were obtained on an Axis Ultra system (Kratos) with a monochromatic Al K_α source. Detail scans were acquired with a pass energy of 20 eV. Samples were prepared by pressing the powders into indium foil. The peaks were fitted after subtraction of a Shirley background. A Gauss/Lorentz ratio of 30% was used for all peaks and the full width half maximum was used as a free fitting parameter. For sputtering an Ar⁺ source was used at 4 kV.

5.4.7. X-ray powder diffraction (XRPD)

The powders were measured using Mo K_α-radiation on Stoe Stadi P equipped with Mythen 1K-detector. Rietveld refinement was performed using the TOPAS 6.0 program⁹⁶ using a structural model previously published¹⁸.

5.4.8. Nuclear Magnetic Resonance spectroscopy (NMR)

For solid-state NMR measurements a Bruker Avance III 400 MHz (B₀ = 9.4 T) instrument was used. The powders were measured by magic angle spinning, with rotation speeds given in the respective figures. The field for ¹¹⁹Sn NMR was set at 149.21 MHz. ¹H NMR spectra were collected at 500.25 MHz.

5.4.9. ¹¹⁹Sn Mössbauer spectroscopy

A Ca^{119m}SnO₃ source was used for the ¹¹⁹Sn Mössbauer spectroscopic investigation. The samples were placed within thin-walled PMMA containers. A palladium foil of 0.05 mm thickness was used to reduce the tin K X-rays concurrently emitted by this source. The measurements (ca. 1 d counting time per spectrum) were carried out at 78 K, while the source was kept at room temperature. The spectra were fitted with the "WINNORMOS FOR IGOR" program package⁹⁷.

5.4.10. Density Functional Theory (DFT)

All calculations regarding SnTiO₃ were performed assuming the idealized ABC-type stacking, unless otherwise stated.

Ab initio calculations on the idealized ABC-stacking of SnTiO₃ ($R\bar{3}$, #148), the black litharge ($P4/nmm$, #129) and red ($Cmc2_1$, #36) polymorphs of SnO, rutile SnO₂ ($P4_2/mnm$), and foolite SnNb₂O₆ ($C2/c$, #15) were performed with the Vienna Ab initio Simulation Package (VASP)⁹⁸⁻¹⁰¹, which implements the Kohn–Sham formulation of density functional theory (DFT) using a plane wave basis set and the projector augmented wave formalism^{102, 103}. The generalized gradient approximation exchange and correlation functional of Perdew, Burke, and Ernzerhof (GGA–PBE) was employed¹⁰⁴. Electrons were included in the valence as follows: Sn, 5s²4d¹⁰5p²; O, 2s²2p⁴; Ti, 3s²3p⁶4s²4d²; Nb, 4s²4p⁶5s²4d³. The plane wave basis set cutoff energy was 600 eV for all calculations. Calculations of the electronic band structure and density of states for ABC-SnTiO₃ revealed negligible influence of spin-orbit coupling (SOC) even for row 5 Sn, particularly in the occupied states, and SOC was omitted from band alignment and COHP calculations.

Momentum-space integration was performed on Γ -centered Monkhorst–Pack grids¹⁰⁵ with densities of 1500 – 2200 k-points per reciprocal atom for relaxations and static calculations of the total potential. This mesh density was preserved in the in-plane directions for slab calculations. Denser grids of 10,000 – 18,000 k-points per reciprocal atom were used for COHP and DOS calculations.

Bulk atom positions were relaxed to a force tolerance of 10 meV Å⁻¹, while lattice parameters were fixed to those observed in experiment. Van der Waals corrections were included using the DFT-D3 method with Becke-Johnson damping^{106, 107}.

Band alignments were computed following the method of Van de Walle and Martin¹⁰⁸. The valence band maximum observed in the bulk was referenced to vacuum potential of the slab calculation via the common reference of the average electrostatic potential (ionic and Hartree contributions) in the bulk and slab interior. In agreement with other works, results were found to be insensitive to the additional inclusion of the XC contribution to the local potential.

Slabs were constructed [(001) for SnO and SnTiO₃, (100) for SnNb₂O₆, (110) for SnO₂] using the method of Sun and Ceder¹⁰⁹ as implemented in pymatgen¹¹⁰. Vacuum thickness was 40 Å, and in all cases terminations which preserve centrosymmetry were selected. The outer layers of each slab were relaxed to a force tolerance of 10 meV Å⁻¹, with the interior layers fixed to the structure of the relaxed bulk.

The LOBSTER program¹¹¹ was employed to compute the crystal orbital Hamilton populations (COHPs)¹¹² and orbital projections of the DOS. Manipulation of crystal structures and LOBSTER

outputs was performed with the pymatgen package¹¹⁰. Crystal structures and electron localization functions (ELF)^{113, 114} were visualized with VESTA¹¹⁵.

Frequency-dependent dielectric functions were computed via the method of Gajdoš and coworkers¹¹⁶ as implemented in VASP and subsequently transformed to absorption spectra. Calculation of the joint DOS (JDOS) from VASP eigenvalues and visualization of transition dipole matrix elements was achieved via custom python code.

5.5. Acknowledgments

Igor Moudrakovski for ¹¹⁹Sn NMR, Tanja Scholz for discussions, Stefan Trenker for assistance with OER evolution experiments. D.H.F. gratefully acknowledges financial support from the Alexander von Humboldt Foundation.

5.6. References

1. Takanabe, K., Photocatalytic Water Splitting: Quantitative Approaches toward Photocatalyst by Design. *ACS Catalysis* **2017**, *7*, (11), 8006-8022.
2. Li, J.; Wu, N., Semiconductor-based photocatalysts and photoelectrochemical cells for solar fuel generation: a review. *Catalysis Science & Technology* **2015**, *5*, (3), 1360-1384.
3. Kato, D.; Hongo, K.; Maezono, R.; Higashi, M.; Kunioku, H.; Yabuuchi, M.; Suzuki, H.; Okajima, H.; Zhong, C.; Nakano, K.; Abe, R.; Kageyama, H., Valence Band Engineering of Layered Bismuth Oxyhalides toward Stable Visible-Light Water Splitting: Madelung Site Potential Analysis. *J. Am. Chem. Soc.* **2017**, *139*, (51), 18725-18731.
4. Fujito, H.; Kunioku, H.; Kato, D.; Suzuki, H.; Higashi, M.; Kageyama, H.; Abe, R., Layered Perovskite Oxychloride Bi₄NbO₈Cl: A Stable Visible Light Responsive Photocatalyst for Water Splitting. *Journal of the American Chemical Society* **2016**, *138*, (7), 2082-2085.
5. Stoltzfus, M. W.; Woodward, P. M.; Seshadri, R.; Klepeis, J.-H.; Bursten, B., Structure and Bonding in SnWO₄, PbWO₄, and BiVO₄: Lone Pairs vs Inert Pairs. *Inorganic Chemistry* **2007**, *46*, (10), 3839-3850.
6. Walsh, A.; Yan, Y.; Huda, M. N.; Al-Jassim, M. M.; Wei, S.-H., Band Edge Electronic Structure of BiVO₄: Elucidating the Role of the Bi s and V d Orbitals. *Chemistry of Materials* **2009**, *21*, (3), 547-551.
7. Zachäus, C.; Abdi, F. F.; Peter, L. M.; van de Krol, R., Photocurrent of BiVO₄ is limited by surface recombination, not surface catalysis. *Chemical Science* **2017**, *8*, (5), 3712-3719.
8. Zhou, Y.; Zhang, Y.; Lin, M.; Long, J.; Zhang, Z.; Lin, H.; Wu, J. C. S.; Wang, X., Monolayered Bi₂WO₆ nanosheets mimicking heterojunction interface with open surfaces for photocatalysis. *Nat Commun* **2015**, *6*.
9. Kadowaki, H.; Saito, N.; Nishiyama, H.; Kobayashi, H.; Shimodaira, Y.; Inoue, Y., Overall Splitting of Water by RuO₂-Loaded PbWO₄ Photocatalyst with d₁₀s₂-d₀ Configuration. *The Journal of Physical Chemistry C* **2007**, *111*, (1), 439-444.
10. Noureldine, D.; Anjum, D. H.; Takanabe, K., Flux-assisted synthesis of SnNb₂O₆ for tuning photocatalytic properties. *Physical Chemistry Chemical Physics* **2014**, *16*, (22), 10762-10769.
11. Mizoguchi, H.; Sleight, A. W.; Subramanian, M. A., Low temperature synthesis and characterization of SnTa₂O₆. *Mater. Res. Bull.* **2009**, *44*, (5), 1022-1024.
12. Boltersdorf, J.; Sullivan, I.; Shelton, T. L.; Wu, Z.; Gray, M.; Zoellner, B.; Osterloh, F. E.; Maggard, P. A., Flux Synthesis, Optical and Photocatalytic Properties of n-type Sn₂TiO₄: Hydrogen and Oxygen Evolution under Visible Light. *Chemistry of Materials* **2016**, *28*, (24), 8876-8889.
13. Xiao, Z.; Du, K.-Z.; Meng, W.; Wang, J.; Mitzi, D. B.; Yan, Y., Intrinsic Instability of Cs₂In(I)M(III)X₆ (M = Bi, Sb; X = Halogen) Double Perovskites: A Combined Density Functional Theory and Experimental Study. *Journal of the American Chemical Society* **2017**, *139*, (17), 6054-6057.
14. Noureldine, D.; Takanabe, K., State-of-the-art Sn²⁺-based ternary oxides as photocatalysts for water splitting: electronic structures and optoelectronic properties. *Catalysis Science & Technology* **2016**, *6*, (21), 7656-7670.
15. Wahila, M. J.; Butler, K. T.; Lebens-Higgins, Z. W.; Hendon, C. H.; Nandur, A. S.; Treharne, R. E.; Quackenbush, N. F.; Sallis, S.; Mason, K.; Paik, H.; Schlom, D. G.; Woicik, J. C.; Guo, J.; Arena, D. A.; White, B. E.; Watson, G. W.; Walsh, A.; Piper, L. F. J., Lone-Pair Stabilization in Transparent Amorphous Tin Oxides: A Potential Route to p-Type Conduction Pathways. *Chem. Mater.* **2016**, *28*, (13), 4706-4713.
16. Hautier, G.; Miglio, A.; Ceder, G.; Rignanese, G.-M.; Gonze, X., Identification and design principles of low hole effective mass p-type transparent conducting oxides. *Nature Communications* **2013**, *4*, 2292.
17. Ha, V.-A.; Ricci, F.; Rignanese, G.-M.; Hautier, G., Structural design principles for low hole effective mass s-orbital-based p-type oxides. *Journal of Materials Chemistry C* **2017**, *5*, (23), 5772-5779.

18. Diehl, L.; Bette, S.; Pielhofer, F.; Betzler, S.; Moudrakovski, I.; Ozin, G. A.; Dinnebier, R.; Lotsch, B. V., Structure-Directing Lone Pairs: Synthesis and Structural Characterization of SnTiO₃. *Chem. Mater.* **2018**, *30*, (24), 8932-8938.
19. Walsh, A.; Payne, D. J.; Egdell, R. G.; Watson, G. W., Stereochemistry of post-transition metal oxides: revision of the classical lone pair model. *Chemical Society Reviews* **2011**, *40*, (9), 4455-4463.
20. Hautier, G.; Miglio, A.; Waroquiers, D.; Rignanese, G.-M.; Gonze, X., How Does Chemistry Influence Electron Effective Mass in Oxides? A High-Throughput Computational Analysis. *Chemistry of Materials* **2014**, *26*, (19), 5447-5458.
21. Zhou, W.; Umezawa, N., Band gap engineering of bulk and nanosheet SnO: an insight into the interlayer Sn-Sn lone pair interactions. *Physical Chemistry Chemical Physics* **2015**, *17*, (27), 17816-17820.
22. Banerjee, T.; Gottschling, K.; Savasci, G.; Ochsenfeld, C.; Lotsch, B. V., H₂ Evolution with Covalent Organic Framework Photocatalysts. *ACS Energy Letters* **2018**, *3*, (2), 400-409.
23. Konta, R.; Ishii, T.; Kato, H.; Kudo, A., Photocatalytic Activities of Noble Metal Ion Doped SrTiO₃ under Visible Light Irradiation. *The Journal of Physical Chemistry B* **2004**, *108*, (26), 8992-8995.
24. Moniz, S. J. A.; Shevlin, S. A.; Martin, D. J.; Guo, Z.-X.; Tang, J., Visible-light driven heterojunction photocatalysts for water splitting – a critical review. *Energy & Environmental Science* **2015**, *8*, (3), 731-759.
25. Matzek, L. W.; Carter, K. E., Activated persulfate for organic chemical degradation: A review. *Chemosphere* **2016**, *151*, 178-188.
26. Sabio, E. M.; Chi, M.; Browning, N. D.; Osterloh, F. E., Charge Separation in a Niobate Nanosheet Photocatalyst Studied with Photochemical Labeling. *Langmuir* **2010**, *26*, (10), 7254-7261.
27. Li, R.; Han, H.; Zhang, F.; Wang, D.; Li, C., Highly efficient photocatalysts constructed by rational assembly of dual-cocatalysts separately on different facets of BiVO₄. *Energy & Environmental Science* **2014**, *7*, (4), 1369-1376.
28. Li, R.; Zhang, F.; Wang, D.; Yang, J.; Li, M.; Zhu, J.; Zhou, X.; Han, H.; Li, C., Spatial separation of photogenerated electrons and holes among {010} and {110} crystal facets of BiVO₄. *Nat Commun* **2013**, *4*, 1432.
29. Lotsch, B. V., Ein Klassiker im neuen Gewand: Perowskit-Solarzellen. *Angewandte Chemie* **2014**, *126*, (3), 647-649.
30. Kojima, A.; Teshima, K.; Shirai, Y.; Miyasaka, T., Organometal Halide Perovskites as Visible-Light Sensitizers for Photovoltaic Cells. *Journal of the American Chemical Society* **2009**, *131*, (17), 6050-6051.
31. Matsumoto, Y., Energy Positions of Oxide Semiconductors and Photocatalysis with Iron Complex Oxides. *J. Solid State Chem.* **1996**, *126*, (2), 227-234.
32. Varley, J. B.; Schleife, A.; Janotti, A.; Walle, C. G. V. d., Ambipolar doping in SnO. *Appl. Phys. Lett.* **2013**, *103*, (8), 082118.
33. Butler, M. A.; Ginley, D. S., Prediction of Flatband Potentials at Semiconductor-Electrolyte Interfaces from Atomic Electronegativities. *Journal of The Electrochemical Society* **1978**, *125*, (2), 228-232.
34. Kılıç, Ç.; Zunger, A., n-type doping of oxides by hydrogen. *Applied Physics Letters* **2002**, *81*, (1), 73-75.
35. Cardon, F.; Gomes, W. P., On the determination of the flat-band potential of a semiconductor in contact with a metal or an electrolyte from the Mott-Schottky plot. *J. Phys. D: Appl. Phys.* **1978**, *11*, (4), L63-L67.
36. Kalyanasundaram, K.; Grätzel, M., Applications of functionalized transition metal complexes in photonic and optoelectronic devices. *Coordination chemistry reviews* **1998**, *177*, (1), 347-414.
37. Gubbala, S.; Chakrapani, V.; Kumar, V.; Sunkara, M. K., Band-Edge Engineered Hybrid Structures for Dye-Sensitized Solar Cells Based on SnO₂ Nanowires. *Advanced Functional Materials* **2008**, *18*, (16), 2411-2418.

38. Hosogi, Y.; Shimodaira, Y.; Kato, H.; Kobayashi, H.; Kudo, A., Role of Sn²⁺ in the Band Structure of SnM₂O₆ and Sn₂M₂O₇ (M = Nb and Ta) and Their Photocatalytic Properties. *Chem. Mater.* **2008**, *20*, (4), 1299-1307.
39. Stevanović, V.; Lany, S.; Ginley, D. S.; Tumas, W.; Zunger, A., Assessing capability of semiconductors to split water using ionization potentials and electron affinities only. *PCCP* **2014**, *16*, (8), 3706-3714.
40. Butler, K. T.; Crespo-Otero, R.; Buckeridge, J.; Scanlon, D. O.; Bovill, E.; Lidzey, D.; Walsh, A., Band energy control of molybdenum oxide by surface hydration. *Applied Physics Letters* **2015**, *107*, (23), 231605.
41. Park, K.-W.; Kolpak, A. M., Optimal methodology for explicit solvation prediction of band edges of transition metal oxide photocatalysts. *Communications Chemistry* **2019**, *2*, (1), 79.
42. Schmidt, P. Thermodynamische Analyse der Existenzbereiche fester Phasen-Prinzipien der Synthesepaltung in der anorganischen Festkörperchemie. Habilitation, Technische Universität Dresden, Dresden, Dresden.
43. Moses, P. G.; Miao, M.; Yan, Q.; Walle, C. G. V. d., Hybrid functional investigations of band gaps and band alignments for AlN, GaN, InN, and InGaN. *The Journal of Chemical Physics* **2011**, *134*, (8), 084703.
44. Brgoch, J.; Lehner, A. J.; Chabiny, M.; Seshadri, R., Ab Initio Calculations of Band Gaps and Absolute Band Positions of Polymorphs of RbPbI₃ and CsPbI₃: Implications for Main-Group Halide Perovskite Photovoltaics. *The Journal of Physical Chemistry C* **2014**, *118*, (48), 27721-27727.
45. De Waele, S.; Lejaeghere, K.; Sluydts, M.; Cottenier, S., Error estimates for density-functional theory predictions of surface energy and work function. *Physical Review B* **2016**, *94*, (23), 235418.
46. Das, C.; Wussler, M.; Hellmann, T.; Mayer, T.; Jaegermann, W., In situ XPS study of the surface chemistry of MAPI solar cells under operating conditions in vacuum. *Physical Chemistry Chemical Physics* **2018**, *20*, (25), 17180-17187.
47. Zhu, Z.; Sarker, P.; Zhao, C.; Zhou, L.; Grimm, R. L.; Huda, M. N.; Rao, P. M., Photoelectrochemical Properties and Behavior of α -SnWO₄ Photoanodes Synthesized by Hydrothermal Conversion of WO₃ Films. *ACS Applied Materials & Interfaces* **2017**, *9*, (2), 1459-1470.
48. Stranick, M. A.; Moskwa, A., SnO by XPS. *Surface Science Spectra* **1993**, *2*, (1), 45-49.
49. Stranick, M. A.; Moskwa, A., SnO₂ by XPS. *Surf. Sci. Spectra* **1993**, *2*, (1), 50-54.
50. Malherbe, J. B.; Hofmann, S.; Sanz, J. M., Preferential sputtering of oxides: A comparison of model predictions with experimental data. *Applied Surface Science* **1986**, *27*, (3), 355-365.
51. Taglauer, E., Surface cleaning using sputtering. *Applied Physics A* **1990**, *51*, (3), 238-251.
52. Katayama, S.; Hayashi, H.; Kumagai, Y.; Oba, F.; Tanaka, I., Electronic Structure and Defect Chemistry of Tin(II) Complex Oxide SnNb₂O₆. *The Journal of Physical Chemistry C* **2016**, *120*, (18), 9604-9611.
53. Göhler, F.; Hamann, D. M.; Rösch, N.; Wolff, S.; Logan, J. T.; Fischer, R.; Speck, F.; Johnson, D. C.; Seyller, T., Electronic structure of designed [(SnSe)_{1+ δ}]_m[TiSe₂]₂ heterostructure thin films with tunable layering sequence. *J. Mater. Res.* **2019**, *34*, (12), 1965-1975.
54. Minohara, M.; Kikuchi, N.; Yoshida, Y.; Kumigashira, H.; Aiura, Y., Improvement of the hole mobility of SnO epitaxial films grown by pulsed laser deposition. *Journal of Materials Chemistry C* **2019**, *7*, (21), 6332-6336.
55. Aiura, Y.; Ozawa, K.; Hase, I.; Bando, K.; Haga, H.; Kawanaka, H.; Samizo, A.; Kikuchi, N.; Mase, K., Disappearance of Localized Valence Band Maximum of Ternary Tin Oxide with Pyrochlore Structure, Sn₂Nb₂O₇. *The Journal of Physical Chemistry C* **2017**, *121*, (17), 9480-9488.
56. Cruz, L. P.; Savariault, J. M.; Rocha, J.; Jumas, J. C.; Pedrosa de Jesus, J. D., Synthesis and Characterization of Tin Niobates. *J. Solid State Chem.* **2001**, *156*, (2), 349-354.
57. Kikuchi, N.; Samizo, A.; Ikeda, S.; Aiura, Y.; Mibu, K.; Nishio, K., Carrier generation in a p-type oxide semiconductor: Sn₂Nb_{2-x}TaxO₇. *Physical Review Materials* **2017**, *1*, (2), 021601.

58. Mahanty, S.; Roy, S.; Sen, S., Effect of Sn doping on the structural and optical properties of sol-gel TiO₂ thin films. *Journal of Crystal Growth* **2004**, 261, (1), 77-81.
59. Shi, T.; Xie, L.; Gu, L.; Zhu, J., Why Sn doping significantly enhances the dielectric properties of Ba(Ti_{1-x}Sn_x)O₃. *Scientific Reports* **2015**, 5, 8606.
60. Cossement, C.; Darville, J.; Gilles, J.-M.; Nagy, J. B.; Fernandez, C.; Amoureux, J.-P., Chemical shift anisotropy and indirect coupling in SnO₂ and SnO. *Magnetic Resonance in Chemistry* **1992**, 30, (3), 263-270.
61. Chen, J.; Wu, X.-P.; Shen, L.; Li, Y.; Wu, D.; Ding, W.; Gong, X.-Q.; Lin, M.; Peng, L., Identification of different tin species in SnO₂ nanosheets with ¹¹⁹Sn solid-state NMR spectroscopy. *Chemical Physics Letters* **2016**, 643, 126-130.
62. Kemp, T. F. Solid state NMR studies of inorganic pigment materials and catalysts. PhD, University of Warwick, 2008.
63. Ozaki, M.; Katsuki, Y.; Liu, J.; Handa, T.; Nishikubo, R.; Yakumar, S.; Hashikawa, Y.; Murata, Y.; Saito, T.; Shimakawa, Y.; Kanemitsu, Y.; Saeki, A.; Wakamiya, A., Solvent-Coordinated Tin Halide Complexes as Purified Precursors for Tin-Based Perovskites. *ACS Omega* **2017**, 2, (10), 7016-7021.
64. Bräuniger, T.; Ghedia, S.; Jansen, M., Covalent Bonds in α -SnF₂ Monitored by J-Couplings in Solid-State NMR Spectra. *Zeitschrift für anorganische und allgemeine Chemie* **2010**, 636, (13-14), 2399-2404.
65. Sousa, C.; Illas, F., Ionic-covalent transition in titanium oxides. *Physical Review B* **1994**, 50, (19), 13974-13980.
66. Amornsakchai, P.; Apperley, D. C.; Harris, R. K.; Hodgkinson, P.; Waterfield, P. C., Solid-state NMR studies of some tin(II) compounds. *Solid State Nuclear Magnetic Resonance* **2004**, 26, (3), 160-171.
67. Gay, I. D.; Jones, C. H. W.; Sharma, R. D., A multinuclear solid-state NMR study of the dimethyltin chalcogenides [(CH₃)₂SnE]₃, E = S, Se, Te. *Journal of Magnetic Resonance (1969)* **1989**, 84, (3), 501-514.
68. Mundus, C.; Taillades, G.; Pradel, A.; Ribes, M., A ¹¹⁹Sn solid-state nuclear magnetic resonance study of crystalline tin sulphides. *Solid State Nuclear Magnetic Resonance* **1996**, 7, (2), 141-146.
69. Menshchikova, T. V.; Rusinov, I. P.; Golub, P.; Sklyadneva, I. Y.; Heid, R.; Isaeva, A.; Kuznetsov, V. M.; Chulkov, E. V., Two- and one-dimensional quantum spin Hall states in stanene-functionalized GaTe and InTe matrices. *Journal of Materials Chemistry C* **2019**, 7, (26), 7929-7937.
70. Cohen, R. L.; D'Amico, J. F.; West, K. W., Mössbauer Study of Tin(II) Sensitizer Deposits on Kapton. *Journal of The Electrochemical Society* **1971**, 118, (12), 2042-2046.
71. Kim, J. Y.; Byk, T. V.; Cho, S. H.; Noh, C.-H.; Song, K. Y.; Kim, J. M.; Gaevskaya, T. V., Selective Electroless Deposition Using Photoinduced Oxidation of Sn(II) Compounds on Surface-Modified Polyimide Layers. *Electrochemical and Solid-State Letters* **2006**, 9, (12), H118-H122.
72. Wei, X.; Roper, D. K., Tin Sensitization for Electroless Plating Review. *Journal of The Electrochemical Society* **2014**, 161, (5), D235-D242.
73. de Kergommeaux, A.; Faure-Vincent, J.; Pron, A.; de Bettignies, R.; Malaman, B.; Reiss, P., Surface Oxidation of Tin Chalcogenide Nanocrystals Revealed by ¹¹⁹Sn-Mössbauer Spectroscopy. *Journal of the American Chemical Society* **2012**, 134, (28), 11659-11666.
74. Lippens, P. E., Interpretation of the ¹¹⁹Sn Mössbauer isomer shifts in complex tin chalcogenides. *Physical Review B* **1999**, 60, (7), 4576-4586.
75. Avadhut, Y. S.; Weber, J.; Hammarberg, E.; Feldmann, C.; Schellenberg, I.; Pöttgen, R.; Schmedt auf der Günne, J., Study on the Defect Structure of SnO₂:F Nanoparticles by High-Resolution Solid-State NMR. *Chemistry of Materials* **2011**, 23, (6), 1526-1538.
76. Hough, E.; Nicholson, D. G., Stereochemical role of lone pairs in main-group elements. Part 2. Structure and bonding in trichloro(tetramethylthiourea)antimony(III) studied by means of X-ray crystallography and antimony-121 Mössbauer spectroscopy. *Journal of the Chemical Society, Dalton Transactions* **1981**, (10), 2083-2087.

77. Solis, J. L.; Frantti, J.; Lantto, V.; Häggström, L.; Wikner, M., Characterization of phase structures in semiconducting SnWO_4 powders by Mossbauer and Raman spectroscopies. *Physical Review B* **1998**, 57, (21), 13491-13500.
78. Kaiser, M.; Wosylus, A.; Gerke, B.; Pöttgen, R.; Prokeš, K.; Ruck, M.; Doert, T., Crystal Growth and Structure Determination of Pigment Orange 82. *Zeitschrift für anorganische und allgemeine Chemie* **2019**, 0, (0).
79. Körner, W.; Elsässer, C., Density-functional theory study of stability and subgap states of crystalline and amorphous Zn–Sn–O. *Thin Solid Films* **2014**, 555, 81-86.
80. Deringer, V. L.; Zhang, W.; Lumeij, M.; Maintz, S.; Wuttig, M.; Mazzarello, R.; Dronskowski, R., Bonding Nature of Local Structural Motifs in Amorphous GeTe. *Angewandte Chemie International Edition* **2014**, 53, (40), 10817-10820.
81. Küpers, M.; Konze, P. M.; Maintz, S.; Steinberg, S.; Mio, A. M.; Cojocar-Mirédin, O.; Zhu, M.; Müller, M.; Luysberg, M.; Mayer, J.; Wuttig, M.; Dronskowski, R., Unexpected Ge–Ge Contacts in the Two-Dimensional Ge₄Se₃Te Phase and Analysis of Their Chemical Cause with the Density of Energy (DOE) Function. *Angewandte Chemie International Edition* **2017**, 56, (34), 10204-10208.
82. Wuttig, M.; Lüsebrink, D.; Wamwangi, D.; Wełnic, W.; Gilleßen, M.; Dronskowski, R., The role of vacancies and local distortions in the design of new phase-change materials. *Nature Materials* **2006**, 6, 122.
83. Esters, M.; Hennig, R. G.; Johnson, D. C., Insights into the Charge-Transfer Stabilization of Heterostructure Components with Unstable Bulk Analogs. *Chem. Mater.* **2018**, 30, (14), 4738-4747.
84. Biswas, K.; Lany, S.; Zunger, A., The electronic consequences of multivalent elements in inorganic solar absorbers: Multivalency of Sn in Cu₂ZnSnS₄. *Appl. Phys. Lett.* **2010**, 96, (20), 201902.
85. Azuma, M.; Sakai, Y.; Nishikubo, T.; Mizumaki, M.; Watanuki, T.; Mizokawa, T.; Oka, K.; Hojo, H.; Naka, M., Systematic charge distribution changes in Bi- and Pb-3d transition metal perovskites. *Dalton Transactions* **2018**, 47, (5), 1371-1377.
86. Dalpian, G. M.; Liu, Q.; Varignon, J.; Bibes, M.; Zunger, A., Bond disproportionation, charge self-regulation, and ligand holes in ABX_3 and in d^0 -electron ABX_3 perovskites by density functional theory. *Physical Review B* **2018**, 98, (7), 075135.
87. Lee, J.; Kang, Y.; Hwang, C. S.; Han, S.; Lee, S.-C.; Choi, J.-H., Effect of oxygen vacancy on the structural and electronic characteristics of crystalline Zn₂SnO₄. *Journal of Materials Chemistry C* **2014**, 2, (39), 8381-8387.
88. Dalpian, G. M.; Liu, Q.; Stoumpos, C. C.; Douvalis, A. P.; Balasubramanian, M.; Kanatzidis, M. G.; Zunger, A., Changes in charge density vs changes in formal oxidation states: The case of Sn halide perovskites and their ordered vacancy analogues. *Physical Review Materials* **2017**, 1, (2), 025401.
89. Xiao, Z.; Lei, H.; Zhang, X.; Zhou, Y.; Hosono, H.; Kamiya, T., Ligand-Hole in [SnI₆] Unit and Origin of Band Gap in Photovoltaic Perovskite Variant Cs₂SnI₆. *Bulletin of the Chemical Society of Japan* **2015**, 88, (9), 1250-1255.
90. Fabini, D. H.; Koerner, M.; Seshadri, R., Candidate Inorganic Photovoltaic Materials from Electronic Structure-Based Optical Absorption and Charge Transport Proxies. *Chemistry of Materials* **2019**, 31, (5), 1561-1574.
91. Kim, S.; Park, J.-S.; Walsh, A., Identification of Killer Defects in Kesterite Thin-Film Solar Cells. *ACS Energy Letters* **2018**, 3, (2), 496-500.
92. Kim, S.; Park, J.-S.; Hood, Samantha N.; Walsh, A., Lone-pair effect on carrier capture in Cu₂ZnSnS₄ solar cells. *Journal of Materials Chemistry A* **2019**, 7, (6), 2686-2693.
93. Cortecchia, D.; Yin, J.; Bruno, A.; Lo, S.-Z. A.; Gurzadyan, G. G.; Mhaisalkar, S.; Brédas, J.-L.; Soci, C., Polaron self-localization in white-light emitting hybrid perovskites. *Journal of Materials Chemistry C* **2017**, 5, (11), 2771-2780.
94. Robertson, J.; Warren, W. L.; Tuttle, B. A.; Dimos, D.; Smyth, D. M., Shallow Pb³⁺ hole traps in lead zirconate titanate ferroelectrics. *Applied Physics Letters* **1993**, 63, (11), 1519-1521.

95. Greenwood, R.; Kendall, K., Selection of Suitable Dispersants for Aqueous Suspensions of Zirconia and Titania Powders using Acoustophoresis. *Journal of the European Ceramic Society* **1999**, 19, (4), 479-488.
96. TOPAS 6.0, Bruker AXS: 2017.
97. Brand, R. A. *WinNormos for Igor6*, Version for Igor 6.2; Universität Duisburg Germany, 2017.
98. Kresse, G.; Furthmüller, J., Efficient iterative schemes for ab initio total-energy calculations using a plane-wave basis set. *Physical Review B* **1996**, 54, (16), 11169-11186.
99. Kresse, G.; Furthmüller, J., Efficiency of ab-initio total energy calculations for metals and semiconductors using a plane-wave basis set. *Computational Materials Science* **1996**, 6, (1), 15-50.
100. Kresse, G.; Hafner, J., Ab initio molecular dynamics for liquid metals. *Physical Review B* **1993**, 47, (1), 558-561.
101. Kresse, G.; Hafner, J., Ab initio molecular-dynamics simulation of the liquid-metal-amorphous-semiconductor transition in germanium. *Physical Review B* **1994**, 49, (20), 14251-14269.
102. Blöchl, P. E., Projector augmented-wave method. *Physical Review B* **1994**, 50, (24), 17953-17979.
103. Kresse, G.; Joubert, D., From ultrasoft pseudopotentials to the projector augmented-wave method. *Physical Review B* **1999**, 59, (3), 1758-1775.
104. Perdew, J. P.; Burke, K.; Ernzerhof, M., Generalized Gradient Approximation Made Simple. *Physical Review Letters* **1996**, 77, (18), 3865-3868.
105. Monkhorst, H. J.; Pack, J. D., Special points for Brillouin-zone integrations. *Physical Review B* **1976**, 13, (12), 5188-5192.
106. Grimme, S.; Antony, J.; Ehrlich, S.; Krieg, H., A consistent and accurate ab initio parametrization of density functional dispersion correction (DFT-D) for the 94 elements H-Pu. *The Journal of Chemical Physics* **2010**, 132, (15), 154104.
107. Grimme, S.; Ehrlich, S.; Goerigk, L., Effect of the damping function in dispersion corrected density functional theory. *Journal of Computational Chemistry* **2011**, 32, (7), 1456-1465.
108. Van de Walle, C. G.; Martin, R. M., Theoretical calculations of heterojunction discontinuities in the Si/Ge system. *Physical Review B* **1986**, 34, (8), 5621-5634.
109. Sun, W.; Ceder, G., Efficient creation and convergence of surface slabs. *Surface Science* **2013**, 617, 53-59.
110. Ong, S. P.; Richards, W. D.; Jain, A.; Hautier, G.; Kocher, M.; Cholia, S.; Gunter, D.; Chevrier, V. L.; Persson, K. A.; Ceder, G., Python Materials Genomics (pymatgen): A robust, open-source python library for materials analysis. *Computational Materials Science* **2013**, 68, 314-319.
111. Maintz, S.; Deringer, V. L.; Tchougréeff, A. L.; Dronskowski, R., LOBSTER: A tool to extract chemical bonding from plane-wave based DFT. *Journal of Computational Chemistry* **2016**, 37, (11), 1030-1035.
112. Dronskowski, R.; Bloechl, P. E., Crystal orbital Hamilton populations (COHP): energy-resolved visualization of chemical bonding in solids based on density-functional calculations. *The Journal of Physical Chemistry* **1993**, 97, (33), 8617-8624.
113. Becke, A. D.; Edgecombe, K. E., A simple measure of electron localization in atomic and molecular systems. *The Journal of Chemical Physics* **1990**, 92, (9), 5397-5403.
114. Silvi, B.; Savin, A., Classification of chemical bonds based on topological analysis of electron localization functions. *Nature* **1994**, 371, (6499), 683-686.
115. Momma, K.; Izumi, F., VESTA 3 for three-dimensional visualization of crystal, volumetric and morphology data. *Journal of Applied Crystallography* **2011**, 44, (6), 1272-1276.
116. Gajdoš, M.; Hummer, K.; Kresse, G.; Furthmüller, J.; Bechstedt, F., Linear optical properties in the projector-augmented wave methodology. *Physical Review B* **2006**, 73, (4), 045112.

6. Conclusions and Outlook

The synthesis of SnTiO₃ was for the first time made possible by the use of a soft chemistry approach, which enabled the examination of the role of lone pairs with regards to stacking faults and local crystal structure distortions. Two perovskite-type SnTiO₃ polymorphs were computationally predicted as high-pressure modifications. Indeed, the application of high pressure on SnTiO₃ enabled three phase transitions, however, none of them clearly led to the emergence of a perovskite-type structure. Functional analyses revealed visible-light photocatalytic activity for H₂ evolution of SnTiO₃, which is relatively low due to the hampering effect of surface and bulk Sn⁴⁺ as well as direct interlayer Sn-Sn interactions, but correlates well with the very low hole effective masses and a close-to-ideal band gap.

The results of this thesis underline the importance of lone pair materials as model systems to study structure-property-relationships. The challenges posed by lone pairs, such as stacking faults, rendering single-crystal growth challenging and the convolution of bulk and surface effects (such as presence of Sn⁴⁺), necessitate a kaleidoscope of different specialized analysis techniques. Yet, lone pairs open up a variety of opportunities due to their extremely rich structural, electronic and catalytic chemistry. The close examination of SnTiO₃ allowed for deep insight into the exact role of the lone pairs in both electronic and crystallographic structure.

As shown by the synthesis of the novel tin titanate SnTiO₃, new lone pair materials are accessible through low temperature, soft chemistry reactions. If suitable layered potassium compounds of Sn, Zr and possibly Ge are found, the established synthesis route may allow for a further expansion of the phase space of Sn(II) compounds. Similar to mixed valence Sn(II)/Sn(IV) systems which were theoretically studied before, these new compounds potentially offer unique chemistry and application as switchable *n*- to *p*-type semiconductors¹⁻³. Furthermore, the extremely low hole effective masses of < 0.2 *m*_e together with the band gap of ~ 1.8 eV promise potential application as *p*-type transparent conducting oxide, if suitable ways of increasing the band gap will be found.

This work shows that the nature of the interlayer interactions in SnTiO₃ does not allow for real exfoliation, as the direct interlayer Sn-Sn interactions on the order of ~ 25 kJ/mol (as obtained computationally) make SnTiO₃ a material of surprisingly strong 3D character. A feasible way to nevertheless realize thin films might involve low-energy input PLD⁴. Furthermore, the redox chemistry offered by the multivalent Sn, potentially allows for ion intercalation reactions, especially in the light of rich battery literature for tin sulfides⁵. In this context, it is of high

priority to understand how surface SnO₂ grows and if ions trying to intercalate into the bulk are fully blocked by this surface shell.

Understanding the direct interlayer Sn-Sn interactions (DFT Chapter 5) allows for rationalizing the found stacking faults in SnTiO₃ and especially their range (XRPD Chapter 2). As discussed for other chalcogenides⁶, the direct interaction of the cations is possibly of longer range than the van der Waals gaps suggest, transferring the “memory” of a layer to the next nearest layer. Sn lone pairs seem to additionally induce medium-range interactions, which are intermediate between stronger bonding as shown for Ge-Ge⁶, and weaker van der Waals gaps as found in BiI₃⁷. Potentially, other 2D lone pair systems have similar types of stacking faults showing an extended range in contrast to more random antiphase boundaries.

Moreover, SnTiO₃ can be thought of as a pseudobinary phase of SnO and TiO₂ and as such as part of the pseudobinary row from (SnTe)_x(TiTe₂)_y (not realized yet), (SnSe)_x(TiSe₂)_y⁸⁻⁹ and (SnS)_x(TiS₂)_y¹⁰ epitaxially grown heterostructures (with x and y = 1). Sn(II) chalcogenides are isovalent to group 15 elements, which have long been shown to obtain Peierls-distorted structures (A7-structure type of As, Sb and Bi), and are proposed as examples for metavalent (sub-stoichiometric metallic) bonding¹¹⁻¹³. For obvious reasons, direct conclusions from simple correlation need to be taken with care and the exact interactions will need to be studied in more detail for the case of SnTiO₃. Especially, as the TiO₂ sublayer in SnTiO₃ has cation “vacancies” due to shared oxygen with Sn. No such shared anions are found in the before mentioned epitaxially grown heterostructures of selenides and sulfides, which are forming structures deduced from the α -Po-type or NaCl-type. Still, thinking of SnTiO₃ as part of this row of heterostructures, allows for a new direction to study these binary heterolayers. Heterostructures of the shown type are usually discussed in the context of thermoelectrics and high- κ dielectrics. The latter has also been theoretically considered for SnTiO₃ in this work (Chapter 3). Consideration of SnTiO₃ as a pseudobinary heterostructure, make it an interesting candidate for realizing real bulk properties in solids by rational design.

Regarding the use of SnTiO₃ in photocatalysis, the advantages initially expected regarding light absorption as well as charge transport and separation are outweighed by disadvantages regarding defect formation and surface instability. Especially, the intrinsic instability of Sn²⁺ lone pairs suggests that internal heterojunctions may remain feasible in principle, but only by using more stable lone pair compounds. If, however, it is possible to stabilize the lone pair state, by for example charge transfer from a substrate¹⁴, SnTiO₃ remains a viable candidate for hole transport, if not catalysis of oxidation half-reactions in general. One of the most important next steps for the improvement of this material is to understand the “on-site” vacancy/defect

chemistry, which will require detailed calculation of charged defects and their delicate equilibria in different synthesis and application environments.

The Sn^{2+} lone pairs induce distortions of TiO_6 -octahedra (NMR/EELS Chapter 2), which is fully in line with the picture of classical ferroelectrics. However, the neighboring octahedra's dipole moments cancel each other out (SHG in Chapter 4). As SnTiO_3 does not form a heterostructure in the sense of $(\text{SnSe})_x(\text{TiSe}_2)_y$ ⁸⁻⁹, the anion is highly important for the formation of the lone pair and hence the local distortions. We thus conclude that the emphasis on the lone pair constituting A-site cation is decisive for realization of ferroelectricity¹⁵⁻¹⁷.

High-pressure experiments (Chapter 4) have expanded the phase space around ilmenite-type derived SnTiO_3 . Strong compression of the ultra-soft oxide SnTiO_3 (XRPD Chapter 4) further supports the presence of Sn-Sn interactions and their influence on the stacking sequence. However, also perovskite-like SnTiO_3 phases may be realized after creation (and examination) of the pressure- and temperature-dependent phase diagram, yet being so much distorted that no ferroelectricity (soft phonons Chapter 3) is expected. The study of the high-pressure phase transitions and phonon behavior again supports the strong influence of A-site cations on the rattling behavior of octahedrally coordinated Ti^{4+} in ferroelectrics.

Taken together, the identified structure-property-relationships of SnTiO_3 position it as a link between the world of 2D transition metal chalcogenides and the world of 3D perovskite solid state chemistry and is as such unique. This work fundamentally improves our understanding of lone pair electrons in solids and therefore promises further revelation of structure-property-relationships and interesting applications thereof.

References

1. Varley, J. B.; Schleife, A.; Janotti, A.; Walle, C. G. V. d., Ambipolar doping in SnO. *Appl. Phys. Lett.* **2013**, *103* (8), 082118.
2. Saji, K. J.; Tian, K.; Snure, M.; Tiwari, A., 2D Tin Monoxide—An Unexplored p-Type van der Waals Semiconductor: Material Characteristics and Field Effect Transistors. *Advanced Electronic Materials* **2016**, *2* (4), 1500453.
3. Ogo, Y.; Hiramatsu, H.; Nomura, K.; Yanagi, H.; Kamiya, T.; Hirano, M.; Hosono, H., p-channel thin-film transistor using p-type oxide semiconductor, SnO. *Appl. Phys. Lett.* **2008**, *93* (3), 032113.
4. Fischer, D.; von Mankowski, A.; Ranft, A.; Vasa, S. K.; Linser, R.; Mannhart, J.; Lotsch, B. V., ZIF-8 Films Prepared by Femtosecond Pulsed-Laser Deposition. *Chem. Mater.* **2017**, *29* (12), 5148-5155.
5. Li, Z.; Ding, J.; Mitlin, D., Tin and Tin Compounds for Sodium Ion Battery Anodes: Phase Transformations and Performance. *Acc. Chem. Res.* **2015**, *48* (6), 1657-1665.
6. Mio, A. M.; Konze, P. M.; Meledin, A.; Küpers, M.; Pohlmann, M.; Kaminski, M.; Dronskowski, R.; Mayer, J.; Wuttig, M., Impact of Bonding on the Stacking Defects in Layered Chalcogenides. *Adv. Funct. Mater.* **2019**, *29* (37), 1902332.
7. Ruck, M., Darstellung und Kristallstruktur von fehlordnungsfreiem Bismuttriodid. In *Zeitschrift für Kristallographie - Crystalline Materials*, 1995; Vol. 210, p 650.
8. Esters, M.; Alemayehu, M. B.; Jones, Z.; Nguyen, N. T.; Anderson, M. D.; Grosse, C.; Fischer, S. F.; Johnson, D. C., Synthesis of Inorganic Structural Isomers By Diffusion-Constrained Self-Assembly of Designed Precursors: A Novel Type of Isomerism. *Angew. Chem. Int. Ed.* **2015**, *54* (4), 1130-1134.
9. Hamann, D. M.; Merrill, D. R.; Bauers, S. R.; Mitchson, G.; Ditto, J.; Rudin, S. P.; Johnson, D. C., Long-Range Order in [(SnSe)_{1.2}][TiSe₂]₁ Prepared from Designed Precursors. *Inorg. Chem.* **2017**, *56* (6), 3499-3505.
10. Wan, C.; Wang, Y.; Wang, N.; Koumoto, K., Low-Thermal-Conductivity (MS)_{1+x}(TiS₂)₂ (M = Pb, Bi, Sn) Misfit Layer Compounds for Bulk Thermoelectric Materials. *Materials* **2010**, *3* (4), 2606-2617.
11. Deringer, V. L.; Dronskowski, R.; Wuttig, M., Microscopic Complexity in Phase-Change Materials and its Role for Applications. *Adv. Funct. Mater.* **2015**, *25* (40), 6343-6359.
12. Wuttig, M.; Deringer, V. L.; Gonze, X.; Bichara, C.; Raty, J.-Y., Incipient Metals: Functional Materials with a Unique Bonding Mechanism. *Adv. Mater.* **2018**, *30* (51), 1803777.
13. Yu, Y.; Cagnoni, M.; Cojocar-Mirédin, O.; Wuttig, M., Chalcogenide Thermoelectrics Empowered by an Unconventional Bonding Mechanism. *Adv. Funct. Mater.* **2019**, *0* (0), 1904862.
14. Esters, M.; Hennig, R. G.; Johnson, D. C., Insights into the Charge-Transfer Stabilization of Heterostructure Components with Unstable Bulk Analogs. *Chem. Mater.* **2018**, *30* (14), 4738-4747.
15. Navrotsky, A., Energetics and Crystal Chemical Systematics among Ilmenite, Lithium Niobate, and Perovskite Structures. *Chem. Mater.* **1998**, *10* (10), 2787-2793.
16. Benedek, N. A.; Fennie, C. J., Why Are There So Few Perovskite Ferroelectrics? *The Journal of Physical Chemistry C* **2013**, *117* (26), 13339-13349.
17. Schütz, D.; Deluca, M.; Krauss, W.; Feteira, A.; Jackson, T.; Reichmann, K., Lone-Pair-Induced Covalency as the Cause of Temperature- and Field-Induced Instabilities in Bismuth Sodium Titanate. *Adv. Funct. Mater.* **2012**, *22* (11), 2285-2294.

A: Supporting Information for Structure-Directing Lone Pairs: Synthesis and Structural Characterization of SnTiO₃

Leo Diehl, Sebastian Bette, Florian Pielnhofner, Sophia Betzler, Igor Moudrakovski, Geoffrey A. Ozin, Robert Dinnebier and Bettina V. Lotsch.

Published in: *Chem. Mater.* **2018**, *30* (24), 8932-8938.

DOI: 10.1021/acs.chemmater.8b04261

Formatting and number of figures were changed.

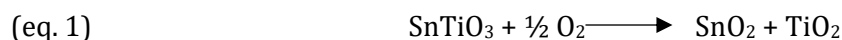
Adapted with permission from The American Chemical Society.

A.1 Synthesis

First, K₂CO₃ (BerndKraft GmbH > 98%) and P25 (TiO₂) (Aldrich ≥ 99.5 %) were thoroughly ground and then reacted at 600 °C for 12 hours to form a potassium titanate precursor. Subsequently, the precursor was ground together with SnCl₂ · 2 H₂O (Sigma-Aldrich > 98% / Grüssing GmbH 99.5 %) until a lemon yellow powder formed. This powder was transferred into an ampoule and dehydrated in two steps: 2.5 hours at 130 °C and then another 2.5 hours at 200 °C under dynamic vacuum. Eventually, the powder was tempered at 300 °C for 24 hours under static vacuum until SnTiO₃ formed. For removal of KCl the obtained red SnTiO₃ powder was washed twice with H₂O and once with Ethanol.

Synthesis of the corresponding titanates (Pb, Fe, Mg, Zn and Cd) was carried out using similar steps and a reaction temperature of 600 °C. Only SrTiO₃ was synthesized directly from a reaction of TiO₂ and SrCO₃ at 800 °C.

The obtained stoichiometry of the red SnTiO₃ was confirmed by ICP-AES analysis (Tab. S A.1). The oxidation state +II of Sn was indirectly proven by oxidation of SnTiO₃ in air according to eq. (1)



, observed by TGA analysis. The obtained weight increase of ≈ 5 wt% is in decent accordance with a theoretical value of ≈ 7 wt%. The small deviation can be explained by partially preoxidized surface species.

A.2 ICP-AES

For elemental analysis a VARIAN VISTA RL CCD Simultaneous ICP-AES was used.

Table S A.1. Elemental analysis by ICP-AES of different washed batches of SnTiO_3 . Obtained values are converted to mmol by dividing by the corresponding atomic mass.

	K (mmol)	Sn (mmol)	Ti (mmol)
SnTiO₃ - I		4.54	4.20
SnTiO₃ - II		2.54	2.70
SnTiO₃ - III	0.04	4.36	4.31
	0.04	3.81	3.74

A.3 TGA

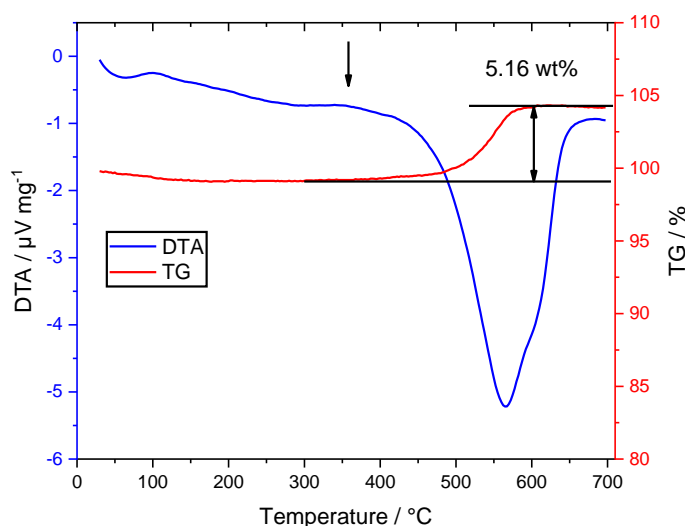


Figure S A.1. TGA measurement of SnTiO_3 in air, showing the weight increase due to oxidation of Sn^{2+} at about 350 °C as indicated by a black arrow.

A.4 TEM

The samples were prepared from a sonicated mixture of the powder sample with pure ethanol. This mixture was drop cast onto a copper grid with a holey carbon film. Low-loss EELS acquisition and C_s corrected STEM images were acquired with a FEI TitanThemis 60-300 equipped with an aberration-corrector for the probe-forming lens system, a high brightness field emission (XFEG™) source, a monochromator and a high-resolution electron-energy loss spectrometer (Gatan 966 GIF) operated at 300 kV.

EELS data were acquired in monochromated STEM spot mode featuring an energy resolution of 0.2 eV. A dispersion of 0.1 eV was used for the spectrum acquisition. Subpixel-scanning and short acquisition times were used to avoid electron beam induced damage of the sample.

A.5 XRPD

A Stoe STADI P diffractometer (Mo $K_{\alpha 1}$ radiation, Ge(111) monochromator, Mythen detector) was used for powder diffraction measurements in Debye-Scherrer geometry. The program package TOPAS 6.0 was for structure refinement.

A.6 Crystal structure details

Table S A.2. Refined atomic coordinates of a layer in the crystal structure of SnTiO₃ at ambient conditions.

site	occ	x ^a	y ^a	z ^{a,b}	site	occ	x ^a	y ^a	z ^{a,b}
Ti(1)	1	0	0	0.0014(26)	Ti(2)	1	$\frac{2}{3}$	$\frac{1}{3}$	-0.010(28)
Sn(1)	1	$\frac{1}{3}$	$\frac{2}{3}$	-0.320(2)	Sn(2)	1	$\frac{1}{3}$	$\frac{2}{3}$	0.322(2)
O(1a)	1	$\frac{1}{3}$	0	0.160(12)	O(2a)	1	$\frac{1}{3}$	$\frac{1}{3}$	-0.140(10)
O(1b)	1	0	$\frac{1}{3}$	0.160(12)	O(2b)	1	$\frac{2}{3}$	0	-0.140(10)
O(1c)	1	$\frac{2}{3}$	$\frac{2}{3}$	0.160(12)	O(2c)	1	0	$\frac{2}{3}$	-0.140(10)

^a For creation of stacking types, the layers have to be added by using the stacking vectors given in eq. 2.

^b The z-coordinates are given for a unit cell containing one layer, i.e. $c = 6.8961(3)$ Å. For the creation of different stacking patterns, they must be divided by the total number of layers in the cell.

In all five crystal structures the layers are described by two tin sites, two titanium sites and six oxygen sites from which three are positioned at the top and three at the bottom site of the layers. The coordinates were refined in real space, in order to keep an identical layer constitution within one polytype and throughout all polytypes. In addition, the z-coordinates for the three oxygen sites at the top and the three oxygen sites at the bottom site of the layers were constrained, as well. The only parameters that were refined for each polytype individually were the scale factors to account for the different relative frequencies of the stacking patterns and the crystallite size parameters to account for different expansions of the coherently scattering domains.

Table S A.3. Atomic distances in SnTiO₃ at ambient conditions.

Atoms	Distance/ Å	Atoms	Distance/ Å
Ti(1)-O(1)	1.99(9) x3	Sn(1)-O(1)	2.10(4) x3
Ti(1)-O(2)	1.98(10) x3	Sn(1)-O(2)	3.97(8) x3
Ti(2)-O(1)	1.92(10) x3	Sn(2)-O(1)	2.03(5) x3
Ti(2)-O(2)	2.05(11) x3	Sn(2)-O(2)	4.08(6) x3

A.7 Structural derivation of possible stacking faults

The stacking order of the layers in SnTiO₃ is determined by the positions of the Sn²⁺ ions, in particular by their electron lone pairs. Due to the repulsive interaction between an electron lone pair and a negatively charged O²⁻ ion, a stacking order appears to be energetically favorable that provides a maximization of the distances between electron lone pairs and oxide ions of adjacent

layers. Hence, one of the Ti^{4+} -ions of layer $i+1$ must be situated exactly above the Sn^{2+} -site of the preceding layer i . According to the honeycomb structural motif (Figure 2.2a) six stacking vectors are theoretically possible, but due to the trigonal symmetry of the honeycomb only two of them are non-symmetry-equivalent: stacking in $\frac{2}{3}x$ - and $\frac{1}{3}y$ -direction, **S1**, and stacking in reverse direction: $\frac{1}{3}x$ and $\frac{2}{3}y$, **S2** (eq. 2).

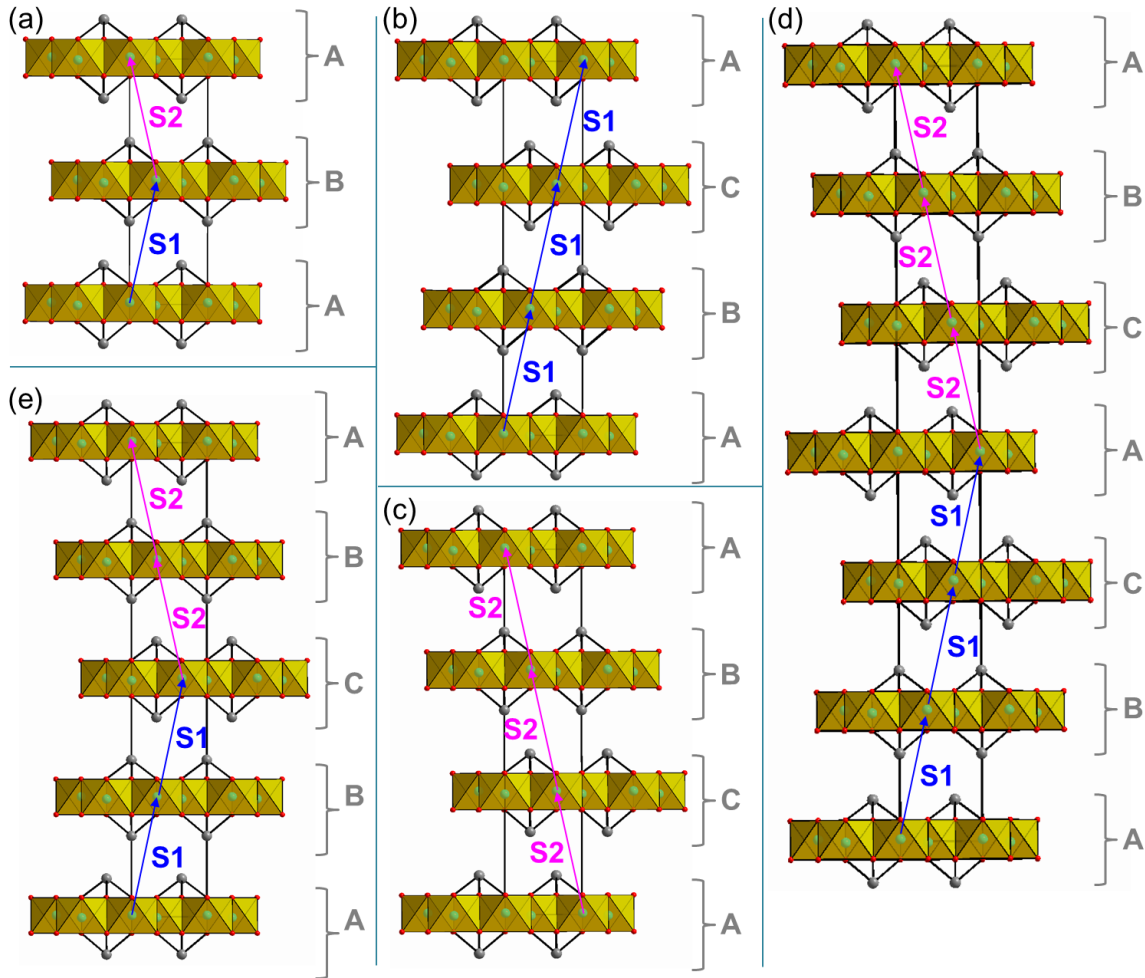


Figure S A.2. Hypothetical stacking orders in the crystal structure of SnTiO_3 with the basic stacking types ABAB (a), ABC (b), ACB (c) and twinning with different ranges: ABCB (e) and ABCACB (d).

Taking the two possible stacking vectors into account, several basic stacking orders can emerge (Figure S A.2). An arrangement of the stacking vectors **S1** and **S2** in an alternating fashion leads to an ABAB-like stacking order (Figure S A.2a), whereas stacking by only **S1** or **S2** leads to an ABC- (Figure S A.2b) and ACB-type (Figure S A.2c) stacking order. The transition from stacking vector **S1** to **S2** can also be regarded as a 120° twin along the c -axis. If twinning has a certain *range*, more basic stacking types can be derived, such as the ABCB-type, which refers to a *range* of 1 layer (Figure S 2d) or the ABCACB-type referring to a *range* of 2 layers (Figure S A.2e).

A.8 DIFFaX-Simulations (Experimental)

XRPD pattern of stacking faulted SnTiO₃ were simulated by using the *DIFFaX*-routine¹ in recursive mode. For the simulation the refined layer constitution was used. The peak profiles were simulated using Pseudo-Voigt functions. With respect to the layer constitution only two stacking vectors are feasible:

$$(eq. 2) \quad \mathbf{S1} = \begin{pmatrix} 2/3 \\ 1/3 \\ 1/N \end{pmatrix} \quad \mathbf{S2} = \begin{pmatrix} 1/3 \\ 2/3 \\ 1/N \end{pmatrix}$$

with N being the total number of layers in the unit cell.

Various faulting models using different combinations of the stacking vectors **S1** and **S2** were simulated. Crystallographic intergrowth between ABC-type (stacking vector: **S1**), ACB-type (stacking vector: **S2**) and AB-type stacking (stacking vector: **S1** and **S2** in alternating fashion) was simulated by using a 4 x 4 transition probability matrix (Table S A.4) with variable parameters, x and y, for the extension of the coherently stacked sections.

Table S A.4. Transition probability matrix with associated stacking vectors (eq. 2) for the simulation of crystallographical intergrowth among ABC-, AB- and ACB. The extension of the AB-stacked section is described by the parameter x and the transitions among ABC/ACB-type and AB-type stacked section is described by the parameter y.

Transition From ↓/ to →	ABC-type	AB-type		ACB-type
		layer 2n	layer 2n+1	
ABC-type	vector: S1 probability: 1-y	vector: S2 probability: y	vector: S1 probability: 0	vector: S2 probability: 0
AB-type layer 2n	vector: S1 probability: x	vector: S2 probability: 0	vector: S1 probability: 1-x	vector: S2 probability: 0
AB-type layer 2n+1	vector: S1 probability: 0	vector: S2 probability: 1-x	vector: S1 probability: 0	vector: S2 probability: x
ACB-type	vector: S1 probability: 0	vector: S2 probability: 0	vector: S1 probability: y	vector: S2 probability: 1-y

Additional simulations were also carried out in which each transition from **S1**- to **S2**-stacking was considered as a fault that may obtain a certain *range*, in such a way that after the occurrence of a fault a minimum number of layers must be faultless. This was realized by $2i \times 2i$ transition probability matrixes (Table S A.5) in which $i-1$ is the range of a fault and the variable parameter s (*sharpness*) being the probability of an additional fault after the minimum faulting range.

In each case a cohort of simulations was carried out in which only one parameter was varied systematically.

Table S A.5. Transition probability matrix with associated stacking vectors (eq. 2) for the simulation of faults that obtain a certain range ($i-1$). The *sharpness* of the range is described by the parameter s .

Transition From ↓/ to →		ABC-type		Fault		ACB-type	
		Layer1	...	Layer i	Layer1	...	Layer i
ABC-type	Layer1	vector: S1	vector: S1	vector: S1	vector: S2	vector: S2	vector: S2
		prob.: 0	prob.: 1	prob.: 0	prob.: 0	prob.: 0	prob.: 0
	...	vector: S1	vector: S1	vector: S1	vector: S2	vector: S2	vector: S2
Fault	Layer i	prob.: 0	prob.: 0	prob.: 1	prob.: 0	prob.: 0	prob.: 0
		vector: S1	vector: S1	vector: S1	vector: S2	vector: S2	vector: S2
	Layer1	prob.: 0	prob.: 0	prob.: 1-s	prob.: s	prob.: 0	prob.: 0
ACB-type		vector: S1	vector: S1	vector: S1	vector: S2	vector: S2	vector: S2
	...	prob.: 0	prob.: 0	prob.: 0	prob.: 0	prob.: 1	prob.: 0
		vector: S1	vector: S1	vector: S1	vector: S2	vector: S2	vector: S2
	Layer i	prob.: 0	prob.: 0	prob.: 0	prob.: 0	prob.: 0	prob.: 1
		vector: S1	vector: S1	vector: S1	vector: S2	vector: S2	vector: S2
	prob.: s	prob.: 0	prob.: 0	prob.: 0	prob.: 0	prob.: 1-s	

A.9 DIFFaX-Simulations (Results)

Consequently, crystallographic intergrowth of ABC-/ACB- and AB-type stacked sections was simulated (Figure A.3b). The increase of the size of the AB-type stacked domains leads to a slight broadening of several reflections, i.e. 101, 104, 015 (for pure ABC-/ACB-type stacking). At a certain expansion of the AB-type stacked domains (Figure A.3b deep blue pattern, $x = 0.20$) additional reflections appear that sharpen during further increase of the domains. These additional reflections lead to the appearance of the characteristic reflection triplets at $\approx 9, 12-14, 20-21$ and $26-27^\circ 2\theta$. The reflections in the measured pattern (Figure A.3 blue line) that are associated with the 012 and 014 reflections of AB-type stacking (Figure A.3, green pattern) are broad and have little intensity, which suggests a small extension of the AB-type stacked domain. This is in contrast to the peaks associated with the 103, 023 and 213 reflection of AB-type stacking (Figure A.3, green pattern), which are sharp and have a high intensity suggesting a large expansion of these domains. In consequence the simple microstructural model containing AB-type stacking with a large coherently scattering domain size is not entirely correct.

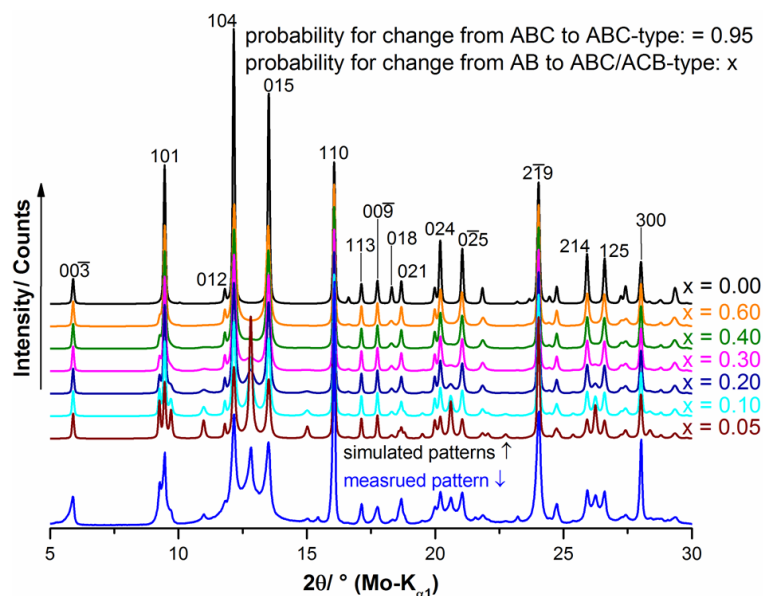


Figure S A.3. Comparison of simulated XRPD patterns of stacking faulted SnTiO_3 that exhibits crystallographic intergrowth of ABC-/ACB-stacked sections with AB-type stacked sections with the measured pattern. For the simulations the extension of the ABC-/ACB-stacked domains was kept constant and the extension of the AB-type stacked sections was gradually increased.

If each transition of the stacking vector from **S1** to **S2** and vice versa is considered as a fault in terms of twinning, each twinning domain may have a certain expansion. In consequence, each fault has a certain *range*. Various simulations of twinning using different *ranges* were carried out (Figure S A.4). When the *range* is set to 0, twinning occurs purely statistically, accordingly an increasing fault probability leads to vast reflection broadening (Figure S A.4a). A further increase of the fault probability finally leads to transformation of the ABC/ACB-type XRPD pattern into an AB-type pattern. By increasing the *range*, the peak broadening due to an increase in fault probability is less pronounced (Figure S A.4b-d). Also the characteristic peak triplets at $\approx 9, 12-14, 20-21$ and $26-27^\circ 2\theta$ occur in the simulated patterns. The greatest similarity between measured and simulated XRPD pattern is achieved by a range of 2 (Figure S A.4c, red pattern).

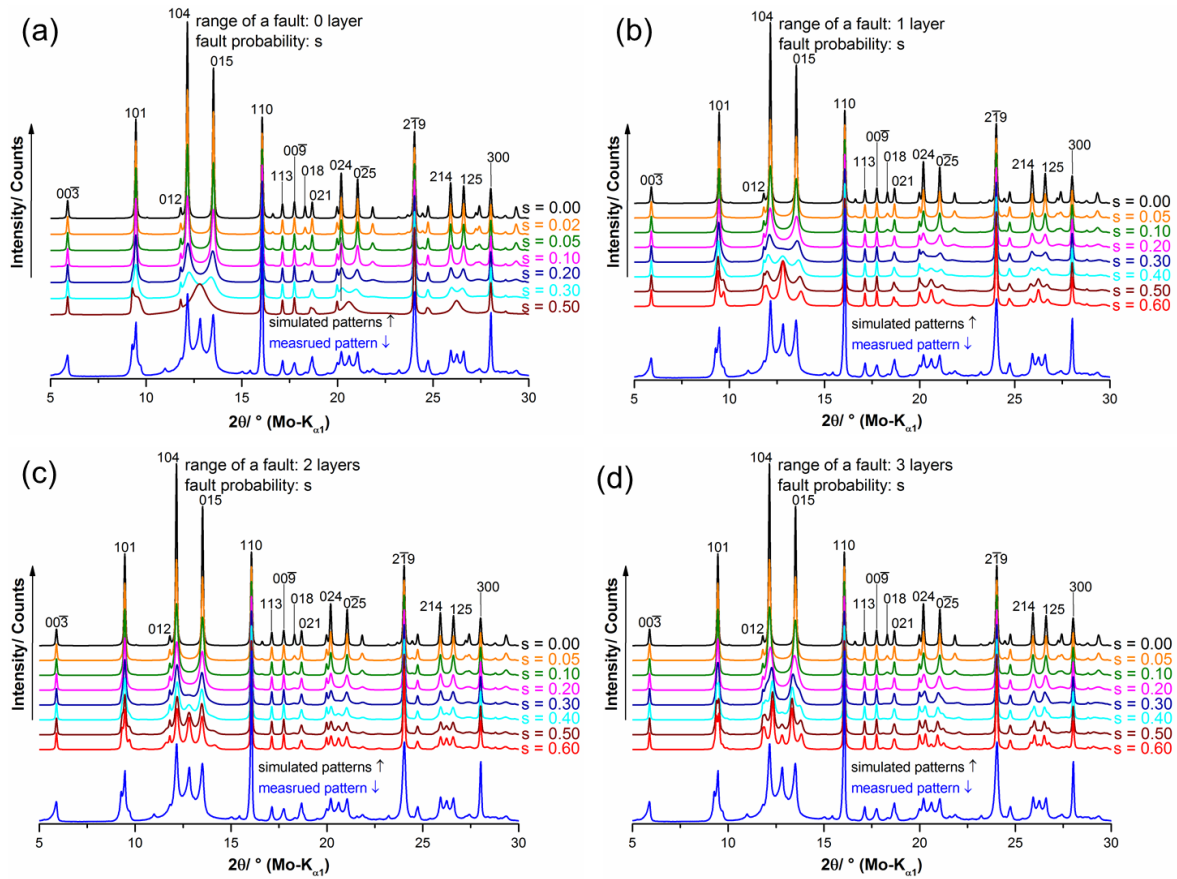


Figure S A.4. Comparison of simulated XRPD patterns of stacking faulted SnTiO_3 that exhibits 120° twinning along the c -axis with the measured pattern. For the simulations the fault probability, the sharpness of the range was gradually increased. Ranges of 0 (a), 1 (b), 2 (c) and 3 (d) layers were applied.

In summary, the presented *DIFFaX* simulations show that coherently scattering domains in which the layers are stacked in an ABC-/ACB- and AB-type pattern, as well as twinning domains of substantial extent are apparent in the microstructure of SnTiO_3 .

A.10 Microstructure Description by a Multiphase Approach

As the *DIFFaX* simulations suggest the presence of several coherently scattering domains, showing a homogeneous stacking order, the microstructure of the sample can be described by superposition of several phases. Hence, in a Rietveld-refinement (Figure S A.5) the measured XRPD pattern was refined by using separate phases of SnTiO_3 , each representing a different stacking order. An identical layer constitution for each phase is used. The only parameters that were refined individually were crystalline size parameters for describing the expansion of coherently scattering domains. In the Rietveld-refinement besides SnTiO_3 phases for describing the basic stacking orders ABC, ACB and AB, also two phases describing twinning domains, ABCB

and ABCACB are used. In addition, the crystal structures of SnO_2 and $\text{K}_2\text{Ti}_8\text{O}_{17}$ were included as impurity phases.

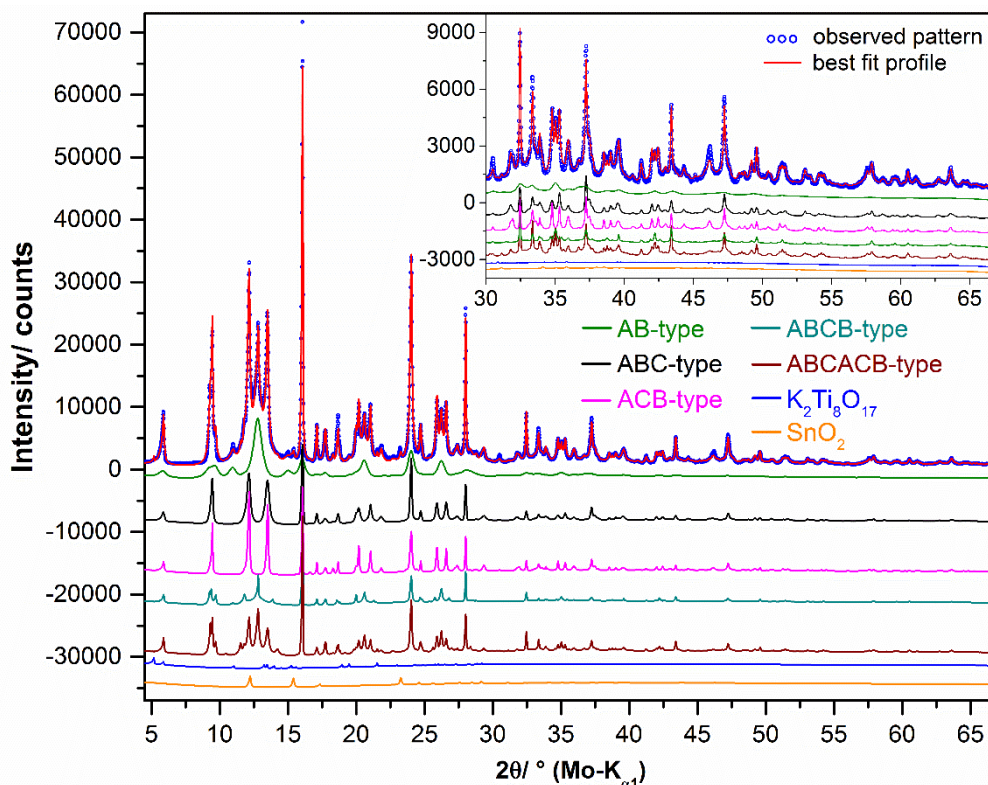


Figure S A.5. Final Rietveld refinement of the measured XRPD pattern of SnTiO_3 by using a multiphase approach that includes five polytypes of SnTiO_3 representing the different basic stacking types and twinning domains (Figure S A.2, with all having an identical layer constitution. SnO_2 and $\text{K}_2\text{Ti}_8\text{O}_{17}$ were included as impurity phases, as well. The section starting at $30^\circ 2\theta$ is enlarged for clarity (insert). The calculated pattern (red line) is decomposed into the contributions of each phase (coloured line, below).

The crystalline size, i.e. the expansion of the AB-type stacked coherently scattering domain was refined to a low value. Therefore, decomposition of the calculated pattern (Figure S A.5, red line) into the single components exhibits broad reflections for the AB-type stacked SnTiO_3 phase (green line). This is in accordance with the systematic *DIFFaX* study. The other SnTiO_3 polytypes exhibit rather sharp reflections indicating a larger expansion of the associated coherently scattering domains. In summary the calculated patterns of all SnTiO_3 polytypes that were considered obtain substantial intensities, which means each of the stacking orders is present to a significant amount in the microstructure. The contribution of the impurity phases to the measured pattern (Figure 2.5, blue and orange line) is almost negligible (calculated content of SnO_2 : 1.3(1) wt%, $\text{K}_2\text{Ti}_8\text{O}_{17}$: 3.1(1) wt%).

A.11 EELS

Ti-L_{2,3} edge**Table S A.6.** Ti-L_{2,3} edge peak positions and crystal field splitting (CFS) with corresponding ESDs.

	Ti L _{2,3} edge Peakpositions [eV]				CFS $\Delta(AB)$ [eV]	CFS $\Delta(CD)$ [eV]
	A	B	C	D	$\Delta(e_g-t_{2g})$	$\Delta(e_g-t_{2g})$
SnTiO₃	457.50(13)	459.92(12)	462.93(19)	465.20(13)	2.42(2)	2.27(8)
CdTiO₃	457.65(8)	459.75(4)	463.07(8)	465.04(4)	2.10(6)	1.97(3)
FeTiO₃	457.70(4)	459.89(6)	463.11(9)	465.18(5)	2.19(1)	2.06(2)
SrTiO₃	457.53(3)	459.85(3)	462.89(4)	465.25(3)	2.32(1)	2.36(3)
PbTiO₃	457.64(9)	459.58(9)	463.06(8)	464.98(9)	1.93(4)	1.91(2)

A power-law fit was used for background subtraction of the edges. In the case of CdTiO₃, the Cd-M_{4,5} edge overlaps with the onset of the Ti-L_{2,3} edge. For better representation in the manuscript its tail was removed from the Ti-L_{2,3} edge.

O-K edge**Table S A.7.** O-K edge peak positions and crystal field splitting (CFS) with corresponding ESDs.

	O-K edge Peak positions [eV]		CFS $\Delta(AB)$ [eV]
	A	B	$\Delta(e_g-t_{2g})$
SnTiO₃	530.66(2)	533.24(15)	2.58(16)
CdTiO₃	530.82(3)	532.97(12)	2.15(10)
FeTiO₃	530.51(5)	533.10(7)	2.59(4)
SrTiO₃	530.24(4)	532.75(4)	2.51(6)
PbTiO₃	528.78(16)	531.31(21)	2.54(8)

In contrast to the observations made for the Titanium L_{2,3}-edge, (Figure 2.4) the CFS in the O-K edge is largely independent of distortions and all obtained values are within ESDs. The signature for SrTiO₃ is significantly different from all other samples. Again, this can be explained by different hybridizations and interrelated transition probabilities. The higher energy peaks above ~535 eV have been assigned to hybridized states of O_{2p} with the respective A-site cations² and hence show the biggest differences in both position and intensity.

The O-K edge of SnTiO₃ is overlapping with the Sn-M_{4,5} edge. The background was removed for the energy region close to the onset of the Sn-M_{4,5} edge.

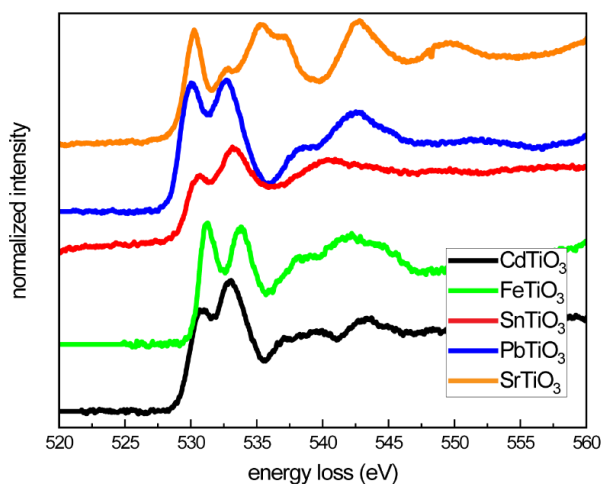


Figure S A.6. O K-edge of different ilmenite-type and perovskite-type structures.

A.12 Solid-State NMR Spectroscopy

$^{47,49}\text{Ti}$ solid-state NMR spectra were obtained at a Larmor frequency of 50.73 MHz on a Bruker Avance II - 900 instrument (magnetic field 21.1T). A Bruker 4mm low- γ MAS probe and Bruker 7mm single-channel MAS probe have been used. External referencing in $^{47,49}\text{Ti}$ spectra was accomplished with a [1M] solution of TiCl_4 in CCl_4 (high frequency signal from ^{49}Ti set to 0ppm) and using solid SrTiO_3 as a secondary reference. A non-selective $\pi/2$ pulse was calibrated on ^{49}Ti in the liquid reference sample. FIDs were collected using Solid-Echo ($\pi/2-\tau-\pi/2-\tau-\text{acq}$)³ and QCPMG ($\pi/2-\tau_1-(-\tau_2-\pi-\tau_3-\text{acq})_n$)⁴ pulse programs. Recycle delays ranged from 1s to 6s depending on the sample and complete relaxation of the signals was tested individually for each sample. Between 2000 and 20000 scans were acquired depending on the sample. Most of the spectra were acquired in a single frequency offset, while on the broadest spectra in MgTiO_3 and ZnTiO_3 three spectral offsets by 100 kHz were required to completely cover the desired spectral region.

Spectral simulations

Analytical simulations of experimental spectra were carried out with the DMFit⁵ and QUEST⁶ simulation packages. Where available, we first fitted the MAS spectra, which provided the isotropic chemical shifts δ_{iso} , quadrupolar constants C_Q and quadrupolar asymmetry parameter η_Q . These parameters were subsequently used in simulations of the static powder pattern to obtain span Ω and skew k , with the Euler angles are commonly set to those obtained from the quantum chemical calculations (below). Special attention was given to reproducing the spectral discontinuities – and shoulders in simulated spectra.

Quantum Chemical Calculations - NMR

Calculations of $^{47,49}\text{Ti}$ electric field gradient and nuclear magnetic shielding tensors in model titanates were accomplished using the available crystallographic data (Table S A.2). Plane wave-based Density Functional Theory calculations were performed using the NMR module of the

CASTEP DFT code that employs the Gauge Including Projector Augmented Wave (GIPAW) algorithm⁷ and is a part of Biovia Materials Studio simulation and modelling package (Version 2017).⁸ This method is specifically designed for extended lattice structures of crystalline materials. The Perdew-Burke-Ernzerhof (PBE) functional was used with the Generalized Gradient Approximation (GGA) for all calculations.⁹⁻¹⁰ The geometry optimization was performed using PBE functional with the convergence tolerance parameters set as follows: Energy: 10^{-5} eV/atom, Maximum force: 0.03 eV/Å, Maximum stress: 0.05 GPa, Maximum displacement: 10^{-3} Å. The Euler angles relating the EFG tensor PAS to the CSA tensor PAS (α , β , γ) were extracted using the program EFG-Shield.¹¹

Experimental and computational results for crystalline titanates of known structure and the studied SnTiO_3 are summarized in Table S A.8 and Figure S A.8.

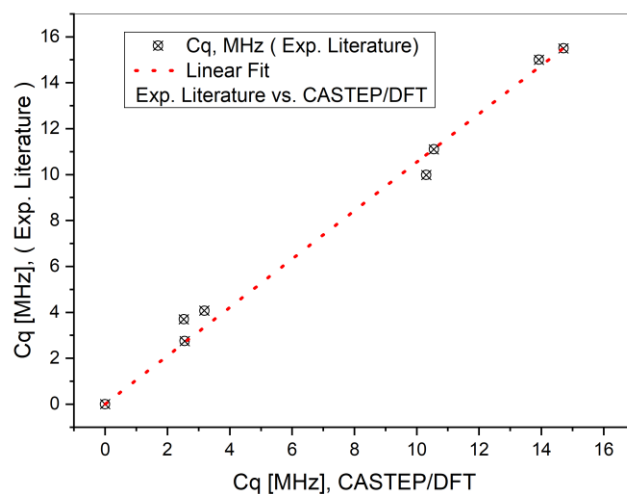


Figure S A.7. Correlation of CASTEP/DFT results with experimental data from literature.¹²

Appendix A

Table S A.8. Theoretical and experimental values for ^{49}Ti isotope of different perovskite and ilmenite-type structures.

	Ti-49			Euler angles / °			Shielding parameters			Ti-49, Experiment, our data				
	ICSD #	C_Q / MHz	η_Q	α	β	γ	δ_{iso} / ppm	Ω / ppm	κ / ppm	C_Q / MHz	η_Q	δ_{iso}^* / ppm	Ω / ppm	κ / ppm
SrTiO₃ ¹³	23076	0.00	0.00	0	0	0	-187.7	0.0	n/a	0.00	0.00	-847	0	
CaTiO₃ ¹⁴	153172	2.55	0.83	78	65	303	-182.9	42.5	0.797	3.01	0.62	-855.5	0	
BaTiO₃ ¹⁵	157806	2.52	0.00	0	0	0	-295.3	60.2	1	SI 2.74	0.00	-732		
BaTiO₃	157806	2.52	0.00	0	0	0	-295.3	60.2	1	SII 3.23	0.20	-735		
CdTiO₃ ¹⁶	62151	3.18	0.93	102	50	268	-221.5	37.2	0.546					
CdTiO₃ ¹⁷	5310	10.55	0.00	90	90	180	-168.9	204.4	-1	11.32	0.00	-789	165	-1.0
FeTiO₃ ¹⁸	153491	-1.57	0.00	90	90	180	-1326.9	545.2	-1					
MgTiO₃ ¹⁹	164766	14.59	0.00	90	90	180	-224.8	184.6	-1	16.00	0.00	-800	180	-1
PbTiO₃ ²⁰	61168	10.31	0.00	0	0	0	-242.8	237.0	1	8.38	0.00	-750.9	380	1
ZnTiO₃ ¹⁷	262709	13.92	0.00	90	90	180	-239.7	180.3	-1	15.25	0.00	-800	200	-1
SnTiO₃ Theoretical / Ilmenite	---	6.04	0.00	90	90	180	-149.3	32.5	-1	7.29	0.00	-865.1	< 40	-1

*from MAS measurements when available

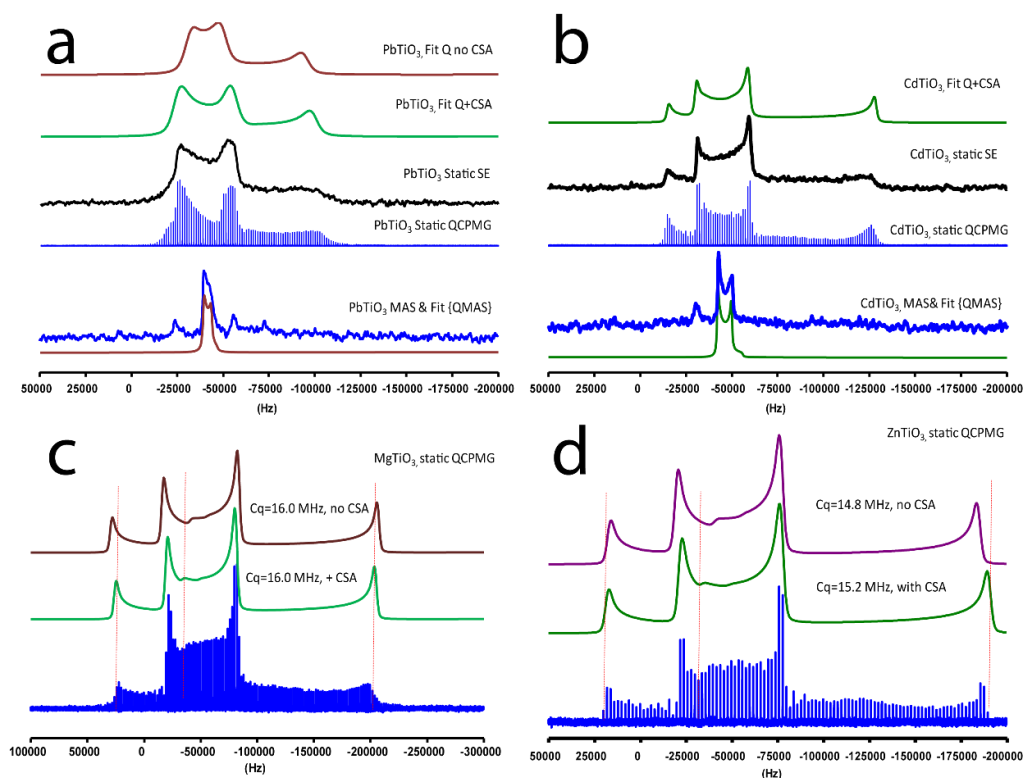


Figure S A.8. Solid-State NMR $^{47,49}\text{Ti}$ static spin-echo and QCPMG spectra for a) PbTiO_3 (P4mm), b) CdTiO_3 (R-3), c) MgTiO_3 (R-3) and d) ZnTiO_3 (R-3), each with corresponding fits with and without Chemical Shift Anisotropy (CSA). For a) and b) MAS spinning was included.

A.13 Quantum Chemical Calculations – Modelling of the polytypes

The stacking faulted nature of SnTiO₃ was further modelled by DFT using the above described models of stacking types AB, ABC/ACB, ABCB and ABCACB. DFT calculations using CRYSTAL14 [21] at different levels of theory were performed to compare total energies. Besides the standard LDA (VWN)^[22] and GGA (PBE)^[9] functionals, the hybrid-functional HSE06^[23] was applied. Optimized all-electron basis sets for all atoms were taken from [24, 25, 26]. The Kohn-Sham matrix was diagonalized on a k-mesh of at least 6 x 6 x 6 and the convergence criterion was set to 10⁻⁹ a.u. For the evaluation of the Coulomb and Exchange integrals (TOLINTEG), tolerance factors of 10 10 10 10 20 were used.

Further, a direct space analysis of the charge density was carried out by calculating the electron localization function (ELF) with TOPOND^[27] interfaced to CRYSTAL14 for the ABC model. 3D plots were visualized with XCrysDen^[28].

Table S A.9. Optimized lattice parameters and cell volumes per formula unit for the stacking models of SnTiO₃. c* corresponds to the fraction of c by the number of layers

	stacking	AB	ABC	ACB	ABCB	ABCACB
	space group	<i>P</i> -31 <i>c</i> (163)	<i>R</i> -3 (148)	<i>R</i> -3 (148)	<i>P</i> -31 <i>c</i> (163)	<i>P</i> -3 (147)
xc-functional						
LDA	<i>a</i> / Å	5.024	5.024	5.024	5.024	5.024
	<i>c</i> / Å	12.965	19.480	19.482	25.952	38.942
	<i>c</i> * / Å	6.483	6.493	6.494	6.488	6.490
	<i>V</i> per f.u. / Å ³	70.87	70.96	70.97	70.91	70.93
GGA	<i>a</i> / Å	5.134	5.134	5.134	5.134	5.134
	<i>c</i> / Å	13.856	20.738	20.743	27.685	41.528
	<i>c</i> * / Å	6.928	6.913	6.914	6.921	6.921
	<i>V</i> per f.u. / Å ³	79.08	78.88	78.91	78.99	78.99
HSE06	<i>a</i> / Å	5.073	5.073	5.073	5.073	5.073
	<i>c</i> / Å	13.940	20.851	20.855	27.809	41.700
	<i>c</i> * / Å	6.970	6.950	6.952	6.952	6.950
	<i>V</i> per f.u. / Å ³	77.68	77.45	77.46	77.47	77.45

A.14 References

1. Treacy, M. M. J.; Newsam, J. M.; Deem, M. W., A General Recursion Method for Calculating Diffracted Intensities from Crystals Containing Planar Faults. *Proc. R. Soc. London, Ser. A* **1991**, *433* (1889), 499-520.
2. de Groot, F. M. F.; Faber, J.; Michiels, J. J. M.; Czyżyk, M. T.; Abbate, M.; Fuggle, J. C., Oxygen 1s x-ray absorption of tetravalent titanium oxides: A comparison with single-particle calculations. *Physical Review B* **1993**, *48* (4), 2074-2080.
3. Hahn, E. L., Spin Echoes. *Physical Review* **1950**, *80* (4), 580-594.
4. Larsen, F. H.; Jakobsen, H. J.; Ellis, P. D.; Nielsen, N. C., QCPMG-MAS NMR of Half-Integer Quadrupolar Nuclei. *Journal of Magnetic Resonance* **1998**, *131* (1), 144-147.
5. Massiot, D.; Fayon, F.; Capron, M.; King, I.; Le Calvé, S.; Alonso, B.; Durand, J.-O.; Bujoli, B.; Gan, Z.; Hoatson, G., Modelling one- and two-dimensional solid-state NMR spectra. *Magn. Reson. Chem.* **2002**, *40* (1), 70-76.
6. Perras, F. A.; Widdifield, C. M.; Bryce, D. L., QUEST—QUadrupolar Exact SoftWare: A fast graphical program for the exact simulation of NMR and NQR spectra for quadrupolar nuclei. *Solid State Nucl. Magn. Reson.* **2012**, *45-46*, 36-44.
7. Yates, J. R.; Pickard, C. J.; Mauri, F., Calculation of NMR chemical shifts for extended systems using ultrasoft pseudopotentials. *Physical Review B* **2007**, *76* (2), 024401.
8. Clarke, S. J.; Fowkes, A. J.; Harrison, A.; Ibberson, R. M.; Rosseinsky, M. J., Synthesis, Structure, and Magnetic Properties of NaTiO₂. *Chem. Mater.* **1998**, *10* (1), 372-384.
9. Perdew, J. P.; Burke, K.; Ernzerhof, M., Generalized Gradient Approximation Made Simple. *Phys. Rev. Lett.* **1996**, *77* (18), 3865-3868.
10. Perdew, J. P.; Burke, K.; Ernzerhof, M., Generalized Gradient Approximation Made Simple [Phys. Rev. Lett. *77*, 3865 (1996)]. *Phys. Rev. Lett.* **1997**, *78* (7), 1396-1396.
11. Adiga, S.; Aebi, D.; Bryce, D. L., EFGShield — A program for parsing and summarizing the results of electric field gradient and nuclear magnetic shielding tensor calculations. *Can. J. Chem.* **2007**, *85* (7-8), 496-505.
12. Mackenzie, K.; Smith, M., *Multinuclear Solid-State NMR of Inorganic Materials*. Pergamon: Amsterdam, 2002; Vol. Volume 6, p v-vii.
13. Hutton, J.; Nelmes, R. J.; Scheel, H. J., Extinction corrections for a highly perfect crystal (SrTiO₃). *Acta Crystallographica Section A* **1981**, *37* (6), 916-920.
14. Ali, R.; Yashima, M., Space group and crystal structure of the Perovskite CaTiO₃ from 296 to 1720K. *J. Solid State Chem.* **2005**, *178* (9), 2867-2872.
15. Hikam, M.; Soegijono, B.; Sofyan, N. I., Crystallographic Structure and Electron Density of Ba_{1-x}Pb_xTiO₃ Ceramic. *Journal of Applied Sciences* **2006**, *6* (15), 3096-3102.
16. Sasaki, S.; Prewitt, C. T.; Bass, J. D.; Schulze, W. A., Orthorhombic perovskite CaTiO₃ and CdTiO₃: structure and space group. *Acta Crystallographica Section C* **1987**, *43* (9), 1668-1674.
17. Kennedy, B. J.; Zhou, Q.; Avdeev, M., The ferroelectric phase of CdTiO₃: A powder neutron diffraction study. *J. Solid State Chem.* **2011**, *184* (11), 2987-2993.
18. Yamanaka, T., Structural changes induced by lattice-electron interactions: SiO₂ stishovite and FeTiO₃ ilmenite. *Journal of Synchrotron Radiation* **2005**, *12* (5), 566-576.
19. Ferri, E. A. V.; Sczancoski, J. C.; Cavalcante, L. S.; Paris, E. C.; Espinosa, J. W. M.; de Figueiredo, A. T.; Pizani, P. S.; Mastelaro, V. R.; Varela, J. A.; Longo, E., Photoluminescence behavior in MgTiO₃ powders with vacancy/distorted clusters and octahedral tilting. *Mater. Chem. Phys.* **2009**, *117* (1), 192-198.
20. Nelmes, R. J.; Kuhs, W. F., The crystal structure of tetragonal PbTiO₃ at room temperature and at 700 K. *Solid State Commun.* **1985**, *54* (8), 721-723.
21. CRYSTAL14 User's Manual, R. Dovesi, V. R. Saunders, C. Roetti, R. Orlando, C. M. Zicovich-Wilson, F. Pascale, B. Civalleri, K. Doll, N. M. Harrison, I. J. Bush, P. D'Arco, M. Llunell, M. Causà, Y. Noël, University of Torino, Torino, Italy: **2014**.
22. S. H. Vosko, L. Wilk, M. Nusair, Accurate spin-dependent electron liquid correlation energies for local spin density calculations: a critical analysis *Can. J. Phys.* **1980**, *58*, 1200-1211.

23. J. Heyd, G. E. Scuseria and M. Ernzerhof, Hybrid functionals based on a screened Coulomb potential. *J. Chem. Phys.* **2003**, *118*, 8207.
24. F. Pielnhofer, F. Bachhuber, J. Rothballer, F. M. Schappacher, R. Pöttgen, R. Wehrich, Half Antiperovskites VI: On the Substitution Effects in Shandites $\text{In}_x\text{Sn}_{2-x}\text{Co}_3\text{S}_2$. *Z. Anorg. Allg. Chem.* 2014, *640*, 286-294.
25. Bredow T., Heitjans P., Wilkening M. Electric field gradient calculations for Li_xTiS_2 and comparison with ^7Li NMR results. *Phys. Rev. B* 70, Art. No. 115111 (2004).
26. F. Corà, The performance of hybrid density functionals in solid state chemistry: the case of BaTiO_3 *Mol. Phys.* 103, 2483-2496 (2005).
27. C. Gatti, S. Cassassa, Topond14. User's Manual <http://www.crystal.unito.it/topond/topond.pdf>. 2016.
28. A. Kokalj, Computer graphics and graphical user interfaces as tools in simulations of matter at the atomic scale *Comp. Mater. Sci.*, **2003**, *Vol. 28*, p. 155. Code available from <http://www.xcrysden.org/>.

B: Supporting Information for High-pressure phase transitions of ilmenite-type derived SnTiO_3

Leo Diehl, Lkhamsuren Bayarjargal, Florian Pielhofer, Victor Milman, Keith Refson, Björn Winkler and Bettina V. Lotsch

To be submitted.

B.1 SHG of SnTiO_3 and three reference materials

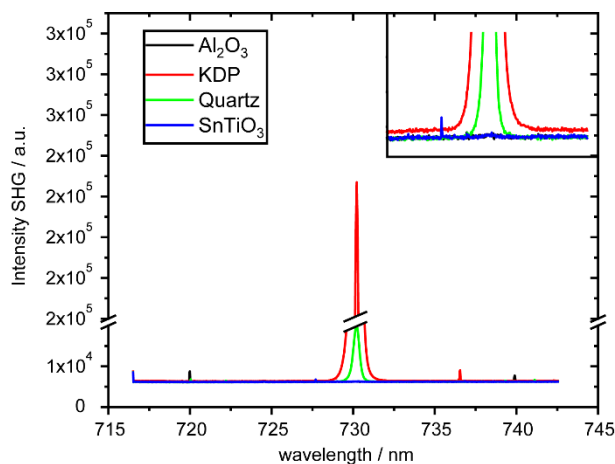
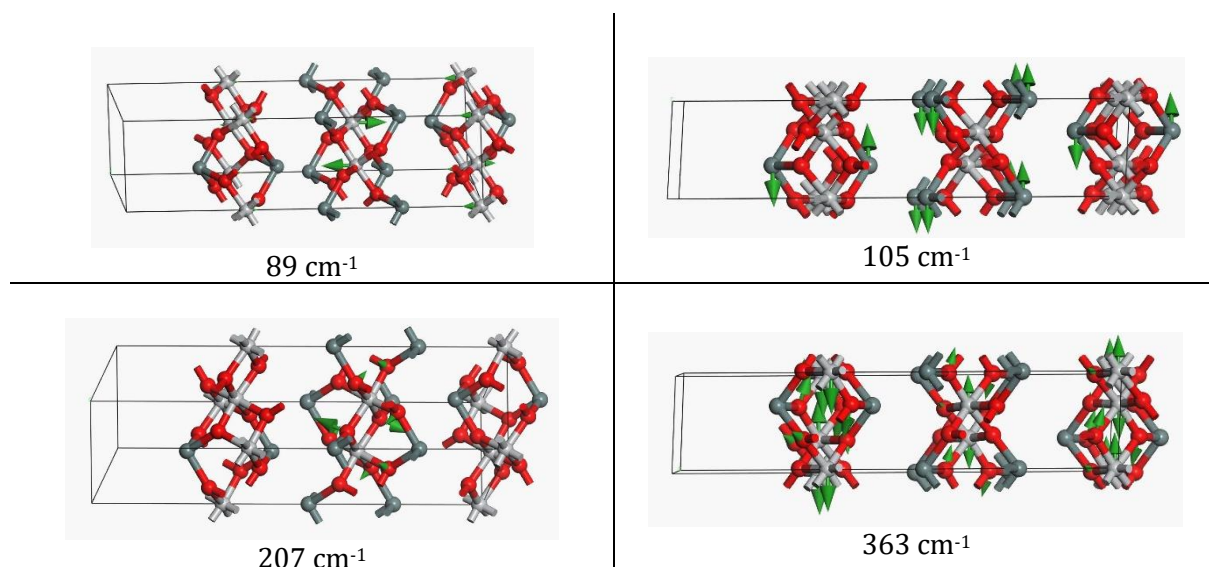


Figure S B.1. Second Harmonic Generation of centrosymmetric Al_2O_3 and the non-centrosymmetric standards KDP (KH_2PO_4) and Quartz (SiO_2) versus polycrystalline SnTiO_3 . In order to avoid absorption problems and potential two photon emission an IR laser with 1463 nm wavelength was used. The signal response of SnTiO_3 is zero and thus confirms the centrosymmetric nature of as-synthesized ilmenite-type derived SnTiO_3 .

B.2 Representation of selected vibrational modes of ABC-type SnTiO_3 ($R\bar{3}$)



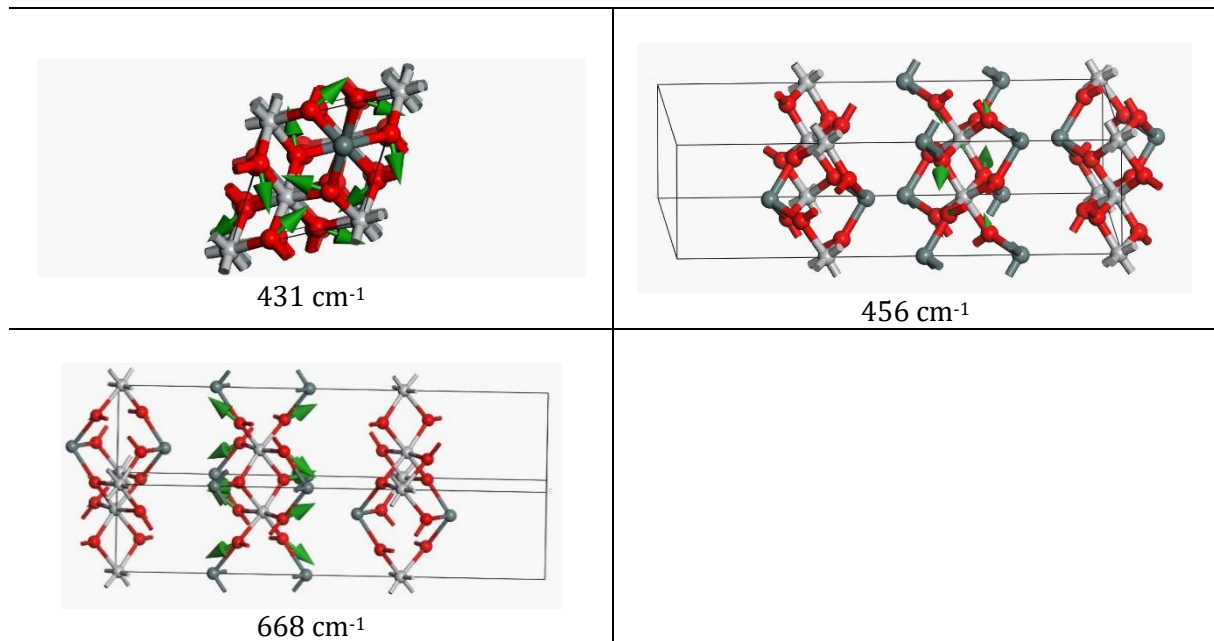


Figure S B.2. Representative visualizations of the calculated Raman modes. Sn atoms in dark grey, Ti atoms in light grey and O atoms in red. The directions and strength of displacement is given by the direction and size of the green vectors.

B.3 Analysis of peak maxima and FWHM

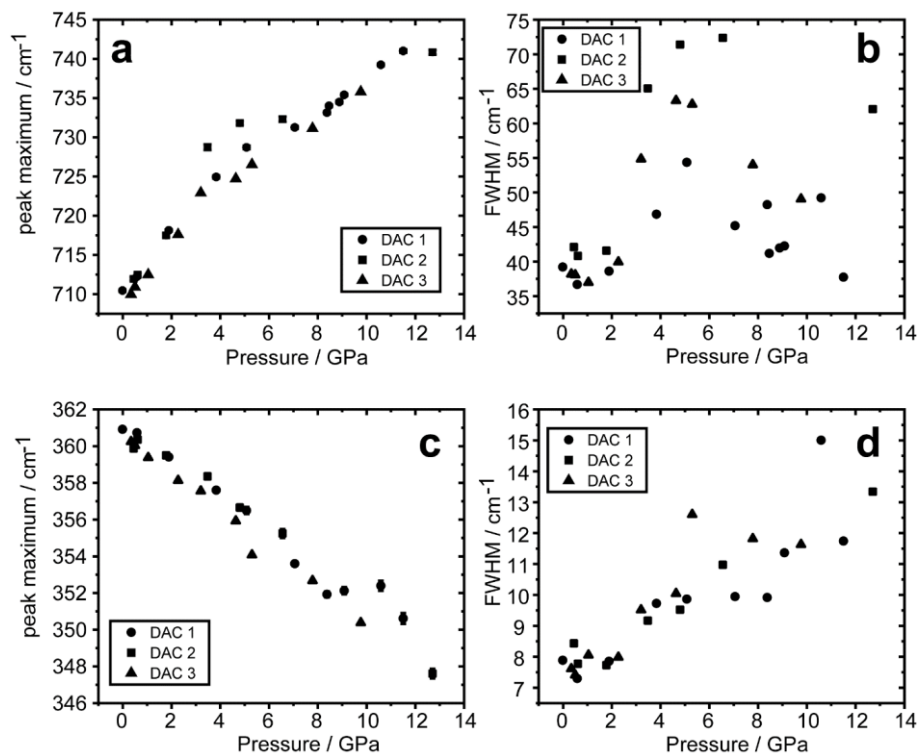


Figure S B.3. a) Analysis of the Peak maxima of the mode at 700 cm^{-1} and b) respective FWHM showing in change at around 4-5 GPa and c) analysis of peak maxima of one soft mode indicating smaller dependence of the phase transition point and d) respective FWHM.

B.4 Computational pressure dependence of Raman modes

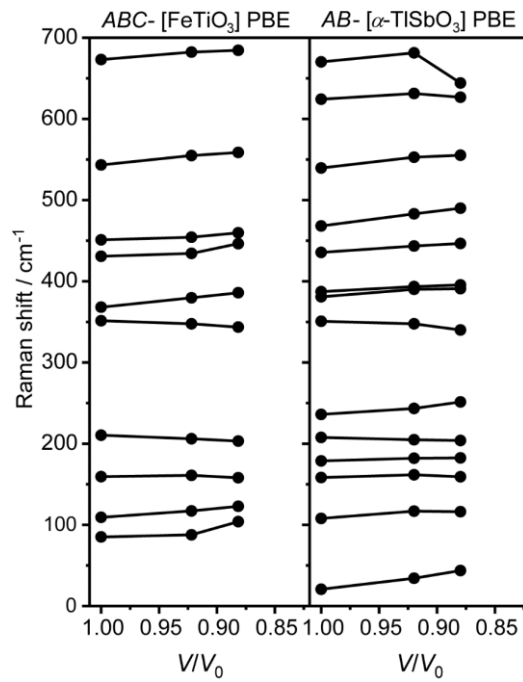


Figure S B.4. Pressure dependent DFT calculations (PBE) of Raman modes for ABC and AB-type SnTiO₃.

B.5 Grüneisen-Parameters

Table S B.1. Mode-Grüneisen parameters for linear regressions before and after PT-II. The bulk modulus 23 GPa was used as fitted from Fig. 4.5.

Mode	<5 GPa		>5 GPa	
	α ($\delta w/\delta P$) cm ⁻¹ /GPa	γ	α ($\delta w/\delta P$) cm ⁻¹ /GPa	γ
60				
86	Not reliably determinable			
113	2.9	0.60	1.4	0.3
167	0.963	0.13	0.39	0.05
183	0.944	0.12	0.97	0.12
216	-0.77	-0.08	-0.69	-0.07
361	-0.89	-0.06	-0.87	-0.06
412	2.66	0.15	1.59	0.09
453	4.7	0.24	2.8	0.14
555	Too broad to fit reliably			
710	3.73	0.12	2.06	0.07

B.6 Temperature dependence

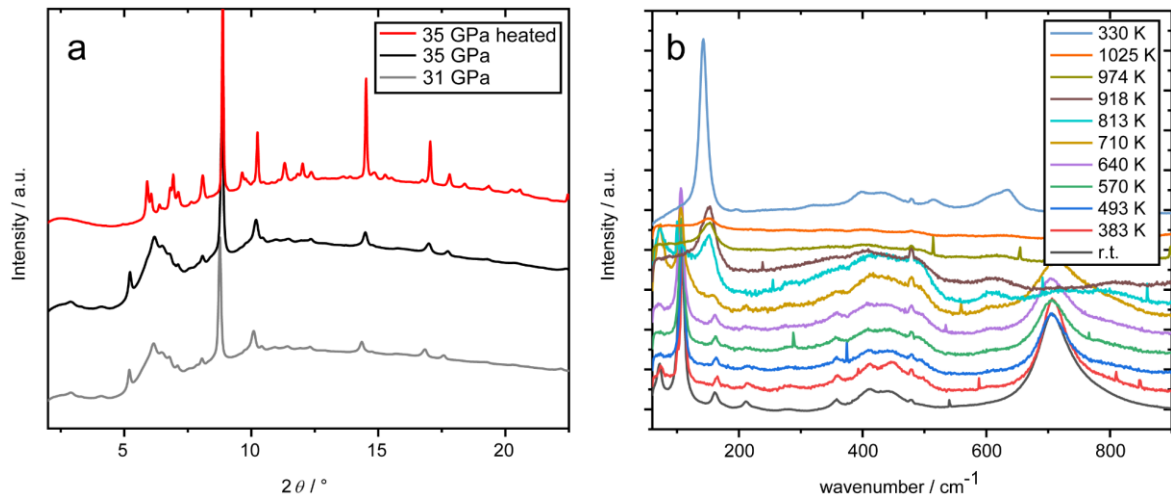


Figure S B.5. a) Diffractogram of cell heated by improvised ruby laser. The found reflections can be assigned to high-pressure phases of TiO_2 and SnO_2 . b) Raman spectra of SnTiO_3 at ambient pressure, heated up to 1025 K, indicating the degradation between 700 K and 800 K. The cooled sample shows Raman modes typical for SnO_2 at $\sim 470 \text{ cm}^{-1}$, 630 cm^{-1} and TiO_2 at $\sim 140 \text{ cm}^{-1}$, 400 cm^{-1} , 520 cm^{-1} and 640 cm^{-1} .

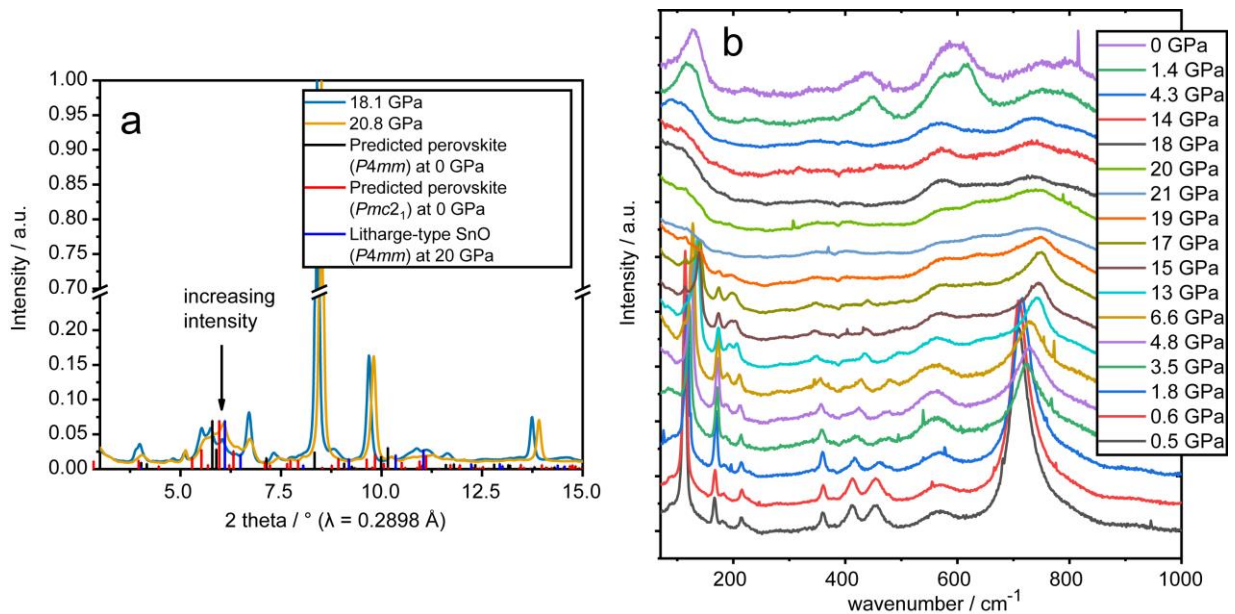
B.7 Possible high-pressure perovskite-like SnTiO_3 

Figure S B.6. a) Increasing intensity at about 6° 2θ , fitting the highest intensity reflection of the predicted perovskite-like structures. Small deviation of peak maximum can be explained by further compression expected at the point of phase transition around 20 GPa. No conclusions about symmetry are possible. Reflections of high intensity at about 8° , 9.5° and 13.8° are solid Neon. SnO lattice parameters at high-pressure are taken from Giefers et al.¹ b) Raman spectra into pressure region above PT-III, showing the loss of any regular vibrations, due to amorphization and dominating rutile TiO_2 vibrations after cooling and proving irreversibility of PT-III.

B.8 References

1. Giefers, H.; Porsch, F.; Wortmann, G., Structural study of SnO at high pressure. *Physica B: Condensed Matter* **2006**, *373* (1), 76-81.

C: Supporting Information for

Competing factors in the directed design of photocatalysts: The case of SnTiO_3

Leo Diehl, Douglas Fabini, Theresa Block, Nella Vargas-Barbosa, Alberto Jiménez-Solano,
Florian Pielhofer, Tanmay Banerjee, Viola Duppel, Kathrin Küster, Rainer Pöttgen
and Bettina V. Lotsch

To be submitted.

C.1 Electronic and Optical properties

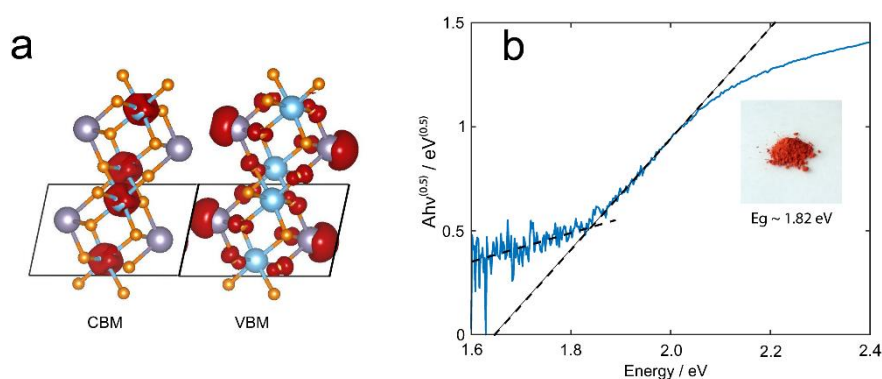


Figure S C.1. a) Scheme of different localizations of the Ti dominated CBM and the Sn-O dominated CBM. b) Tauc-plot for SnTiO_3 assuming an indirect band gap including picture of SnTiO_3 powder.

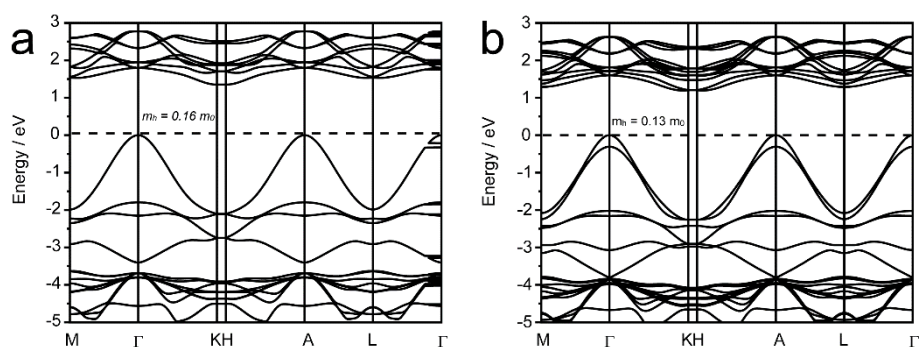


Figure S C.2. 2-layer (a) and 3-layer (b) band structures including hole effective masses, $0.16 m_e$ for 2L and $0.13 m_e$ for 3L slab.

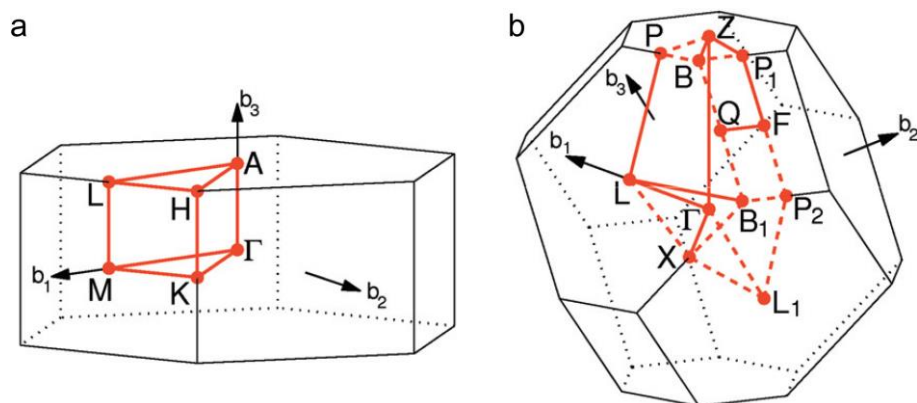


Figure S C.3. Brillouin-Zones of space group $R\bar{3}$ in hexagonal setting a) and rhombohedral b) with indication of paths as proposed by Setyawan *et al.*¹ (Reproduced with permission of Elsevier 2010).

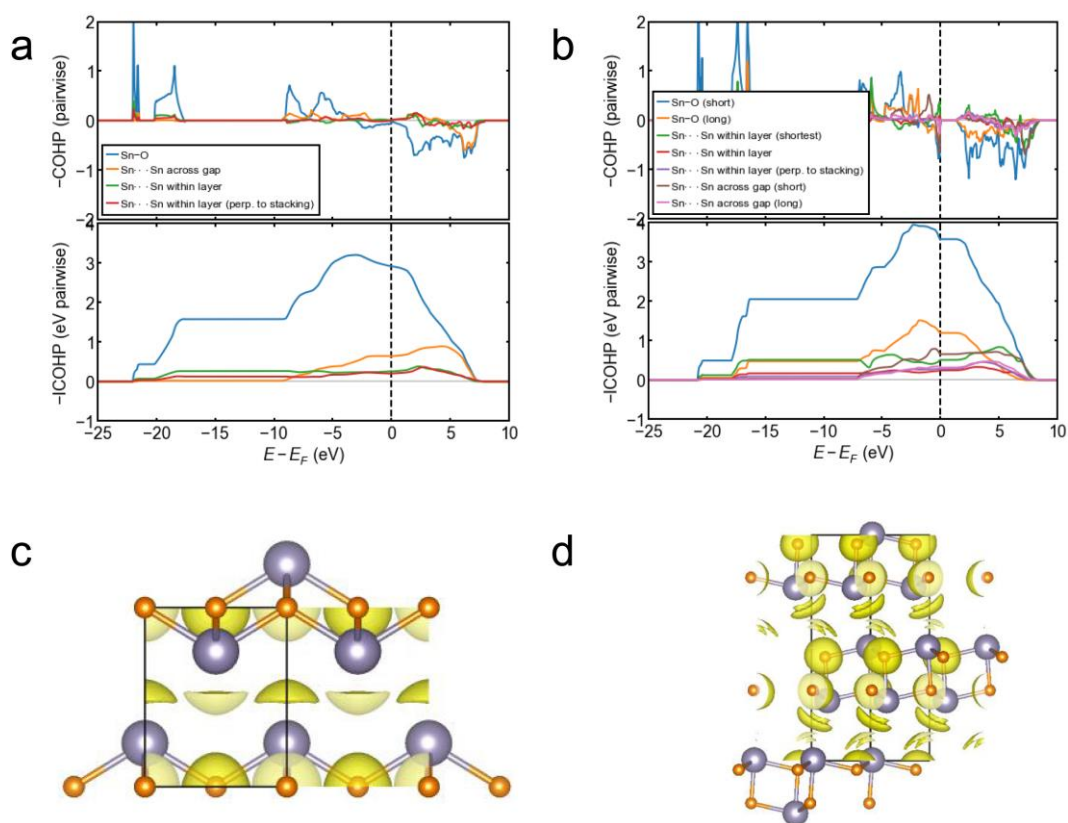


Figure S C.4. a) COHP for litharge-type SnO ($P4/nmm$), showing bonding interaction of interlayer Sn-Sn and b) COHP for red SnO ($Cmc2_1$) with 2/3 of the bonding Sn-Sn interactions compared to black SnO, probably due to different orientation of the lone pairs as seen from the ELF. Electron Localization function (ELF) at 0.6 of c) black SnO and d) red SnO.

C.2 Thermogravimetric Analysis (TGA)

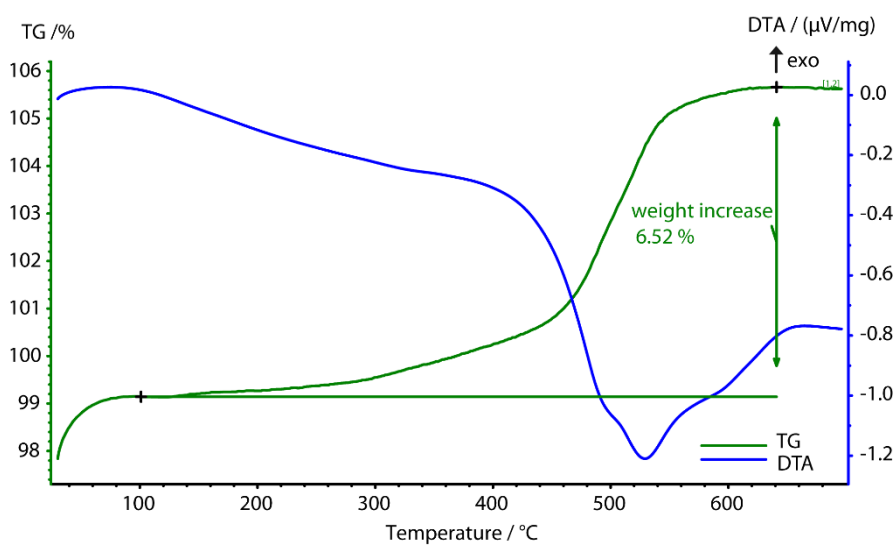


Figure S C.5. Thermogravimetric analysis (TGA) of full oxidation of SnTiO_3 powder, also measured in NMR and Mössbauer spectroscopy. Complete oxidation with weight increase of $\sim 6.5\%$ corresponding initial presence of about 12 % Sn^{4+} .

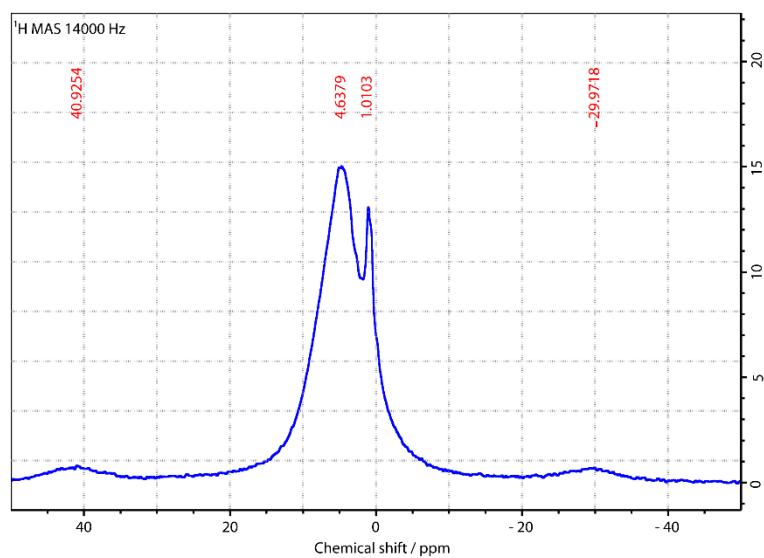
C.3 ^1H ss-NMR

Figure S C.6. ^1H -NMR showing side bands (40 and 30 ppm) and two ^1H species at 4.6 ppm and 1 ppm.

C.4 X-ray photoelectron spectroscopy (XPS)

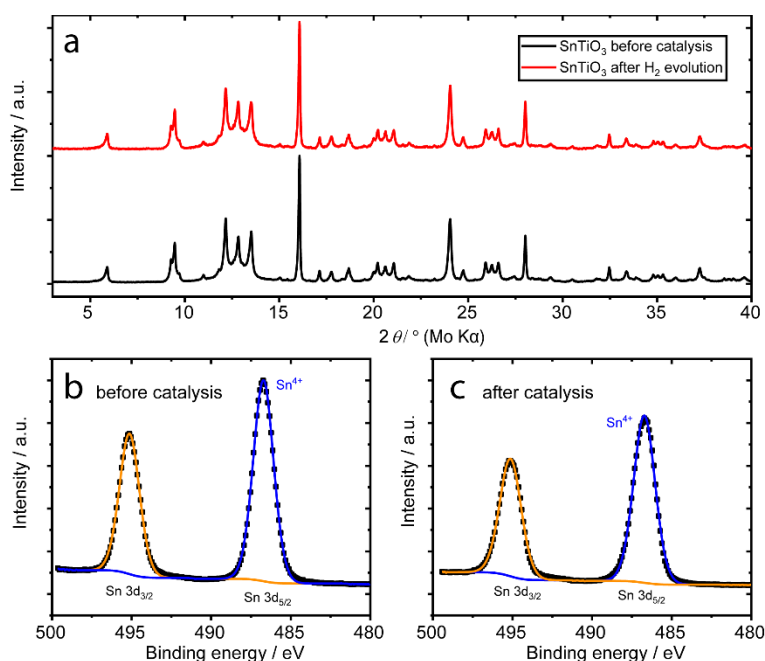


Figure S C.7. a) XRPD before and after catalysis ($\lambda = \text{Mo K}\alpha_1$) b) XP spectrum before catalytic testing in a basic (0.1 M KOH), 10vol% methanolic solution, showing Sn⁴⁺ on surface c) XP spectrum after catalysis, unchanged compared to before catalysis.

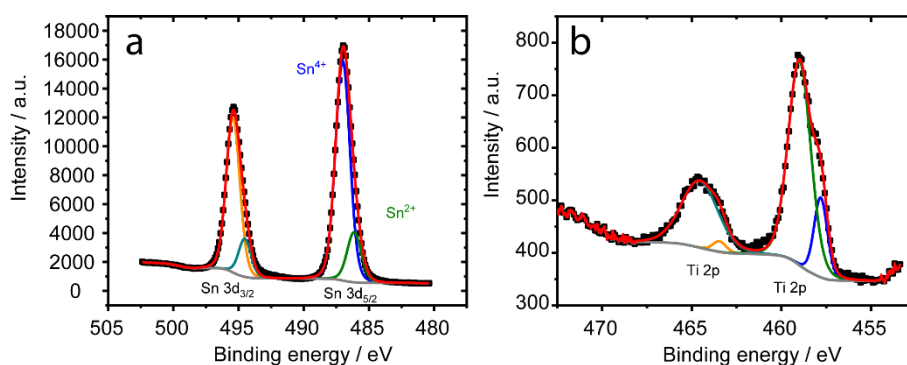


Figure S C.8. a) XP spectrum of Sn 3d Sn₂TiO₄ with similar peak positions compared to SnTiO₃ and very similar ratios of Sn⁴⁺ to Sn²⁺ and b) XP spectrum of Ti 2p showing two Ti species. The ratio of Sn:Ti is also underestimated by a factor of 5 similar to SnTiO₃.

C.5 Exfoliation Energy

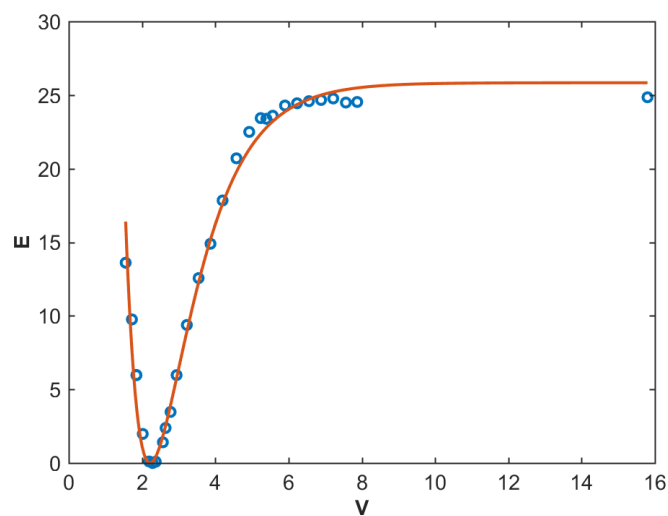


Figure S C.9. Computational determination of exfoliation energy for SnTiO_3 on PBE-D2 level of theory. It can be seen that the datapoints cannot be perfectly fit by a Morse potential (red line).

C.6 Composition

Table S C.1. Elemental analysis for Ti and Sn (ICP-OES) from different SnTiO_3 samples showing Ti to Sn ratio.

	Ti	Sn
LD-lp-81b-red	4.39	4.62
II	4.37	4.32
LD-lp-81b-red/heavy	4.22	4.31
II	4.47	4.75
LD-lp-81b-yellow	4.21	4.18
II	4.25	4.27
LD-lp-71w-red	4.08	4.32
II	4.10	4.40
LD-lp-71w-red2	4.33	4.27
II	4.44	4.32
LD-lp-71w-yellow	4.07	4.48
II	4.02	4.51
	4.25	4.40
	3.5 mol% excess Sn	

C.7 Photocurrent switching

SnTiO₃ showed a rather exotic behavior in photoelectrochemical measurements. Figure S 10a shows the photocurrent response of a thin film electrode of SnTiO₃ visible-light (cut-off filter 420 nm). At a potential of about 0.74 V vs. RHE the photocurrent direction switches from photoanodic at higher potentials to photocathodic at lower potentials. This phenomenon has been observed in other (lone pair) materials and has been coined “photocurrent switching”². The stability of the photoresponse was proven over five minutes (Fig. S 10b). The most accurate description for the observed process was given by Gaweda *et al.*³ and they explain the switching by thermodynamically blocked hole transfer to the electrolyte, due to a valence band that is too negative (on the electrochemical scale) for effectively quenching the hole. Consequently, the electrode will prefer reacting as a photocathode, draining the holes through FTO (Fig. S 10c). The photocurrent switching effect has been observed for akin materials such as Cu₂O⁴ and BiVO₄². The potentials of current switching were at - 0.6 V and +0.7 V against Ag/AgCl (pH = 6.5 for Cu₂O => 0.283 V vs RHE and pH = 7 for BiVO₄ => 1.113 V vs RHE) respectively. The switching potential for SnTiO₃ lies well above the known redox potentials for Sn⁴⁺ + 2 e⁻ -> Sn²⁺ from the galvanic series. It fits however the expected trend of oxidizability from Cu¹⁺ over Sn²⁺ to Bi³⁺. (+0.16 V Cu²⁺ + e⁻ -> Cu⁺, but as one electron process, Sn⁴⁺ + 2 e⁻ -> Sn²⁺ +0.15 V, Bi⁵⁺ + 2e⁻ -> Bi³⁺ ~ +2 V).

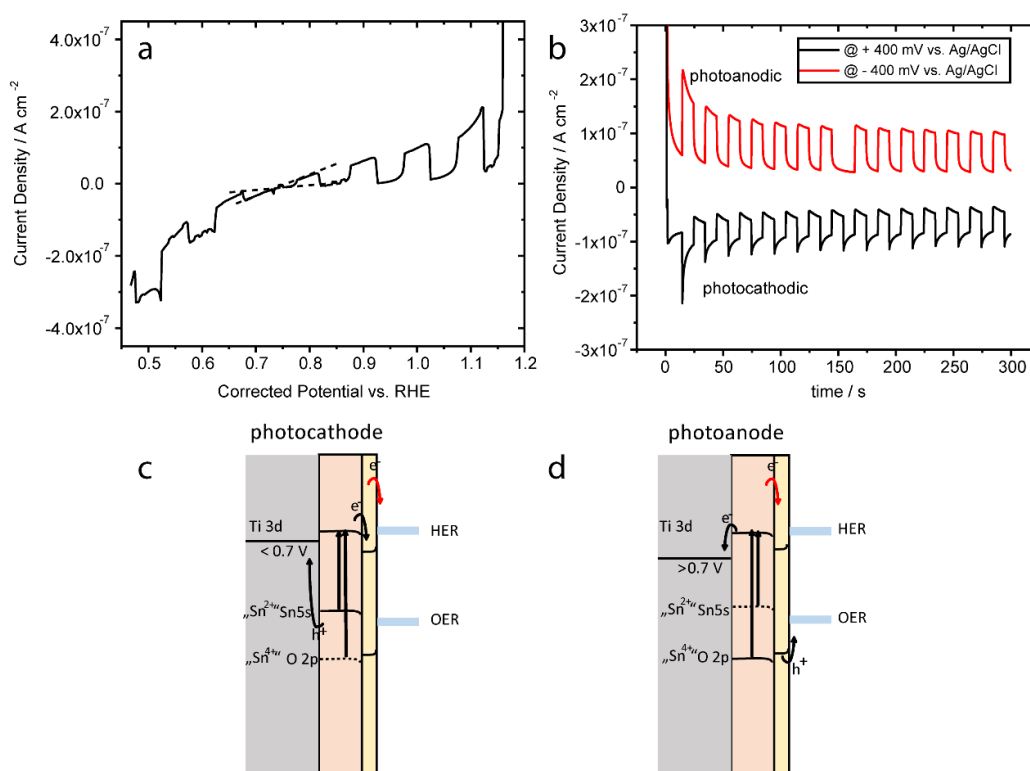


Figure S C.10. a) Photocurrent switching effect under visible light for thin film SnTiO₃ on FTO. b) Stability test at potentials positive and negative of the photocurrent switching potential, indicating stable currents over minutes. Schemes explaining occupation of in-gap states and corresponding c) photocathodic or d) photoanodic response.

For BiOCl it was discussed that the presence of surface states induced by Bi³⁺ corrosion are inducing the unusual photocurrent response⁵ and Kudo found surface states in BiVO₄ to be correlated with the photocurrent switching potential². As we have seen in the main text SnTiO₃ on the surface is indeed prone to oxidation to Sn⁴⁺ species. The observed photocurrent switching further supports this observation. In fact the surface states present, may be thought of as the in-gap states of “empty” Sn⁴⁺. This would drastically change the valence band position under reaction conditions and may change the hole transfer behavior to the electrolyte. The resulting surface state/Sn⁴⁺ species might be required to enable hole transfer to water such that the electrode optimizes the surface chemistry at the cost of holes needed for Sn²⁺ oxidation first. Thus the valence band maximum at the surface of the electrode which is mostly consisting of the filled *s*-orbital of Sn²⁺ is now empty, leaving “surface states” within the band gap.

C.8 Wavelength dependent H₂ evolution

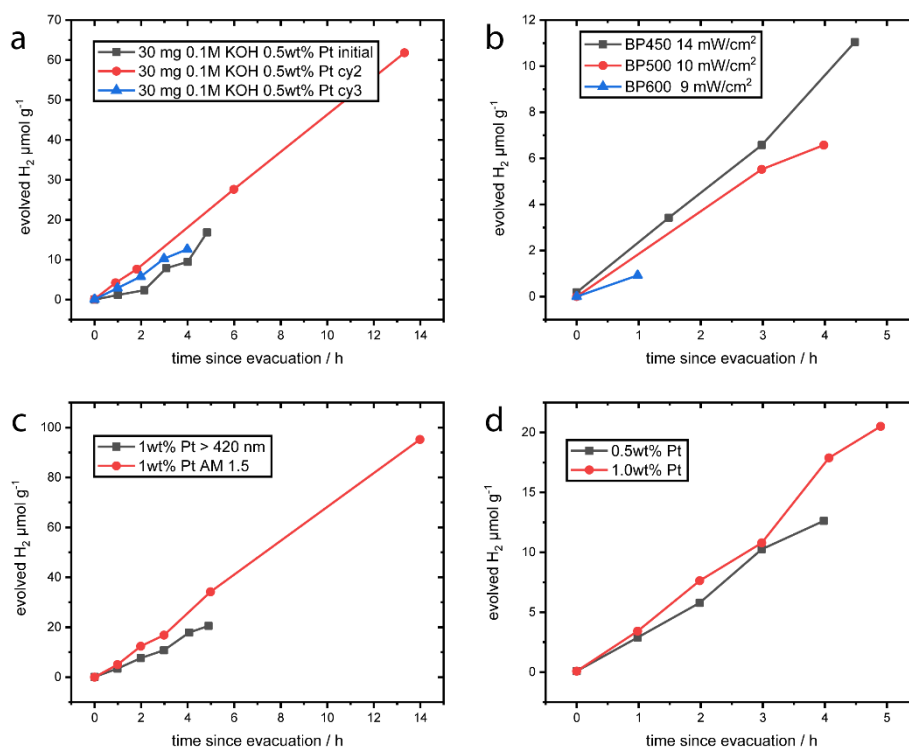


Figure S C.11. Direct comparison of different photocatalytic conditions. a) Cycle number dependence, b) wavelength dependence, c) AM1.5 vs visible light only and d) co-catalyst loading.

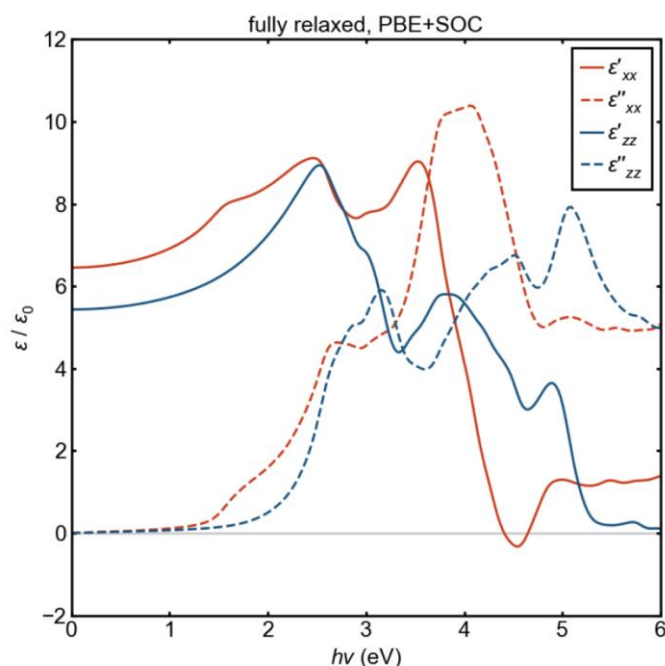
C.9 Dielectric constants for SnTiO₃, directional dependence

Figure S C.12. Theoretically determined (DFT-GGA) dielectric functions (imaginary and real parts) into in-plane (ϵ_{xx}) and out-of-plane direction (ϵ_{zz}).

Depending on the depth of the trapped charge carrier or defect, excitonic recombination might also lead to increased luminescence, sometimes with strong Stokes shifts. A shift between absorption and emission spectra has been observed in other 2D materials and is explained by a combination of quantum and dielectric confinement effects⁶⁻⁷. In the group of Karunadasa⁸⁻⁹ it was shown that strong anisotropy of the dielectric constant between an organics dominated “barrier” and the transition metal dominated “well” in hybrid perovskites induces white-light emission from self-trapped charge carriers¹⁰. For SnTiO₃, the dielectric constants in the optical regime also show some degree of anisotropy (Fig. S C.12).

C.10 References

1. Setyawan, W.; Curtarolo, S., High-throughput electronic band structure calculations: Challenges and tools. *Computational Materials Science* **2010**, *49* (2), 299-312.
2. Antuch, M.; Millet, P.; Iwase, A.; Kudo, A., The role of surface states during photocurrent switching: Intensity modulated photocurrent spectroscopy analysis of BiVO₄ photoelectrodes. *Applied Catalysis B: Environmental* **2018**, *237*, 401-408.
3. Gawęda, S.; Kowalik, R.; Kwolek, P.; Macyk, W.; Mech, J.; Oszajca, M.; Podborska, A.; Szaciłowski, K., Nanoscale Digital Devices Based on the Photoelectrochemical Photocurrent Switching Effect: Preparation, Properties and Applications. *Isr. J. Chem.* **2011**, *51* (1), 36-55.
4. Qi, H.; Wolfe, J.; Fichou, D.; Chen, Z., Cu₂O Photocathode for Low Bias Photoelectrochemical Water Splitting Enabled by NiFe-Layered Double Hydroxide Co-Catalyst. *Scientific Reports* **2016**, *6*, 30882.
5. Stephenson, J.; Celorrio, V.; Tiwari, D.; Hall, S. R.; Green, D. C.; Fermín, D. J., Photoelectrochemical properties of BiOCl microplatelets. *J. Electroanal. Chem.* **2018**, *819*, 171-177.
6. Muljarov, E. A.; Tikhodeev, S. G.; Gippius, N. A.; Ishihara, T., Excitons in self-organized semiconductor/insulator superlattices: PbI-based perovskite compounds. *Physical Review B* **1995**, *51* (20), 14370-14378.
7. Hanamura, E.; Nagaosa, N.; Kumagai, M.; Takagahara, T., Quantum wells with enhanced exciton effects and optical non-linearity. *Materials Science and Engineering B: Solid-State Materials for Advanced Technology* **1988**, *1* (3-4), 255-258.
8. Smith, M. D.; Pedesseau, L.; Kepenekian, M.; Smith, I. C.; Katan, C.; Even, J.; Karunadasa, H. I., Decreasing the electronic confinement in layered perovskites through intercalation. *Chemical Science* **2017**, *8* (3), 1960-1968.
9. Smith, M. D.; Watson, B. L.; Dauskardt, R. H.; Karunadasa, H. I., Broadband Emission with a Massive Stokes Shift from Sulfonium Pb-Br Hybrids. *Chem. Mater.* **2017**, *29* (17), 7083-7087.
10. Williams, R. T.; Song, K. S., The self-trapped exciton. *J. Phys. Chem. Solids* **1990**, *51* (7), 679-716.

D. List of Publications and Contributions

Publications included in this thesis are marked with an asterisk.

1. Junggeburth, S. C.; Diehl, L.; Werner, S.; Duppel, V.; Sigle, W. and Lotsch, B. V.; Ultrathin 2D Coordination Polymer Nanosheets by Surfactant-Mediated Synthesis. *J. Am. Chem. Soc.* **2013**, *135* (16), 6157-6164. DOI: 10.1021/ja312567v
2. Zeller, P.; Henß, A.-K.; Weinl, M.; Diehl, L.; Keefer, D.; Lippmann, J.; Schulz, A.; Kraus, J.; Schreck, M.; and Wintterlin, J.; Detachment of CVD-grown graphene from single crystalline Ni films by a pure gas phase reaction. *Surf. Sci.* **2016**, *653*, 143-152. DOI: 10.1016/j.susc.2016.06.014
3. *Diehl, L.; Bette, S.; Pielhofer, F.; Betzler, S.; Moudrakovski, I.; Ozin, G. A.; Dinnebier, R. and Lotsch, B. V., Structure-Directing Lone Pairs: Synthesis and Structural Characterization of SnTiO₃. *Chem. Mater.* **2018**, *30* (24), 8932-8938. DOI: 10.1021/acs.chemmater.8b04261

LD synthesized the material and wrote the manuscript. LD and SB solved the crystal structure and SB developed the model of polytypes. FP performed the DFT calculations, SB measured the HRTEM and EELS, IM measured and fit the NMR spectra and GAO, RD proofread the manuscript and contributed through discussions, while BVL supervised the project.

4. Diehl, L.; Pielhofer, F. and Lotsch, B. V., European Patent Application PCT/EP2019/061231, **2019**.
5. Podjaski, F.; Weber, D.; Zhang, S.; Diehl, L.; Eger, R.; Duppel, V.; Alarcon-Llado, E.; Richter, G.; Haase, F.; Fontcuberta i Morral, A.; Scheu, C. and Lotsch, B.V., Rational strain engineering in delafossite oxides for highly efficient hydrogen evolution catalysis in acidic media. *Nature Catalysis* **2019**. DOI: 10.1038/s41929-019-0400-x
6. Zhang, S.#; Diehl, L.#; Wrede, S.; Lotsch, B. V. and Scheu, C.; Structural Evolution of Ni-Based Co-Catalysts on [Ca₂Nb₃O₁₀]⁻ Nanosheets during Heating and Their Photocatalytic Properties. *Catalysts* **2019**, *10*(1), 13. DOI: 10.3390/catal10010013
equal contributions.
7. *Pielhofer, F.; Diehl, L.; Jiménez-Solano, A.; Bußmann-Holder, A.; Schön J. C. and Lotsch, B. V.; Examining experimentally accessible structural candidates of SnTiO₃: The search for novel ferroelectric materials, *to be submitted*.

FP and LD wrote the manuscript and conceptualized the work. FP performed all DFT calculations, AJS fit the bulk moduli, ABH calculated the soft mode behavior and JCS implemented the global search algorithm. BVL supervised the project.

8. *Diehl, L.; Bayarjargal, L.; Pielhofer, F.; Milman, V.; Refson, K.; Winkler, B. and Lotsch, B. V.; High-pressure phase transitions of ilmenite-type derived SnTiO₃, *to be submitted*.

LD wrote the manuscript. LD and BVL conceptualized the work, LB experimentally helped with the Raman spectroscopy and diffraction experiments, FP performed DFT calculations, as well as VM, KR and BW. BVL supervised the project.

9. *Diehl, L.; Fabini, D.; Block, T.; Vargas-Barbosa, N.; Jiménez-Solano, A.; Pielhofer, F.,; Banerjee, T.; Duppel, V.; Küster, K.; Pöttgen, R. and Lotsch, B. V.; Competing factors in the directed design of photocatalysts: The case of SnTiO₃, *to be submitted*.

LD characterized the material photocatalytically and wrote the manuscript, supported in the passages about DFT interpretation by DF. DF calculated most DFT results. TB measured the Mössbauer spectra, NVB helped with the measurement of photoelectrochemistry, AJS measured PL spectra, FP contributed exfoliation energies, TB also measured PL spectra, VD prepared the TEM images, KK the XP-spectra, RP provided help with the interpretation of the Mössbauer data and BVL supervised the project.

10. Oral presentation “Schicht für Schicht – Struktur und Eigenschaften von SnTiO₃“ at Hirschegg-Seminar **2018**, Kleinwalsertal.
11. Posters at Green Chemistry Symposium Toronto **2016**, at CeNS meeting Venice, Italy **2017** and NIM and CeNS winter and summer schools.